

Report PME-FM-91-3

2

AD-A246 651



**TURBULENCE STRUCTURE AND POLYMER DRAG REDUCTION IN
ADVERSE PRESSURE GRADIENT BOUNDARY LAYERS**

John E. Koskie and William G. Tiederman
School of Mechanical Engineering
Purdue University
West Lafayette, Indiana 47907

DTIC
SELECTED
FEB 24 1992
S B D

December 1991

Technical Report for Period 01 December 1990 - 31 December 1991

Approved for public release, distribution unlimited

Prepared for

OFFICE OF NAVAL RESEARCH
800 North Quincy Street
Arlington, VA 22217-5000

92 2 18 185

92-04153



REPORT DOCUMENTATION PAGE		READ INSTRUCTIONS BEFORE COMPLETING FORM
1. REPORT NUMBER PME-FM-91-3	2. GOVT ACCESSION NO.	3. RECIPIENT'S CATALOG NUMBER
4. TITLE (and Subtitle) TURBULENCE STRUCTURE AND POLYMER DRAG REDUCTION IN ADVERSE PRESSURE GRADIENT BOUNDARY LAYERS		5. TYPE OF REPORT & PERIOD COVERED Technical Report 01 Dec. 1990 -31 Dec. 1991
		6. PERFORMING ORG. REPORT NUMBER
7. AUTHOR(s) John E. Koskie and William G. Tiederman		8. CONTRACT OR GRANT NUMBER(s) N00014-91-J-1446
9. PERFORMING ORGANIZATION NAME AND ADDRESS School of Mechanical Engineering Purdue University West Lafayette, IN 47907		10. PROGRAM ELEMENT, PROJECT, TASK AREA & WORK UNIT NUMBERS 4322754---08
11. CONTROLLING OFFICE NAME AND ADDRESS Office of Naval Research 800 North Quincy Street Arlington, VA 22217-5000		12. REPORT DATE December 1991
		13. NUMBER OF PAGES 214
14. MONITORING AGENCY NAME & ADDRESS (if different from Controlling Office)		15. SECURITY CLASS. (of this report)
		15a. DECLASSIFICATION/DOWNGRADING SCHEDULE
16. DISTRIBUTION STATEMENT (of this Report) Approved for Public Release Distribution Unlimited		
17. DISTRIBUTION STATEMENT (of the abstract entered in Block 20, if different from Report)		
18. SUPPLEMENTARY NOTES		
19. KEY WORDS (Continue on reverse side if necessary and identify by block number) Drag reduction; Turbulent structure; boundary layers		
20. ABSTRACT (Continue on reverse side if necessary and identify by block number) The objective of this study was to compare the turbulent structure of one zero pressure gradient Newtonian boundary layer and two adverse pressure gradient equilibrium boundary layers with and without the injection of water soluble, drag reducing polymers. The momentum thickness Reynolds numbers, Re_θ were in the range 1360 to 4980. The adverse pressure gradient boundary layers were characterized by equilibrium parameters, β , of 1.8 and 2.4. These boundary layers were modified by injecting a 1000 wppm solution of the polyacrylamide Separan AP-273 at 2.6 and 5.1 times the flow rate of the undisturbed linear sublayer ($y^+ \leq 5$).		

20. (continued)

The sum of viscous and Reynolds shear stresses was less than the total shear stress in the drag reduced boundary layer when the wall strain rate and polymer concentration were both high enough. In these cases the production of Reynolds shear and normal stresses was virtually eliminated. The mean streamwise velocity measurements in the drag reduced boundary layers showed that both parameters, κ and B, of the logarithmic velocity profile changed. The slope parameter, κ , varied linearly with the percent drag reduction. The peak in the root-mean-square streamwise velocities remained essentially unchanged in the presence of polymer but its location moved away from the wall. The root-mean-square normal velocities and the Reynolds shear stress were reduced in the inner region of the boundary layer during drag reduction. The adverse pressure gradient boundary layers did not separate during drag reduction even when large amounts of polymer were injected. The influence of the polymer on the turbulent boundary layer structure was greatly reduced, but the effects of polymer were consistent with those in the zero pressure gradient boundary layer. The present data are consistent with the hypothesis that the extensional motions in the flow must be strong enough to stretch the polymer molecules so that stretched molecules will form an anisotropic viscosity that damps the small scales of the turbulence (Hinch, 1977). Walker's (1985) modified mixing length model correctly predicted the wall shear stress coefficient, c_f , in all the drag reduced boundary layers as long as the measured polymer concentration in the linear sublayer was within the range of concentrations for which the model was derived and the non-Newtonian shear stresses in the boundary layer were small. When these conditions were not satisfied the predictions of c_f were conservative (too high). Mixed scaling of the average burst period best scaled the present zero and adverse pressure gradient Newtonian boundary layer data. Comparison of the present data with other Newtonian boundary layer burst measurements suggests that the method of tripping the boundary layer affects the average burst period at very low Reynolds numbers.



Accession For	
NTIS GRA&I	<input checked="" type="checkbox"/>
DTIC TAB	<input type="checkbox"/>
Unannounced	<input type="checkbox"/>
Justification	
By _____	
Distribution/	
Availability Codes	
Dist	Avail and/or Special
A-1	

TABLE OF CONTENTS

	Page
LIST OF TABLES	iii
LIST OF FIGURES	iv
LIST OF SYMBOLS	xiii
CHAPTER 1 - INTRODUCTION	1
1.1 Newtonian boundary layers.....	2
1.2 Drag reduced boundary layers.....	5
1.3 Turbulent burst structure	9
1.4 Objectives	13
CHAPTER 2 - EXPERIMENTAL APPARATUS AND PROCEDURES	16
2.1 Water channel.....	16
2.2 Velocity and concentration measurements.....	23
2.3 Polymer solution preparation	35
CHAPTER 3 - NEWTONIAN BOUNDARY LAYERS	36
3.1 Zero pressure gradient experiments	36
3.2 Adverse pressure gradient data.....	43
3.3 Mixing length models.....	56
CHAPTER 4: DRAG REDUCED BOUNDARY LAYERS	65
4.1 Shear stress in polymer flows.....	69
4.2 Polymer concentration measurements.....	76
4.3 Mean streamwise velocity statistics	79
4.4 Velocity fluctuation statistics	83
4.5 Mixing length models.....	94

	Page
4.6 Turbulence production	105
4.7 Postulated mechanism of drag reduction	105
CHAPTER 5: BURST RESULTS.....	118
5.1 Newtonian boundary layers.....	122
5.2 Drag reduced boundary layers.....	140
CHAPTER 6: SUMMARY, CONCLUSIONS, AND RECOMMENDATIONS	145
REFERENCES	149
APPENDICES	
Appendix A: Data Plots.....	155
Appendix B: Experimental Data	170

LIST OF TABLES

Table	Page
2.1 Channel dimensions	18
2.2 Measurement window locations	19
3.1 Summary of Newtonian data	39
3.2 Mixing length models for the inner region	61
3.3 Turbulent viscosity models for the outer region	61
4.1 Summary of drag reduction experiments	67
5.1 Summary of burst data	126
Appendix	
Table	
A.1 Zero pressure gradient Newtonian data	171
A.2 Drag reduced zero pressure gradient data	171
A.3 Adverse pressure gradient Newtonian data	172
A.4 Adverse pressure gradient drag reduced data	172
A.5 Drag reduction and viscometry tests	173

LIST OF FIGURES

Figure	Page
2.1 Schematic diagram of water channel	17
2.2 Schematic diagram of injector slot assembly (not to scale, dimensions in mm and degrees). (a) Cross sectioned side view (b) Top-view of baffle plate (c) Top-view of back plate	21
2.3 Schematic diagram of two-component, four beam LDV optics.....	24
2.4 Measurement beam geometry	27
2.5 Schematic diagram of concentration measurement optics	33
3.1 Variation of the Coles wake parameter, Π as a function of Re_θ for zero pressure gradient Newtonian boundary layers. \circ present study; Δ Purtell et. al. (1981); \square Murlis et al. (1982); \times Erm et al. (1985) (8 m/s); + Erm et al. (14 m/s); \blacklozenge Shah & Antonia (1989); \bullet Wieghardt (Coles re-analysis, 1968); — Coles (1962).....	37
3.2 Mean streamwise velocity in a Newtonian zero pressure gradient boundary layer without injection. \blacklozenge $Re_\theta = 1358$; \circ $Re_\theta = 2478$; \square $Re_\theta = 2978$; Δ $Re_\theta = 3527$; + $Re_\theta = 3935$ — $U^+ = (1/0.41) \ln y^+ + 5.0$	40
3.3 Comparison of root-mean-square velocities and Reynolds stresses in Newtonian zero pressure gradient boundary layers without injection. \circ present Newtonian data $Re_\theta = 3527$; Δ Purtell et al. $Re_\theta = 3480$; \square Murlis et al. $Re_\theta = 3362$; + Erm et al. $Re_\theta = 3575$; \blacksquare Fontaine et al. $Re_\theta = 3100$	42
3.4 Skewness of the streamwise and normal velocity fluctuations for a zero pressure gradient Newtonian boundary layer. \circ $Re_\theta = 2478$. ∇ $Re_\theta = 2685$, Balint et al.. Typical uncertainty shown in upper right corner	44

Figure	Page
3.5 Flatness factor of the streamwise and normal velocity fluctuations for a zero pressure gradient Newtonian boundary layer. \circ $Re_\theta = 2478$. ∇ $Re_\theta = 2685$, Balint et al..Typical uncertainty shown in upper right corner	45
3.6 Velocity defect profiles in an adverse pressure gradient boundary layer with $\beta = 1.8$. \blacklozenge $Re_\theta = 2664$; \triangle $Re_\theta = 3080$; \circ $Re_\theta = 3570$; ∇ $Re_\theta = 3870$; \bullet $Re_\theta = 4210$	47
3.7 Velocity defect profiles in an adverse pressure gradient boundary layer with $\beta = 2.4$. $+$ $Re_\theta = 3784$; \square $Re_\theta = 4588$; \blacksquare $Re_\theta = 4978$	48
3.8 Freestream velocity as a function of streamwise distance from trip. (a) zero pressure gradient, (b) moderate adverse ——— $U_e = 4.98x^{-.273}$ (c) strong adverse ——— $U_e = 5.43x^{-.288}$. Note that both scales are logarithmic.....	50
3.9 Mean streamwise velocity in Newtonian, equilibrium, adverse pressure gradient boundary layers without injection. $\beta = 1.8$: \circ $Re_\theta = 3570$, \bullet $Re_\theta = 4210$; $\beta = 2.4$: \square $Re_\theta = 4588$, \blacksquare $Re_\theta = 4978$; ——— $U^+ = (1/0.41) \ln y^+ + 5.0$	51
3.10 Mean streamwise velocity in the linear sublayer of Newtonian, equilibrium, adverse pressure gradient boundary layers without injection. $\beta = 1.8$: \circ $Re_\theta = 3570$, \bullet $Re_\theta = 4210$; $\beta = 2.4$: \square $Re_\theta = 4588$, \blacksquare $Re_\theta = 4978$; ——— $U^+ = y^+$	52
3.11 Root-mean-square velocities and Reynolds shear stress in a Newtonian equilibrium adverse pressure gradient boundary layer without injection, $\beta = 1.8$. \circ $Re_\theta = 3570$; \bullet $Re_\theta = 4210$; \blacklozenge White $Re_\theta = 2085$; \square East and Sawyer flow 5, $Re_\theta = 26800$	53
3.12 Root-mean-square streamwise and normal velocity fluctuations and Reynolds shear stress in a Newtonian equilibrium adverse pressure gradient boundary layer without injection $\beta = 2.4$. $+$ $Re_\theta = 3784$; \square $Re_\theta = 4588$; \blacksquare $Re_\theta = 4978$	55
3.13 Root-mean-square velocities and Reynolds shear stress in Newtonian equilibrium boundary layers without injection. $+$ $Re_\theta = 3935$, $\beta = 0.0$; \bullet $Re_\theta = 4210$, $\beta = 1.8$; \square $Re_\theta = 4588$, $\beta = 2.4$	57
3.14 Mixing length in Newtonian equilibrium boundary layers without injection. $+$ $Re_\theta = 3935$, $\beta = 0$; \bullet $Re_\theta = 4210$, $\beta = 1.8$; \square $Re_\theta = 4588$; $\beta = 2.3$	58

Figure	Page
3.15 Mixing length in Newtonian equilibrium boundary layers without injection. (a) \square $Re_\theta = 4588$, $\beta = 2.3$; (b) \bullet $Re_\theta = 4210$, $\beta = 1.8$; (c) $+$ $Re_\theta = 3935$, $\beta = 0$; Inner models: — Van Driest; \cdots Cebeci-Smith; - - - Granville, Outer models: \cdots Cebeci-Smith; - - - Baldwin-Lomax using Granville coefficients	63
4.1 Drag reduction as a function of streamwise distance from slot. (a) zero pressure gradient (b) moderate adverse (c) strong adverse. \circ $Q_i/Q_s = 2.6$, \bullet $Q_i/Q_s = 5.1$	68
4.2 Sum of viscous shear stress, $(\mu d\bar{U}/dy)$, and Reynolds shear stress, $(-\rho\bar{u}\bar{v})$, in a zero pressure gradient boundary layer. (a) polymer injection $(x - x_s)^+ = 29000$; (b) polymer injection $(x - x_s)^+ = 43200$; (c) polymer injection $(x - x_s)^+ = 64400$; (d) polymer injection $(x - x_s)^+ = 81000$; (e) \square water injection; \blacklozenge no injection, $(x - x_s)^+ = 29000$. \bullet Wall shear stress determined from the log region	71
4.3 Sum of viscous and Reynolds shear stresses in an adverse pressure gradient boundary layer with and without polymer injection. $Re_\theta _N = 3570$, $\beta = 1.8$. (a) $Q_i/Q_s = 5.1$, (b) $Q_i/Q_s = 2.6$, (c) no injection — Equation 4.4, - - - error bounds	74
4.4 Average polymer concentration in a zero pressure gradient boundary layer normalized by the injected concentration. (a): $\beta = 0.0$, $Q_i/Q_s = 5.1$ (b): $\beta = 0.0$, $Q_i/Q_s = 2.6$. \circ $(x - x_s)^+ = 29000$; \square $(x - x_s)^+ = 43200$; Δ $(x - x_s)^+ = 64400$; \bullet $(x - x_s)^+ = 81000$	77
4.5 Average polymer concentration normalized by the injected concentration in the adverse pressure gradient boundary layer, $\beta = 1.8$, $x^+ = 33700$. Note larger scale compared to figure 4.4. (a) $Q_i/Q_s = 5.1$ (b) $Q_i/Q_s = 2.6$	78
4.6 Mean streamwise velocity for a zero pressure gradient boundary layer with and without drag reduction. $+$ $(x - x_s)^+ = 29000$; \square $(x - x_s)^+ = 43200$; (\blacksquare repeated points); Δ $(x - x_s)^+ = 64400$; \circ $(x - x_s)^+ = 81000$ (\bullet repeated points); \times $(x - x_s)^+ = 29000$, water injection. — $U^+ = (1/0.41) \ln y^+ + 5.0$	80
4.7 Plot of κ as a function of drag reduction; Δ Newtonian: $\beta = 0$: \circ $Q_i/Q_s = 2.6$, \bullet $Q_i/Q_s = 5.1$; $\beta = 1.8$: \square $Q_i/Q_s = 2.6$, \blacksquare $Q_i/Q_s = 5.1$; $\beta = 2.4$: \ominus $Q_i/Q_s = 2.6$, \otimes $Q_i/Q_s = 5.1$; — $\kappa = 0.41 - 0.004DR$	82

Figure	Page
4.8 Root-mean-square velocities and Reynolds shear stresses for a zero pressure gradient boundary layer at $(x - x_s)^+ = 29000$, $Re_\theta = 2478$ with and without drag reduction. \circ unmodified Newtonian; \bullet water injection $Q_i/Q_s = 5.1$; Δ polymer injection $Q_i/Q_s = 2.6$; \square polymer injection $Q_i/Q_s = 5.1$	85
4.9 Root-mean-square velocities and Reynolds shear stresses for a zero pressure gradient boundary layer at $(x - x_s)^+ = 81000$, $Re_\theta = 3935$ with and without drag reduction. \circ unmodified Newtonian; Δ polymer injection $Q_i/Q_s = 2.6$; \square polymer injection $Q_i/Q_s = 5.1$; \blacksquare $Q_i/Q_s = 5.1$, repeated points	87
4.10 Root-mean-square velocities and Reynolds shear stresses for an adverse pressure gradient boundary layer at $Re_\theta = 3570$, $\beta = 1.8$ with and without drag reduction. \circ unmodified Newtonian; Δ $Q_i/Q_s = 2.6$; \square $Q_i/Q_s = 5.1$	89
4.11 Skewness of the streamwise and normal velocity fluctuations in the inner region of a zero pressure gradient boundary layer at $(x - x_s)^+ = 29000$, $Re_\theta = 2478$ with and without drag reduction. \circ unmodified Newtonian; \bullet water injection at $Q_i/Q_s = 5.1$. Δ $Q_i/Q_s = 2.6$; \square $Q_i/Q_s = 5.1$	91
4.12 Mean streamwise velocity for the inner region of a zero pressure gradient boundary layer at $(x - x_s)^+ = 29000$, $Re_\theta = 2478$ with and without drag reduction. \circ unmodified Newtonian; \bullet water injection $Q_i/Q_s = 5.1$; Δ polymer injection $Q_i/Q_s = 2.6$; \square polymer injection $Q_i/Q_s = 5.1$	92
4.13 Flatness of the streamwise and normal velocity fluctuations in the inner region of a zero pressure gradient boundary layer at $(x - x_s)^+ = 29000$, $Re_\theta = 2478$ with and without drag reduction. \circ unmodified Newtonian; \bullet water injection at $Q_i/Q_s = 5.1$. Δ $Q_i/Q_s = 2.6$; \square $Q_i/Q_s = 5.1$	93
4.14 Skewness of the streamwise and normal velocity fluctuations in the inner region of an adverse pressure gradient boundary layer at $Re_\theta = 3570$, $\beta = 1.8$ with and without drag reduction. \circ unmodified Newtonian; Δ $Q_i/Q_s = 2.6$; \square $Q_i/Q_s = 5.1$	95
4.15 Flatness of the streamwise and normal velocity fluctuations in the inner region of an adverse pressure gradient boundary layer at $Re_\theta = 3570$, $\beta = 1.8$ with and without drag reduction. \circ $Re_\theta = 3570$, $\beta = 1.8$; Δ $Q_i/Q_s = 2.6$; \square $Q_i/Q_s = 5.1$	96

Figure	Page
4.16 Mixing length in a Newtonian equilibrium boundary layer and corresponding drag reduced layers. (a) adverse pressure gradient, $Re_{\theta} _N = 3570$, $\beta = 1.8$ (b) zero pressure gradient $Re_{\theta} _N = 3527$. \circ no injection; $\Delta Q_i/Q_s = 2.6$; $\square Q_i/Q_s = 5.1$	97
4.17 Friction coefficient, c_f , as a function of streamwise distance from the slot in the zero pressure gradient boundary layer. (a) high injection flowrate (b) low injection flowrate. \circ no injection ; \square drag reduced data; predicted, no injection; —— predicted with polymer injection. Typical error bound on measured c_f on right.....	100
4.18 Friction coefficient, c_f , as a function of streamwise distance from the slot in the adverse pressure gradient boundary layer, $\beta = 1.8$. (a) high injection flowrate (b) low injection flowrate. \circ no injection ; \square drag reduced data; predicted, no injection; —— predicted with polymer injection. Typical error bound on c_f on right	102
4.19 Friction coefficient, c_f , as a function of streamwise distance from the slot in the adverse pressure gradient boundary layer, $\beta = 2.4$. (a) low injection flowrate (b) high injection flowrate. \circ Newtonian data; \square drag reduced data; predicted Newtonian; —— predicted with polymer injection. Typical error bound on c_f on right	103
4.20 Reynolds shear stress (\overline{uv}) and normal stress ($\overline{u^2}$) production in a zero pressure gradient boundary layer with and without polymer injection. $\circ (x - x_s)^+ = 29000$, $Re_{\theta} = 2478$, Newtonian $\Delta Q_i/Q_s = 2.6$; $\square Q_i/Q_s = 5.1$..	106
4.21 Reynolds shear stress (\overline{uv}) and normal stress ($\overline{u^2}$) production in a zero pressure gradient boundary layer with and without polymer injection. $\circ (x - x_s)^+ = 81000$, $Re_{\theta} = 3935$, Newtonian $\Delta Q_i/Q_s = 2.6$; $\square Q_i/Q_s = 5.1$..	107
4.22 Reynolds shear stress (\overline{uv}) and normal stress ($\overline{u^2}$) production in a zero pressure gradient boundary layer with and without polymer injection. \circ Newtonian , $\beta = 1.8$, $Re_{\theta} = 3570$; $\Delta Q_i/Q_s = 2.6$; $\square Q_i/Q_s = 5.1$	108
4.23 Joint probability function of u and v fluctuations in a zero pressure gradient boundary layer (a) Newtonian and (b) drag reduced $Q_i/Q_s = 2.6$, $Re_{\theta} _N = 2497$, $x^+ = 29000$, $y^+ _N = 33$	109

Figure	Page
4.24 Kolmogoroff length scale at a single streamwise location in zero pressure gradient boundary layers with and without drag reduction. \circ $Re_{\theta} = 2497$ Newtonian; Δ polymer injection $Q_i/Q_s = 2.6$	112
4.25 Correlation coefficient for a zero pressure gradient boundary layer at $(x - x_s)^+ = 29000$, $Re_{\theta} = 2478$ with and without drag reduction. \circ unmodified Newtonian; Δ polymer injection $Q_i/Q_s = 2.6$; \square polymer injection $Q_i/Q_s = 5.1$	114
4.26 Joint probability function of u and v fluctuations in the moderate adverse pressure gradient boundary layer, (a) Newtonian (b) drag reduced $Q_i/Q_s = 2.6$, $Re_{\theta} _N = 3570$, $x^+ = 31000$, $y^+ _N = 30$	115
4.27 Correlation coefficient for an adverse pressure gradient boundary layer at $Re_{\theta} = 3570$, $\beta = 1.8$ with and without drag reduction. \circ unmodified Newtonian; Δ $Q_i/Q_s = 2.6$; \square $Q_i/Q_s = 5.1$	117
5.1 Quadrants of the uv plane.....	119
5.2 Schematic of idealized probability distribution of time between ejections. (after Luchik & Tiederman, 1987).....	121
5.3 White & Tiederman method for determining grouping times	123
5.4 Computed average burst period as a function of threshold.....	124
5.5 Inner normalized burst period for Newtonian zero pressure gradient boundary layers. \circ Koskie mulev; \square White & Tiederman mulev; Δ Shah & Antonia mulev; \oplus Antonia & Bisset mulev; \otimes Antonia, Bisset & Browne mulev; \blacklozenge Barlow & Johnston uv2.....	127
5.6 Burst period for Newtonian zero pressure gradient boundary layers normalized with inner, mixed and outer variables. \circ Koskie \square White & Tiederman; \bullet Antonia & Bisset; \bullet Antonia, Bisset & Browne; \blacklozenge Barlow & Johnston	129
5.7 Burst period for Newtonian zero and adverse pressure gradient boundary layers normalized with inner, mixed and outer variables. \circ Koskie; \square White & Tiederman; \bullet Antonia & Bisset; \bullet Antonia, Bisset & Browne	130
5.8 Burst period for Newtonian zero pressure gradient boundary layers normalized with inner, mixed and outer variables. \circ Koskie; \square White & Tiederman; —— assumes inner scaling is valid; --- assumes mixed scaling is valid; assumes outer scaling is valid	133

Figure	Page
5.9 Burst period for Newtonian adverse pressure gradient boundary layers normalized with inner mixed and outer variables. ○ Koskie; □ White & Tiederman; ——— assumes inner scaling is valid; --- assumes mixed scaling is valid; assumes outer scaling is valid.....	136
5.10 Normalized burst period for Newtonian zero pressure gradient boundary layers as a function of the Coles wake parameter, Π . ○ Koskie; □ White & Tiederman; ● Antonia & Bisset, Antonia, Bisset & Browne; ◆ Barlow & Johnston. ——— $\bar{T}(u_{\tau}^2 U_e / \nu \theta)^{1/2} = 42.4(\Pi - 0.62) + 35$	139
5.11 Burst period for Newtonian zero pressure gradient boundary layers using modified mixed normalization. ○ Koskie; □ White & Tiederman; ● Antonia & Bisset; ● Antonia, Bisset & Browne; ◆ Barlow & Johnston	141
5.12 Ratio of the average burst period in a drag reduced boundary layer to that in the corresponding Newtonian boundary layer compared to the variation of inner normalized streak spacing in a fully developed channel flow of homogeneous polymer solutions. ○ $\beta = 0$; □ $\beta = 1.8$; $\Delta \beta = 2.4$; ——— Oldaker & Tiederman $\lambda^+ = 99.7 + 1.9DR$	143
Appendix	
Figure	
A.1 Dimensionless velocity profiles for the zero pressure gradient boundary layer using outer normalization. ◆ $Re_{\theta} = 1358$; ○ $Re_{\theta} = 2478$; □ $Re_{\theta} = 2978$; $\Delta Re_{\theta} = 3527$; + $Re_{\theta} = 3935$	156
A.2 Variation of skin friction coefficient, C_f , as a function of Re_{θ} for a Newtonian zero pressure gradient boundary layer: ○ present data; Δ Purtell et. al. (1981); □ Murlis et al. (1982); ● Wieghardt (Coles re-analysis, 1968); ——— Coles (1962).....	157
A.3 Variation of shape factor, H , as a function of Re_{θ} for a zero pressure gradient Newtonian boundary layer: ○ present data; Δ Purtell et. al. (1981); ● Wieghardt (Coles re-analysis, 1968); ——— Coles (1962).....	158
A.4 Root-mean-square velocities and Reynolds shear stress in a Newtonian zero pressure gradient boundary layer without injection. ◆ $Re_{\theta} = 1358$; ○ $Re_{\theta} = 2478$; □ $Re_{\theta} = 2978$; $\Delta Re_{\theta} = 3527$; + $Re_{\theta} = 3935$	159

Appendix Figure	Page
A.5 Velocity defect profiles in an adverse pressure gradient boundary layer. ○ $Re_\theta = 3570, \beta = 1.8, G = 10.6$; ♦ J. B. White $Re_\theta = 2085, \beta = 1.9, G = 10.8$; □ East & Sawyer flow 5 $Re_\theta = 26800, \beta = 1.89, G = 10.60$; ⊕ Clauser flow 1 $Re_\theta = 14000, \beta = 1.89, G = 9.66$	160
A.6 Velocity defect profiles in an adverse pressure gradient boundary layer. + $Re_\theta = 3784, \beta = 2.4, G = 12.2$; □ $Re_\theta = 4588, \beta = 2.3, G = 13.0$; ■ $Re_\theta = 4978, \beta = 2.7, G = 13.0$. ——— Bradshaw (1969) $Re_\theta = 22370, \beta = 2.9, G = 12.58$	161
A.7 Sum of viscous shear stress, $(\mu d\bar{U}/dy)$, and Reynolds shear stress, $(-\rho\bar{u}v)$, in a zero pressure gradient boundary layer with and without polymer injection at $Q_i/Q_s = 2.6$. (a) polymer injection $(x - x_s)^+ = 29000$; (b) polymer injection $(x - x_s)^+ = 43200$; (c) polymer injection $(x - x_s)^+ = 64400$; (d) polymer injection $(x - x_s)^+ = 81000$; (e) □ water injection, ♦ no injection, $(x - x_s)^+ = 29000$. ● Wall shear stress determined from the log region.....	162
A.8 Root-mean-square polymer concentration in the zero pressure gradient drag reduced boundary layers normalized by the injected concentration. (a): $Q_i/Q_s = 5.1$ (b): $Q_i/Q_s = 2.6$. ○ $(x - x_s)^+ = 29000$; □ $(x - x_s)^+ = 43200$; △ $(x - x_s)^+ = 64400$; ● $(x - x_s)^+ = 81000$	163
A.9 Root-mean-square polymer concentration normalized by the injected concentration in the adverse pressure gradient boundary layer, $\beta = 1.8$, $x^+ = 33700$. Note larger scale. (a) $Q_i/Q_s = 5.1$ (b) $Q_i/Q_s = 2.6$	164
A.10 Mean streamwise velocity for a zero pressure gradient boundary layer with and without drag reduction. Fluid injected at $Q_i/Q_s = 2.1$. + $(x - x_s)^+ = 29000$; □ $(x - x_s)^+ = 43200$; △ $(x - x_s)^+ = 64400$; ○ $(x - x_s)^+ = 81000$; x $(x - x_s)^+ = 29000$, water injection. ——— $U^+ = (1/0.41) \ln y^+ + 5.0$	165
A.11 Root-mean-square velocities and Reynolds shear stresses in a zero pressure gradient boundary layer with and without drag reduction. ○ $(x - x_s)^+ = 43200, Re_\theta = 2978$; △ polymer injection $Q_i/Q_s = 2.6$; □ polymer injection $Q_i/Q_s = 5.1$; ■ $Q_i/Q_s = 5.1$, repeated points.....	166
A.12 Root-mean-square velocities and Reynolds shear stresses in a zero pressure gradient boundary layer with and without drag reduction. ○ $(x - x_s)^+ = 64400, Re_\theta = 3527$; △ polymer injection $Q_i/Q_s = 2.6$; □ polymer injection $Q_i/Q_s = 5.1$	167

- A.13 Root-mean-square velocities and Reynolds shear stresses in the adverse pressure gradient boundary layer, $\beta = 2.4$ with and without drag reduction. $\circ (x - x_s)^+ = 40400, Re_\theta = 4588;$
 Δ polymer injection $Q_i/Q_s = 2.6;$ \square polymer injection $Q_i/Q_s = 5.1$168
- A.14 Root-mean-square streamwise velocity in the adverse pressure gradient boundary layer, $\beta = 2.4$ with and without drag reduction. $\circ (x - x_s)^+ = 45200, Re_\theta = 4978;$
 Δ polymer injection $Q_i/Q_s = 2.6;$ \square polymer injection $Q_i/Q_s = 5.1$169

LIST OF SYMBOLS

Symbol	Description
c_f	wall friction coefficient
B	intercept of the logarithmic velocity profile
%DR	percent drag reduction defined by equation 4.1
e	fluctuation of hot film voltage
F_{wake}, C_{cp}	coefficients for the Baldwin-Lomax model (chapter 3)
C_{kleb}	coefficient for the Baldwin-Lomax model (chapter 3)
G	Clauser shape factor
H, L	thresholds used in burst detectors
H	shape factor
I	hot film current
l	mixing length
Q_i	volumetric injection flow rate
Q_s	volumetric flow rate in the linear sublayer ($y^+ < 5$)
Re_θ	momentum thickness Reynolds number
R_w	hot film resistance at operating temperature
R_g	hot film resistance at water temperature
$S_{c,t}$	hot film sensitivity
t	time
T	time period
\bar{T}	average period of the turbulent bursts
\bar{T}_{mod}	modified mixed scaled average burst rate
U_e	freestream velocity
U, V	velocity in the x and y directions respectively

Symbol	Description
u, v	velocity fluctuations in the x and y directions respectively
x, y, z	coordinates in the streamwise, normal and spanwise directions respectively
x_s	x location of slot
x_t	x location of trip
α	an angle
β	equilibrium pressure gradient parameter, $\beta = \frac{\delta^*}{\tau_w} \frac{dp}{dx}$
δ	boundary layer thickness
δ^*	displacement thickness
θ	momentum thickness
Δ	Clausner boundary layer thickness
δ_s	unmodified boundary layer thickness at the slot
λ^+	spanwise streak spacing normalized with u_τ and v
κ	von Karman parameter
ρ	density
μ	dynamic viscosity
ν	kinematic viscosity
ν_t	turbulent viscosity
τ	shear stress
τ_w	wall shear stress
τ_1, τ_2	times used in the grouping process (chapter 5)
τ_g	grouping time (chapter 5)
Π	Coles wake parameter
dp/dx	streamwise derivative of the freestream pressure

Superscripts and subscripts:

'	(prime) root-mean-square
—	(over bar) denotes Reynolds averaging
₀	quantity evaluated at the same location before drag reduction

CHAPTER 1 - INTRODUCTION

The ability of some solutions of long chain polymers to greatly reduce the pressure drop in pipes is well documented and commercially applied. In addition, a number of experiments indicate that large reductions of wall friction are possible by injecting polymer into a boundary layer. Therefore, it is reasonable to expect that drag reducing polymers could significantly improve the performance of submersibles when introduced into the boundary layers on the fore and sides of the vessel. However, once polymer is injected at these locations it is unlikely to leave the boundary layer because these polymers have very low mass diffusivities in water and boundary layers continually entrain fluid rather than eject it. As a result, one can expect that drag reducing polymers will be present in the adverse pressure gradient boundary layers on the aft of a vessel whenever the frictional drag on the fore and sides is reduced with polymers.

Direct measurements of adverse pressure gradient turbulent boundary layers in which drag reducing polymers are present are not available. However, at fixed speeds, the net drag on a propeller hydrofoil increases while lift decreases when submerged in polymer solution (Kowalski, 1971; Wu, 1969). This apparent increase in form drag suggests a sudden increase in the displacement thickness of the boundary layers which may indicate separation. Therefore, it is necessary to establish whether conditions exist under which turbulent boundary layers of polymer solutions will not separate when they

encounter adverse pressure gradients.

Assuming that such conditions exist, it is important from an engineering standpoint to model the flow. This study tests whether data from fully developed channel flows can be used in modeling boundary layers; because, experiments in such channels are usually much easier to perform than actual boundary layer experiments. Finally, it addresses the fundamental scientific issue of the turbulent bursting rate in Newtonian boundary layers and drag reduced boundary layers.

1.1 Newtonian boundary layers

The first experiments were designed to verify the performance of the new test section used in this study. This was accomplished by establishing a zero pressure gradient Newtonian boundary layer and two adverse pressure gradient equilibrium boundary layers. These boundary layers also provided a reference against which the drag reduced boundary layers were directly compared.

The zero pressure gradient provided the best test of the facility because zero pressure gradient boundary layers have been fully characterized. The mean streamwise velocity profile of zero pressure gradient boundary layers has been investigated by numerous investigators. Coles (1962, 1968) thoroughly reviewed these experiments and established that the time averaged velocity profile can be described by:

$$U^+ = \overset{\text{I}}{\frac{1}{\kappa} \ln y^+} + \overset{\text{II}}{B} + \overset{\text{III}}{\frac{2\Pi}{\kappa} \sin^2 \left[\frac{\pi}{2} \frac{y}{\delta} \right]} \quad (1.1)$$

In this equation U^+ is the mean velocity normalized by the shear velocity, u_τ , y^+ is the

distance normal to the wall normalized by u_τ and the kinematic viscosity, ν , and δ is the boundary layer thickness. The parameters κ and B of the logarithmic region of the profile, parts I and II, are constants with recommended values of 0.41 and 5.0. The Coles wake parameter, Π , is a function of the momentum thickness Reynolds number, Re_θ , and the effectiveness of the boundary layer trip in zero pressure gradient boundary layers. There are two experimentally useful consequences of these relationships. First, the logarithmic portion of the equation can be used to determine the wall shear stress from a measured velocity profile (Clauser, 1954; Coles, 1968). Second, the Coles wake parameter can be used to evaluate a boundary layer trip because it follows a fixed relationship as a function of Re_θ when the boundary layer is properly tripped. Equation 1.1 basically fully described zero pressure gradient velocity profiles. However, since the values of κ and B given above were determined with data at momentum Reynolds numbers in excess of approximately 5000, some debate remained as to whether they were universal at lower Reynolds numbers. Purtell et al. (1981) proved that these constants do not change at low Reynolds numbers.

In addition to the mean velocity profiles in the zero pressure gradient boundary layer, the velocity fluctuation statistics including the root-mean-square streamwise and normal velocity fluctuations, u' and v' respectively, the Reynolds shear stress, \overline{uv} , and skewness and flatness of the streamwise and normal velocities were deduced from two-component measurements. In chapter 3 these statistics are compared to previous studies in the same Reynolds number range by Purtell et al. (1981), Murlis et al. (1982), Erm et al. (1985), Fontaine et al. (1990), and Balint et al. (1991).

Two Newtonian adverse pressure gradient equilibrium boundary layers were formed. Equilibrium boundary layers were used because their streamwise history is implicitly specified. In non-zero pressure gradient boundary layers the parameters κ and B in equation 1.1 remain unchanged. However, the Coles wake parameter, Π , is a function of the pressure history of the flow. Velocity profiles can only be meaningfully compared if the freestream pressure distributions upstream of each profile is the same. However, Clauser (1954) demonstrated that certain variable pressure gradient boundary layers have a degree of similarity in the outer flow. For such a flow, the velocity defect $(\bar{U} - U_e)/u_\tau$ can be plotted on a single curve as a function of the integral thickness Δ , for fixed values of the equilibrium pressure gradient parameters, β , and G . These parameters are defined by:

$$\Delta = \int_0^{\infty} \frac{U_e - \bar{U}}{u_\tau} dy \quad (1.2)$$

$$\beta = \frac{\delta^*}{\tau_w} \frac{dP}{dx} \quad (1.3)$$

$$G = \left[\frac{2}{c_f} \right]^{1/2} \left[1 - \frac{1}{H} \right] \quad (1.4)$$

These boundary layers allow direct comparisons of data at different Reynolds for the same equilibrium condition and different pressure gradients at fixed Reynolds number. Both the parameters β and G are constant when a boundary layer is in equilibrium. Therefore, both parameters were evaluated in the present experiments to demonstrate that the boundary layers were in an equilibrium state.

The adverse pressure gradient data acquired in the present facility also provided an opportunity to verify that adverse pressure gradient data acquired at lower Reynolds numbers can be scaled to higher Reynolds numbers. Bradshaw (1967,1969) and East & Sawyer (1979) have thoroughly investigated the fluctuation statistics in adverse pressure gradient equilibrium boundary layers at Reynolds numbers above 20 000. These data provide essentially all the information required to statistically model these boundary layers from the start of the logarithmic velocity profile to the free stream. Comparison of these data with the present verified that there is no Reynolds number effect in the inner region of the boundary layer.

1.2 Drag reduced boundary layers

The present drag reduction experiments were first conducted in a zero pressure gradient boundary layer to test methods of determining wall shear stress and to test simple methods which have been proposed to scale drag reduction data. In order to predict drag reduction in geometries which are not easily tested in laboratories and in boundary layers where pressure drop measurements cannot be used to find wall shear stress, many authors have proposed that the logarithmic velocity profile only undergoes a change in the intercept. The key assumption in this hypothesis is that κ is unchanged by polymer drag reduction (see Virk, 1975; Berman, 1978). The resulting logarithmic profile is given by equation 1.5 where κ and B retain their Newtonian values.

$$U^+ = \frac{1}{\kappa} \ln y^+ + B + \Delta B \quad (1.5)$$

When this relationship is valid, the drag reduction in large pipes can be easily determined from smaller pipe flow experiments (Granville, 1977; Hoyt, 1991). It can

also be used to determine the wall shear stress in boundary layers (Fontaine et al., 1991). However, Harder & Tiederman (1991) found that the value of κ changed during drag reduction experiments in a two dimensional channel using the same polymer used in this study. Therefore, it was assumed that the slope would change in the present experiments, and the experiments were designed to test for changes in κ .

Because κ and B were expected to change during drag reduction, it was necessary to measure wall shear stress using a method which was independent of equation 1.5. Wall shear stress was determined from the velocity gradient in the linear sublayer using equation 1.6.

$$\tau_w = \mu \left. \frac{d\bar{U}}{dy} \right|_{y=0} \quad (1.6)$$

The viscosity of the polymer solution viscosity, μ , was approximated by the solvent viscosity in the linear sublayer. The flow in the linear sublayer is a simple shear flow, so additional elastic stress terms are not expected (see Leal, 1990). Therefore, equation 1.6 is valid as long as the correct value of the shear viscosity is used. The shear viscosity of polymer solutions is a function of the local strain rate. However, when the concentration of the polymer is sufficiently low, the shear viscosity can be approximated by that of the solvent, water. The range of concentrations over which this approximation is valid was determined by viscometry, and the experiments were designed so that the approximation could be used. However, it was necessary to verify that the actual polymer concentration in the boundary layer near the wall was within the range where the approximation is valid. The data and correlations of Poreh & Cermak (1964) and Morkovin (1965) for passive scalars mixing into Newtonian boundary layers

could not be used to predict polymer concentration because the polymer interacts with the turbulent momentum transport. Therefore, the turbulent mass transport is influenced by the polymer (Walker & Tiederman, 1989). Near wall polymer measurements and correlations (Fruman & Tulin, 1976; Vdovin & Smol'yakov, 1978, 1981; Latta & El Reidy, 1984) which are specific to boundary layers modified with other polymers can not be relied on to accurately predict the concentration of the present polymer. Therefore, it was necessary to measure the polymer concentration in the boundary layers.

The velocity fluctuation statistics, including the root-mean-square streamwise and normal velocity fluctuations, u' and v' respectively, the Reynolds shear stress, \overline{uv} , and skewness and flatness of the streamwise and normal velocities were deduced and compared to the corresponding Newtonian data. The changes in these statistics were compared with the trends observed in fully developed channel flows to determine whether there exist fundamental differences in the manner in which the polymer influences the turbulence.

The data were used to evaluate Newtonian boundary layer codes that had been modified to predict drag reduction without explicitly including the true non-Newtonian constitutive equation. One step in determining the validity of this modeling concept was comparing the sum of the viscous and Reynolds shear stress to the total shear stress. Harder & Tiederman (1991) showed that in many fully developed two dimensional channel flows, the total shear stress profiles during drag reduction could be accurately represented by the sum of the viscous and Reynolds stress. However, they found at

least one combination of polymer concentration and wall strain rate where an additional non-Newtonian stress term was needed to account for the total shear stress. This test was accomplished by measuring the sum of the viscous and Reynolds shear stresses in the boundary layers and comparing them to the total shear stress distribution.

Even if the sum of the viscous and Reynolds shear stresses do not equal the total shear stress, a modified boundary layer code would be useful in an engineering sense if it correctly predicted wall shear stress during drag reduction. Because this objective involves testing a concept rather than a specific boundary layer code, a modified mixing length model was chosen for simplicity. Walker's (1985) modified mixing length model was used. This model was derived using data from fully developed channel flows of drag reducing polymer solutions. The mixing lengths in the Newtonian boundary layers were calculated to verify the performance of existing mixing length models at low Reynolds numbers. Then the modified mixing length model was compared to the present drag reduction data.

It is widely believed that the polymer molecules in the flow must be stretched in order for drag reduction to take place (see Berman, 1978). In drag reduced flows, the concentration of the polymer is typically low enough that interaction of the polymer molecules is probably not important (Leal, 1990). In this situation, the equilibrium state of polymer molecules in solution is a randomly coiled ball. Leal determined that the molecules must undergo a major change from equilibrium (stretching) in order for the polymer to have a direct measurable effect on the flow. He also showed that strong, rapid extensional motions are necessary to stretch polymer molecules. Hinch (1977)

hypothesized that the polymer molecules can be stretched by the extensional motions associated with bursts. Gyr (1984) showed that laminar flows with extensional strains which are of the same magnitude as the extensional motions expected in bursts are adequate to stretch polymer molecules. Luchik & Tiederman (1988) showed that the large amplitude extensional motions in turbulent channel flows were not significantly altered by the presence of polymer. Therefore, these motions provided a means to stretch the polymer molecules. Harder & Tiederman (1991) showed that this theory explaining drag reduction is consistent with the observed structure of two dimensional channel flows. From the probability distribution functions of u and v fluctuations, they established that strong extensional motions in the flow remain nearly unchanged but small scale motions are damped in drag reduced flows. The hypothesis was similarly confirmed with the present data. This supports the hypothesis that the fundamental influence of drag reducing polymers on turbulence is the same in boundary layers and channel flows. The results are in agreement with theory that polymer molecules are stretched by strong extensional motions in the flow, and the solution of stretched molecules has anisotropic stress properties which damp the small scale motions in the flow.

1.3 Turbulent burst structure

The turbulent momentum transport in the near wall region is dominated by vortical structures (Robinson et al., 1990). These structures are coherent, that is, they have distinct measurable characteristics by which they can be identified. However, distribution of these characteristics in space varies widely from structure to structure. Typically, these structures contain a spanwise vortex, called the head, in the overlap

(logarithmic) region. This vortex can be visualized in numerical data bases by marking the instantaneous low pressure regions which form at its core. This vortex curves toward the wall in the form of a vortex called the neck, which is oriented at approximately 45 degrees from the wall which extends toward the wall. Finally, as the neck approaches the wall it becomes an elongated vortex, called the leg, which is inclined at a small angle to the wall. Together, these vortices act to move low speed fluid away from the wall (on one side of the vortex) and high speed fluid toward the wall (on the other side). Therefore, the product of the streamwise, u , and normal, v , velocity fluctuations is negative in regions around the structure. The leg vortices also cause low speed fluid to gather in long streak like structures in the linear sublayer.

These characteristics were visualized from Spalart's (1988) full numerical simulation of turbulent flows by marking combinations of instantaneous velocity fluctuations, the velocity fluctuation products, streamwise and spanwise vorticity, or pressure fluctuations (Robinson et al., 1990). However, physical experiments are usually limited to Eulerian observations. Therefore, the majority of work involving coherent structures has studied Eulerian characteristics of these structures. One apparent part of the structure is the motion of low speed fluid away from the wall. Low speed fluid marked by smoke or dye seeped through the wall concentrates in long streamwise streak like structures (Kline et al., 1967) which appear to break apart in a sudden motion outward from the wall. This motion could appear as one filament of low speed fluid or several closely related filaments. The individual filaments became known as ejections. It is important to note that streaks and ejections in the Eulerian framework are associated with the Lagrangian vortical structure. Because these events

are highly three dimensional, more than one ejection typically occurs for each event. A group of ejections from the same structure is called a burst.

Ejections received much experimental attention because the majority of the Reynolds stress production was associated with them even though they only were observed approximately 30 percent of the total time in an Eulerian viewpoint (Corino & Brodkey, 1969; Kim et al., 1971). A number of investigators have proposed techniques by which ejections can be detected from a velocity signal measured at a single point in the flow. These techniques all mathematically model the velocities associated with an observed physical aspect of the flow. They have been critically reviewed by Bogard & Tiederman (1986), Luchik & Tiederman (1987) and Tubergen (1991). Because ejection detectors view a three dimensional Lagrangian structure from a single Eulerian point, the most useful information which can be obtained from them is the frequency of occurrence of structures. This is typically expressed as an average time between bursts. This measurement is complicated by the three dimensional nature of the structures. One Lagrangian structure may appear as several ejections when viewed from a single Eulerian point. Therefore, in order to determine the rate at which structures occur, it is necessary to distinguish between multiple ejections from a single structure and single ejections from a single structure (Bogard & Tiederman, 1986). This process is known as grouping and the end result is typically termed the average burst period or time between grouped events. This average time between Lagrangian structures was measured in the present study using single point velocity techniques. The detection and grouping techniques will be described in chapter 5.

The main interest is to determine how the average burst period varies with Reynolds number. Three methods have been proposed to normalize the burst period: inner variables, $\bar{T}u_{\tau}^2/\nu$, outer variables, $\bar{T}U_e/\theta$, or a combination of these, mixed variables, $\bar{T}(u_{\tau}^2U_e/\nu\theta)^{1/2}$ (Alfredsson & Johansson, 1984). Tiederman (1990) showed that inner scaling is appropriate for two-dimensional channel flows in the range $8700 < Re_h < 50\,000$, where Re_h is the Reynolds number based on channel height. Shah & Antonia (1989) concluded that mixed scaling or possibly outer scaling was appropriate in a zero pressure gradient boundary layer over a momentum thickness Reynolds number range of 651 to 13 173. However, Antonia & Bisset (1990) and Antonia, Bisset & Browne (1990) repeated some of Shah & Antonia's experiments using the same boundary layer and measured a much lower bursting period at $Re_{\theta} \cong 2200$ than that determined by Shah & Antonia. They attributed this difference to Shah & Antonia's choice of grouping parameter. As a result of this discrepancy, it is uncertain whether Shah & Antonia's conclusion about scaling is correct.

The present study evaluated these methods of scaling burst periods in Newtonian boundary layers. These data were used in conjunction with those of White & Tiederman (1990) who measured burst rates in Newtonian adverse pressure gradients over a smaller Reynolds number range. White & Tiederman established that the burst period decreased in adverse pressure gradients and that the inner normalized burst period changed as a direct function of the Clauser equilibrium pressure gradient parameters. However, they did not test mixed or outer normalization. The range of Reynolds numbers covered by their experiments was too small to determine the effects of Reynolds number on the scaling of the burst period. The data of Barlow & Johnston

(1988) were also used. They studied the effects of wall curvature on boundary layers. However, as a reference case, they measured the bursting rate in an unmodified zero pressure gradient boundary layer in water at a Reynolds number, Re_0 of 1140.

Finally, the turbulent burst period in drag reduced boundary layers was evaluated. Luchik & Tiederman (1988) and Harder & Tiederman (1991) concluded that the average burst period in channel flows of homogeneous polymer solutions varies in the same manner as does the streak spacing. This result indicates that the polymer affects the flow by decreasing the number of structures in the flow, but does not necessarily change the nature of the event. Therefore, streak spacing, which correlates linearly with drag reduction in these flows (Oldaker & Tiederman, 1977) could be used to predict the change in the burst period during drag reduction. On the other hand, McComb & Rabie (1982), Tiederman et al. (1985) and Walker et al. (1986) found that the burst period increases faster than the streak spacing in flows where there were strong concentration gradients normal to the wall. Therefore, the data from the present study will be used to examine the hypothesis that the streak spacing in drag reduced boundary layers changes as a function of drag reduction in the same manner that it changes in well mixed channel flows, and that the average burst period in the drag reduced boundary layers can be predicted from channel flow data.

1.4 Objectives

This study concentrates on the effects of drag reducing polymers on boundary layers and the modeling of these flows. It also provides some useful new Newtonian data. It has the following objectives:

- Verify that there is no Reynolds number effect on the inner region velocity statistics of adverse pressure gradient boundary layers in the range $3500 \leq Re_\theta \leq 25\,000$.
- Determine whether methods of determining wall shear stress which assume a constant slope of the logarithmic velocity profile can be used in polyacrylamide drag reduced boundary layers.
- Test whether it is possible to establish adverse pressure gradient boundary layers of drag reducing polymer solution that do not separate.
- Test whether Newtonian boundary layer codes which have been modified using drag reduction data from channel flows can be used to predict drag reduction in boundary layers.
- Determine whether the sum of the viscous and Reynolds stresses is equal to the total shear stress in boundary layers of polymer solutions.
- Determine whether the present data agrees with the hypothesis that large extensional motions in the boundary layer stretch the polymer molecules so that the solution of stretched molecules causes an anisotropic viscosity which damps the small scale motions.
- Determine the most appropriate variables for scaling the average burst period in Newtonian boundary layers.

- Determine whether the change in the average burst period caused by the drag reducing polymer can be predicted using results from channel flows.

CHAPTER 2 - EXPERIMENTAL APPARATUS AND PROCEDURES

2.1 Water channel

Experiments were performed using a new test section inserted into an existing closed loop water facility shown schematically in figure 2.1. The existing facility had four parallel centrifugal pumps each rated at $5.7 \cdot 10^{-3} \text{ m}^3/\text{s}$. Water was pumped into the upstream settling chamber which contained a perforated plate and an open cell foam section. Water entered the test section through a pair of smooth two dimensional contractions followed by a plastic honeycomb with 3.2 mm (1/8 in) cell size and 25 mm (1 in) streamwise length which removed any large scale vorticity. The honeycomb is followed by two 18 mesh screens to reduce turbulence into smaller scales which will dissipate quickly. Water flowed out of the test section through a series of three screens and a perforated plate which diffused the flow into the downstream chamber. This chamber also contained a copper coil through which cooling water flowed to maintain the channel temperature constant. Water left the chamber through a perforated pipe section to prevent a drain vortex at the exit pipe. A 2000 liter tank was available to store extra water. When needed, the water was filtered using a diatomaceous earth filter.

The test section was rectangular with three fixed walls and one flexible wall. The dimensions of the channel at the inlet were 100 mm in y , the direction normal to the measurement wall, and 200 mm in z , the spanwise direction. The total length of the

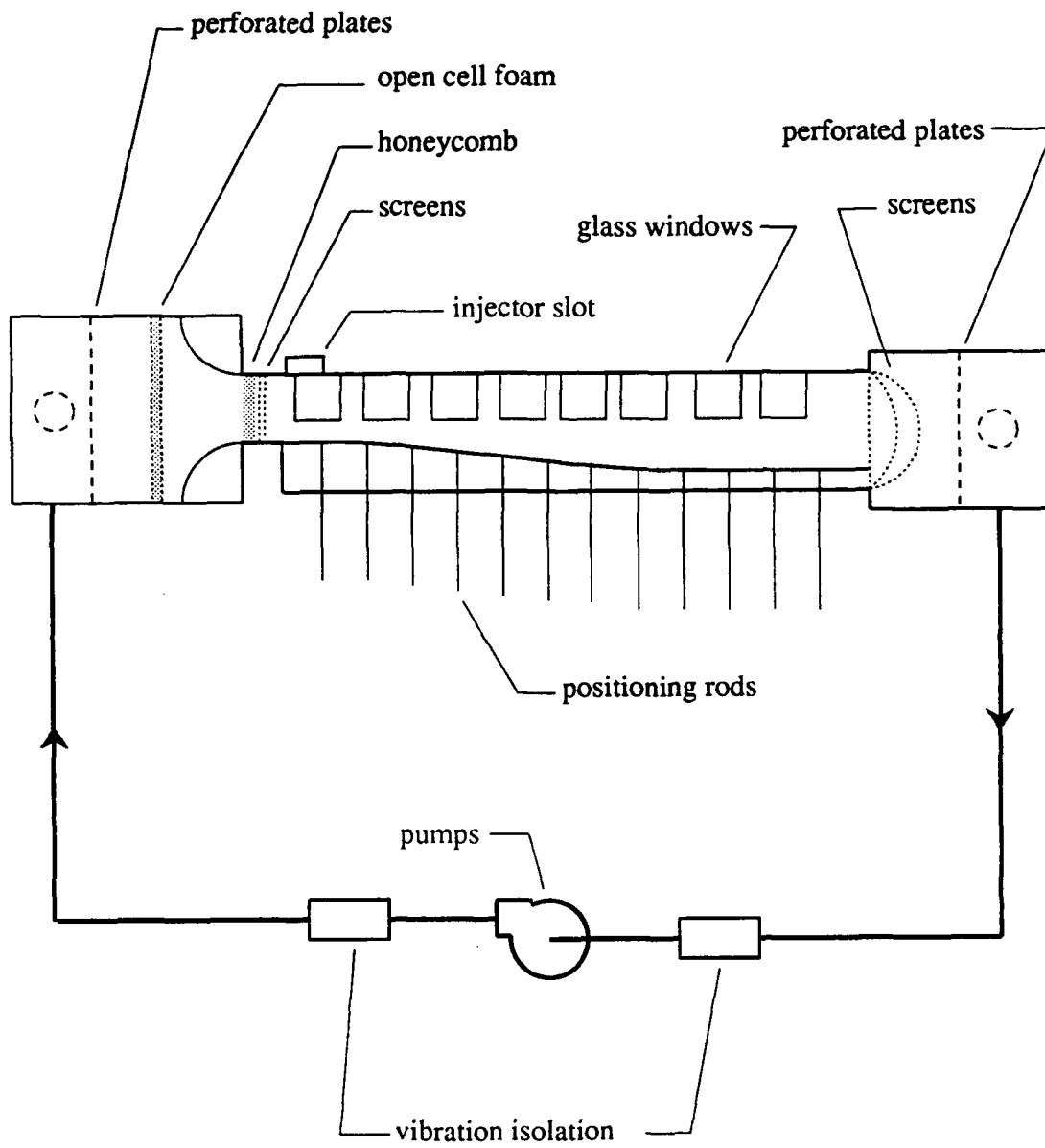


Figure 2.1 Schematic diagram of water channel.

channel was 2460 mm. The first 150 mm consisted of a fixed wall entrance section. In the remainder of the channel the flexible wall was adjusted to set the freestream pressure gradient. The flexible wall could move so that the outlet had a maximum total dimension in the y direction of 200 mm. The flexible wall was made of 3.2 mm acrylic. Its position was controlled by a set of rods which were positioned from outside the channel. All velocity and concentration measurements were made in the boundary layer which formed on the fixed vertical wall opposite the flexible wall. All fixed walls of the test section were made from 13 mm polycarbonate sheet. Channel dimensions are summarized in table 2.1.

Table 2.1 Channel dimensions.

item	locations or size (mm)
total length	2460
spanwise size	200
inlet width	100
maximum outlet width	200
trip rod location	197
trip diameter	0.80
injector location	331
slot width	2.5
slot angle	25 deg.

Glass windows were inserted into the walls of the channel to allow optical access for laser Doppler velocimetry (LDV) measurements in the channel. These windows were mounted so that one side was flush with the measurement wall, and they extended 100 mm from the measurement wall. The streamwise locations of the windows are summarized in table 2.2.

Table 2.2 Measurement window locations.

window number	from trip (mm)	from inlet (mm)
1	115-227	312-424
2	471-661	668-858
3	713-863	910-1060
4	933-1133	1130-1330
5	1155-1351	1352-1448
6	1363-1562	1560-1759
7	1728-1902	1925-2103
8	1982-2160	2179-2357

Suction ports were placed in the top and bottom walls to prevent separation at the corners of the flexible wall when an adverse pressure gradient was imposed on the flow. These were 3 mm diameter holes through which liquid was withdrawn by a small centrifugal pump and dumped into the downstream tank. At three streamwise locations, 524, 799 and 1090 mm downstream of the trip, one port was drilled in the top wall and one was drilled in the bottom wall. Flow visualization was used to identify streamwise locations where suction was required, and then flow visualization was used to verify that the suction successfully prevented separation.

The boundary layer was tripped to obtain a turbulent boundary layer. Spalart (1988) found that a fully turbulent boundary layer can exist for $Re_{\theta} \geq 225$. Therefore, the trip was located 197 mm downstream of the inlet where the boundary layer code of Cebeci & Bradshaw (1977), here named CBTSL, predicted that the momentum thickness Reynolds number, Re_{θ} , would be greater than 225. A 0.8 mm diameter copper rod was used as a trip which meets Gibbing's (1959) criterion for fully tripping a boundary layer.

During drag reduction and water injection experiments, fluid was injected into the boundary layer through a slot located 331 mm downstream of the inlet. The slot was 2.5 mm wide in the streamwise direction, and it injected fluid at an angle of 25 degrees from the wall. Walker et al. (1986) determined that this geometry produces optimal drag reduction in a two dimensional channel flow with Separan AP-273. The spanwise length of the slot was 180 mm. This length was made less than the total channel width to avoid injection into the secondary flows which form at the corners of the channel wall. The slot assembly is shown schematically in figure 2.2. All critical dimensions are given in mm or degrees. The injected fluid was initially stored in one of two 100 liter reservoirs. Shortly before injection, it was fed by gravity into a 13 liter tank which could be pressurized with nitrogen. During injection, the fluid was then forced from this tank by nitrogen regulated at a constant pressure of approximately 100 kPa gauge. The flow rate was determined by a Gilmont rotameter. After exiting the flow meter, the polymer supply line was split with a tee connector into two lines each of which had the same cross sectional area as the first. The two streams of fluid entered the injector through two holes in the back plate. These holes were positioned so that the lines supply equal spanwise lengths of the slot. The injector contains a baffle plate to evenly distribute the polymer solution over the spanwise length of the injector. This plate consists of 54 holes drilled through 3.1 mm nominal thickness polycarbonate. After passing through this baffle plate the fluid enters a final plenum before exiting the slot.

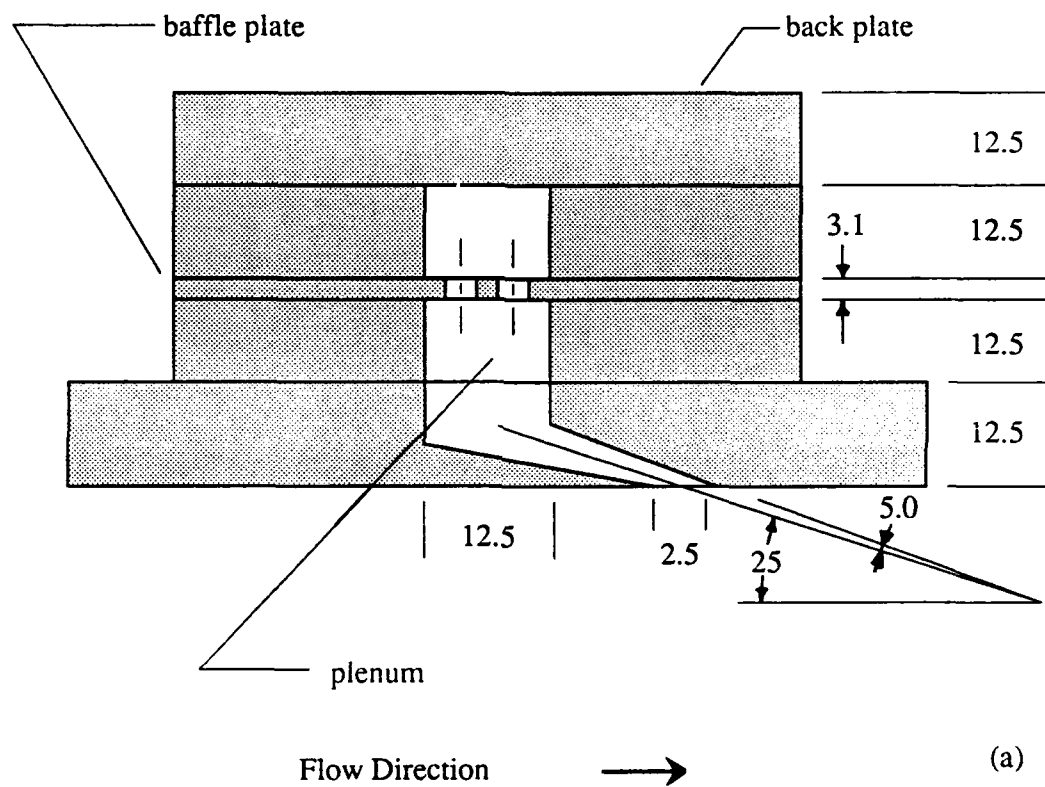


Figure 2.2 Schematic diagram of injector slot assembly (not to scale, dimensions in mm and degrees). (a) Cross sectioned side view (b) Top-view of baffle plate (c) Top-view of back plate.

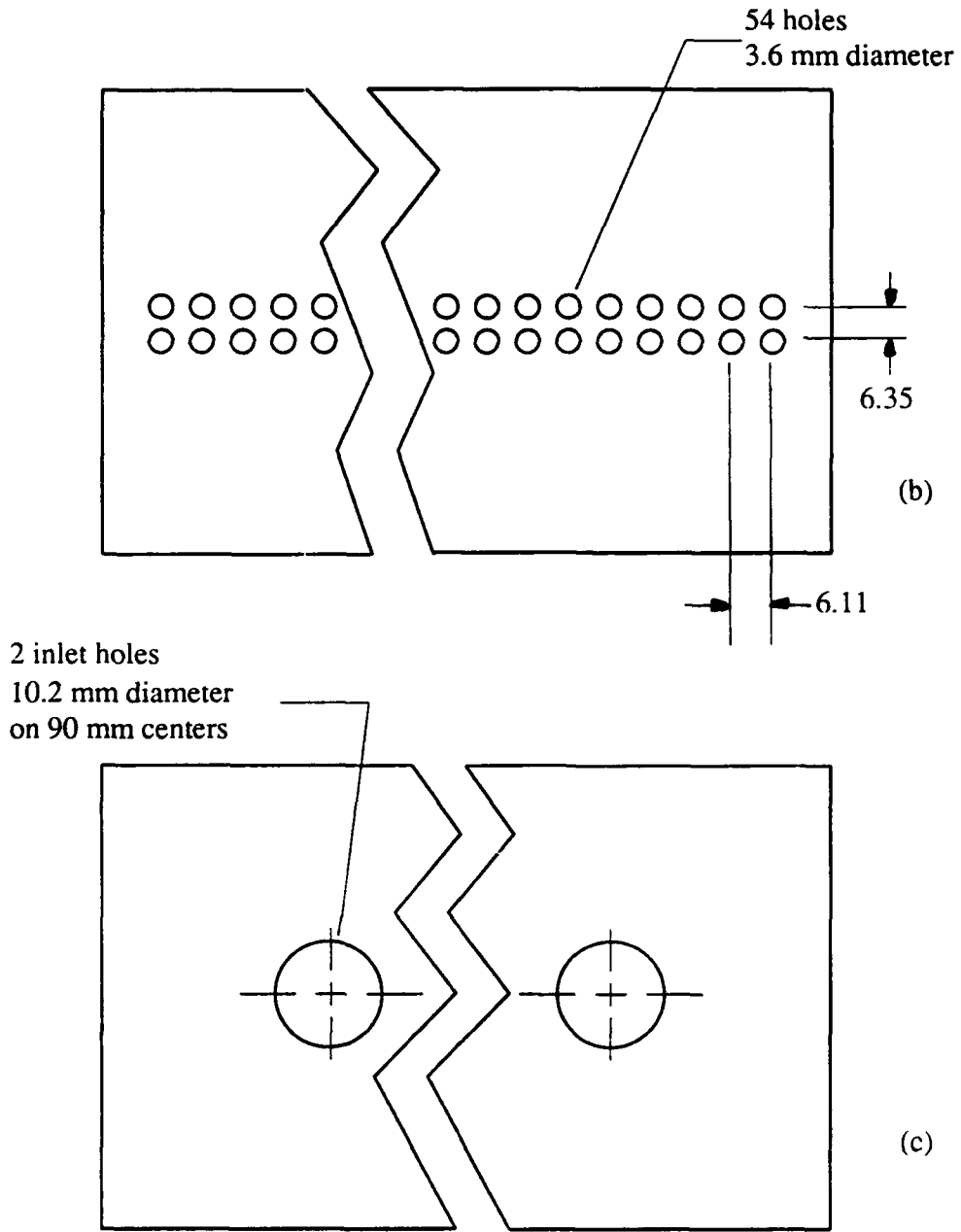


Figure 2.2 Continued

2.2 Velocity and concentration measurements

Two component velocity measurements were performed with a laser Doppler velocimeter (LDV). The system was a standard Thermo Systems Incorporated (TSI) two color, four beam system. The beams were oriented so that they measured velocity components which were approximately $\pm 45^\circ$ to the streamwise direction. These measured velocity components were transformed into streamwise and normal velocities using a procedure which will be described later. A Lexel model 85 Argon ion laser rated at 500 mW provided the incident beams for the system. Signal processing was performed using TSI model 1980 counter processors. The output of these processors was linked digitally to a Masscomp model 5520 minicomputer so that data could be taken either with data acceptance inhibited to obtain statistically independent samples or in a continuous mode with time between velocity realizations recorded. Single component measurements were performed with the same basic system; however, only the 514 nm line of the laser was used and the beams were oriented to directly measure the streamwise velocity.

The transmitting and receiving optics are shown schematically in figure 2.3. The system was operated in the forward scatter mode. In order to make measurements very near the wall, the center line of the probe volume formed an angle of approximately 3.5 degrees with the wall in the spanwise direction. The transmitting lens, transmitting mirror, and all the receiving optics were mounted as one assembly which translated in the direction normal to the measurement wall. During the initial zero pressure gradient measurements, the location of the probe volume relative to the wall was determined by the markings on the micrometer drives of the translation stage. However, these drives

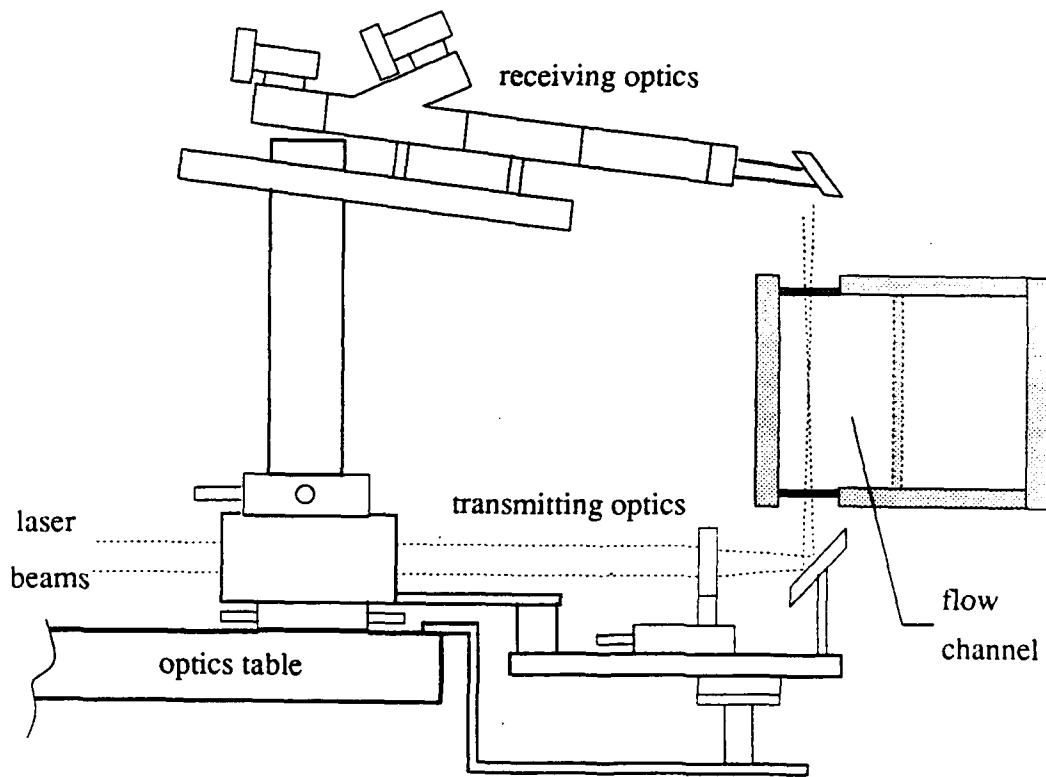


Figure 2.3 Schematic diagram of two-component, four beam LDV optics.

did not have sufficient resolution to make accurate position measurements in the linear sublayer. For all later measurements, a Mitutoyo dial gauge model 3058-11 calibrated to 0.01 mm was used for measuring the position of the probe volume. The location of the wall was determined by visually observing the probe volume and its reflection on the wall through the receiving optics. The wall was found by merging these two images. In experiments performed after the dial gauge was installed, the wall location was further refined by making streamwise mean velocity measurements at three points in the linear sublayer and extrapolating a least squares fit line through these points to zero velocity. The result was assumed to be the correct wall location. The correction determined by this method was always less than 0.06 mm and was generally less than 0.05 mm.

A TSI 9143 field stop assembly with an aperture was used to ensure the spatial coincidence of the two component measurements. For the initial zero pressure gradient measurements, a 200 μm aperture was used. For all later experiments a 100 μm aperture was used. The spatial resolution of the system was governed by both the receiving and transmitting optics. Received light was collected at approximately 10 degrees from the axis of the transmitting optics. This orientation limits the effective length of the probe volume. The approximate diameter of the resulting probe volume was 63 μm . The length was approximately 707 μm for the zero pressure gradient data and 530 μm for the adverse pressure gradients. The resulting dimensionless diameter, normalized by u_τ and v , varied between 1 and 2 for both cases, and the length, normalized by u_τ and v , was approximately 27 for the zero pressure gradient cases and 12 to 15 for the adverse cases. The flow was seeded with fat particles from

homogenized cream at a concentration of 2.5 ml/m³. All injected fluid was also seeded with this material at the same concentration.

The instantaneous velocity components measured by the velocimeter, U'_1 and U'_2 , were corrected for slight non-orthogonality of the probe volumes. This was accomplished by computing the orthogonal velocities, U_1 and U_2 .

$$U_1 = U'_1 \quad (2.1)$$

$$U_2 = \frac{1}{\cos\alpha} U'_2 + U'_1 \tan\alpha \quad (2.2)$$

The angle α is the actual angle between the measured velocity components which was determined by measurements of the beam geometry as shown in figure 2.4.

The velocity statistics were first determined for the U_1 and U_2 velocities then transformed to the streamwise and normal coordinates using the following procedure. For any angle θ measured from the instantaneous streamwise direction the streamwise and normal velocity components are determined from:

$$U = U_2 \cos\theta + U_1 \sin\theta \quad (2.3)$$

$$V = U_2 \sin\theta - U_1 \cos\theta \quad (2.4)$$

These equations are substituted into the definitions of the Reynolds averaged statistics ($U = \bar{U} + u$). The resulting equations for the fluctuation statistics in the streamwise and normal coordinates are:

$$\overline{u^2} = \overline{u_1^2} \sin^2\theta + \overline{u_2^2} \cos^2\theta + 2\overline{u_1 u_2} \cos\theta \sin\theta \quad (2.5)$$

$$\overline{v^2} = \overline{u_1^2} \cos^2\theta + \overline{u_2^2} \sin^2\theta - 2\overline{u_1 u_2} \cos\theta \sin\theta \quad (2.6)$$

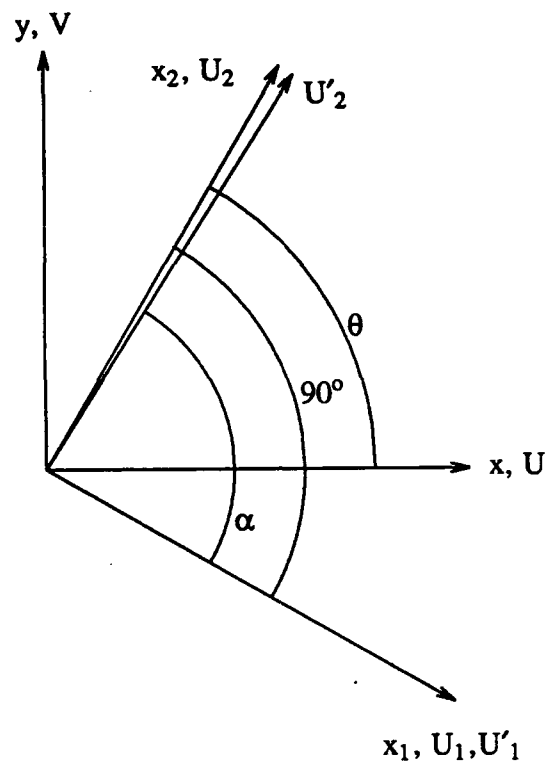


Figure 2.4 Measurement beam geometry.

$$\overline{uv} = (\overline{u_2^2} - \overline{u_1^2})\cos\theta\sin\theta + \overline{u_1u_2}(\sin^2\theta - \cos^2\theta) \quad (2.7)$$

$$\overline{u^3} = \overline{u_2^3}\cos^3\theta + 3\overline{u_1u_2^2}\sin\theta\cos^2\theta + 3\overline{u_1^2u_2}\sin^2\theta\cos\theta + \overline{u_1^3}\sin^3\theta \quad (2.8)$$

$$\overline{v^3} = -\overline{u_2^3}\sin^3\theta - 3\overline{u_1^2u_2}\sin\theta\cos^2\theta + 3\overline{u_1u_2^2}\sin^2\theta\cos\theta + \overline{u_1^3}\cos^3\theta \quad (2.9)$$

$$\begin{aligned} \overline{u^4} = & \overline{u_2^4}\cos^4\theta + 4\overline{u_1u_2^3}\sin\theta\cos^3\theta + 6\overline{u_1^2u_2^2}\sin^2\theta\cos^2\theta \\ & + 4\overline{u_1^3u_2}\sin^3\theta\cos\theta + \overline{u_1^4}\sin^4\theta \end{aligned} \quad (2.10)$$

$$\begin{aligned} \overline{v^4} = & -\overline{u_2^4}\sin^4\theta - 4\overline{u_1^3u_2}\sin\theta\cos^3\theta + 6\overline{u_1^2u_2^2}\sin^2\theta\cos^2\theta \\ & - 4\overline{u_1u_2^3}\sin^3\theta\cos\theta + \overline{u_1^4}\cos^4\theta \end{aligned} \quad (2.11)$$

The angle θ was determined during the zero pressure gradient measurements by changing the angle θ until the normal velocity in the free stream was equal to zero. In the adverse pressure gradient case, this angle was set at 45 degrees by careful alignment of the laser beams with the wall. The accuracy of both procedures is believed to be ± 1 degree based on comparison of the two techniques when applied to the zero pressure gradient boundary layers.

Various numbers of data realizations were acquired depending on the type of statistical estimate that was being made. The two component profiles for all the Newtonian cases and the zero pressure gradient drag reduced cases consisted of 20 000 realizations for all points outside the linear sublayer. Inside the sublayer, where only mean streamwise velocity was of interest, only 5000 points were acquired. The number of data realizations acquired for the adverse pressure gradient drag reduced cases was reduced to 10 000 for two component statistics to keep polymer usage within practical

limits. The single component velocity profiles used to iteratively determine the wall shape for the adverse pressure gradient boundary layers consisted of 2500 data realizations, since only mean streamwise velocity was of interest.

For all of the average profiles, the processors were inhibited so that a period of at least ten times the inverse of the validation rate occurred between recorded velocity realizations. In addition, the validation rate was maintained in excess of the peak estimated Kolmogoroff frequency in the flow. The Kolmogoroff frequency in the flow was estimated by assuming that dissipation and production of turbulent kinetic energy were balanced at the y location where these quantities reach a maximum. Because the peak value of production was not known before a given experiment, the peak of production was approximated by the wall shear stress multiplied by the wall strain rate. This approximation is conservative, because in equilibrium flows of the type encountered, the actual peak of production was less than that calculated by this approximation. For all of the profiles of fluctuation statistics, the present combination of inhibit time and record length results in a total time period for each measurement which approximately meets or exceeds the recommended times of Klewicki & Falco (1990). All burst records, whether one or two component consisted of 100 000 velocity realizations with time between realizations recorded. In all burst records, the data validation rate was maintained in excess of the reciprocal wall strain rate.

All experiments were conducted at 22° C resulting in a water viscosity of $0.96 \cdot 10^{-6}$ m²/s determined from tabular data. The temperature could be controlled to within an estimated $\pm 0.2^\circ$ C resulting in only ± 0.5 percent variation in viscosity. The

corresponding density, 998 kg/m^3 , varied negligibly. The flow rate in the channel was monitored throughout each experiment by measuring the pressure drop across an elbow in the piping on the pressure side of the pumps. The pressure drop was measured using a U-tube manometer with carbon tetrachloride as the manometer fluid.

The free stream turbulence level in the channel was measured using a TSI model 1261-10W hot film probe. The probe is $25 \mu\text{m}$ in diameter and 0.5 mm in effective length. The standard probe body was extended by gluing it into the end of a 6.35 mm diameter stainless steel tube with 1.65 mm wall thickness. The large diameter of the tube was chosen to provide stiffness to prevent vibration. The Reynolds number based on tube diameter was approximately 6500, so the wake was fully turbulent (Roshko, 1955). This tube passed through one of two removable plugs set in the top wall of the channel at 318 and 1950 mm downstream of the boundary layer trip and 50 mm in the normal direction from the measurement wall. It was only inserted into the channel during experiments conducted specifically to measure the freestream turbulence.

A DISA 55M10 constant temperature bridge powered the probe at an overheat ratio of 1.035. This low overheat ratio prevented gas bubble formation on the film. The frequency response of the bridge was tested with a 3 kHz square wave. The output of the bridge was measured using a TSI model 1076 integrating voltmeter. Linearization was not used because of the low turbulence intensities involved. The turbulence intensity was approximated by estimating the sensitivity defined by (Hinze, 1975, equation 2.40):

$$\sqrt{e^2} = s_{c.t.} \sqrt{u^2} \quad (2.12)$$

Where e is the fluctuation voltage and u is the velocity fluctuation. The sensitivity was determined from the equation (Hinze equation 2-43):

$$s_{c.t.} = \frac{(\bar{R}_w - R_g)nB\bar{U}^{n-1}}{2\bar{I}} \quad (2.13)$$

Where \bar{R}_w is the hot resistance of the film, R_g is the resistance of the film at the water temperature n and B are the exponent and coefficient of the calibration curve and \bar{I} is the average current in the film. The measured turbulence intensity at the inlet was less than 0.1 percent which is within the range recommended by Coles (1962) for boundary layer studies. Linearization of the bridge output was deemed unnecessary because of this low turbulence value.

Concentration measurements were made using a laser induced fluorescence technique based on that of Walker & Tiederman (1989). The only difference between the present measurement technique and that presented in the paper is a change in the equation relating intensity to diode voltage. Walker & Tiederman's paper gives a linear relation between the diode voltage and the diode intensity (their equation 8). A more accurate relationship between the diode output voltage, V_n and the fluoresced intensity, I_n is given by equation 2.14:

$$V_n = a_n b_n I_n^{1/g} + V_{dn} \quad (2.14)$$

where g is a constant which is a property of the photodiodes, a_n and b_n are constants, and V_{dn} is the dark voltage of the n th diode. The concentration at the n th diode, C_n ,

(equation 9 of the paper) then has the form:

$$C_n = (V_n - V_{dn})^g \left[\frac{1}{(a_n b_n)^g I_0 \alpha \beta_d d} \prod_{i=1}^{n-1} \exp \beta_d C_i s \right] \quad (2.15)$$

where I_0 is the initial intensity of the laser beam and α is a constant. Please note that the dye extinction coefficient is given here as β_d to prevent confusion with the Clauser pressure gradient coefficient. The final result is therefore:

$$C_n = \frac{1}{A_n} \left[\prod_{i=1}^{n-1} \exp \beta_d C_i s \right] (V_n - V_{dn})^g \quad (2.16)$$

where A_n are calibration coefficients for each diode. Note that this is identical to equation 10 in Walker & Tiederman except that the exponent g appears on the voltage difference.

The equipment is shown schematically in figure 2.5. The LDV optics are shown in dashed lines because they were in place during these experiments, but simultaneous velocity and concentration measurements were not performed. A beam from an argon ion laser (488 nm) entered the channel normal to the wall and excited fluorescein disodium salt which was dissolved into the polymer solution. A linear diode array camera which was mounted on a small mill table underneath the channel recorded the intensity of the fluoresced light along the beam. Dye concentration as a function of distance along the beam was determined from the intensity profile. The output of the camera was digitized and processed by the Masscomp computer.

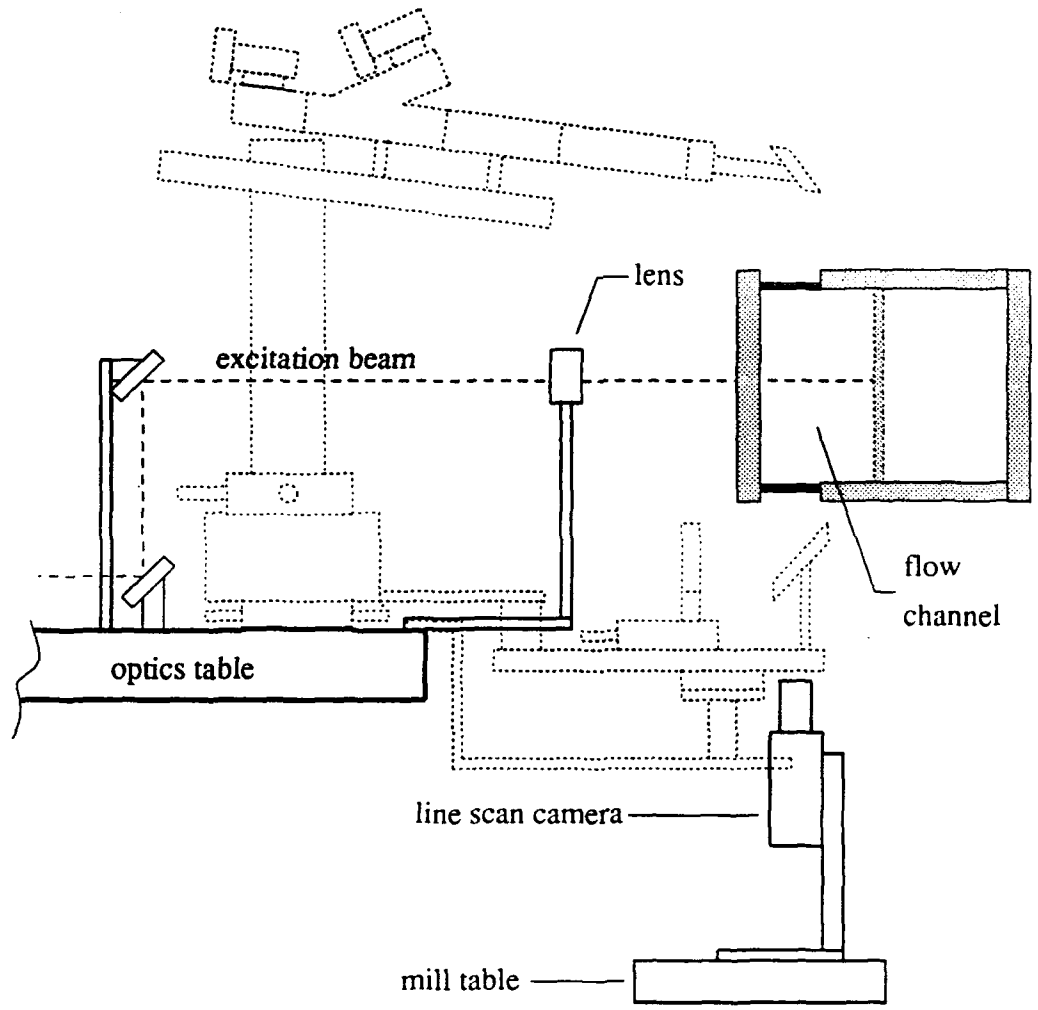


Figure 2.5 Schematic diagram of concentration measurement optics.

Each diode in the array has dimensions of $25\ \mu\text{m}$ by $425\ \mu\text{m}$ and they are located on $50\ \mu\text{m}$ centers. The effective area of the flow viewed by these elements varied with the magnification used. The effective streamwise and spanwise length were limited by the width of the laser beam which excites the dye, $115\ \mu\text{m}$. The array was focused so that it measured from the wall to $y^+ \cong 500$ which was well outside the log region of the mean velocity profile. The resulting effective dimensionless element sizes, normalized by u_τ and v , varied from 1.5 to 2.0 in the y direction and 3.3 to 4.9 in the streamwise and spanwise direction. The effective dimensionless element spacing was 3.0 to 4.0.

As in Walker & Tiederman's case, the channel water was dyed to a low background concentration, approximately 0.06 wppm. This concentration was measured before each concentration measurement. The channel water was buffered with sodium hydroxide so that its pH value was within ± 0.1 of the pH of the polymer. Because the resulting pH was in excess of 8 the extinction coefficient of the dye was effectively independent of pH (Walker, 1987). Concentration records covered an integration time of 10 seconds. Since this time was smaller than the mean time for the channel water to make one complete circuit of the flow loop, the background dye concentration was constant during injection. In order to ensure that this integration time was adequate, a second concentration measurement was performed in several cases. This second measurement was performed several minutes after the first thereby ensuring that the two records were statistically independent. The concentration records were accepted if the near wall polymer concentration of the two records differed by less than 0.1 percent of the injected concentration.

2.3 Polymer solution preparation

The drag reducing agent was a 1000 wppm aqueous solution of Separan AP-273, a polyacrylamide manufactured by Dow Chemical. The injectant was prepared in a two part procedure. The polymer, which was initially a dry powder, was suspended in isopropyl alcohol then mixed into deaerated softened tap water to produce a solution of approximately 5000 wppm. The initial temperature of this solution was always in the range 32° to 38° C. After mixing, it was allowed to hydrate approximately 12 hours. It was then mixed to the final concentration of 1000 wppm using softened filtered tap water. The LDV seed and fluorescein dye, when needed, were added to the water in this dilution. The solution was further hydrated so that the total hydration time was at least 24 hours. The temperature was maintained within $\pm 0.5^\circ$ C of the channel temperature of the polymer during injection which ensured that the solvent viscosity was within 1.2 percent of the viscosity of the channel water.

Since several batches of polymer were used in these experiments over a period of several months, the polymer solutions were tested for repeatability. The shear viscosity of the polymer solutions was tested directly using a Brookfield LVT-SCP cone and plate viscometer and indirectly by checking the calibration of the injection flowmeter for each batch of polymer. A sample from each polymer batch was diluted to 100 wppm and run through a 16 mm diameter tube to test for drag reduction. The percent drag reduction obtained in the tube for each batch was compared with previous polymer solutions mixed by the present and previous investigators in the same laboratory. Replication of the drag reduction within 10 percent was considered adequate.

CHAPTER 3 - NEWTONIAN BOUNDARY LAYERS

The information in this chapter verifies that good equilibrium boundary layers can be produced with the channel and compares existing mixing length models against the data. The first section addresses Newtonian zero pressure gradient boundary layer studies which were done to verify the performance of the facility and to provide a data base to which drag reduced flows can be compared. The next section demonstrates that two adverse pressure gradient, Newtonian, equilibrium boundary layers were successfully produced. The final section presents the performance of the mixing length models.

3.1 Zero pressure gradient experiments

The effectiveness of the boundary layer trip was evaluated using the Coles wake parameter, Π , which is defined in equation 1.1. The wake parameter and the boundary layer thickness, δ , were determined for each experiment following Coles (1968). Equation 1.1 was least squares fit to the data from $y^+ \cong 100$ to $y = 0.9\delta$ with Π and δ as undetermined parameters. In practice, the lower bound does not affect the result, as long as the lower bound is in the log region.

Coles (1962) recommended that the wake parameter, Π , in a Newtonian zero pressure gradient boundary layer vary as a function of the momentum thickness Reynolds number, Re_θ , along the solid curve shown in Figure 3.1. The present data are

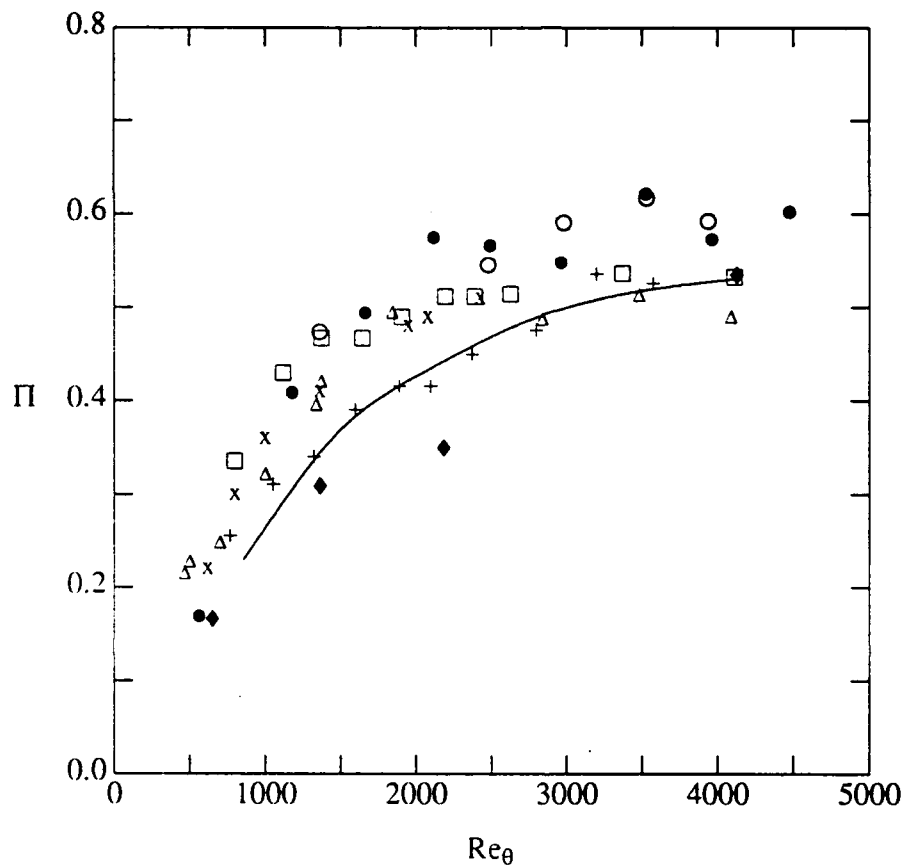


Figure 3.1 Variation of the Coles wake parameter, Π as a function of Re_θ for zero pressure gradient Newtonian boundary layers. \circ present study; Δ Purtell et. al. (1981); \square Murlis et al. (1982); \times Erm et al. (1985) (8 m/s); $+$ Erm et al. (14 m/s); \blacklozenge Shah & Antonia (1989); \bullet Wieghardt (Coles re-analysis, 1968); — Coles (1962).

shown as circles and are also given in table 3.1. The data of Wieghardt, as reanalyzed by Coles (1968), are also shown because the original data set was included in the data used to establish the 1962 curve. A number of more recent studies are also shown. Purtell et al. (1981), Murlis et al. (1982) and the 8 m/s case of Erm et al. (1985) follow the trend of Coles' 1962 curve, but are somewhat higher. The 14 m/s data of Erm et al. very closely follows the curve for all Reynolds numbers. The only data which lie distinctly below the curve are those of Shah & Antonia (1989). The major conclusion from the plot is that the present data, shown as open circles, are consistent with the data of other investigators. When the zero pressure gradient data are plotted in the form \bar{U}/U_e as a function of y/δ^* , as suggested by Klebanoff & Diehl (1952), the data collapse very well to the same curve. This plot is in the appendix. Therefore the present trip was judged to be satisfactory using both Coles' wake criterion and Klebanoff & Diehl's velocity profile analysis. The values of the skin friction, c_f and shape factor, H , compare well with previous data and are given in the appendix.

Figure 3.2 shows the zero pressure gradient, Newtonian, mean streamwise velocity data for all Reynolds numbers, Re_θ , in the present study. The Reynolds number is varied by moving the streamwise measurement location while the freestream velocity remains fixed therefore the plot also shows the streamwise variation of the velocity profiles. A brief summary of these data and the adverse pressure gradient data are given in table 3.1. Also shown is a line representing the standard logarithmic relationship using constants of 0.41 and 5.0 as recommended by Coles (1968). All of the present data agree well with the standard log relation in the region $30 \leq y^+ \leq 300$ except for the lowest Reynolds number of 1358 for which the range is approximately

Table 3.1 Summary of Newtonian data.

$(x - x_t)$ (mm)	Re_θ	β	G	Π
181	1358	0.0	7.29	0.48
754	2478	0.0	7.09	0.55
1058	2978	0.0	7.06	0.59
1513	3527	0.0	7.22	0.62
1867	3935	0.0	7.12	0.59
636	2664	1.7	9.6	-
747	3080	2.0	10.4	-
854	3566	1.8	10.6	1.58
984	3868	1.7	11.0	-
1101	4210	1.8	11.2	1.80
840	3784	2.4	12.2	2.10
1008	4588	2.3	13.0	2.20
1102	4978	2.7	13.0	2.20

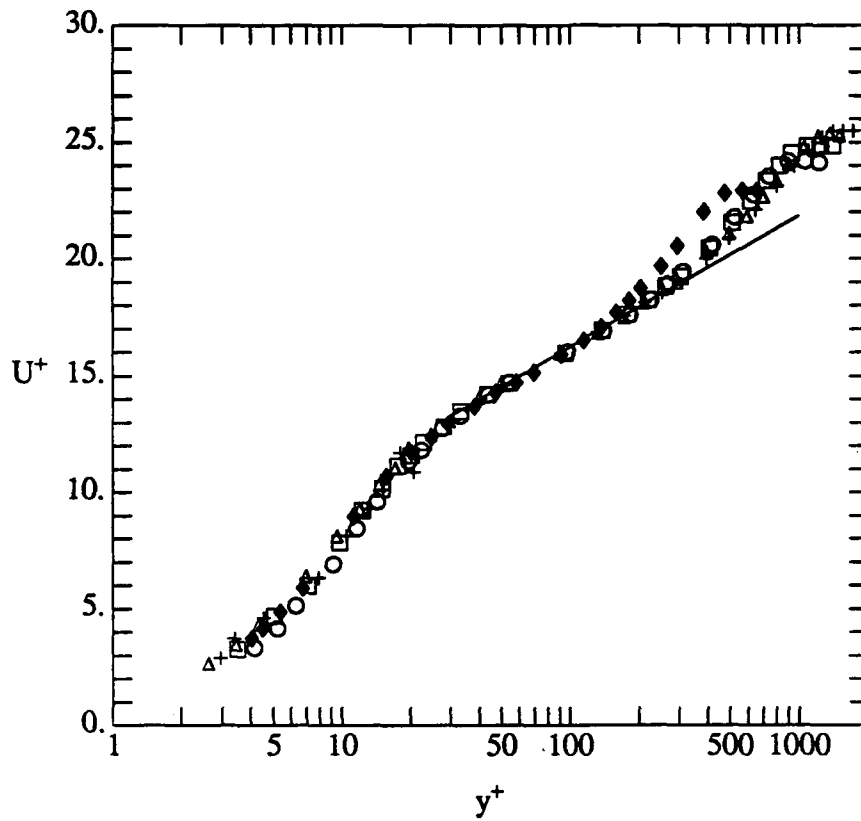


Figure 3.2 Mean streamwise velocity in a Newtonian zero pressure gradient boundary layer without injection. \blacklozenge $Re_\theta = 1358$; \circ $Re_\theta = 2478$; \square $Re_\theta = 2978$; \triangle $Re_\theta = 3527$; $+$ $Re_\theta = 3935$; — $U^+ = (1/0.41) \ln y^+ + 5.0$.

$30 \leq y^+ \leq 200$. The start of the wake region at a smaller value of y^+ for $Re_\theta = 1358$ is a low Reynolds number effect which has been observed by other authors including Purtell et al., Erm et al. and Murlis et al.

Recent streamwise and normal velocity fluctuation data in zero pressure gradient boundary layers at a momentum thickness Reynolds number of approximately 3500 are compared in figure 3.3. Agreement in the near-wall region, where inner normalization is expected to be correct, is excellent except that u' for the present data between y^+ of 20 and 50 is slightly higher than that of Purtell et al. (1981) and Erm et al. (1985). The data of Fontaine et al. (1990), who have also measured values of u'/u_τ in a water boundary layer using a LDV, are also slightly higher than those of Purtell et al. and Erm et al. This difference between LDV and hot-wire data is probably due to limited spatial resolution of the hot wires used in Purtell's and Erm's studies where the dimensionless length was approximately 20 wall units for Purtell et al. and 30 for Erm et al. These lengths are expected to yield slightly low rms velocity readings very near the wall (Willmarth & Sharma, 1984). The lower section of figure 3.3 compares the inner normalized Reynolds shear stress of the present zero pressure gradient boundary layer to other studies. Agreement with other data in the inner region is very good. These profiles are typical for all the other Reynolds numbers at which velocities were measured in the present experiments, because no Reynolds numbers influences were observed in the inner region of the flow. These data are shown in the appendix, figure A.4. This result supports Pantón's (1990) theory which states that scaling velocities with u_τ is appropriate in this region for friction velocity Reynolds numbers ($u_\tau \delta/\nu$) in the present range, 550 to 1460.

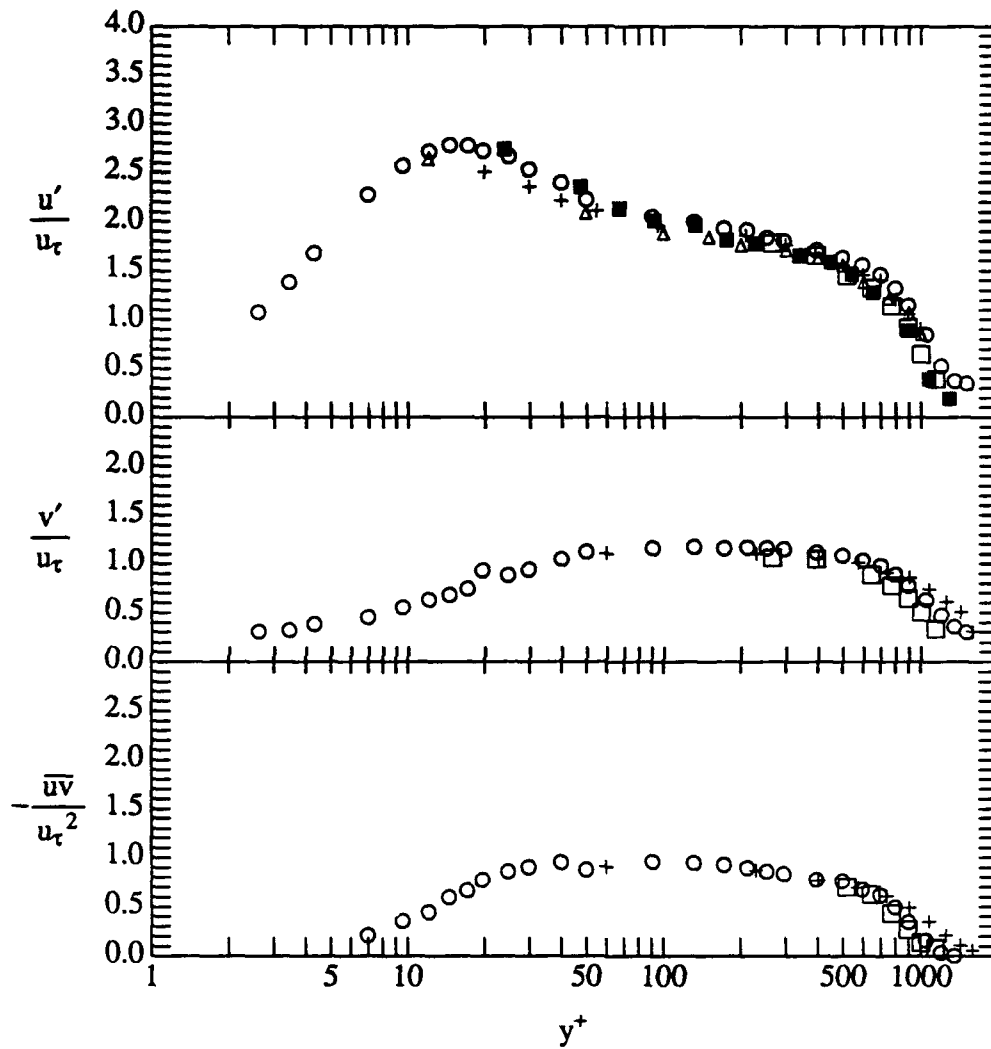


Figure 3.3 Comparison of root-mean-square velocities and Reynolds stresses in Newtonian zero pressure gradient boundary layers without injection. \circ present data $Re_\theta = 3527$; Δ Purtell et al. $Re_\theta = 3480$; \square Murlis et al. $Re_\theta = 3362$; $+$ Erm et al. $Re_\theta = 3575$; \blacksquare Fontaine et al. $Re_\theta = 3100$.

The skewness and flatness factors of the velocity in Newtonian flows provide another check to determine whether the present data are consistent with previous data. Figure 3.4 shows streamwise and normal velocity fluctuation skewness for the present data at a Reynolds number of $Re_0 = 2478$ compared to that of Balint et al. (1991). The present streamwise data demonstrate excellent agreement with the Balint et al. data. The agreement of the skewness of the normal velocity fluctuation is not as good. However, the present data agree with Balint et al.'s data when the uncertainty is taken into account. Typical error bounds were estimated using the bootstrap method (Efron, 1982) following the basic procedure of Johnson and Barlow (1989). This uncertainty on the normal velocity statistics represents an inherent limitation imposed by measuring velocities at an angle of 45 degrees to the flow. Figure 3.5 shows the flatness factors for the same data. The agreement between the data sets is excellent for both cases. Note that the flatness of the normal fluctuations increases significantly inside of $y^+ \cong 50$. This increase indicates that the normal velocity is becoming more intermittent. This change indicates that the flow is dominated by the strong outward and inward fluctuations which are associated with the coherent structures in this region.

3.2 Adverse pressure gradient data

One of the boundary layers had a relatively strong adverse gradient which was characterized by $\beta = 2.4$ and $G = 13.0$. The second had a moderate adverse gradient with $\beta = 1.8$ and $G = 11.0$. The first step in establishing equilibrium in a boundary layer is to establish equilibrium velocity profiles. In the present study each boundary layer was initially established by adjusting the flexible wall to establish the streamwise

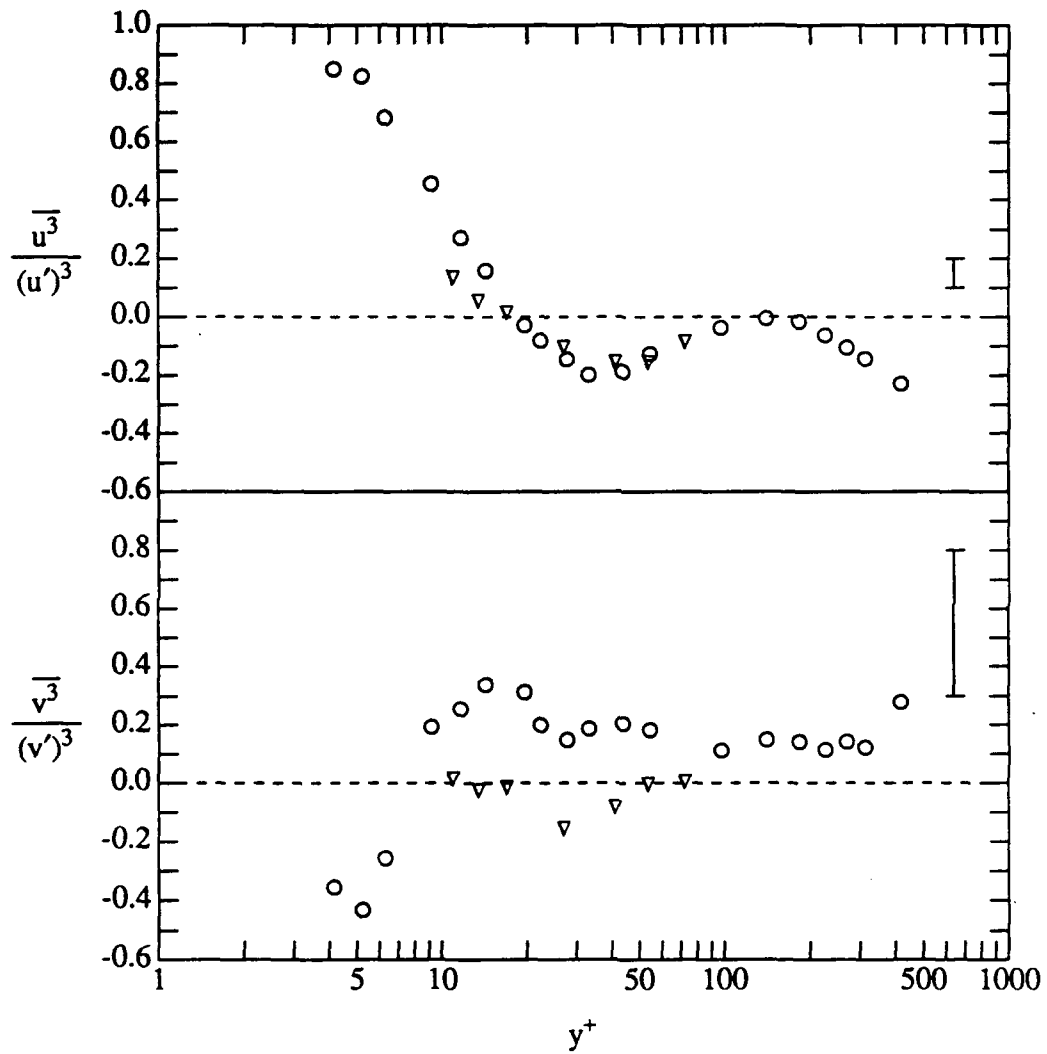


Figure 3.4 Skewness of the streamwise and normal velocity fluctuations for a zero pressure gradient Newtonian boundary layer. \circ $Re_\theta = 2478$. ∇ $Re_\theta = 2685$, Balint et al.. Typical uncertainty shown in upper right corner.

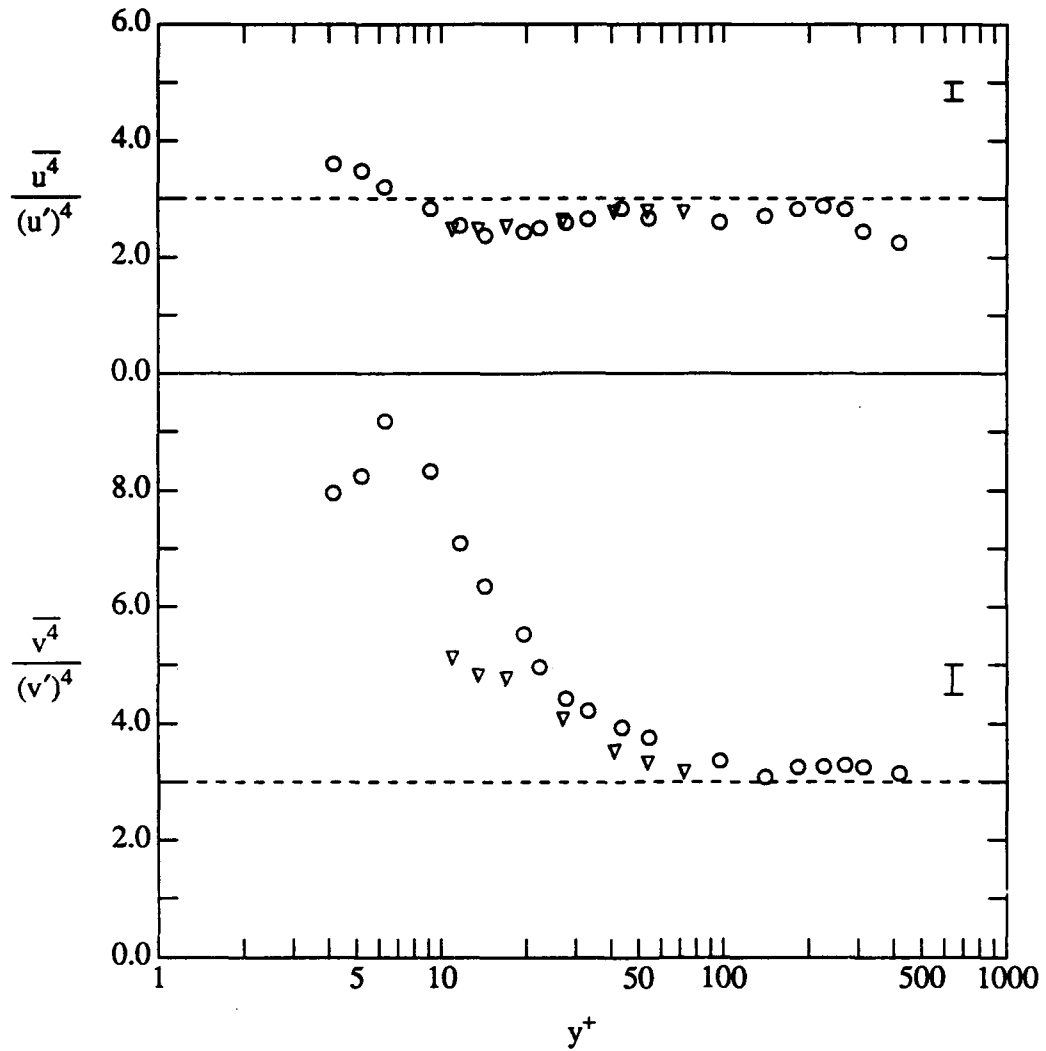


Figure 3.5 Flatness factor of the streamwise and normal velocity fluctuations for a zero pressure gradient Newtonian boundary layer. \circ $Re_\theta = 2478$. ∇ $Re_\theta = 2685$, Balint et al.. Typical uncertainty bound shown at right.

freestream pressure distribution predicted by the boundary layer code CBTSL. This prediction was computed by iteratively varying the freestream velocity profile input to the code until it predicted a constant value of β for the adverse pressure gradient region of the flow. Profiles of mean streamwise velocity were acquired along the expected useful length of the boundary layer. Using these profiles as a guide, the flexible wall was then adjusted as needed to force the boundary layer into equilibrium. The freestream velocity derivatives were calculated by averaging the one sided derivatives calculated both upstream and downstream of each point.

Figure 3.6 shows the mean streamwise velocity defect profiles as a function of the wall normal distance normalized by the Clauser integral thickness, Δ , for the boundary layer with $\beta = 1.8$. The Reynolds number, Re_θ , increases with streamwise distance as is given in table 3.1. The data show that the boundary layer is not in equilibrium at the first streamwise location (represented by \diamond). The streamwise extent of the boundary layer which is in equilibrium is approximately eight boundary layer thickness. The streamwise variation of β is less than that in a comparable boundary layer of Clauser. Therefore this boundary layer represents an excellent equilibrium case. As shown in the appendix, these data compare well with similar equilibrium data of Clauser (1954), East & Sawyer (1979), and White & Tiederman (1990). Figure 3.7 is the same type of plot for the stronger pressure gradient case. Agreement of the three profiles is very good over a streamwise distance of approximately 7 boundary layer thicknesses. As shown in the appendix, these velocity profiles compare well to a near equilibrium case of Bradshaw (1969) which had the same β and G .

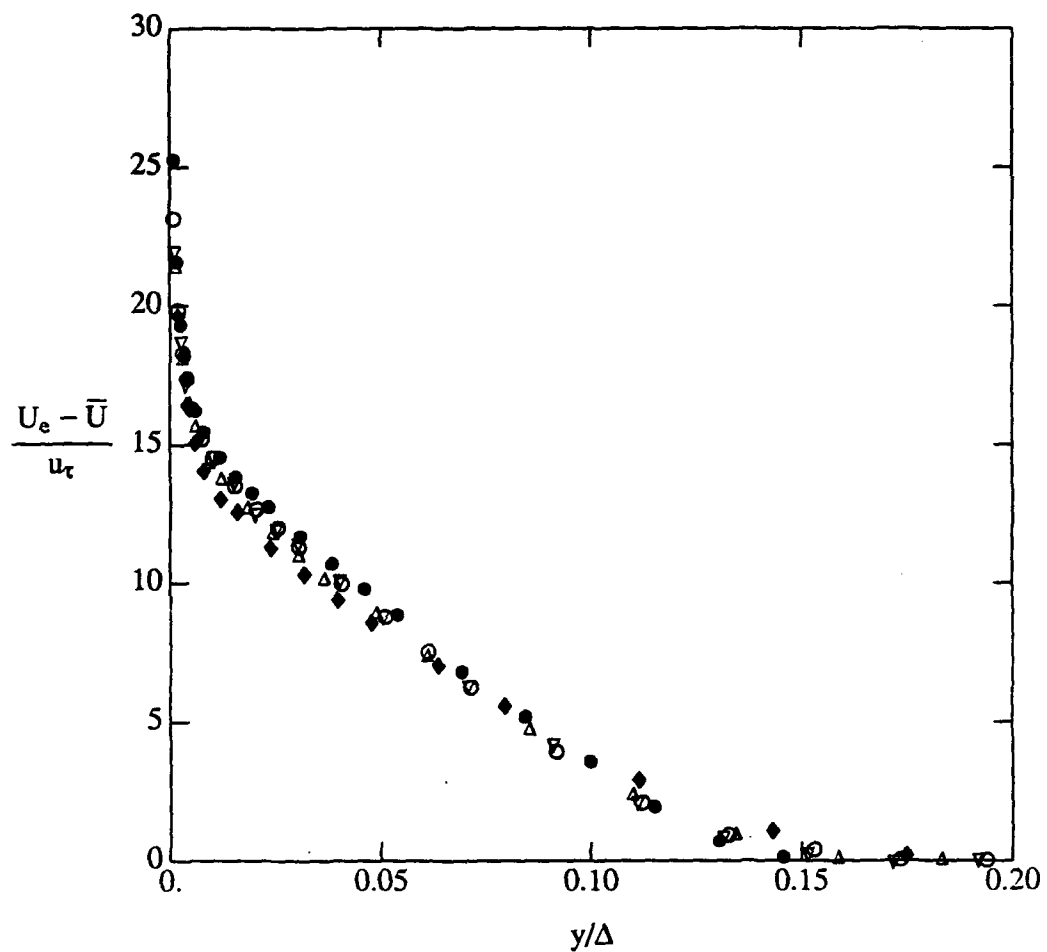


Figure 3.6 Velocity defect profiles in an adverse pressure gradient boundary layer with $\beta = 1.8$. \blacklozenge $Re_\theta = 2664$; \triangle $Re_\theta = 3080$; \circ $Re_\theta = 3570$; ∇ $Re_\theta = 3870$; \bullet $Re_\theta = 4210$.

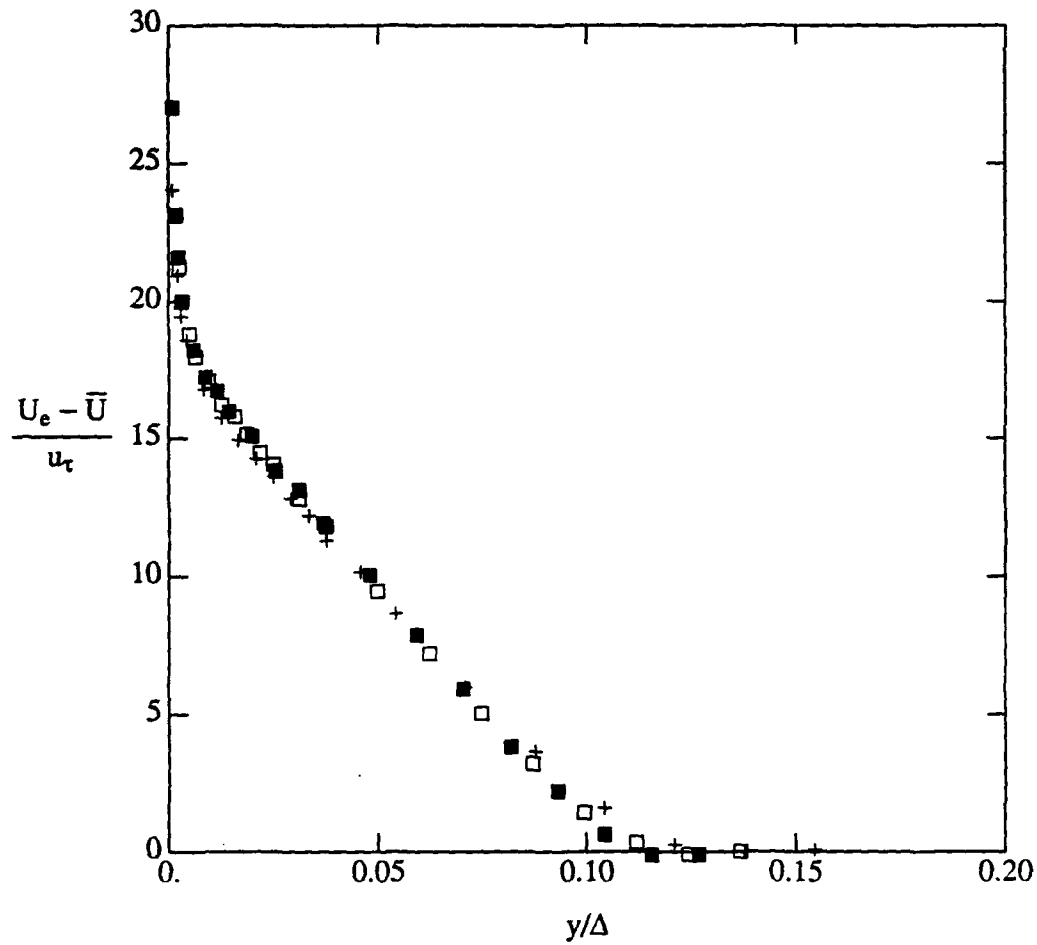


Figure 3.7 Velocity defect profiles in an adverse pressure gradient boundary layer with $\beta = 2.4$. + $\text{Re}_\theta = 3784$; \square $\text{Re}_\theta = 4588$; \blacksquare $\text{Re}_\theta = 4978$.

The resulting freestream velocity profiles are shown in figure 3.8. The curves fit to the data are of the form $U_e \propto x^a$ because Townsend (1961) found that freestream velocity variations of this type will approximate equilibrium boundary layers. The present data are summarized in table 3.1. The wake parameter was only calculated for the final equilibrium profiles.

Figure 3.9 shows the mean velocity data for both adverse pressure gradient boundary layers in inner variables. The line shown is the standard logarithmic relationship. The shear velocity, u_τ , for the data presented in this plot was deduced from mean velocity measurements in the linear sublayer. Agreement with the standard logarithmic profile is good. Figure 3.10 shows the velocity in the linear sublayer for the same data on a linear plot. The three points in the linear sublayer of each case were used to find u_τ by using linear regression to find the velocity gradient in the wall normal direction. The expected uncertainty at 95 percent confidence for this measurement of u_τ was 4 percent (White, 1989).

Figure 3.11 compares inner normalized velocity fluctuation statistics for two streamwise locations (different Re_θ) in the moderate pressure gradient case with comparable statistics of East & Sawyer (1979) and White & Tiederman (1990). In all cases the streamwise velocity fluctuation (u'/u_τ) profiles exhibit excellent agreement through the outer edge of the log region of the mean velocity profile. This result supports Panton's (1990) theory that inner scaling is sufficient inside of $y^+ \cong 30$. The normal velocity statistic (v'/u_τ) for the two present cases agree very well in this region, but the innermost two points of East & Sawyer's data are somewhat lower. East &

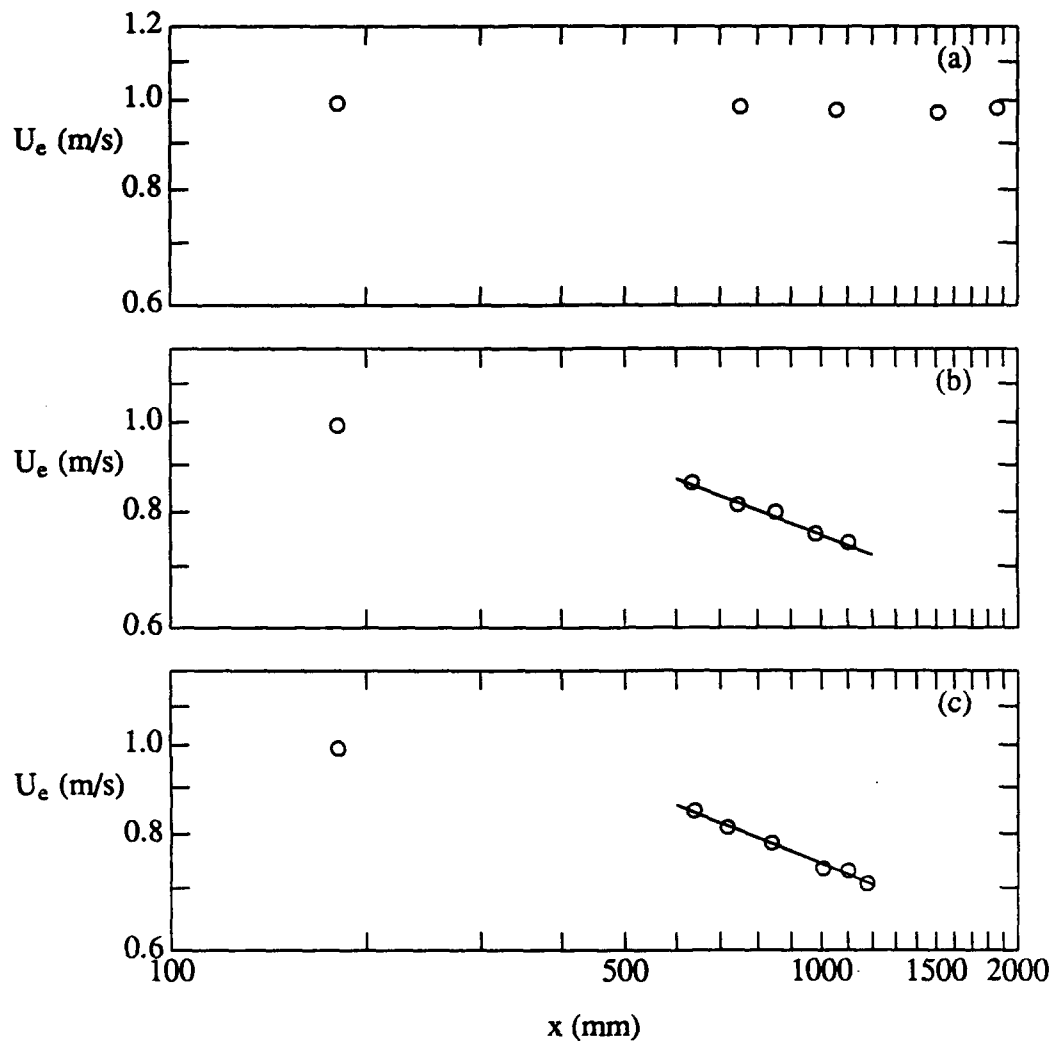


Figure 3.8 Freestream velocity as a function of streamwise distance from trip. (a) zero pressure gradient, (b) moderate adverse — $U_e = 4.98x^{-273}$ (c) strong adverse — $U_e = 5.43x^{-288}$. Note that both scales are logarithmic.

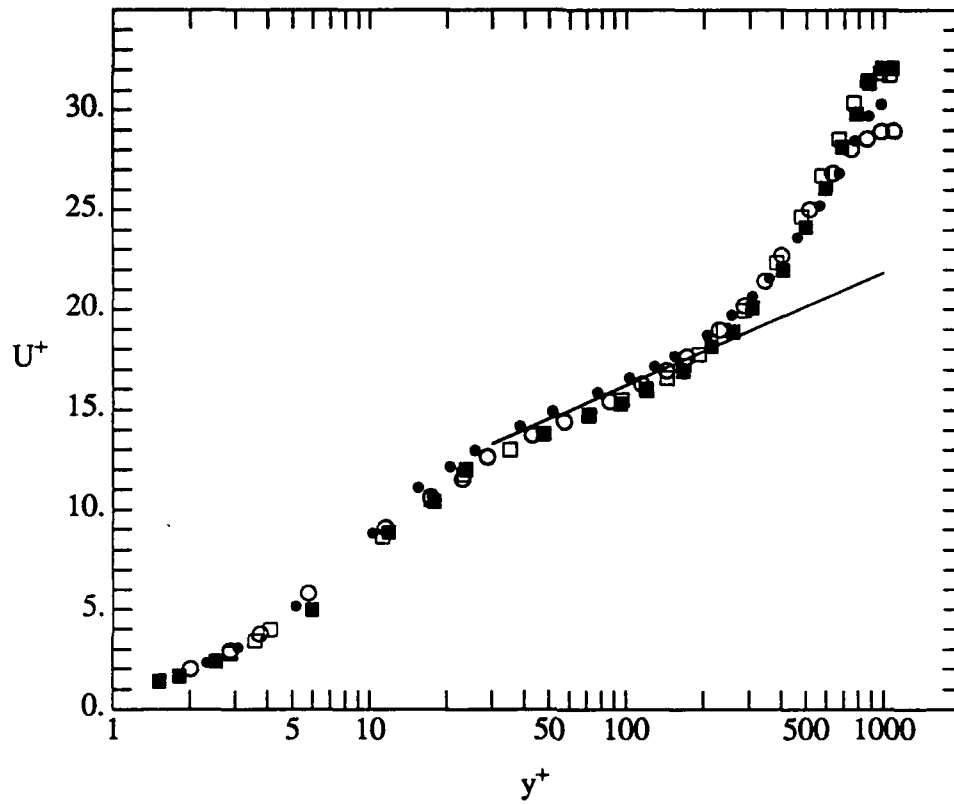


Figure 3.9 Mean streamwise velocity in Newtonian, equilibrium, adverse pressure gradient boundary layers without injection. $\beta = 1.8$: \circ $Re_\theta = 3570$, \bullet $Re_\theta = 4210$; $\beta = 2.4$: \square $Re_\theta = 4588$, \blacksquare $Re_\theta = 4978$; — $U^+ = (1/0.41) \ln y^+ + 5.0$.

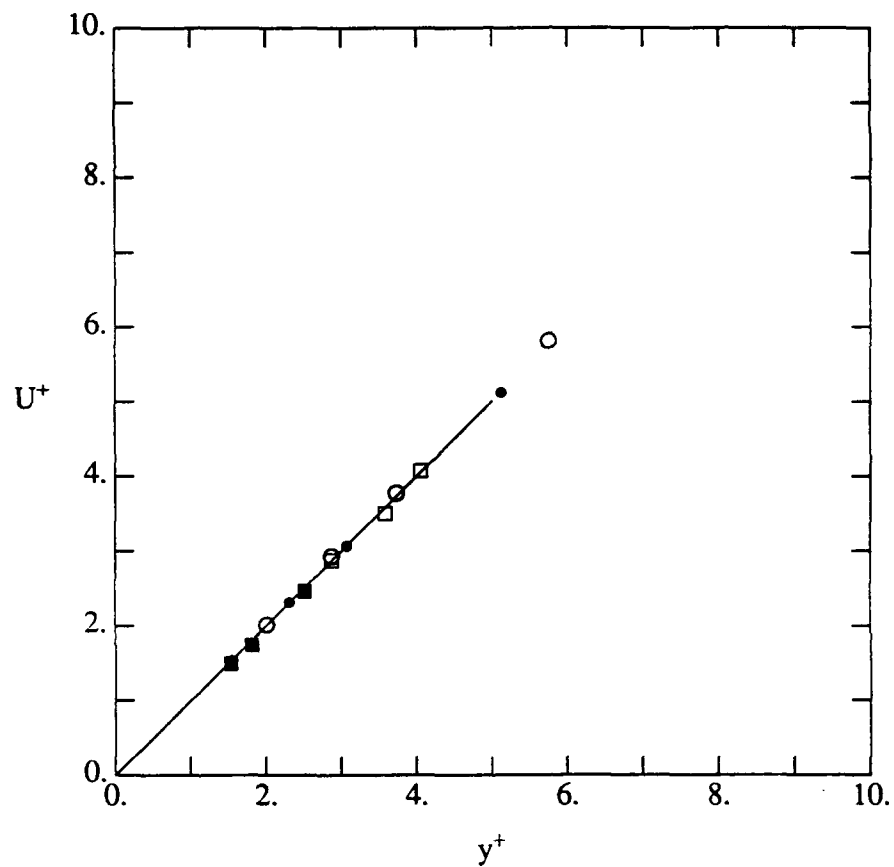


Figure 3.10 Mean streamwise velocity in the linear sublayer of Newtonian, equilibrium, adverse pressure gradient boundary layers without injection. $\beta = 1.8$: \circ $Re_\theta = 3570$, \bullet $Re_\theta = 4210$; $\beta = 2.4$: \square $Re_\theta = 4588$, \blacksquare $Re_\theta = 4978$; — $U^+ = y^+$.

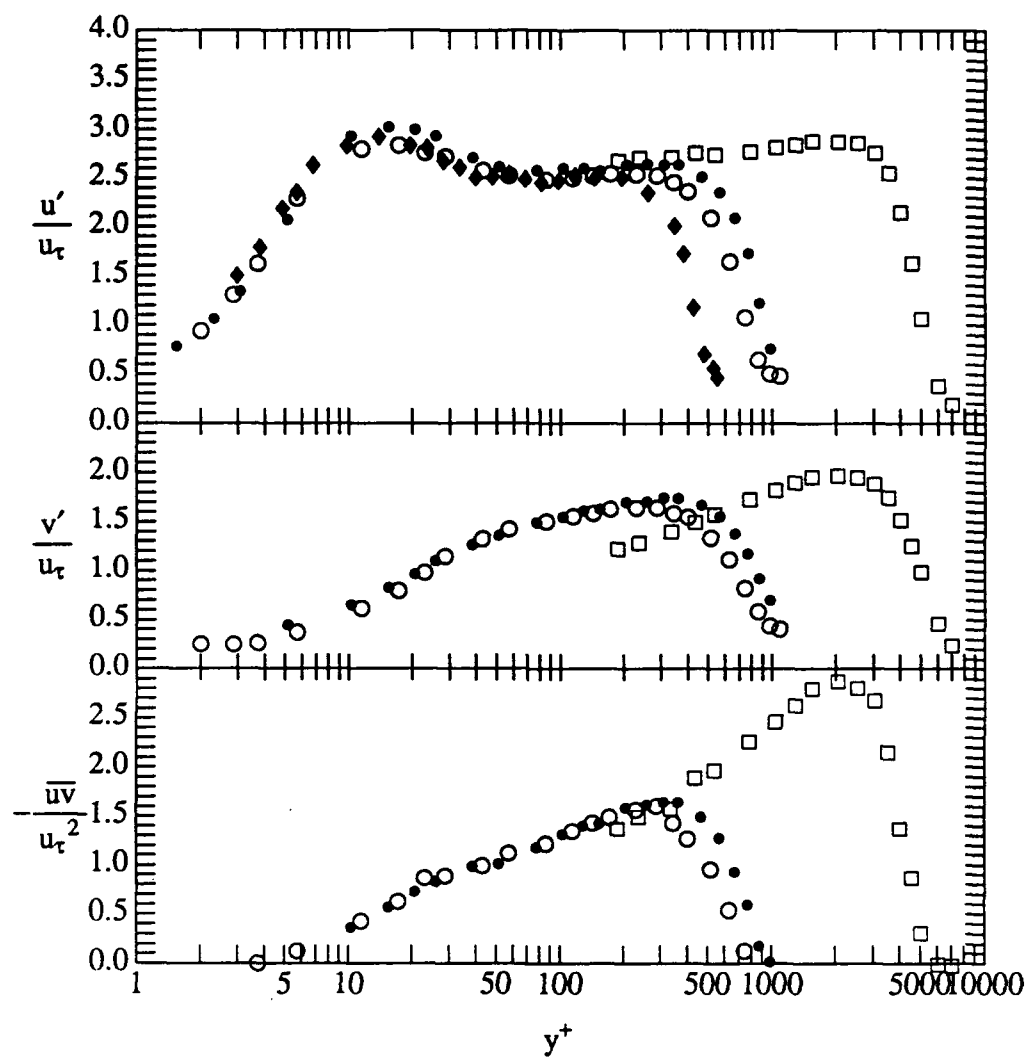


Figure 3.11 Root-mean-square velocities and Reynolds shear stress in a Newtonian equilibrium adverse pressure gradient boundary layer without injection, $\beta = 1.8$. \circ $Re_{\theta} = 3570$; \bullet $Re_{\theta} = 4210$; \blacklozenge White $Re_{\theta} = 2085$; \square East and Sawyer flow 5, $Re_{\theta} = 26800$.

Sawyer used a hot wire probe and these points apparently represent the closest possible measurements to their wall. Therefore, the present data are expected to be the best estimate of v'/u_τ . The Reynolds shear stress data (\overline{uv}/u_τ^2) for the two present flows are nearly identical and very close to those of East & Sawyer out to the outer limit of the log region. It is important to note that the two present profiles are separated by a streamwise distance of approximately 8 times the boundary layer thickness, δ , at the first location. It can therefore be concluded that the flow is, in some sense, in equilibrium for the fluctuation statistics as well as the mean velocity. However, as is expected, inner normalization does not properly scale the data in the wake region. The maximum Reynolds shear stress in the present boundary layers in the wake region is significantly lower than that of East & Sawyer. This result is expected since the Reynolds number, Re_θ , of East & Sawyers flow is 26 800 which is more than six times the present Re_θ values.

Figure 3.12 shows the fluctuation statistics in the strong adverse pressure gradient boundary layer. These profiles are separated by a streamwise distance of approximately 8 boundary layer thicknesses as measured at the first location. The streamwise fluctuations profiles at all three locations show good agreement inside of the wake region, indicating that the boundary layer is in equilibrium, at least in the streamwise fluctuations. The normal fluctuations and Reynolds stresses were measured only at one location. Note that there are two peaks of u'/u_τ . The innermost peak is at $y^+ \cong 12$, which is the same approximate location as the peak of u'/u_τ in a zero pressure gradient boundary layer. The second peak occurs at the inner edge of the wake region of the mean velocity profile. This second peak has also been observed by White &

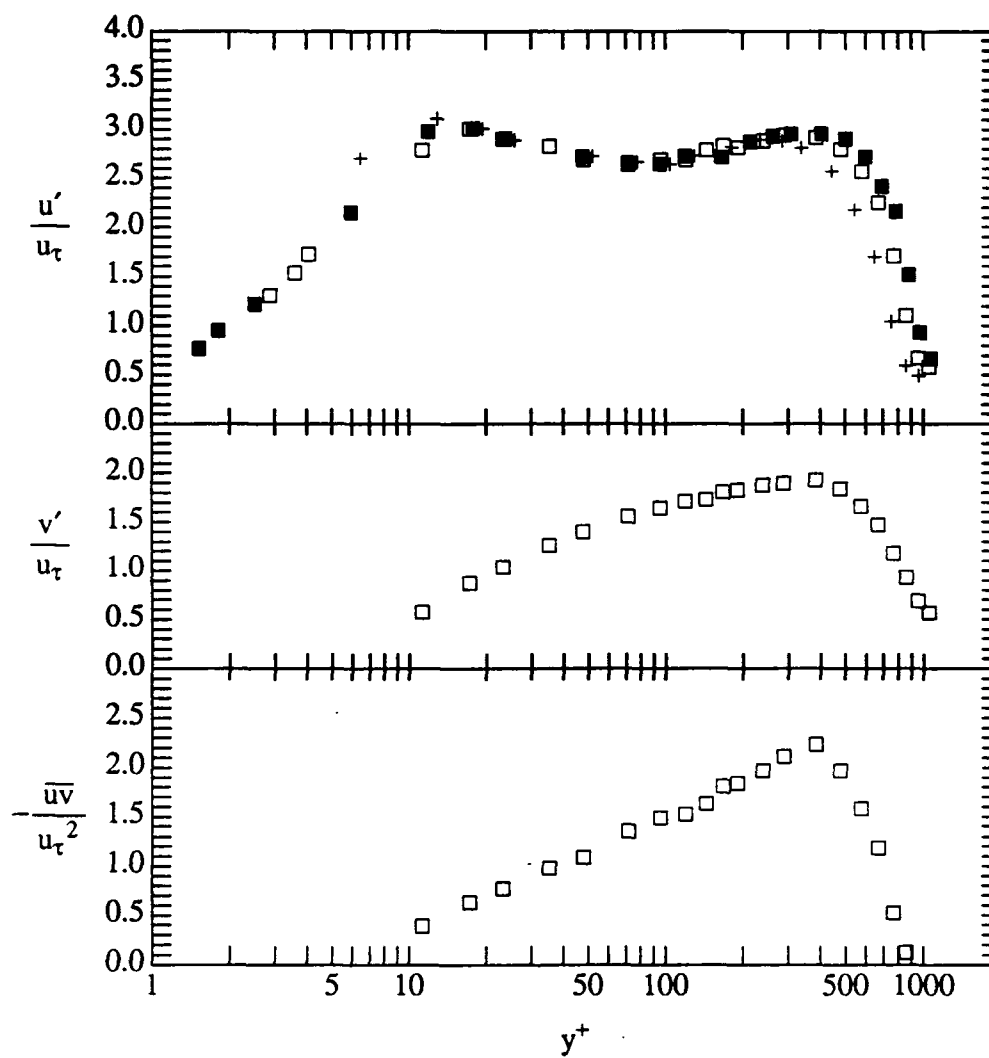


Figure 3.12 Root-mean-square streamwise and normal velocity fluctuations and Reynolds shear stress in a Newtonian equilibrium adverse pressure gradient boundary layer without injection $\beta = 2.4$. + $Re_\theta = 3784$; \square $Re_\theta = 4588$; \blacksquare $Re_\theta = 4978$.

Tiederman. It is the same peak in u' in the wake region observed by Bradshaw (1967) in his most adverse pressure gradient flow. By evaluating spectra of the turbulence in the boundary layer, Bradshaw established that this outer peak was produced by the large eddies which occur in the interaction of the boundary layer with the outer flow. He did not perform turbulence measurements close enough to the wall to observe the peak at $y^+ = 12$.

3.3 Mixing length models

Figure 3.13 shows the variation of the velocity fluctuation statistics in Newtonian equilibrium boundary layers with changes in adverse pressure gradient parameters with Reynolds number nearly fixed. Inner normalization collapses each of these statistics only for regions very near the wall ($y^+ \leq 30$). This observation supports Pantón's (1990) theory that the normalized Reynolds stress in this region is not influenced directly by the pressure gradient. The magnitude of the second peak in u'/u_τ in the adverse pressure gradient boundary layers increases with increasing β , because the interaction of the boundary layer with the freestream flow increases as the freestream pressure gradient becomes more adverse (Bradshaw, 1967). This same physical argument explains the increase in the peak values of v'/u_τ and \overline{uv}/u_τ^2 . The practical implications of this observation can better be understood in terms of the mixing length, $l = [\overline{uv} |d\overline{U}/dy|^{-1}]^{1/2}$, the quantity which is commonly modeled to provide algebraic closures for computational models. In the present analysis the mixing length is normalized with inner variables, u_τ and v . Figure 3.14 compares the mixing length profiles for these three Newtonian cases. Inside $y^+ \cong 100$ the mixing length for all three cases is nearly identical. The adverse pressure gradient increases the normalized

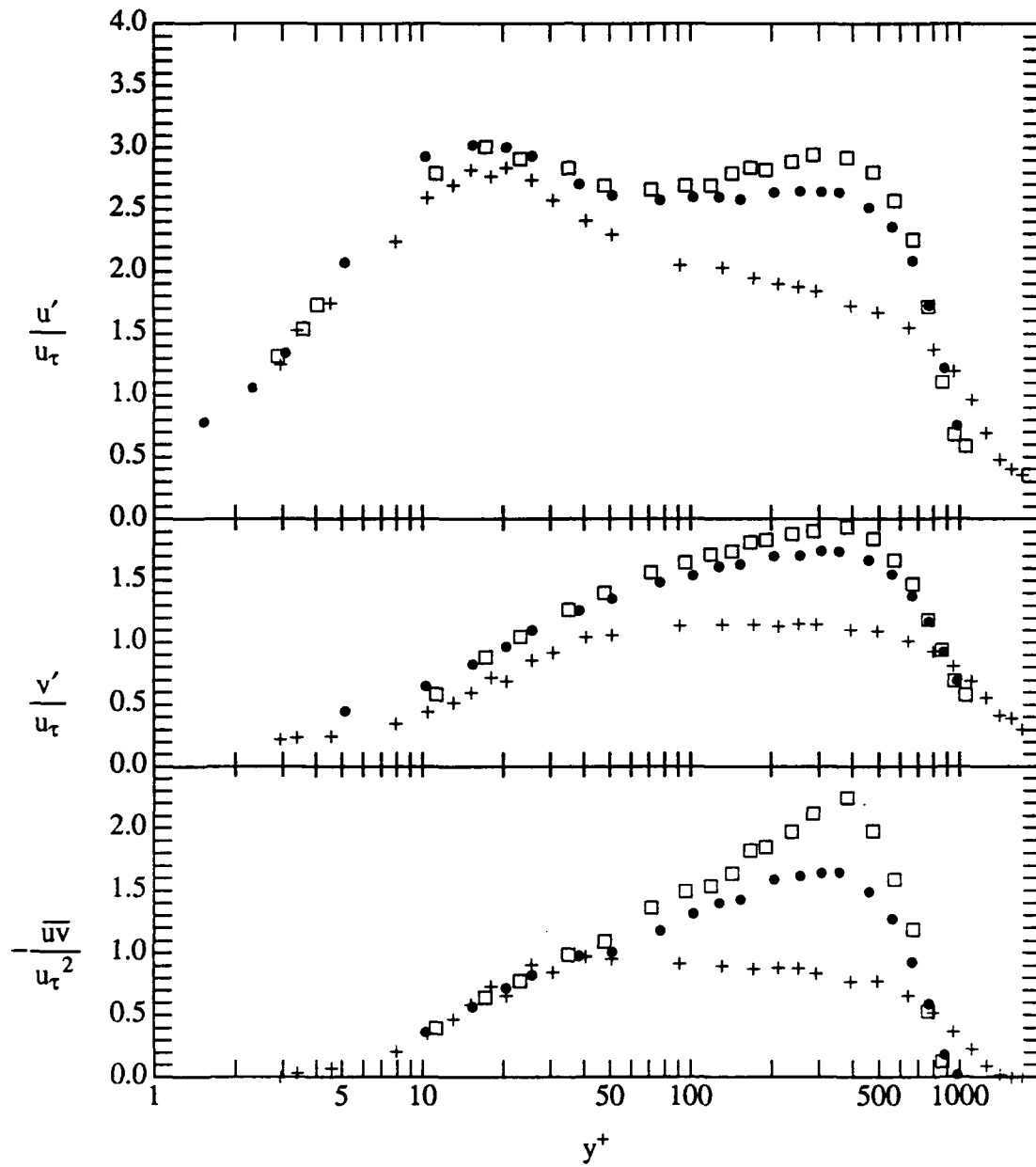


Figure 3.13 Root-mean-square velocities and Reynolds shear stress in Newtonian equilibrium boundary layers without injection. + $Re_\theta = 3935, \beta = 0.0$; • $Re_\theta = 4210, \beta = 1.8$; □ $Re_\theta = 4588, \beta = 2.4$.

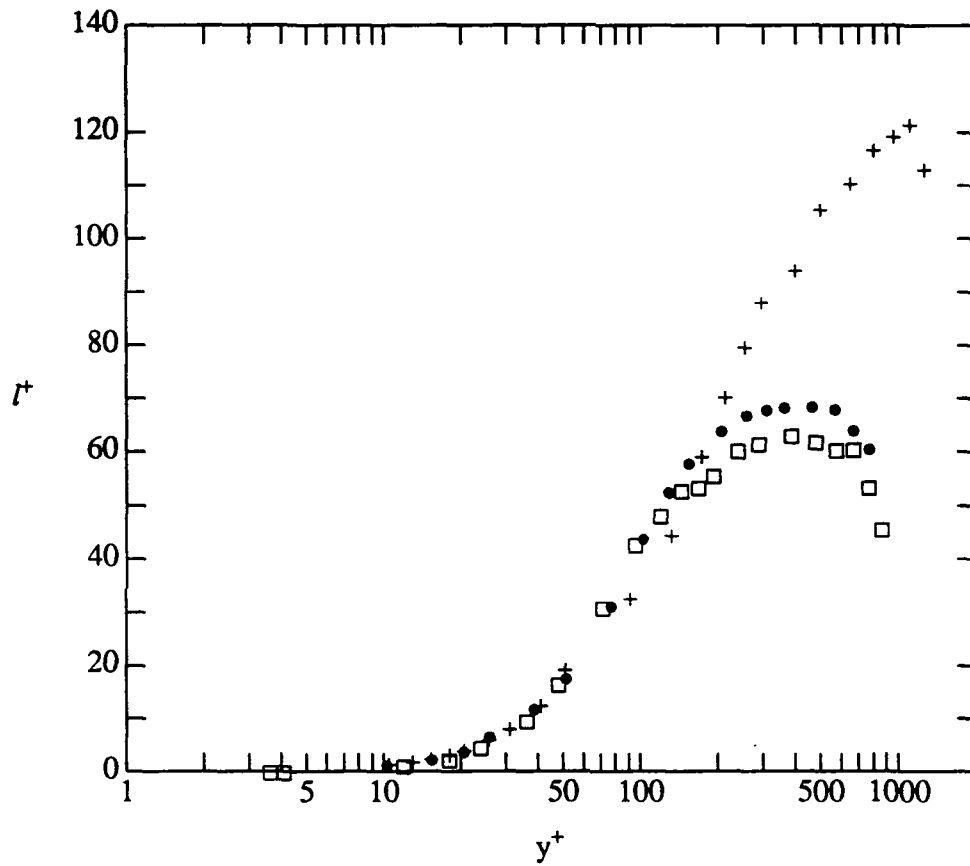


Figure 3.14 Mixing length in Newtonian equilibrium boundary layers without injection. + $Re_\theta = 3935$, $\beta = 0$; • $Re_\theta = 4210$, $\beta = 1.8$; □ $Re_\theta = 4588$; $\beta = 2.3$.

mixing length slightly in the region $100 \leq y^+ \leq 250$, the log region of the mean profiles, but the most significant differences occur in the wake region of the mean velocity profile where the adverse pressure gradient greatly reduces the normalized mixing length.

Boundary layer codes which use algebraic closures typically use two separate models for the mixing length in a boundary layer, one for the inner region and one for the outer region of the flow (see eg. Cebeci & Bradshaw, 1977). The present data have been used to test various models for the inner and the outer flow which have been proposed in the literature. The mean velocity and pressure gradient data were used as input to these equations and the output was compared to the experimentally determined mixing length. The inner models tested are the Van Driest (1956) model for the zero pressure gradient boundary layer, the Patankar & Spalding model (see Patankar, 1970), Cebeci & Smith's model for the inner region (see Cebeci & Bradshaw, 1977), and a recent model proposed by Granville (1989) for the inner region. The Van Driest model is modified in the latter three models to account for pressure gradient influences. For a zero pressure gradient boundary layer they reduce to the Van Driest model. These models are summarized in table 3.2, where p^+ is the inner normalized pressure gradient, $p^+ = (v/\rho u_\tau^3) dp/dx$. The values of p^+ in the present experiments range from 0 to 0.01. This range represents only a moderate variation in p^+ . For comparison, East & Sawyer's flow 7, which is an adverse pressure gradient boundary layer near separation, had a dimensionless pressure gradient of approximately 0.04. The Cebeci & Bradshaw model was derived for a range of $-0.08 < p^+ < 0.08$.

Two outer models were also tested. These models were actually formulated as turbulent viscosities, ν_t , as shown in table 3.3. For the present purposes, they have been converted to mixing lengths using equation 3.1 in order to compare the inner models and outer models together.

$$l^2 = \nu_t \left| \frac{d\bar{U}}{dy} \right|^{-1} \quad (3.1)$$

The Cebeci & Smith model is a very simple model; however, it requires knowledge of the boundary layer thickness, δ . The parameter k in this model and in the following Baldwin-Lomax model is a constant with a numerical value 0.0168. Baldwin & Lomax (1978) derived their model in order to eliminate the need to evaluate the boundary layer thickness, δ , in separated transonic turbulent flows where determination of an appropriate value of δ can be difficult. Their new model requires determination of the value of F_{wake} (see table 3.3) at each streamwise location in the flow. It also requires specification of the empirical coefficients C_{cp} and C_{kleb} which Baldwin & Lomax assigned the values 1.6 and 0.3 respectively. The parameter D is a damping factor which has a constant value of 1.0 for boundary layers. York & Knight (1985) proposed values of $C_{cp} = 1.2$ and $C_{kleb} = 0.646$ for low speed boundary layers. Granville (1987) proposed that these coefficients are functions of pressure gradient for these boundary layers. He derived equations for the coefficients based on empirical relations which describe equilibrium boundary layers. For the present data, the coefficients predicted by Granville's model are within 12 percent of the coefficients of York & Knight. The resulting model is more complicated algebraically than the Cebeci model; however,

Table 3.2 Mixing length models for the inner region.

Author	Formula
van Driest	$l^+ = \kappa y^+ [1 - \exp(-y^+/26)]$
Patankar-Spalding	$l^+ = \kappa y^+ [1 - \exp(-y^+ \sqrt{1 + 0.9p^+ y^+}/26)]$
Cebeci & Bradshaw	$l^+ = \kappa y^+ [1 - \exp(-y^+ \sqrt{1 + 11.8p^+}/26)]$
Granville	$l^+ = \kappa y^+ \sqrt{1 + 0.9p^+ y^+} [1 - \exp(-y^+ \sqrt{1 + bp^+}/26)]$ $b = 14.0$ for $p^+ > 0$ $b = 16.4$ for $p^+ < 0$

Table 3.3 Turbulent viscosity models for the outer region.

Author	Formula
Cebeci-Smith	$\nu_t = \kappa U_e \delta^* [1 + 5.5(y/\delta)^6]^{-1}$
Baldwin-Lomax	$\nu_t = \kappa C_{cp} F_{wake} [1 + 5.5(C_{kleb} y/y_{max})^6]^{-1}$ $F_{wake} = y_{max} F_{max}$ $F_{max} = \max[y du/dy D]$ $y_{max} = y _{F=F_{max}}$
Granville	$\tilde{\beta} = (y_{max}/u_\tau) dU_e/dx$ $C_{kleb} = 2/3 - 0.01312[(0.1724 + \tilde{\beta})^{-1}]$ $C_{cp} = [3 - 4C_{kleb}][2C_{kleb}(2 - 3C_{kleb} + C_{kleb}^3)]^{-1}$

these additional terms are only evaluated once at each streamwise location and therefore would probably not significantly influence the overall computation time required by a boundary layer code.

Figure 3.15 compares these models with the actual data for the zero pressure gradient, moderate equilibrium, and strong equilibrium cases respectively. Because the differences between the predictions of the Cebeci model and the Patankar-Spalding models are smaller than the resolution on the plot, only the model of Cebeci is shown. One interesting observation from these data is that the influence of the pressure gradient on the inner region of the flow is so small that even the Van Driest model reasonably predicts the inner region of all three flows. The Patankar-Spalding and Cebeci-Smith inner models adequately predict the mixing length because their pressure gradient terms are small. However, Granville's inner model overpredicts the pressure gradient effect.

Both outer models give essentially the same mixing length distribution in the flow. They provide an excellent model for the zero pressure gradient case, but they overpredict the mixing length in the adverse pressure gradient cases. Neither model has a distinct advantage in the present case because there is no particular problem with evaluating the boundary layer thickness, δ . However, the performance of Granville's model in these flows suggests that the model should be tested in situations such as low Reynolds number separated boundary layers where determining an appropriate thickness is difficult.

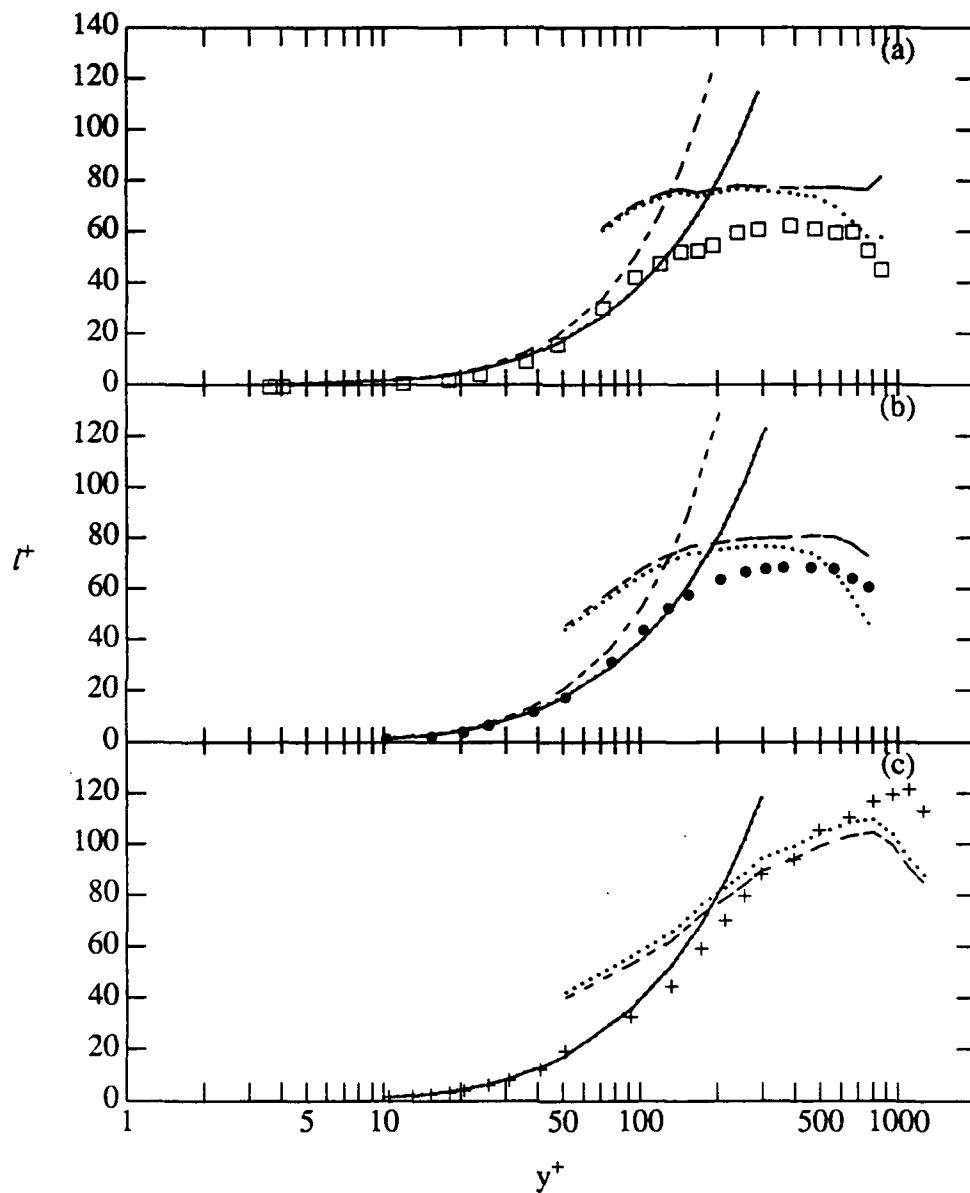


Figure 3.15 Mixing length in Newtonian equilibrium boundary layers without injection. (a) \square $Re_\theta = 4588$, $\beta = 2.3$; (b) \bullet $Re_\theta = 4210$, $\beta = 1.8$; (c) $+$ $Re_\theta = 3935$, $\beta = 0$; Inner models: — Van Driest; \cdots Cebeci-Smith; - - - Granville, Outer models: \cdots Cebeci-Smith; - - - Baldwin-Lomax using Granville coefficients.

In conclusion, the established models of Cebeci & Bradshaw and Patankar-Spalding predict the inner mixing length very well. Either outer model works adequately. Therefore, either the boundary layer code STAN5, which uses the Patankar-Spalding inner model or Cebeci & Bradshaw's boundary layer code would be adequate for modification to account for drag reduction. This modification is discussed in the next chapter.

CHAPTER 4: DRAG REDUCED BOUNDARY LAYERS

Injection of 1000 wppm aqueous solutions of Separan AP-273 reduced the wall shear stress and modified the Newtonian boundary layers described in chapter 3. The freestream velocity distributions for the modified boundary layers were the same as for the boundary layer before injection of polymer. The injection flow rates, Q_i were 2.6 and 5.1 times Q_s , the volumetric flow rate of the undisturbed flow between the wall and $y^+ = 5$ (the linear sublayer).¹ Measurements in the zero pressure gradient boundary layer were made at four streamwise locations which were 620 to 1733 mm downstream of the slot. These measurement locations yielded a momentum thickness Reynolds number range of 2478 to 3935 for the corresponding Newtonian boundary layer. In the adverse pressure gradient boundary layers, velocity profiles were measured at 720 mm in the moderately adverse flow and at 876 mm and 966 mm in the strong adverse flow. These locations corresponded to momentum thickness Reynolds numbers of 3570, 4590 and 4980 respectively in the corresponding Newtonian boundary layers. The drag reduction alone was measured at 706 mm in the strong adverse case and at 356 mm in both boundary layers. This latter location was immediately downstream of the start of

1. This assumption differs from Walker et al.'s (1986) assumption that the linear sublayer extended to $y^+ = 8$.

the adverse pressure gradient region. Drag reduction was defined as:

$$\%DR = 100 \frac{c_f - c_{f|N}}{c_{f|N}} \quad (4.1)$$

The amount of the drag reduction at these locations is summarized in table 4.1. In this table, δ_s is the unmodified Newtonian boundary layer thicknesses at the slot. Figure 4.1 shows the drag reduction as a function of distance downstream of the injector slot. The increase in the measured drag reduction in the zero pressure gradient boundary layer at the high injection flow rate indicates a limitation of the ability to reproduce the polymer solution. Experiments at the second and fourth streamwise locations were made approximately 5 months after the experiments of the first and third locations. These solutions were deemed acceptable by the tube drag reduction and viscosity tests. Their viscosities were the highest values accepted. These data are given in the second appendix. This suggests that additional control of the polymer solution preparation is needed.

Flow visualization showed that the drag reduced adverse pressure gradient boundary layers did not separate even when the injection flow rate was quite high. Polymer was injected into the strong adverse boundary layer at multiples of the linear sublayer flow rate, starting at $Q_i/Q_s = 2.6$ and increasing to approximately 34 times the sublayer flow rate. Dye was injected through tubes into the boundary layer at several streamwise locations along the entire adverse pressure gradient region. At each location dye was injected along the centerline of the measurement wall and in each corner of the measurement wall boundary layer.

Table 4.1 Summary of drag reduction experiments.

β	Q_i/Q_s	$(x - x_s)$ (mm)	$(x - x_s)/\delta_s$	$(x - x_s)^+$	%DR
0.0	2.6	620	52	29000	46
0.0	2.6	924	77	43200	28
0.0	2.6	1379	115	64400	25
0.0	2.6	1733	144	81000	16
0.0	5.1	620	52	29000	50
0.0	5.1	924	77	43200	56
0.0	5.1	1379	115	64400	33
0.0	5.1	1733	144	81000	38
1.8	2.6	354	29	16500	39
1.8	2.6	720	60	33600	10
1.8	5.1	354	29	16500	69
1.8	5.1	720	60	33600	22
2.4	2.6	356	29	16500	47
2.4	2.6	706	59	33000	19
2.4	2.6	876	72	40400	5
2.4	2.6	966	80	45200	0
2.4	5.1	356	29	16500	61
2.4	5.1	706	59	33000	25
2.4	5.1	876	72	40400	16
2.4	5.1	966	80	45200	5

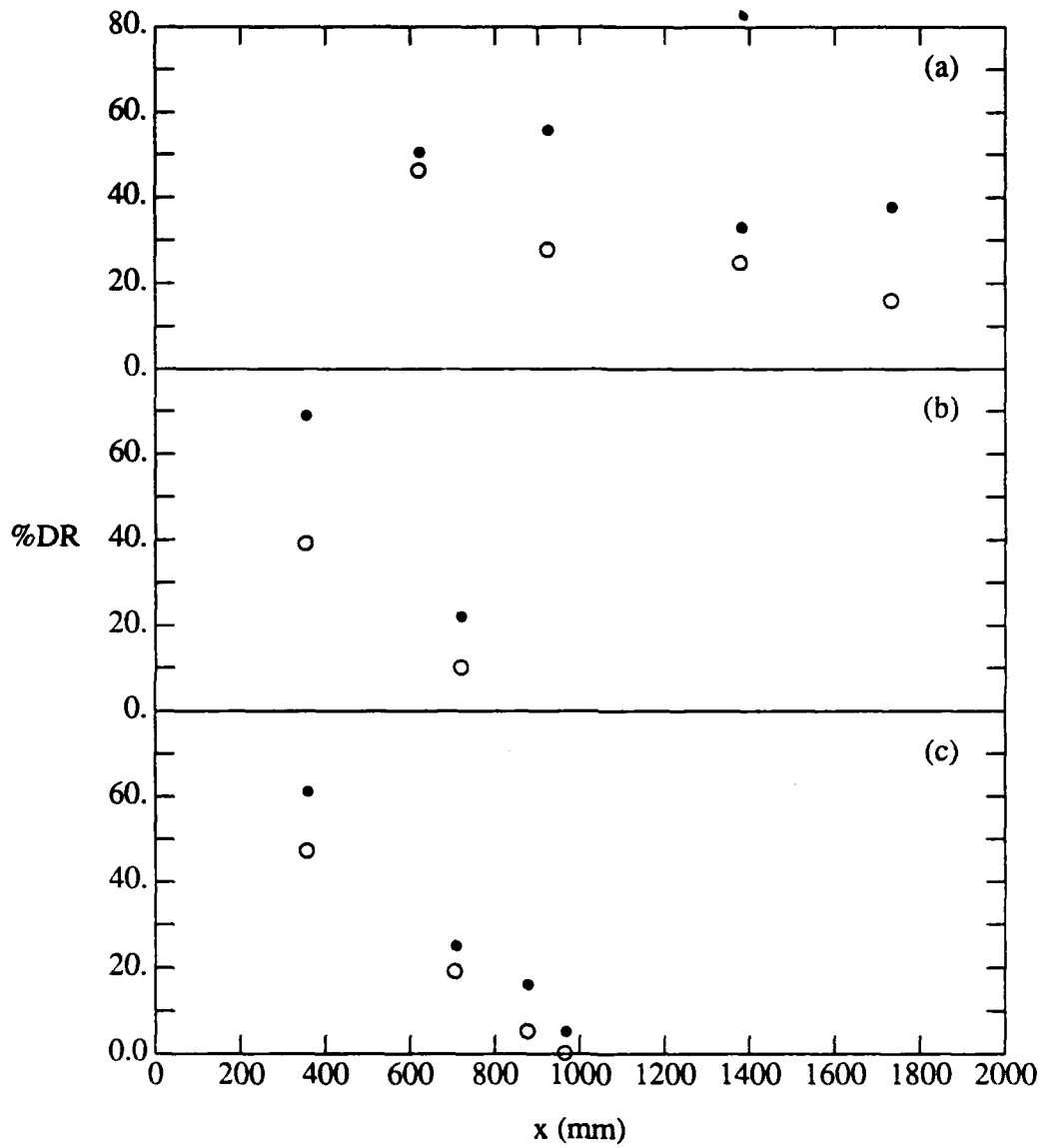


Figure 4.1 Drag reduction as a function of streamwise distance from slot. (a) zero pressure gradient (b) moderate adverse (c) strong adverse. \circ $Q_i/Q_s = 2.6$, \bullet $Q_i/Q_s = 5.1$.

Dye was also injected into the boundary layer on the flexible wall at the same spanwise locations. Flow separation was not observed in any situation.

In this chapter the streamwise distance from the injector slot is normalized in inner variables, x^+ . Because the shear velocity varies with streamwise distance, the strain rate of the unmodified boundary layer near the slot was used in all cases to maintain consistent normalization. Distance normal to the wall was made dimensionless with the local shear velocity or with the measured displacement thickness, δ^* , when appropriate. In all cases the solvent (water) viscosity was used when needed.

4.1 Shear stress in polymer flows

In Newtonian two-dimensional, steady boundary layers the Reynolds averaged momentum equation is:

$$\rho \bar{U} \frac{\partial \bar{U}}{\partial x} + \rho \bar{V} \frac{\partial \bar{V}}{\partial y} = - \frac{\partial \bar{P}}{\partial x} + \frac{\partial \tau}{\partial y} \quad (4.2)$$

In the inner region of zero pressure gradient boundary layer, the streamwise derivative of the mean streamwise velocity is zero and the mean normal velocity is negligible. Therefore, the left hand side of equation 4.2 can be neglected, and the total shear stress is constant. All the terms which are cancelled are independent of the constitutive properties of the fluid, therefore the constant stress distribution is valid for both Newtonian and non-Newtonian boundary layers.

For a Newtonian fluid, the total shear stress, τ is given by the sum of the viscous and Reynolds shear stresses:

$$\tau = \mu \frac{\partial \bar{U}}{\partial y} - \rho \bar{u} \bar{v} \quad (4.3)$$

Profiles of the sum of the viscous and Reynolds shear stresses in the zero pressure gradient boundary layers are shown in figure 4.2. The expected constant shear stress is shown as a line in each section. The stresses are normalized by $\rho U_e^2/2$ where ρ is the density and U_e is the freestream velocity. The lowest set of curves (part e) represents the stress at $x^+ = 29\,000$ for the Newtonian boundary layer with and without water injection at $Q_i/Q_s = 5.1$. The uncertainty of the Reynolds stress was estimated to be ± 5 percent at 95 percent confidence (see Walker, 1988). The velocity derivatives were calculated using a least squares second order polynomial fit to five data points centered on the point of interest. It is not clear how to evaluate the uncertainty in this calculation. It is assumed that the uncertainty in the derivative accounts for the scatter in the Newtonian data which is slightly more than 5 percent. Because the non-Newtonian data were taken using the same techniques the uncertainty on these data is expected to be the same. The first important feature of this plot is that the sum of the viscous and Reynolds shear stresses in the no-injection case (represented by \blacklozenge) has a nearly constant value from the linear sublayer, $y^+ \leq 5$, where the viscous stress is dominant, to approximately $y^+ = 250$, where the Reynolds stress is dominant. For Newtonian cases, this value is always within 5 percent of the wall shear stress (\bullet on left axis) determined from the mean velocity data between $100 \leq y^+ \leq 300$ using the standard log-law relation with constants $\kappa = 0.41$ and $B = 5.0$ as recommended by Coles (1968). This constant stress region is a fundamental characteristic of an unmodified Newtonian zero pressure gradient boundary (Sreenivasan, 1989). The other important feature is that the sum of viscous and Reynolds stress at the same location with water injection (represented by \square)

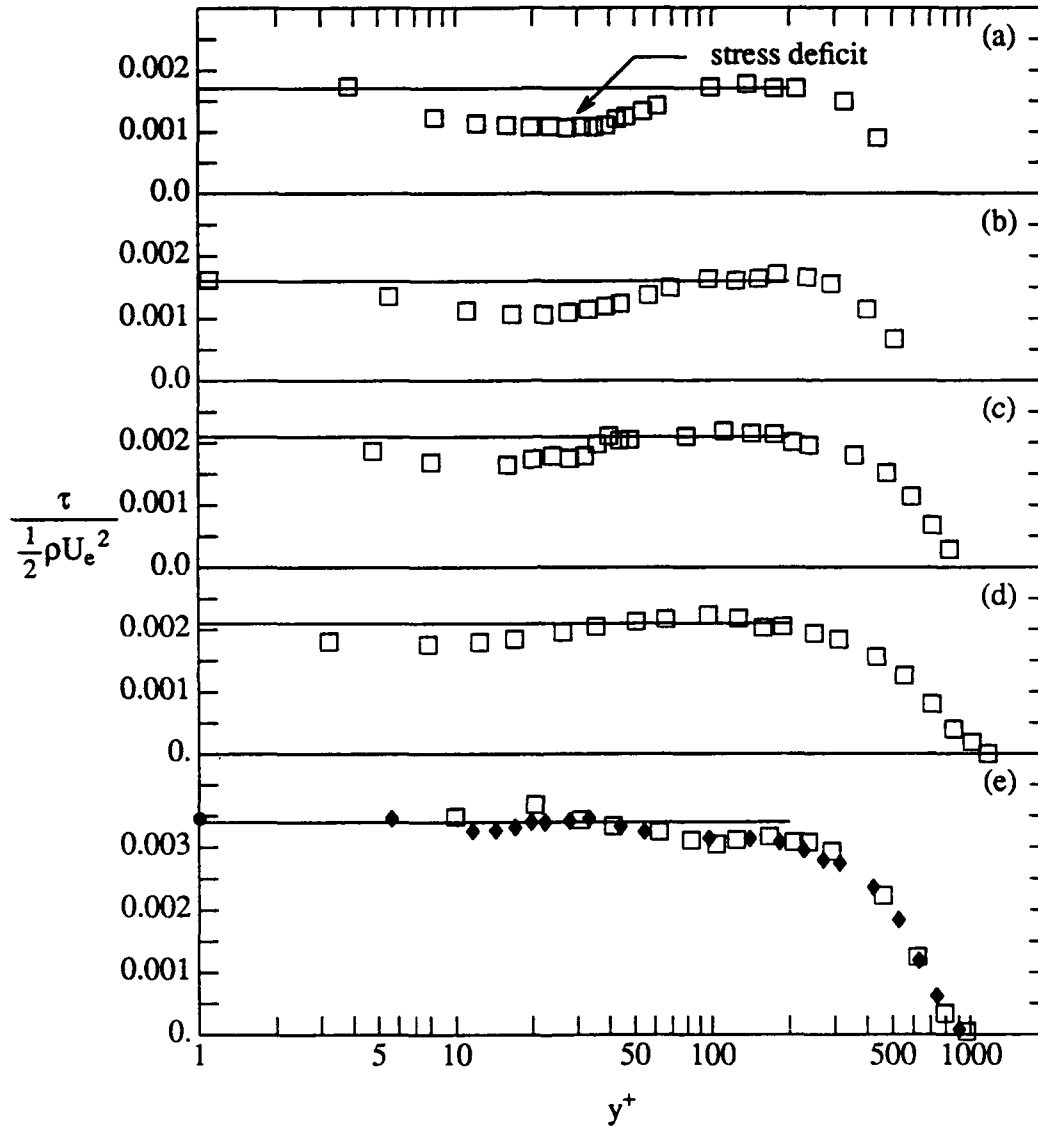


Figure 4.2 Sum of viscous shear stress, $(\mu d\bar{U}/dy)$, and Reynolds shear stress, $(-\rho\bar{u}\bar{v})$, in a zero pressure gradient boundary layer (a) polymer injection $x^+ = 29000$; (b) polymer injection $x^+ = 43200$; (c) polymer injection $x^+ = 64400$; (d) polymer injection $x^+ = 81000$; (e) \square water injection; \blacklozenge no injection, $x^+ = 29000$. \bullet Wall shear stress determined from the log region.

is the same as the standard boundary layer. Therefore, injection of water at 5.1 times the linear sublayer flow rate does not influence the shear stress distribution in the boundary layer.

The four other curves on figure 4.2 represent the sum of the Reynolds and viscous shear stresses at each streamwise location during polymer injection when $Q_i/Q_s = 5.1$. For these cases the shear stress has a nearly constant value in the region $100 \leq y^+ \leq 250$, and this value is the same as the shear stress in the linear sublayer, $y^+ \leq 6$. For this reason it is believed that the viscous stress measured in the linear sublayer is the correct wall shear stress. However, between these two regions the sum of the viscous and Reynolds stress is distinctly lower. This "stress deficit" is most apparent at the first location and decreases as the streamwise distance from the slot increases. Because the freestream velocity remains constant, there is no mechanism by which the actual shear stress would decrease in the region, $6 \leq y^+ \leq 100$; rather, it should remain constant from the wall to $y^+ \cong 250$, as in the Newtonian flow. The most plausible explanation for the apparent deficit in the stress is the existence of a non-Newtonian shear stress caused by the polymer solution. Therefore, equation 4.3, which gives the total shear stress for a Newtonian boundary layer, is no longer valid. A new constitutive equation is necessary to complete equation 4.2. The experiments at the lower injection rate, $Q_i/Q_s = 2.1$, showed the same apparent non-Newtonian stress. The magnitude of this added stress at each given location was somewhat smaller than that for the corresponding high injection case. Data for the $Q_i/Q_s = 2.1$ case are presented in the first appendix.

Similar non-Newtonian shear stresses have been observed in fully developed pipe flows of homogeneous polymer solutions (see Bewersdorff & Berman, 1988). Harder & Tiederman (1991) detected a *similar apparent total stress deficit* in a homogeneous, fully developed, polymer drag reducing, two-dimensional channel flow of the same polymer when the polymer concentration and wall stain rate were 5 wppm and 4000 s^{-1} . Willmarth et al. (1987) and Bewersdorff (1984) have also found that the sum of the Reynolds stress and viscous shear stresses do not always add up to the expected distribution. However, these latter two cases are different from the present study because high concentration polymer threads were present in Bewersdorff's and Willmarth et al.'s flows. Flow visualization and concentration measurements in the present case clearly demonstrated that polymer threads are not present.

In adverse pressure gradient boundary layers the total shear stress in the inner region is not constant; rather, the total shear stress peaks away from the wall. However, the behavior of the total shear stress near the wall can be approximated by the linear relationship.

$$\tau = \tau_w + (dp/dx)y \quad (4.4)$$

This relationship results from taking the limit of the Reynolds averaged momentum equation as the wall is approached. Figure 4.3 shows the shear stress distribution in the moderate pressure gradient boundary comparing the Newtonian case to the corresponding drag reduced cases with $Q_i/Q_s = 2.6$ and $Q_i/Q_s = 5.1$. Please note the linear scale on both axes. Equation 4.4 is plotted in dimensionless form along with *estimated error bounds for each case. The error bounds were computed assuming sum*

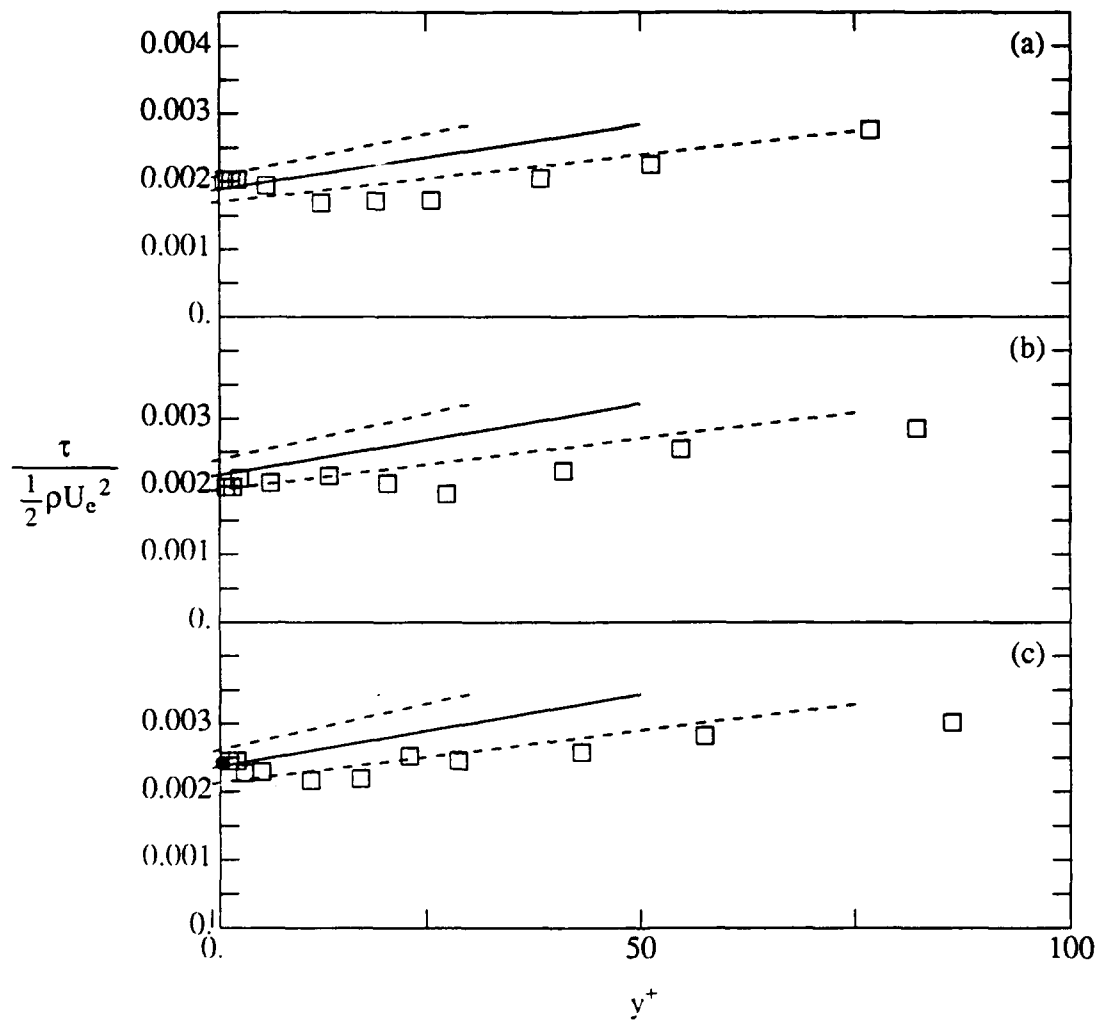


Figure 4.3 Sum of viscous and Reynolds shear stresses in an adverse pressure gradient boundary layer with and without polymer injection. $Re_{\theta}|_N = 3570$, $\beta = 1.8$. (a) $Q_i/Q_s = 5.1$, (b) $Q_i/Q_s = 2.6$, (c) no injection
 — Equation 4.4, - - - error bounds.

of squares error propagation from the measurement of the freestream velocity gradient and the wall shear stress. The Newtonian data (lowest curve) mostly follow the lower of these bounds. Bradshaw (1967) also found that the shear stress predicted by equation 4.4 was slightly higher than the measured data. The behavior of the drag reduced data is very similar, except that the data are slightly more scattered because fewer velocity realizations were acquired for each point. The uncertainty in the data is larger than the magnitude of any non-Newtonian stress which may be present. The polymer is apparently relaxing faster than the flow and becoming less effective. This hypothesis is consistent with the observation that the polymer did not cause separation of the boundary layer.

When the extra polymer induced stress occurs, it probably is only observed in the region $6 \leq y^+ \leq 100$ because of the extensional nature of the flow in this region. Hinch (1977) proposed that drag reduction occurs when the polymer molecules are stretched by an extensional flow. Leal (1990) showed that polymer molecules cannot be stretched by steady shear flows. Therefore, in the linear sublayer, $y^+ \leq 6$, the polymer molecules are probably not stretched and extended because the flow is essentially viscous and not extensional. This hypothesis is consistent with results of Tiederman et al. (1985) who found that drag reduction does not occur when the polymer is entirely inside $y^+ = 10$. Outside of the buffer region $y^+ \geq 100$, the extensional motions in the flow are weaker and at the same time the polymer concentration decreases. Therefore, significant numbers of polymer molecules are less likely to be extended. This second hypothesis is consistent with the observation of McComb and Rabie (1982) that polymer solutions do not yield drag reduction if they are outside $y^+ = 100$.

4.2 Polymer concentration measurements

Polymer concentration and shear viscosity measurements were performed to determine the appropriate values for the shear viscosity in the drag reduced boundary layers. Polymer concentration profiles for the zero and moderate adverse pressure gradient boundary layers are shown in figures 4.4 and 4.5 respectively. Please note that the vertical scale on the latter figure is twice that of the first. The polymer concentration decreases smoothly as distance from the wall increases. The regions of greatest importance on these plots are the linear sublayer in which the velocity measurements were performed to determine wall shear stress and the region inside of $y^+ = 50$ where non-Newtonian stresses were apparent. Note that the polymer concentration for the high injection flow rate at the two farthest upstream locations is distinctly higher than all other cases. The average polymer concentration in the linear sublayer of the zero pressure gradient boundary layer for the high injection flow rate was approximately 50 wppm at the first streamwise location, 20 wppm at the second, 6 wppm at the third, and 5 wppm at the fourth location. For the low injection flowrate case, the concentrations in the linear sublayer were approximately 7.5 wppm at the first location, 4.5 wppm at the second, 3 wppm at the third, and less than 2 wppm at the final location. In the moderate adverse case the sublayer polymer concentration was 4.5 for the high flow rate and 2.7 wppm for the low flow rate. Concentration measurements were not obtained in the strong adverse case. Because the displacement thickness of the more adverse pressure gradient boundary layer grew faster as a function of streamwise distance it entrained more water from the freestream. Therefore, the mean polymer concentration in the stronger adverse pressure gradient boundary layer at any given

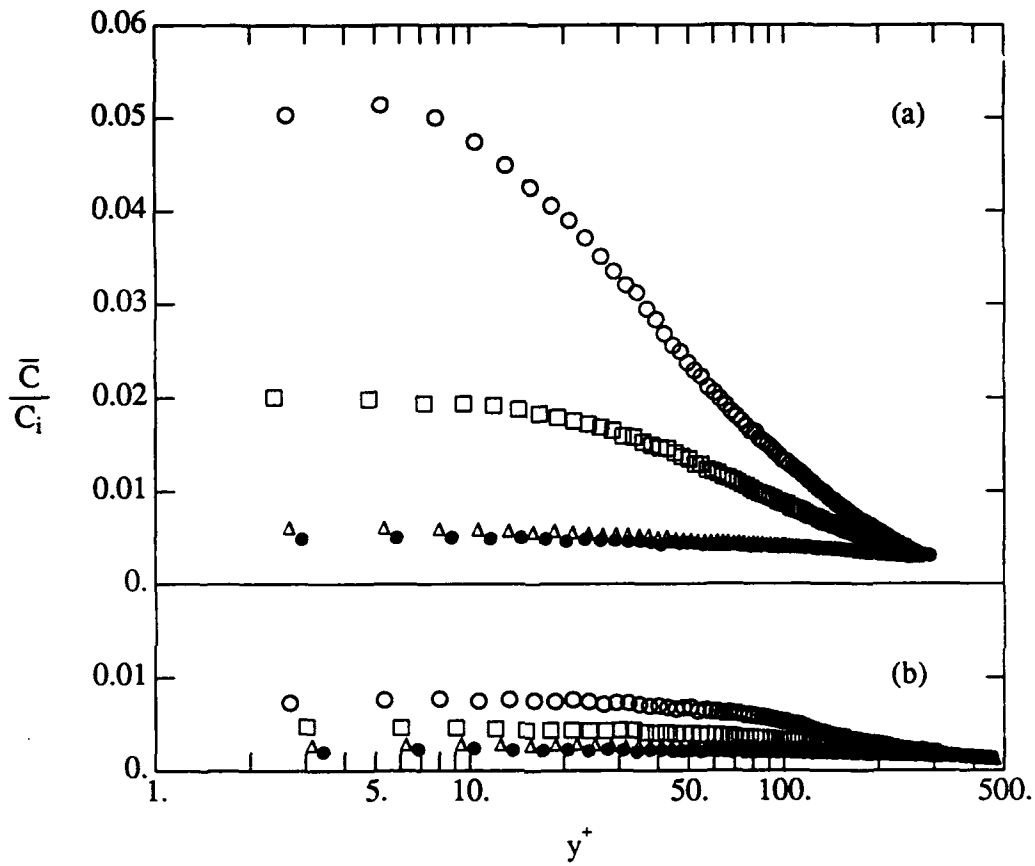


Figure 4.4 Average polymer concentration in a zero pressure gradient boundary layer normalized by the injected concentration. (a): $\beta = 0.0$, $Q_i/Q_s = 5.1$
 (b): $\beta = 0.0$, $Q_i/Q_s = 2.6$. \circ $x^+ = 29000$; \square $x^+ = 43200$; Δ $x^+ = 64400$;
 \bullet $x^+ = 81000$.

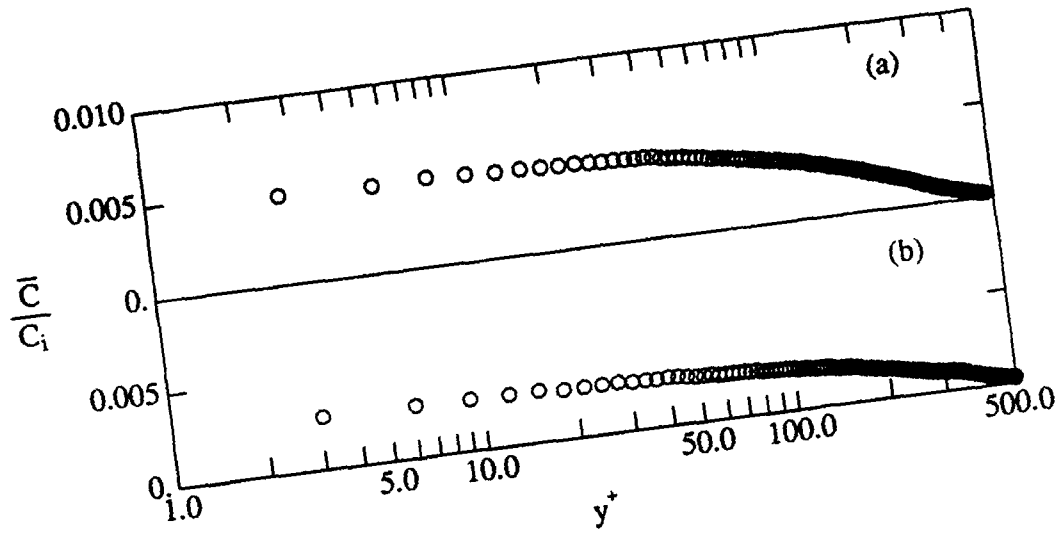


Figure 4.5 Average polymer concentration normalized by the injected concentration in the adverse pressure gradient boundary layer, $\beta = 1.8$, $x^+ = 33700$. Note larger scale compared to figure 4.4. (a) $Q_i/Q_s = 5.1$ (b) $Q_i/Q_s = 2.6$.

streamwise location should be lower than in the moderate adverse pressure gradient boundary layer at the same location. Profiles of the root mean square concentration are given in the appendix.

The apparent steady shear viscosity for 10, 20 and 50 wppm homogeneous polymer solutions was measured using a Brookfield model LVT cone and plate viscometer at a strain rate approximately one third the wall strain rate in the flow. At this low strain rate the increase in apparent shear viscosity over that of water was negligible for 10 wppm, 5 percent for 20 wppm, and 22 percent for 50 wppm. Because these polymer solutions are shear thinning, the viscosity of the fluid in the boundary layer will be considerably less than that measured in the viscometer. Therefore, the shear viscosity of the polymer solutions was assumed to be that of water.

4.3 Mean streamwise velocity statistics

In an attempt to use data from small pipes to predict drag reduction in large pipes various authors, for example Granville (1977) and Hoyt (1991), have proposed scaling procedures based on the commonly held view of a parallel upward shift of the log region of the time average velocity profile for polymer drag reduced flows (see Berman, 1978). Figure 4.6 shows mean streamwise velocity profiles for the zero pressure gradient boundary layer in inner normalized form at all locations at the high injection flow rate. One Newtonian case with water injection is also shown for reference. The Newtonian data exhibit a logarithmic region which closely follows the standard relationship. All of the drag reduced flows have a log region, but the normalized velocities are distinctly higher than in the Newtonian case and the slope of

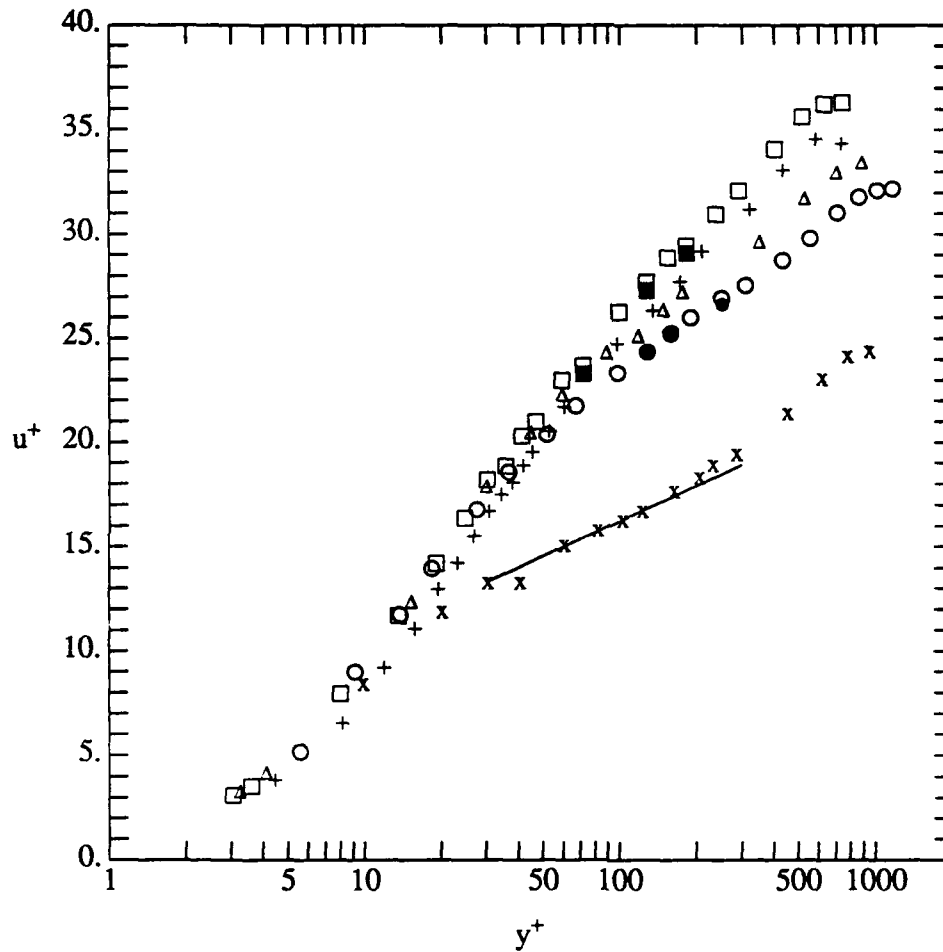


Figure 4.6 Mean streamwise velocity for a zero pressure gradient boundary layer with and without drag reduction. + $(x - x_s)^+ = 29000$; \square $(x - x_s)^+ = 43200$; \blacksquare repeated points; \triangle $(x - x_s)^+ = 64400$; \circ $(x - x_s)^+ = 81000$ (\bullet repeated points); x $(x - x_s)^+ = 29000$, water injection. — $U^+ = (1/0.41) \ln y^+ + 5.0$.

the log region clearly increases over that of the Newtonian case. This change in slope directly negates the assumption of a parallel shift of the velocity profile which is inherent in these scale-up procedures. The zero pressure gradient boundary layer experiments at the low injection flow rate and all the adverse pressure gradient drag reduction experiments have demonstrated similar trends in the change of slope. These data are shown in the appendix.

The von Karman coefficient, κ , for each drag reduced profile was determined from a least squares fit to data in the logarithmic region of the velocity profile. These values are plotted as open symbols on figure 4.7 as a function of percent drag reduction. The triangle on the left axis refers to the Newtonian value of 0.41. A least squares fit for the von Karman constant as a function of drag reduction for 9 zero pressure gradient velocity profiles that range from 0 to 55 percent drag reduction yields:

$$\kappa = 0.41 - 0.004(\%DR) \quad (4.5)$$

The change in slope has been observed in well mixed, fully developed channel flows by Harder & Tiederman (1991), whose data flowed the line:

$$\kappa = 0.41 - 0.003(\%DR) \quad (4.6)$$

The change in slope has also been observed in heterogeneous pipe flows by Bewersdorff (1984) and in homogeneous flat plate boundary layers by Kumor and Sylvester (1973).

Also shown on figure 4.7 are the von Karman coefficients for the adverse pressure gradient cases. Note that there is one case in the most adverse pressure gradient

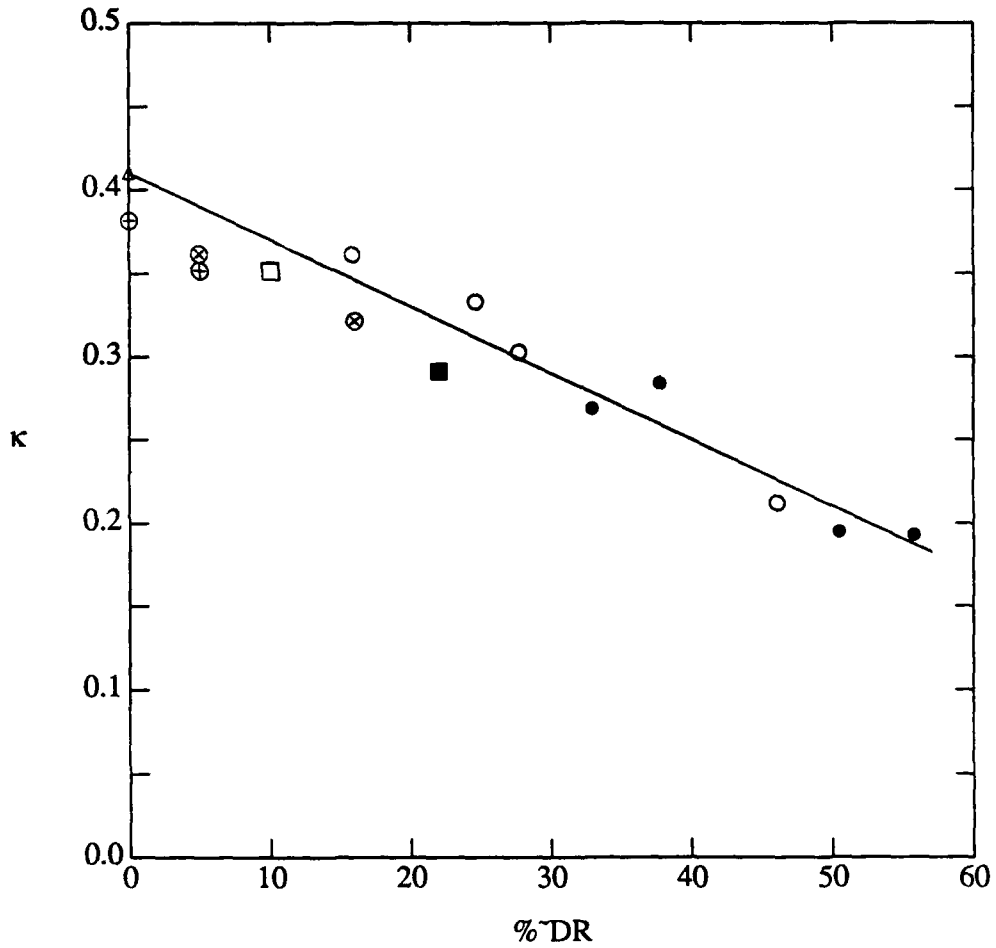


Figure 4.7 Plot of κ as a function of drag reduction; Δ Newtonian; $\beta = 0$:
 \circ $Q_i/Q_s = 2.6$, \bullet $Q_i/Q_s = 5.1$; $\beta = 1.8$: \square $Q_i/Q_s = 2.6$, \blacksquare $Q_i/Q_s = 5.1$;
 $\beta = 2.4$: \oplus $Q_i/Q_s = 2.6$, \otimes $Q_i/Q_s = 5.1$; — $\kappa = 0.41 - 0.004DR$.

(corresponding to $\beta = 2.4$) for which the symbol lies on the axis. The von Karman constant is less than the standard Newtonian value although significant drag reduction was not measured. It is not clear whether this difference indicates hysteresis in the slope of the log region or whether there was actually a small value of drag reduction which could not be resolved.

Significant polymer buildup in the channel was avoided by periodically monitoring the velocity at a point in the logarithmic region of the flow without injection. When the velocity measured in the channel with no polymer injection changed from the original Newtonian case before any polymer entered the channel by more than 1.5 percent, the channel was drained and refilled with new water from the storage tank. As a further test, two of the high flow rate experiments were performed with the probe volume moving outward from the wall until it reached the outer limits of the log region, $y^+ \cong 300$. The water in the channel was then changed to eliminate all residual polymer from the system and then three of the points in the overlap region (log region) were immediately repeated with the probe volume moved toward the wall. The measured velocities for these locations were within one percent of that measured before the water change. These three points are plotted on Figure 4.6 along with the remainder of the data for the high flow rate. The observed change in slope clearly does not result from polymer build up in the channel.

4.4 Velocity fluctuation statistics

This section describes the influence of the polymer on the velocity fluctuation statistics. The normalization used in plotting data will be changed from inner to outer

variables. The reduction in friction velocity, u_τ , during drag reduction causes an increase in u'/u_τ which masks the actual changes in u' . Outer variables will be used instead because the freestream velocity was not allowed to change during drag reduction. The displacement thickness, δ^* , was used to non-dimensionalize the distance normal to the wall. Although it changed with drag reduction, at any given location it only decreases by approximately 10 percent. Therefore, this change does not greatly influence the plots.

Figure 4.8 shows the second order streamwise fluctuation statistics for the drag reduced zero pressure gradient boundary layer at the farthest upstream location in the zero pressure gradient boundary layer with polymer injection at both rates. Both the unmodified Newtonian data and the data with water injection at $Q_i/Q_s = 5.1$ are shown. It is important to note that water injection does not cause any significant change in any of these statistics. The top part of the plot shows the root-mean-square (rms) streamwise velocity fluctuation. The peak value remains essentially unchanged when polymer is present. However, the location of the peak moves out with increasing polymer concentration. This change is entirely due to the presence of polymer because no change in the statistic occurs when water is injected into the boundary layer. The physical location of the peak moves; that is, the shift which appears on the plot is not an artifact of the change in δ^* . A similar shift in the location of this peak occurred at all other locations.

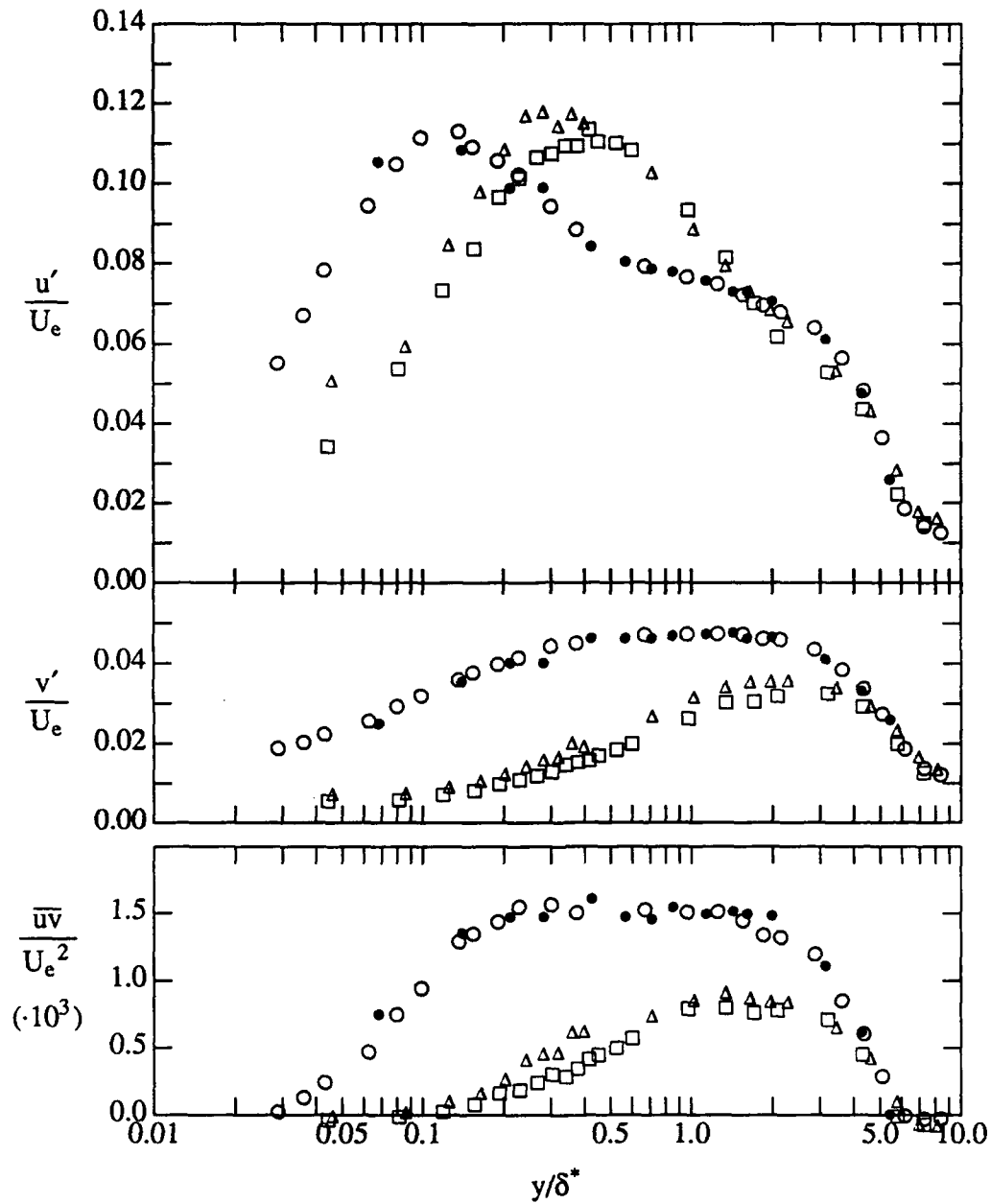


Figure 4.8 Root-mean-square velocities and Reynolds shear stresses for a zero pressure gradient boundary layer at $(x - x_s)^+ = 29000$, $Re_\theta = 2478$ with and without drag reduction. \circ unmodified Newtonian; \bullet water injection $Q_i/Q_s = 5.1$; Δ polymer injection $Q_i/Q_s = 2.6$; \square polymer injection $Q_i/Q_s = 5.1$.

Figure 4.9 shows these same statistics at the last streamwise location, $(x-x_s) = 81000$. The trends in amplitude and location of the peak of u'/U_e are the same as those at the farthest upstream location. At this location, measurements were performed during the high injection flow rate experiments to test for polymer buildup, as described previously in the section on the time average velocity profile. This plot demonstrates that the fluctuation statistics, u' , v' and \overline{uv} did not exhibit any change which would reflect polymer buildup.

The observations of the streamwise velocity fluctuation statistics are consistent with those of Fontaine et al. (1990) in zero pressure gradient boundary layers. They are also consistent with data in two-dimensional channels (Reichman & Tiederman, 1975; Willmarth et al, 1987; Luchik & Tiederman, 1988; Walker & Tiederman 1990; Harder & Tiederman, 1991), in two-dimensional open channel flows (Schmid, 1984) and in developing boundary layers with slot injection (Maksimovic, 1984). El Reidy & Latta (1984) found that slot injection of polymer solution into a zero pressure gradient boundary layer resulted in an increase in u' for injected concentrations of 500 wppm and 1000 wppm. In circular pipe flows, u' has been observed to increase (McComb & Rabie, 1982); although some authors found a decrease, (Mizushima & Usui, 1977; Bewersdorff, 1984).

From figure 4.8, it is apparent that the normal velocity fluctuation data, v'/U_e is strongly diminished from the Newtonian value inside of approximately $y/\delta^* = 4$. Although the polymer concentration changes significantly between the high and low

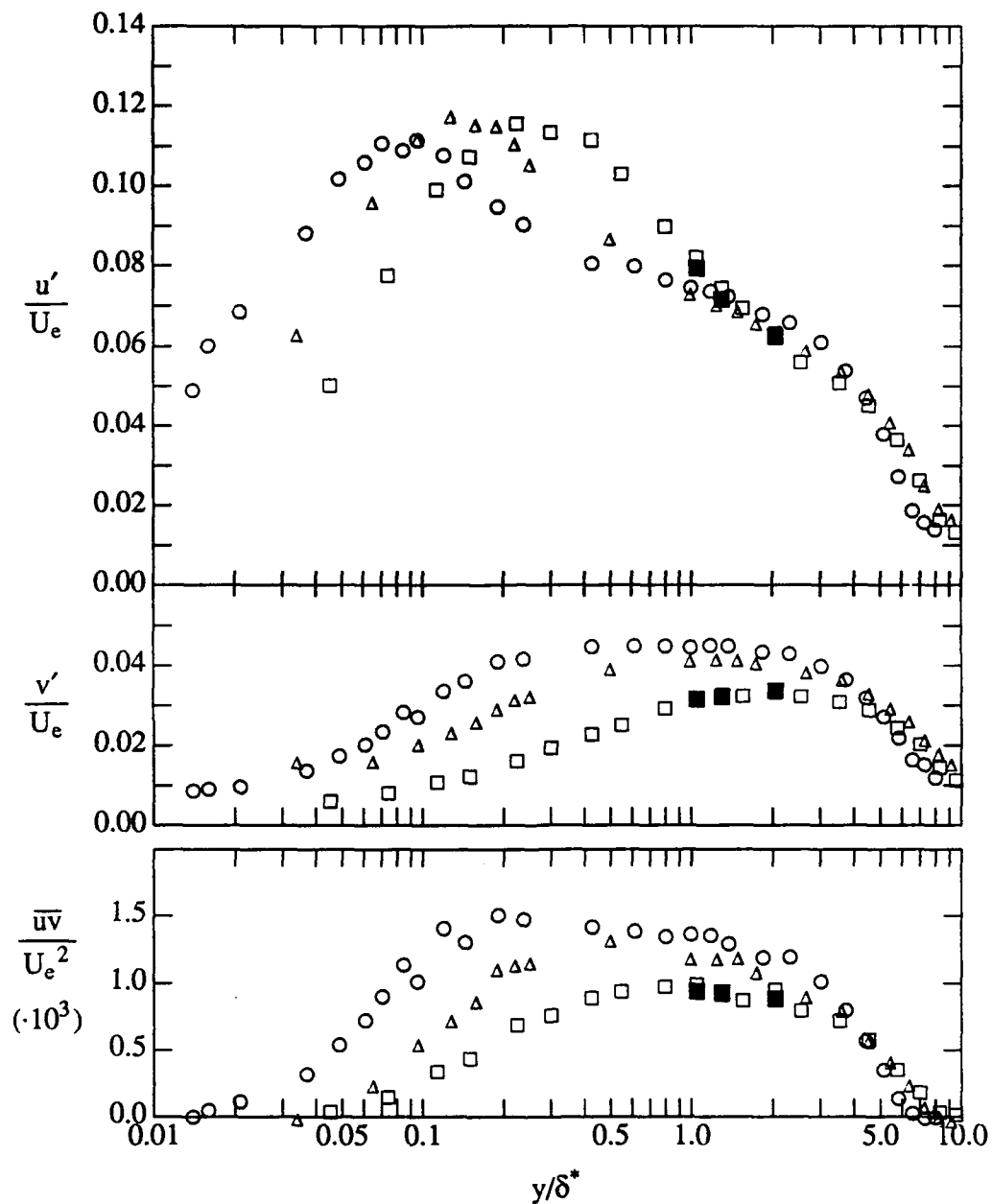


Figure 4.9 Root-mean-square velocities and Reynolds shear stresses for a zero pressure gradient boundary layer at $(x - x_s)^+ = 81000$, $Re_\theta = 3935$ with and without drag reduction. \circ unmodified Newtonian; Δ polymer injection $Q_i/Q_s = 2.6$; \square polymer injection $Q_i/Q_s = 5.1$; \blacksquare $Q_i/Q_s = 5.1$, repeated points.

injection flow rate, the reduction in v' is approximately the same for the two cases. This result is probably linked to the small change in drag reduction between these cases, 46 percent at the low injection flow rate and 50 at the high flow rate. Farther downstream (figure 4.9), the higher polymer flow rate data exhibit a much more pronounced reduction than at the low injection flow rate. The change in drag reduction was also more pronounced for these cases, with 16 percent drag reduction at the low injected flows rate and 38 percent at the high injected flowrate. These two figures also show that water injection does not influence the fluctuation statistics and that polymer remaining in the channel was sufficiently degraded that it did not affect the v' statistics. The v' decrease has been observed in polymer drag reduced flows in zero pressure gradient boundary layers (Fontaine et al.,1990), two-dimensional channels (Willmarth et al., 1987; Luchik & Tiederman, 1988; Walker & Tiederman, 1990; Harder & Tiederman, 1991), in developing boundary layers with slot injection (Maksimovic, 1984), and in pipe flow (Bewersdorff, 1984).

Figure 4.10 presents similar data for the moderate adverse pressure gradient flow. The same basic changes in u'/U_e , v'/U_e , and \overline{uv}/U_e which occurred in the zero pressure gradient case also occur in this boundary layer. However, the magnitude of these changes is dramatically reduced, reflecting the much lower drag reduction observed. These observations further indicate that the polymer relaxes and becomes less effective in the adverse pressure gradient flows. The stronger adverse pressure gradient boundary layer exhibited similar trends. These data are shown in the appendix.

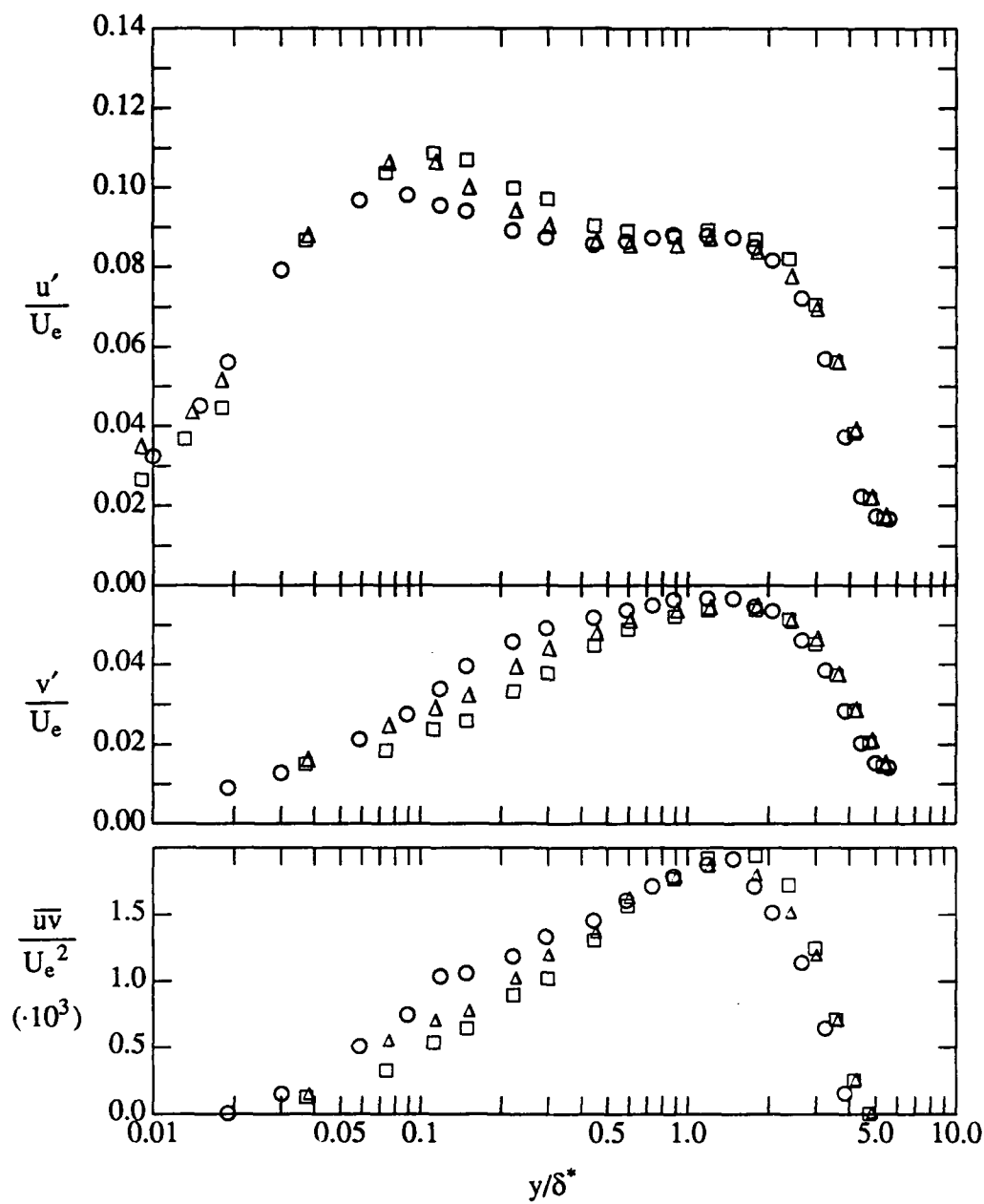


Figure 4.10 Root-mean-square velocities and Reynolds shear stresses for an adverse pressure gradient boundary layer at $Re_\theta = 3570$, $\beta = 1.8$ with and without drag reduction. \circ unmodified Newtonian; Δ $Q_i/Q_s = 2.6$; \square $Q_i/Q_s = 5.1$.

Figure 4.11 shows the skewness of the velocity fluctuations in the drag reduced zero pressure gradient boundary layer. Please note that a linear scale has been used for the distance normal to the wall. For reference, the Gaussian value of skewness, 0, is indicated by a dashed line. In all cases, the skewness is only plotted in the inner region of the flow. In the wake region, proper measurement of the skewness of the turbulence would require knowledge of the intermittency. This information is not available from velocity data acquired using LDV in the inhibited sampling mode. The skewness of the streamwise velocity fluctuations inside of approximately $y/\delta^* = 0.5$ increases during drag reduction. This region when translated into inner variables is approximately $y^+ < 50$. The skewness increases because the mean velocity profile in this region of the flow decreases from its Newtonian value, as can be seen from figure 4.12 which shows the mean streamwise velocity profile in the inner region of the boundary layer. Because the mean velocity has decreased, the negative fluctuations are limited to smaller magnitudes than in the Newtonian flow. Outside of $y/\delta^* \cong 0.5$ the skewness decreases where the mean velocity in the drag reduced boundary layers increases over that of the Newtonian flow. There are two possible explanations for this change in skewness. First, because the mean velocity has increased while the maximum velocity is unchanged, the positive fluctuations are limited and the skewness of the streamwise velocity decreases. Second, the decrease in skewness could indicate that the intermittent region of the flow extends farther into the boundary layer. However, because the flatness factor (figure 4.13) for the same data does not increase, the flow is not intermittent in this region (Sandborn, 1958). In the region $y/\delta^* \leq 0.5$ where the skewness is positive the positive u fluctuations will have the strongest influence on the flatness factor which would cause a

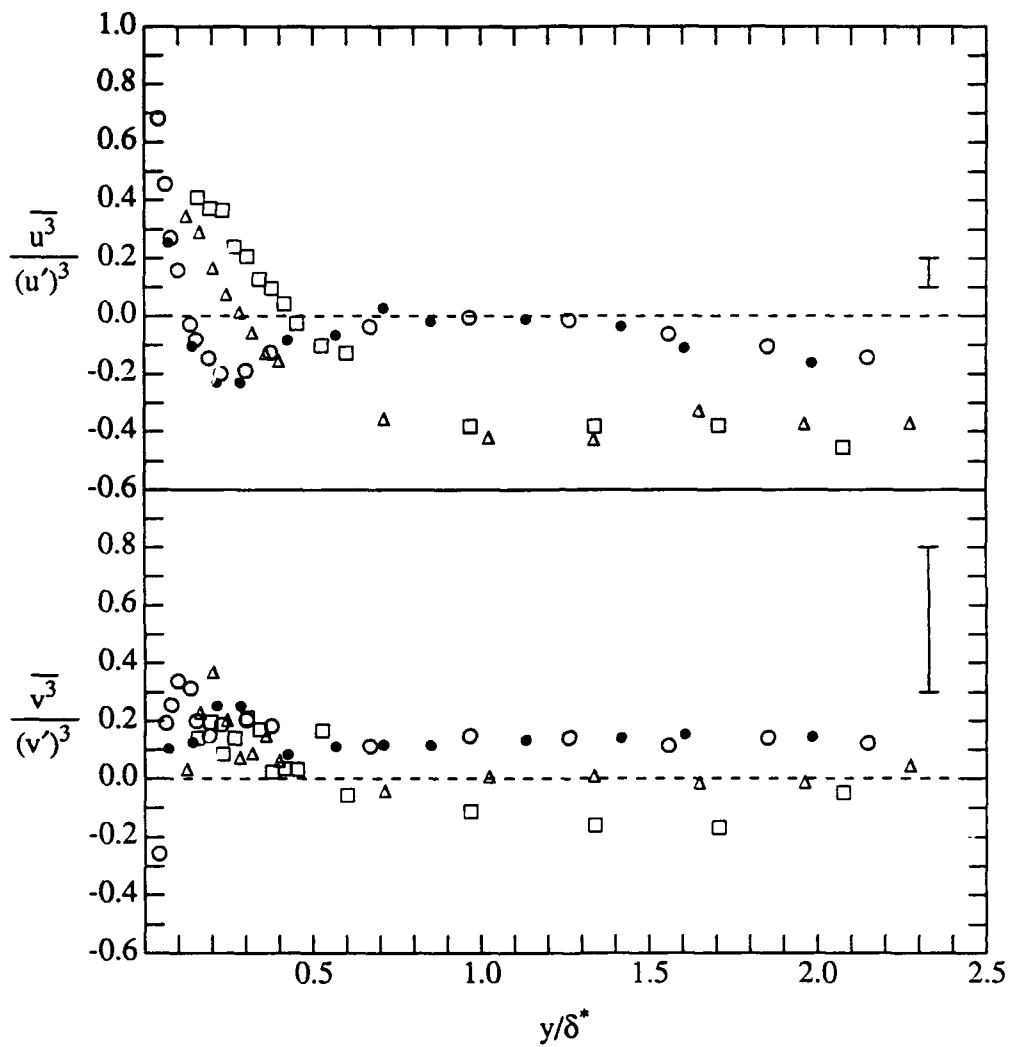


Figure 4.11 Skewness of the streamwise and normal velocity fluctuations in the inner region of a zero pressure gradient boundary layer at $(x - x_s)^+ = 29000$, $Re_\theta = 2478$ with and without drag reduction. \circ unmodified Newtonian; \bullet water injection at $Q_i/Q_s = 5.1$. Δ $Q_i/Q_s = 2.6$; \square $Q_i/Q_s = 5.1$.

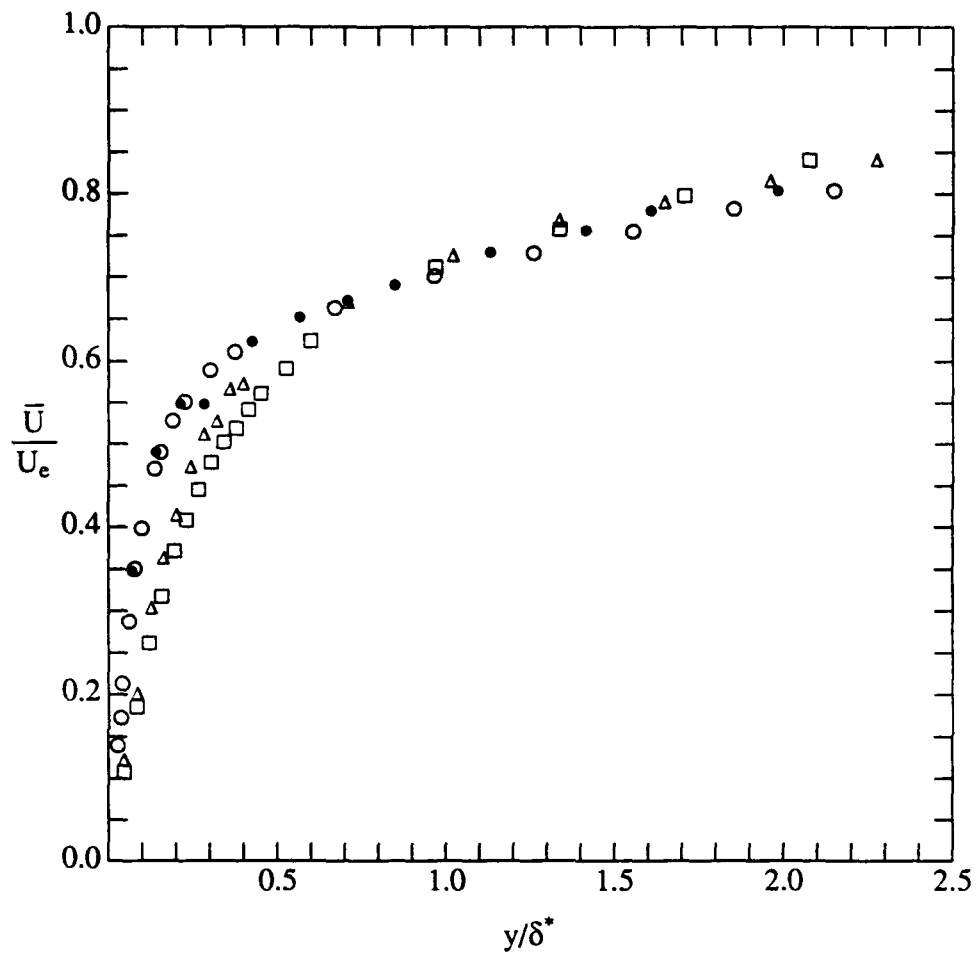


Figure 4.12 Mean streamwise velocity for the inner region of a zero pressure gradient boundary layer at $(x - x_s)^+ = 29000$, $Re_\theta = 2478$ with and without drag reduction. \circ unmodified Newtonian; \bullet water injection $Q_i/Q_s = 5.1$; \triangle polymer injection $Q_i/Q_s = 2.6$; \square polymer injection $Q_i/Q_s = 5.1$.

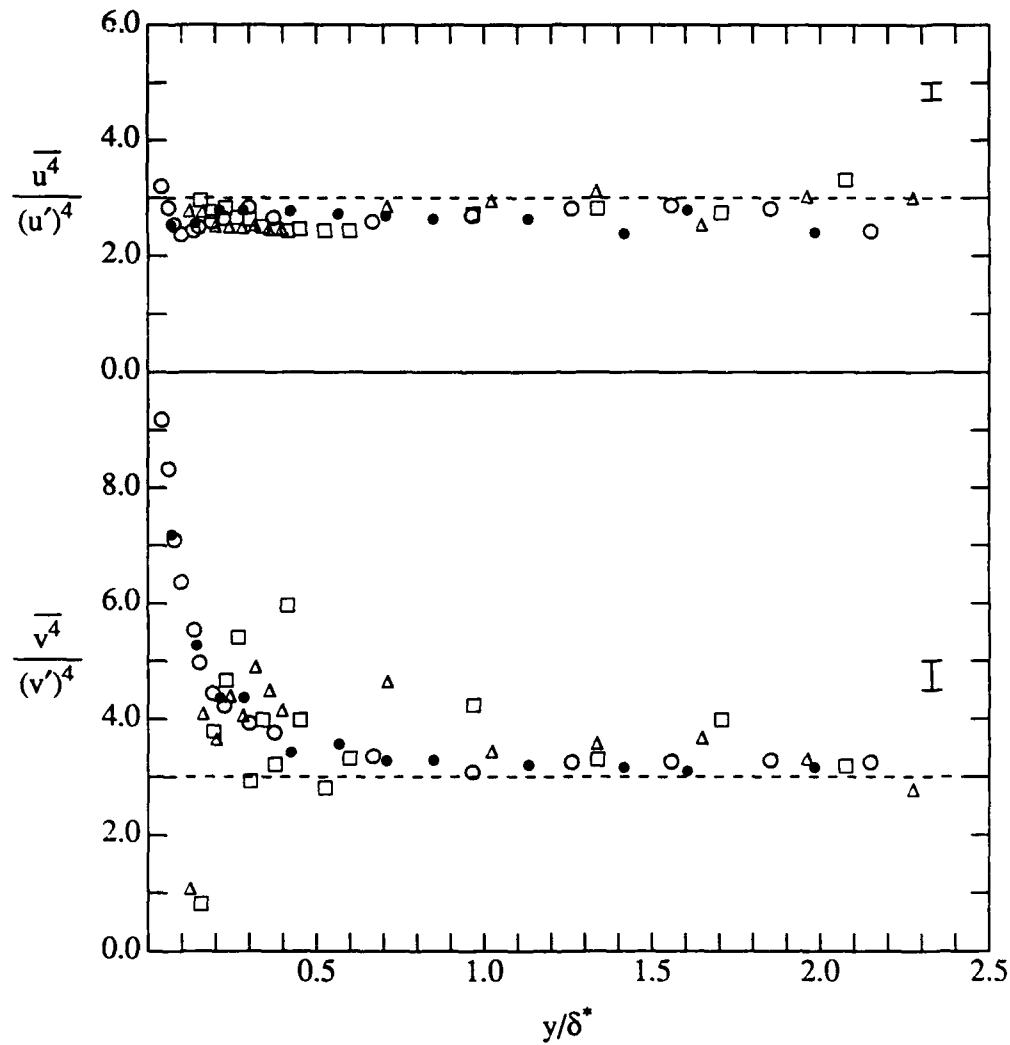


Figure 4.13 Flatness of the streamwise and normal velocity fluctuations in the inner region of a zero pressure gradient boundary layer at $(x - x_s)^+ = 29000$, $Re_\theta = 2478$ with and without drag reduction. \circ unmodified Newtonian; \bullet water injection at $Q_i/Q_s = 5.1$. Δ $Q_i/Q_s = 2.6$; \square $Q_i/Q_s = 5.1$.

reduction in flatness. The fact that any such change is less than the uncertainty of the data suggests that the positive fluctuations are not significantly different from those in the Newtonian flow. These changes are analogous to the changes in the skewness of the velocity fluctuations observed by Barlow & Johnston (1985) in boundary layers on concave and convex surfaces. The uncertainty in the skewness of the normal velocity fluctuations is larger than any changes during drag reduction. Note that the uncertainty in this statistic is higher than in the streamwise case because the velocity was measured in a coordinate system which is approximately 45 degrees from the streamwise direction. The flatness of the normal velocity fluctuations is scattered for the drag reduced cases. This scatter demonstrates the limitations of measuring the velocities at 45 degrees from the laboratory axes. These plots are typical of the zero pressure gradient data. The skewness of the data is given in tabular form in the appendix.

Figure 4.14 and 4.15 show the skewness and flatness of the velocity fluctuations in the moderate adverse pressure gradient boundary layer with and without drag reduction. Because the drag reduction was very small in these cases, the skewness and flatness of the velocities did not change significantly.

4.5 Mixing length models

As in Newtonian flows, the major practical interest in drag reduced boundary layers is in modeling them numerically. Figure 4.16 compares the mixing length in Newtonian and corresponding drag reduced boundary layers for the zero and moderate adverse pressure gradient cases. Note that the presence of polymer in the boundary

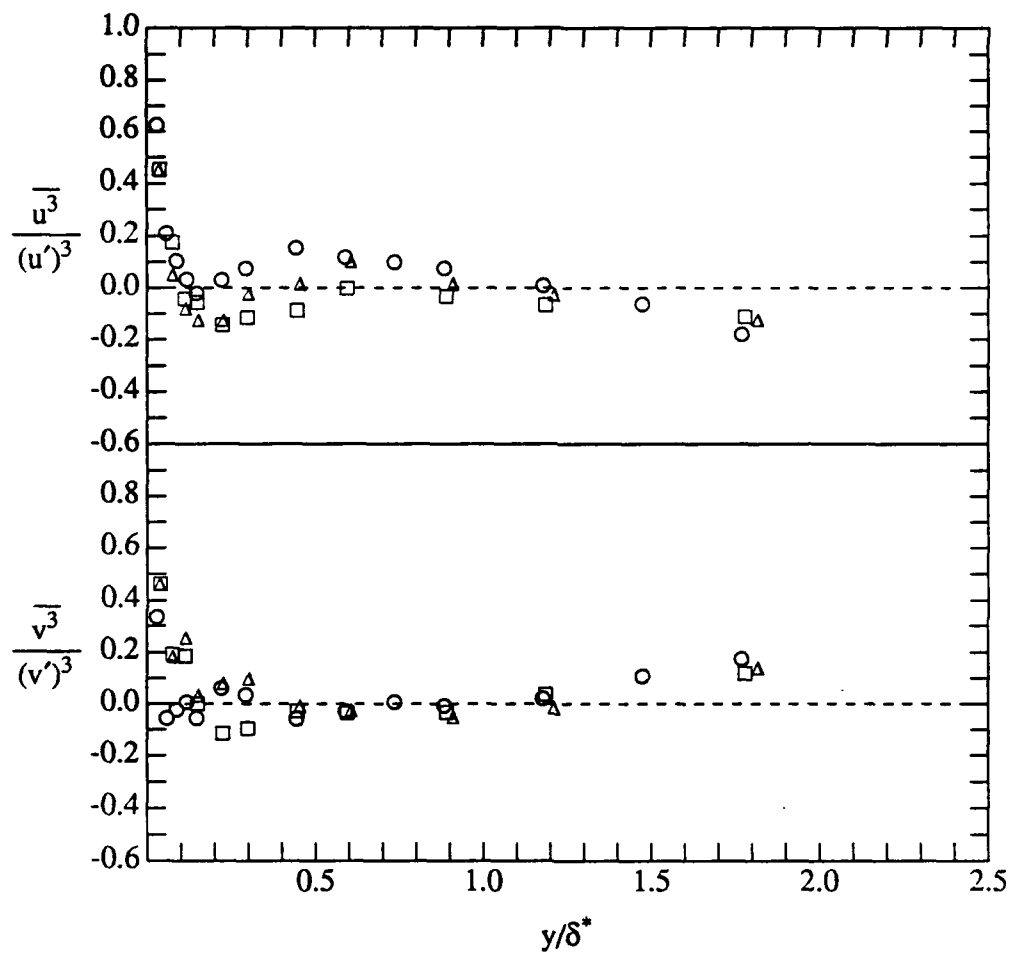


Figure 4.14 Skewness of the streamwise and normal velocity fluctuations in the inner region of an adverse pressure gradient boundary layer at $Re_\theta = 3570$, $\beta = 1.8$ with and without drag reduction. \circ unmodified Newtonian; Δ $Q_i/Q_s = 2.6$; \square $Q_i/Q_s = 5.1$.

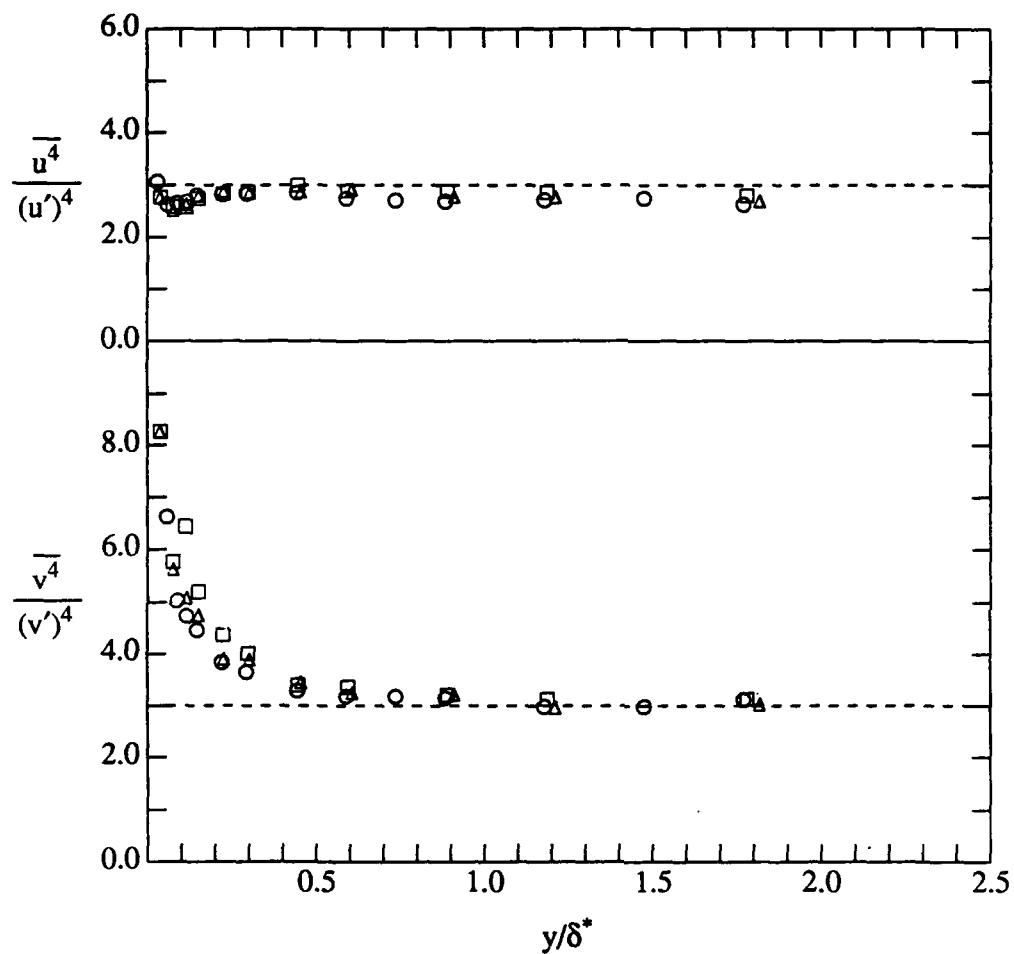


Figure 4.15 Flatness of the streamwise and normal velocity fluctuations in the inner region of an adverse pressure gradient boundary layer at $Re_\theta = 3570$, $\beta = 1.8$ with and without drag reduction. \circ $Re_\theta = 3570$, $\beta = 1.8$; Δ $Q_i/Q_s = 2.6$; \square $Q_i/Q_s = 5.1$.

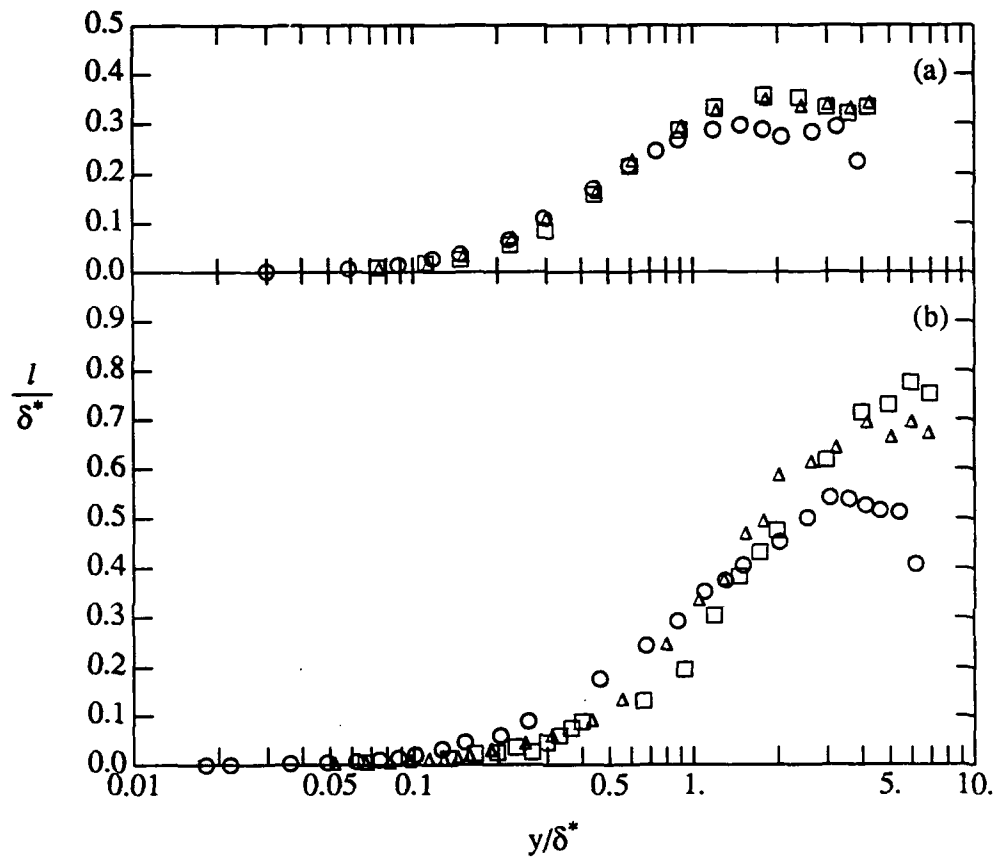


Figure 4.16 Mixing length in a Newtonian equilibrium boundary layer and corresponding drag reduced layers. (a) adverse pressure gradient, $Re_{\theta}|_N = 3570$, $\beta = 1.8$ (b) zero pressure gradient $Re_{\theta}|_N = 3527$. \circ no injection; Δ $Q_i/Q_s = 2.6$; \square $Q_i/Q_s = 5.1$.

layer reduces the mixing length, especially in the zero pressure gradient case. The mixing lengths are reduced because the Reynolds stress, \overline{uv} is reduced. Note that the mixing length is reduced across the majority of the boundary layer in the zero pressure gradient case where drag reduction is high and the non-Newtonian stresses are important, but in the adverse pressure gradient case, where the drag reduction is small and non-Newtonian stresses are negligible, the mixing length is changed only in the buffer region.

Walker (1985) demonstrated the feasibility of using simplified models in polymer drag reduction of turbulent channel flows by modifying a Patankar-Spalding type computer code for boundary layers and turbulent channel flows, STAN5 (see Crawford and Kays, 1975). STAN5 achieves closure of the Reynolds averaged momentum equations with an algebraic expression for the mixing length, l . In order to modify the closure, Walker hypothesized that damping increases with decreasing mixing length, that is smaller fluctuations are damped more than large ones. He also hypothesized that damping increases with increasing polymer concentration and that the damping capability of a molecule is related to its physical size. Therefore Walker defined a modified mixing length:

$$l' = l(1 - e^{-lr}) \quad (4.7)$$

where l is the Newtonian mixing length, in this case calculated from the Newtonian model. The variable r was a length scale which was a function of the size of the polymer molecule, l_p , and local concentration, \overline{C} . Namely, r in units of μm is given by:

$$r = l_p f(\bar{C}) \quad (4.8)$$

Walker measured pressure drop and flow rate for several fully developed channel flows of homogeneous AP-273 solutions with concentrations in the range 1.65 to 4.5 wppm. He then determined r by requiring that the velocity profiles calculated with l' yield the correct flow rate and pressure drop for these flows. This procedure resulted in the equation:

$$r = 60.3(\bar{C})^{0.67} \quad (4.9)$$

where the concentration is in wppm. Walker successfully predicted drag reduction downstream of slot injection of polyacrylamide solutions into a fully developed channel flow using this model.

Walker's modification of STAN5 was used to predict drag reduction as a function of distance downstream of the slot for the present experiments. The code was started with an approximate turbulent velocity profile 383 mm upstream of the slot. It then required 75 streamwise steps to establish stable predictions of the wall shear stress coefficient, c_f . Each step represented 0.5 local boundary layer thicknesses. The location at which the statistics became stable is 300 mm upstream of the slot. This distance for starting the code was determined by changing the location at which the code was started until the code correctly predicted the measured zero pressure gradient wall shear stress coefficients.

Figure 4.17 compares the code predictions of c_f to the measured drag reduction in the zero pressure gradient boundary layers. The unmodified (no injection) Newtonian boundary layer predictions are shown as dotted curves. These predictions are in

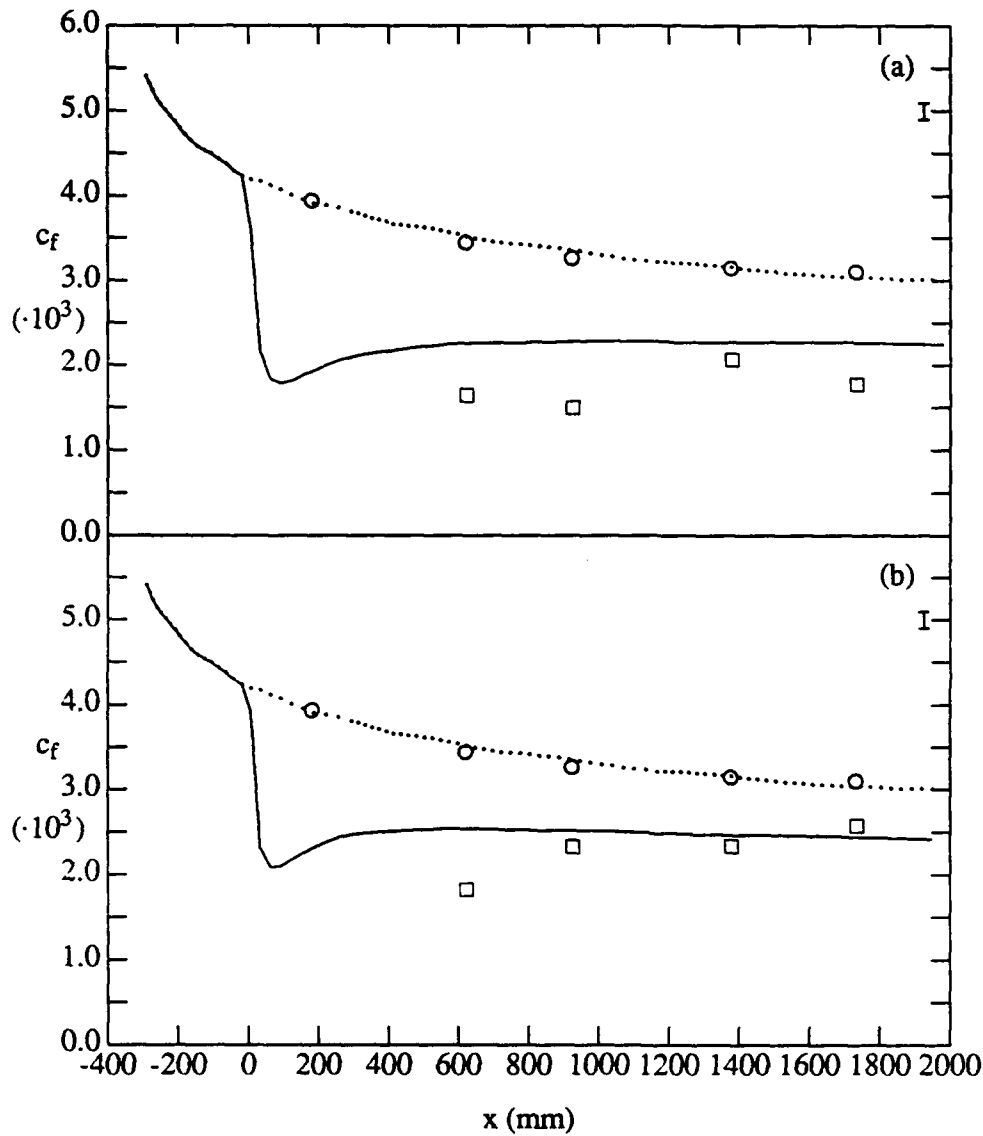


Figure 4.17 Friction coefficient, c_f , as a function of streamwise distance from the slot in the zero pressure gradient boundary layer. (a) high injection flowrate (b) low injection flowrate. \circ no injection ; \square drag reduced data; predicted, no injection; — predicted with polymer injection. Typical error bound on measured c_f on right.

excellent agreement with the data. The slight variation in the curve is the result of variations in the third significant digit of the predicted c_f . The bottom section of the plot shows the friction coefficient predicted for the low polymer injection rate. The code predictions are excellent for the three locations farthest from the slot. The polymer concentration in the linear sublayer at these locations was within the range of concentrations for which the model was derived. At the location closest to the slot where the polymer concentration in the linear sublayer exceeds the range of the model, the code predicts a value of c_f that is too high. At the high injection flow rate, the code always underpredicts the actual drag reduction. In all of these cases polymer concentrations in the linear sublayer were higher than the concentrations used by Walker to form his model and there was a non-Newtonian shear stress shown in figure 4.2. A small non-Newtonian stress was also observed in two of the low injection flow rate cases (924 and 1379 mm from the slot) where the code correctly predicted c_f .

Figure 4.18 and 4.19 compare the code predictions to data for the moderate and strong adverse pressure gradients respectively. The calculations were started in exactly the same manner as in the zero pressure gradient case. However, at 400 mm downstream of the slot, the freestream velocity distribution was changed to the adverse distribution. This corresponds closely to the physical location where the flexible wall of the water channel began to curve. The measured freestream velocity profile in the adverse pressure gradient region was smoothed in each case by a least squares fit of the form $U_e \propto x^n$. The transition from the zero pressure gradient region to this curve was smoothed by a second order polynomial from 25 mm upstream of the slot to 25 mm downstream of the slot. The polynomial was tangent to the respective curves at its

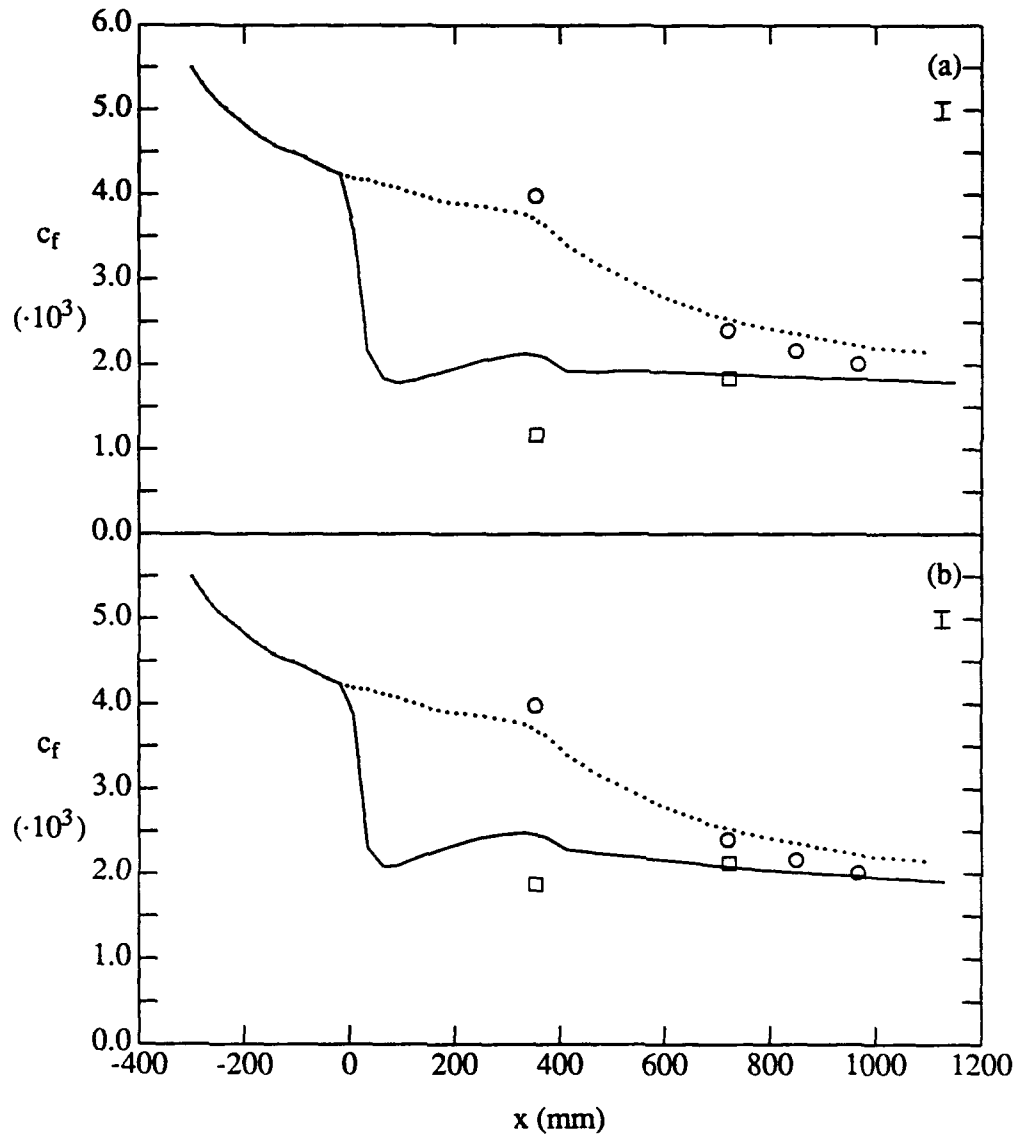


Figure 4.18 Friction coefficient, c_f , as a function of streamwise distance from the slot in the adverse pressure gradient boundary layer, $\beta = 1.8$. (a) high injection flowrate (b) low injection flowrate. \circ no injection ; \square drag reduced data; predicted, no injection; — predicted with polymer injection. Typical error bound on c_f on right.

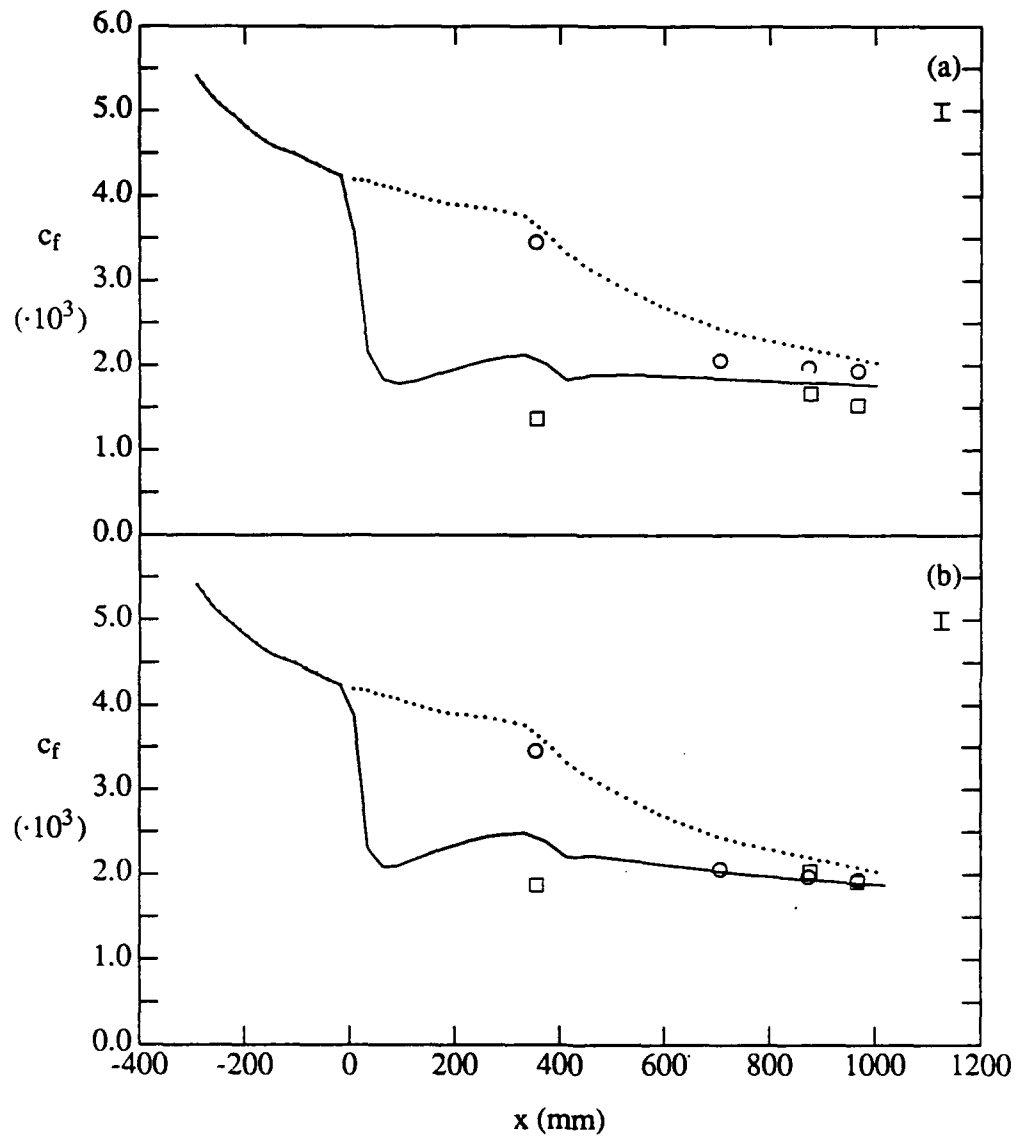


Figure 4.19 Friction coefficient, c_f , as a function of streamwise distance from the slot in the adverse pressure gradient boundary layer, $\beta = 2.4$. (a) low injection flowrate (b) high injection flowrate. \circ Newtonian data; \square drag reduced data; \cdots predicted Newtonian; — predicted with polymer injection. Typical error bound on c_f on right.

endpoints. The code predictions reasonable match all of the data except near the streamwise location where the pressure gradient changes. The predicted c_f curve has a bump in it which does not appear realistic. This bump does not occur in the no injection case, so it is assumed to be linked to the modified mixing length model. The output of the code was checked to verify that the computed freestream velocity gradients varied smoothly. Also, the lag parameter which controls the speed at which the code adjusts for pressure changes was increased by 50 percent and decreased by 25 percent without eliminating the problem. Therefore, this problem seems to be an interaction between the two factors, pressure and polymer, which modify the mixing length. The predicted value of c_f is also too high in this region. As in the zero pressure gradient cases, this over-prediction is in a region where the polymer concentration is outside the range for which the model was derived. Despite these problem at the change in pressure gradient, the model correctly predicts c_f farther downstream. It was assumed that significant non-Newtonian stresses occurred at the upstream locations because non-Newtonian stresses were observed farther downstream in the zero pressure gradient boundary layers.

In conclusion, the concept of modifying Newtonian boundary layer codes to predict polymer drag reduction is successful as long as the models are not extrapolated to higher concentrations than those for which they were derived and as long as strong non-Newtonian shear stresses are not present. When these two criteria are not met, the model overpredicts the shear stress, providing a conservative estimate. Walker's mixing length model itself has difficulty handling rapid changes in freestream pressure gradient, but it is believed that this problem is inherent to this particular model and not

to the concept.

4.6 Turbulence production

The reduction of the Reynolds stresses in the drag reduced boundary layer naturally leads to examination of the Reynolds stress production during drag reduction. Figures 4.20 and 4.21 show production of the Reynolds shear and normal stresses in the drag reduced zero pressure gradient boundary layer at the same two streamwise locations as previously examined. Both production terms are almost completely eliminated by the presence of polymer at the first location. Strong non-Newtonian stresses were also observed in this region. At the farther downstream location, where the polymer is more dilute and there is less drag reduction, both production terms are reduced, but not so dramatically as in the first case. When the even lower drag reduction case of the adverse pressure gradient boundary layer is considered, figure 4.22, it can be seen that production is only slightly reduced by the presence of the polymer.

4.7 Postulated mechanism of drag reduction

The final section of this chapter will examine whether the present data support Hinch's (1977) hypothesis that the polymer molecules in a turbulent flow are stretched by large extensional motions in the flow, and that once stretched, these molecules cause an anisotropic viscosity which damps the small scales of turbulence which are the dissipational eddies in a Newtonian flow. The first part of this hypothesis requires that strong extensional motions remain in the drag reduced flow. Figure 4.23 compares joint probability density functions of the streamwise and normal velocity fluctuations in the Newtonian zero pressure gradient flow and the zero pressure gradient drag reduced flow

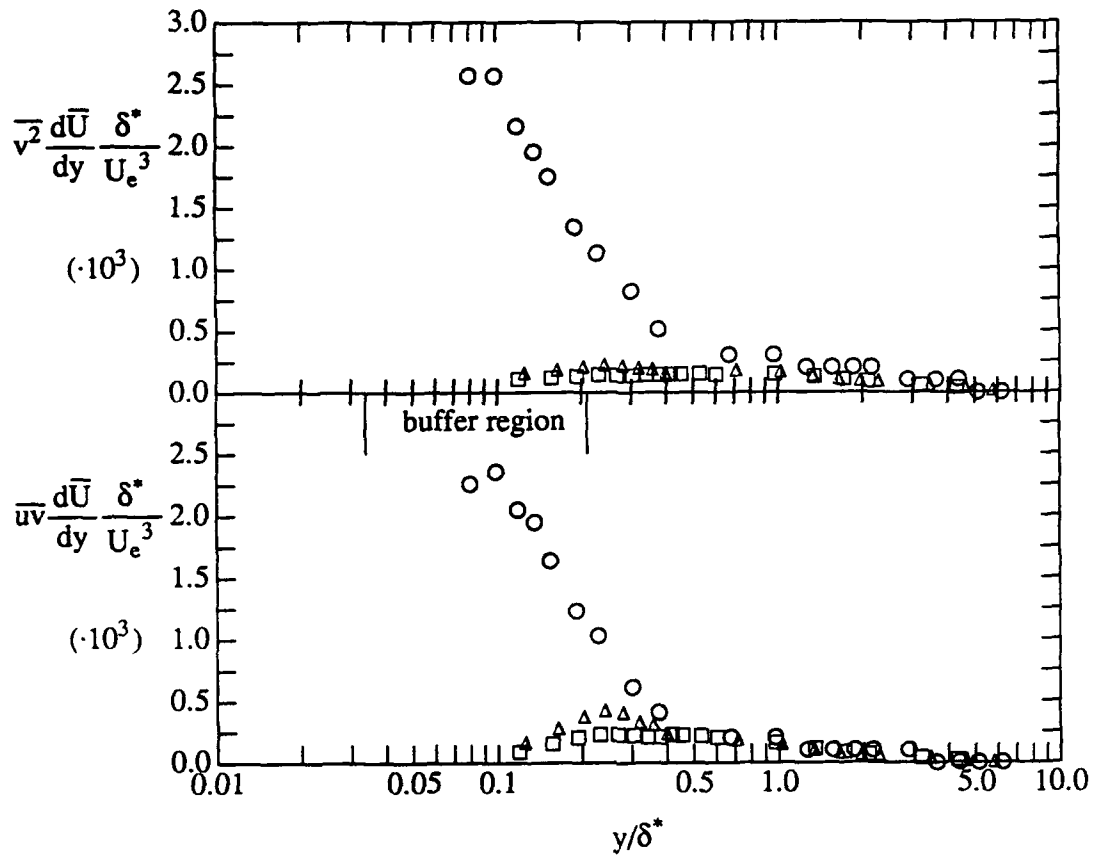


Figure 4.20 Reynolds shear stress (\overline{uv}) and normal stress ($\overline{v^2}$) production in a zero pressure gradient boundary layer with and without polymer injection.

\circ $(x - x_s)^+ = 29000$, $Re_\theta = 2478$, Newtonian Δ $Q_i/Q_s = 2.6$;
 \square $Q_i/Q_s = 5.1$.

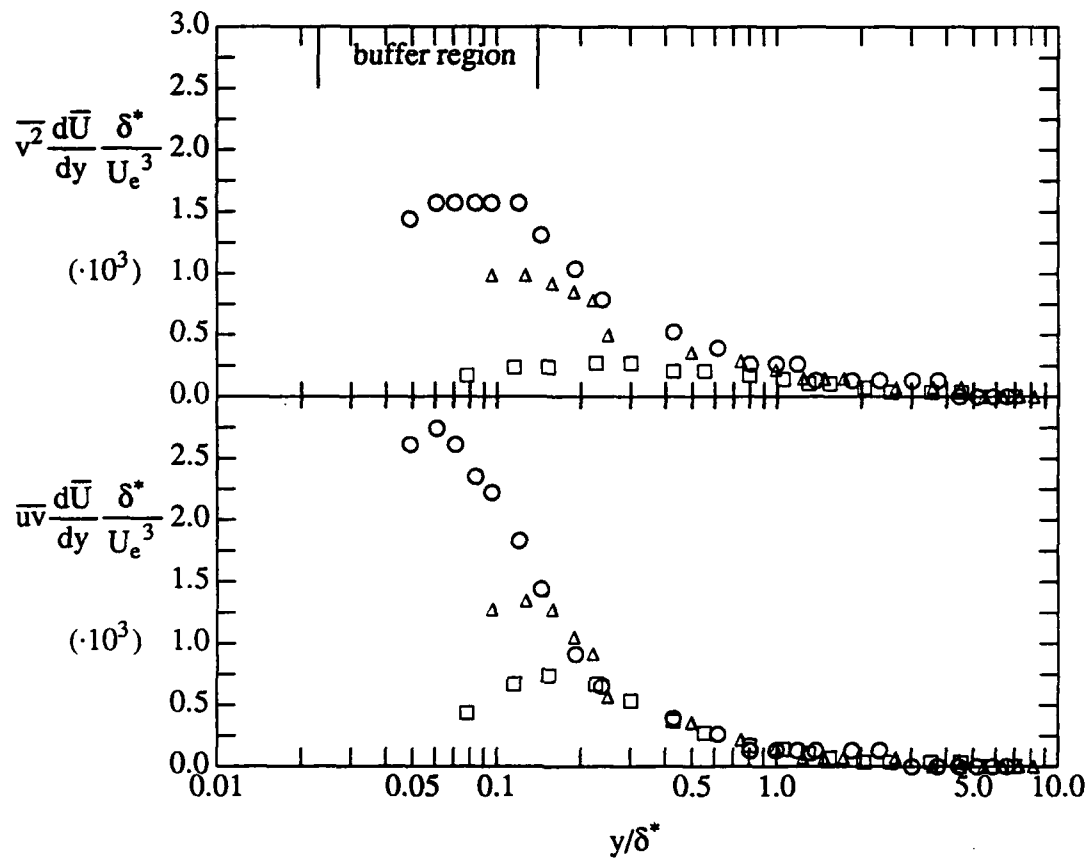


Figure 4.21 Reynolds shear stress (\overline{uv}) and normal stress ($\overline{u^2}$) production in a zero pressure gradient boundary layer with and without polymer injection.
 ○ $(x - x_s)^+ = 81000$, $Re_\theta = 3935$, Newtonian △ $Q_i/Q_s = 2.6$;
 □ $Q_i/Q_s = 5.1$.

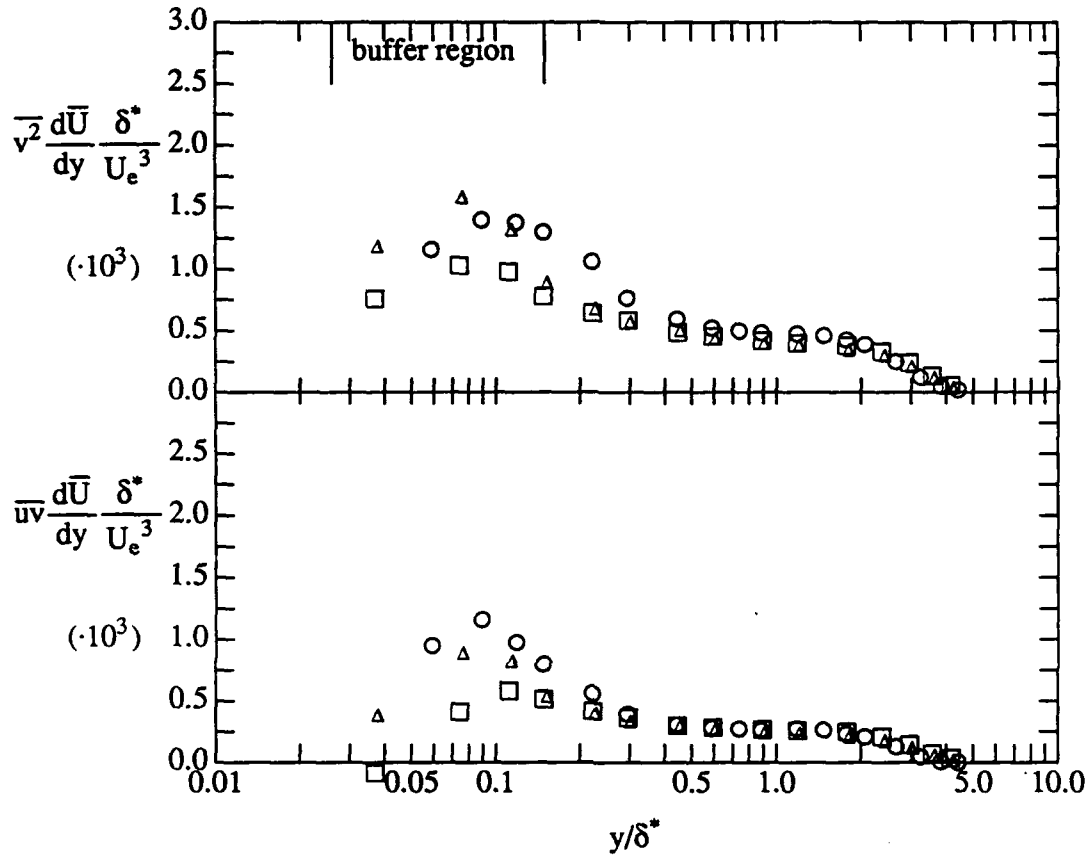


Figure 4.22 Reynolds shear stress (\overline{uv}) and normal stress ($\overline{u^2}$) production in an adverse pressure gradient boundary layer with and without polymer injection \circ Newtonian, $\beta = 1.8$, $Re_\theta = 3570$; \triangle $Q_i/Q_s = 2.6$; \square $Q_i/Q_s = 5.1$.

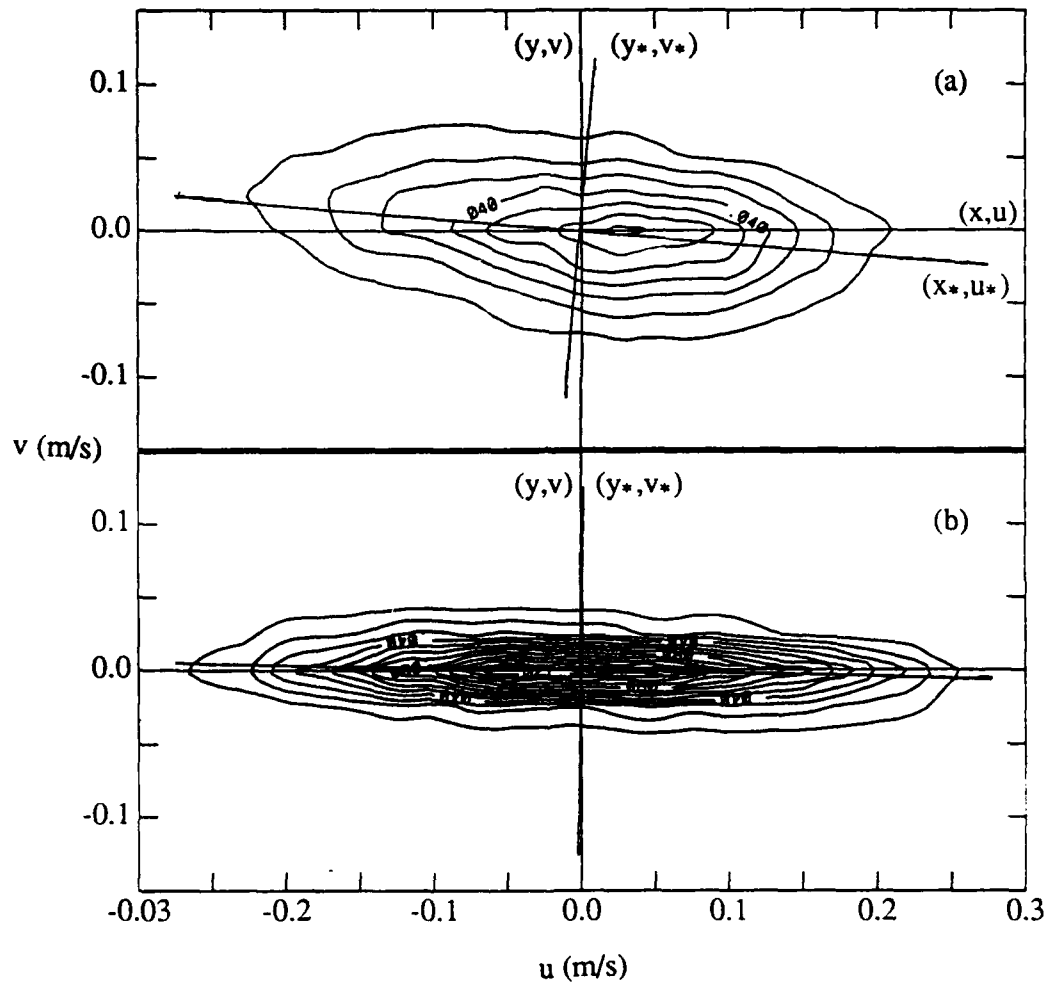


Figure 4.23 Joint probability function of u and v fluctuations in a zero pressure gradient boundary layer (a) Newtonian and (b) drag reduced $Q_i/Q_s = 2.6$, $Re_{\theta}|_N = 2497$, $x^+ = 29000$, $y^+|_N = 33$.

with $Q_i/Q_s = 2.6$ respectively. The axis have been intentionally left in dimensional units to allow direct comparisons. In each of the two cases the data were acquired at the same streamwise location and the same location normal to the wall, 0.78 mm. For the Newtonian case, this location corresponds to the outer edge of the buffer region, at $y^+ = 33$. The drag reduced case is one of the cases which exhibited a strong non-Newtonian stress. The axis of principal normal stress are shown on each figure. The shear stress in the laboratory coordinates, (x, y) , can be rotated to a new coordinate system, (x^*, y^*) , using equation 4.10 (Hinze, 1975).

$$\overline{u^*v^*} = (\overline{v^2} - \overline{u^2})\sin\alpha\cos\alpha + \overline{uv}(\cos^2\alpha - \sin^2\alpha) \quad (4.10)$$

This equation can be solved for the angle, α , of the principal planes at which the rotated shear stress is maximum by differentiating it with respect to α and setting the result equal to zero. The final equation is:

$$\alpha = 0.5 \arctan \left[\frac{\overline{v^2} - \overline{u^2}}{2\overline{uv}} \right] \quad (4.11)$$

It is clear that the angle of the principal stress axes has rotated from $\alpha = -4.9^\circ$ in the Newtonian flow to $\alpha = -0.9^\circ$ in the drag reduced flow. However, the principal shear stress, $\overline{u^*v^*}$, actually increases from 0.10 (m/s) to 0.13 (m/s). In other words, although the average value of \overline{uv} in the laboratory coordinates decreases during drag reduction, the magnitude of the large amplitude fluctuations is not reduced. The mechanism therefore exists to stretch the polymer in this flow.

The measured magnitude of \overline{uv} is lower in the drag reduced case only because the orientation relative to the laboratory coordinates has changed. This change in the apparent magnitude of the stress is analogous to the problem in solid mechanics where the apparent magnitude of the shear and elongational stresses change as the planes in which they are computed changes (Mohr's circle). However, in each case, the magnitude of the elongational and shear stresses which affect the material are always the maximum which occur, regardless of the orientation of the coordinates. This rotation of the probability density function is consistent with that reported by Schmid (1984), Walker & Tiederman (1990), Harder & Tiederman (1991), and Fontaine et al. (1990).

In order to test whether the small scales in the flow were damped, the Kolmogoroff length scale was determined for each flow. The Kolmogoroff length scale is a measure of the size of the smallest eddies in the flow. Therefore, if the Kolmogoroff length scale increases in a flow with polymer present, it indicates that the smallest eddies have been damped, leaving only larger eddies. The Kolmogoroff length scale was calculated in the Newtonian boundary layers from dissipation calculated by assuming that the production and dissipation of kinetic energy are equal. It was approximated in the drag reduced boundary layers by assuming that the production and dissipation of kinetic energy remain equal. The results of this analysis are shown in figure 4.24. Only the inner region of the flow where the approximation is most valid is displayed on the graph. It is immediately clear that the Kolmogoroff scale in the drag reduced flow has increased over that of the Newtonian flow for all cases, although this increase is exaggerated about ten percent by an increase in δ^* . Therefore, both parts of the

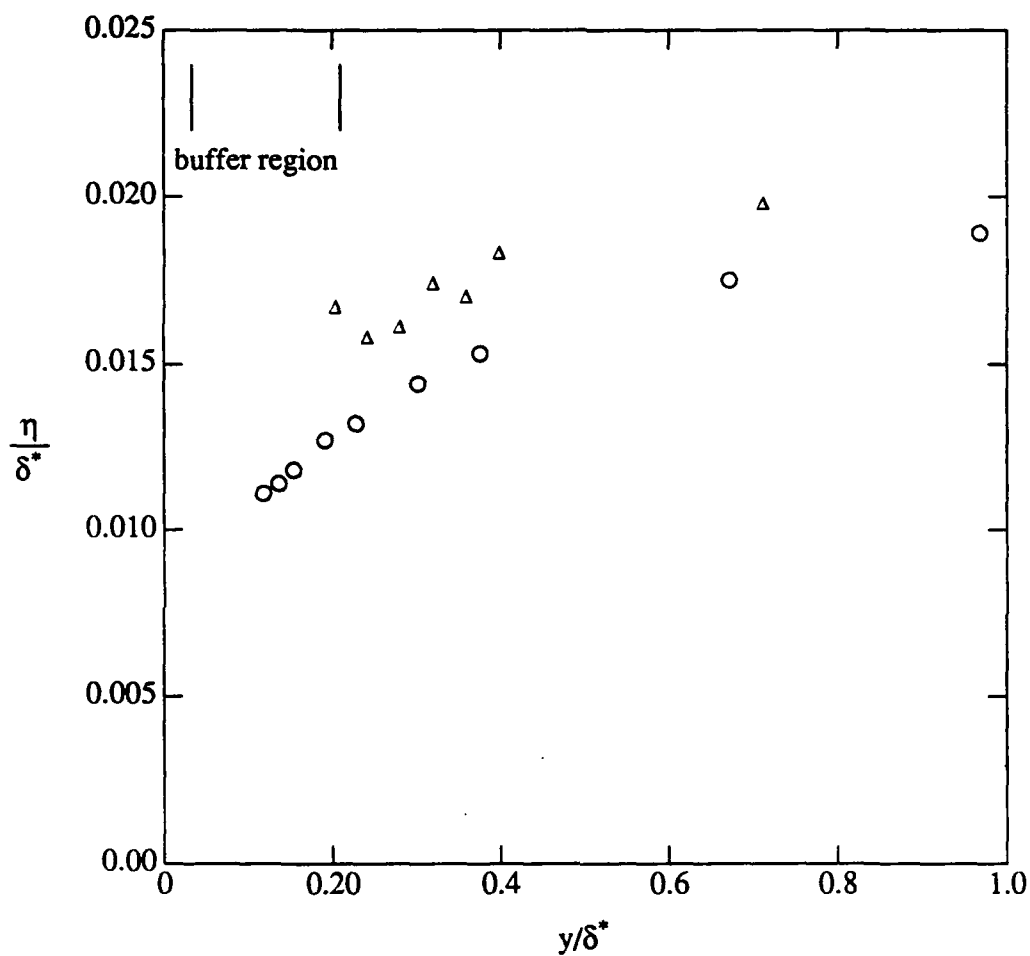


Figure 4.24 Kolmogoroff length scale at a single streamwise location in zero pressure gradient boundary layers with and without drag reduction. \circ $Re_\theta = 2497$ Newtonian; Δ polymer injection $Q_i/Q_s = 2.6$.

hypothesis are supported by the present data. The changes in the Reynolds shear stress correlation coefficient also are consistent with the hypothesis. Figure 4.25 shows the correlation coefficient profiles in the Newtonian zero pressure gradient boundary layer and the corresponding drag reduced boundary layers. The observed reduction of the correlation coefficient in the inner region of the flow can be explained by the rotation of the principal stress axes. It is therefore consistent with a flow which becomes dominated by large amplitude fluctuations in the streamwise direction with small amplitude fluctuations damped.

The hypothesis may also explain the decreased drag reduction in the adverse pressure gradient flows. If the polymer in the moderate pressure gradient flow is not stretched sufficiently by the flow, it will not be effective in reducing drag and will therefore not cause the flow to separate. This is consistent with Leal's (1990) finding that the amount to which polymer molecules stretch is a strong function of the magnitude of the extensional motions and that in turn the anisotropic changes in the viscosity are a function of the degree to which the polymer molecules are stretched. Figure 4.26 shows the probability density function of u and v for the Newtonian moderate adverse pressure gradient ($\beta = 1.8$) and compares it to the drag reduced case at the same point, 1.5 mm from the wall. This point is at nearly the same streamwise location as in figure 4.23 and the two Newtonian cases are at the same y^+ values. Please note that the plot has the same absolute scale as figure 4.23. The general shape and orientation of the histogram is essentially the same as in the zero pressure gradient case. The principal stress axes only rotate from 4.1° to 3.9° and the magnitude of the maximum shear stress remains the same at 0.06 (m/s). Note that this peak shear stress is

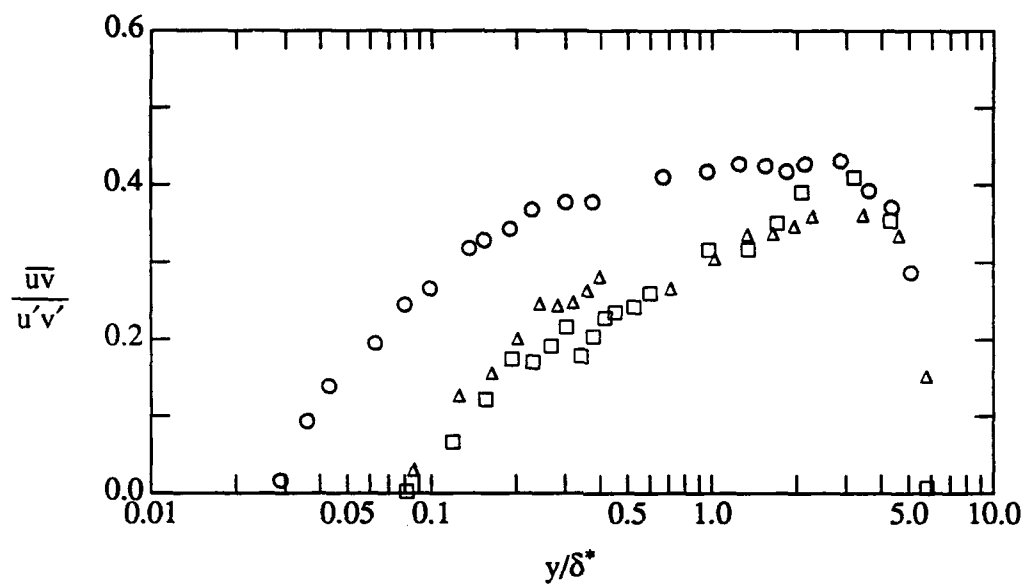


Figure 4.25 Correlation coefficient for a zero pressure gradient boundary layer at $(x - x_s)^+ = 29000$, $Re_\theta = 2478$ with and without drag reduction. \circ unmodified Newtonian; Δ polymer injection $Q_i/Q_s = 2.6$; \square polymer injection $Q_i/Q_s = 5.1$.

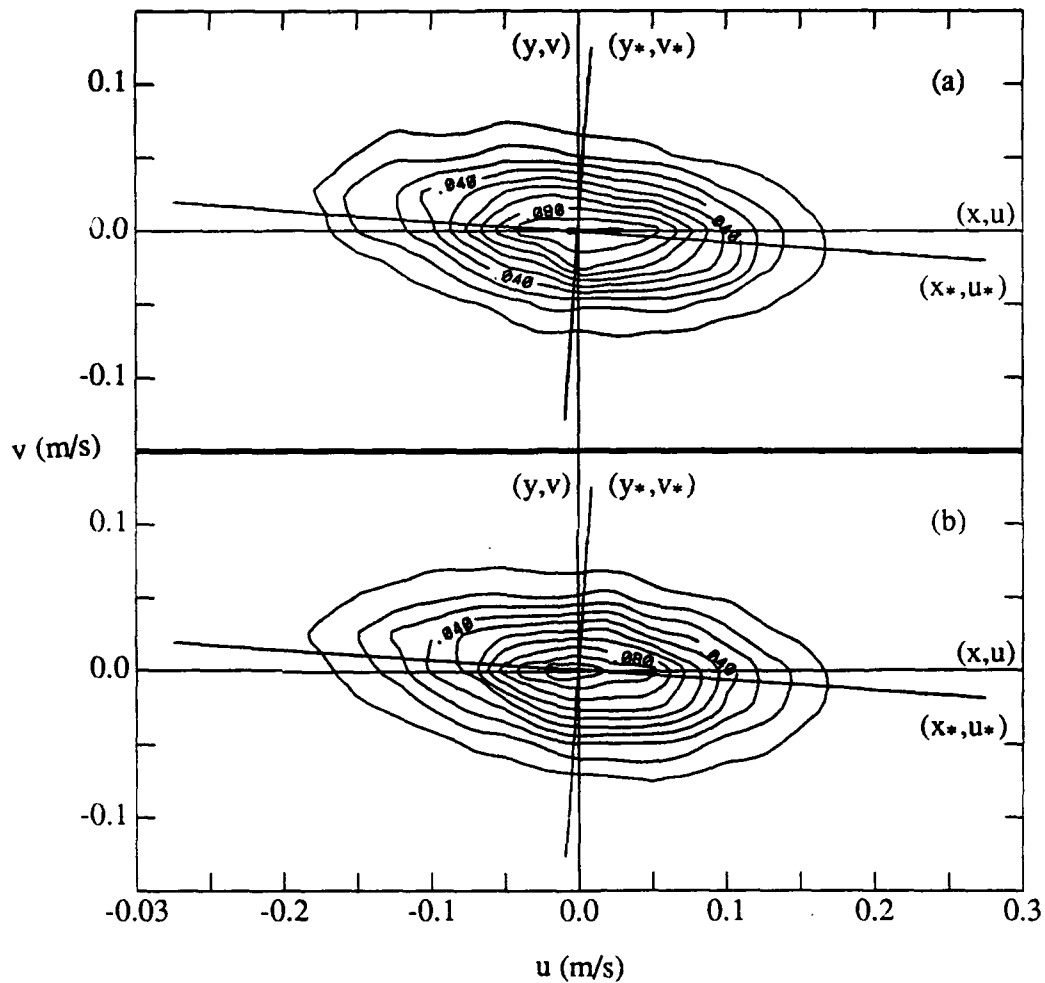


Figure 4.26 Joint probability function of u and v fluctuations in the moderate adverse pressure gradient boundary layer, (a) Newtonian (b) drag reduced $Q_i/Q_s = 2.6$, $Re_\theta|_N = 3570$, $x^+ = 31000$, $y^+|_N = 30$.

much less than in either the Newtonian or drag reduced zero pressure gradient boundary layer. Therefore, the extensional motions which stretch the polymer are somewhat smaller in amplitude in the adverse pressure gradient than they are in the zero pressure gradient flow. As a result, the polymer will not be stretched as much in the adverse pressure gradient flow as in the zero pressure gradient flow. The behavior of the correlation coefficient also supports this result. As can be seen from figure 4.27, the correlation coefficient changes little in the drag reduced flow. This reduction in the ability of the flow to stretch the polymer, along with the lower polymer concentrations observed in the adverse pressure gradient boundary layer therefore combine to provide a plausible explanation of the reduced drag reduction.

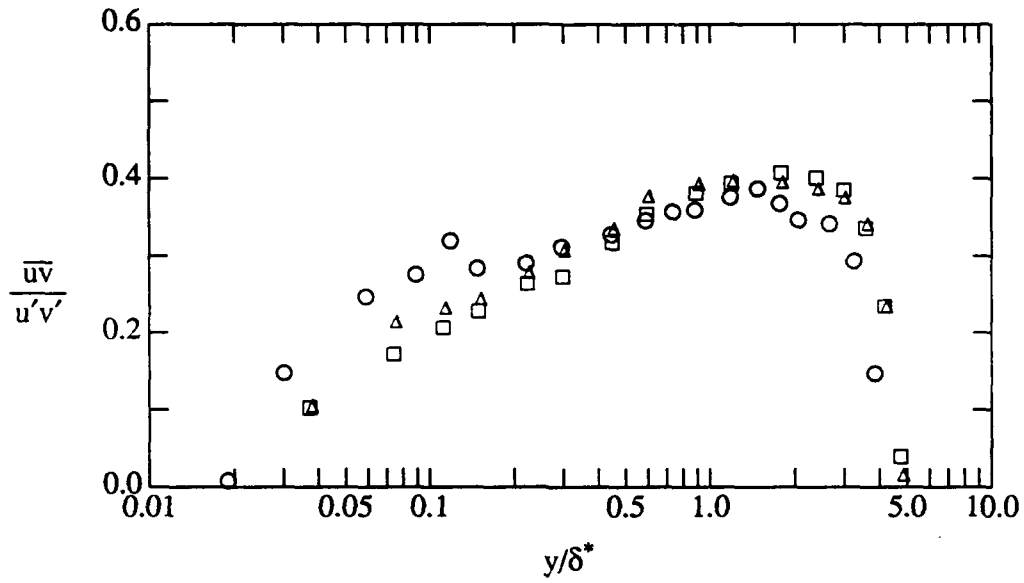


Figure 4.27 Correlation coefficient for an adverse pressure gradient boundary layer at $Re_\theta = 3570$, $\beta = 1.8$ with and without drag reduction. \circ unmodified Newtonian; \triangle $Q_i/Q_s = 2.6$; \square $Q_i/Q_s = 5.1$.

CHAPTER 5: BURST RESULTS

As described in the first chapter, the burst structure is fundamental to wall turbulence. This chapter describes the present experiments which examined the scaling of time between bursts in boundary layers. The specific techniques used to detect and group ejections as well as the burst period results will be described.

The two ejection detection techniques which were used, the second quadrant uv technique and the modified u -level technique ($mulev$), search for the same physical characteristic of an ejection. During an ejection, the low speed fluid near the wall undergoes an acceleration away from the wall so that it mixes with the high speed fluid above it. Therefore the v fluctuation is positive and the u fluctuation is negative. These characteristics led Lu & Willmarth (1973) to propose the second quadrant uv detector. This detector triggers on large negative values in the product of the streamwise and normal velocity components which are in the second quadrant when plotted in the u - v plane (figure 5.1). Mathematically, an event is characterized as an ejection if:

$$uv(t) < -Hu'v' \quad (5.1a)$$

and

$$u(t) < 0 \quad \text{or} \quad v(t) > 0 \quad (5.1b)$$

Where $u(t)$, $v(t)$ and $uv(t)$ are instantaneous values and H is a threshold which must be

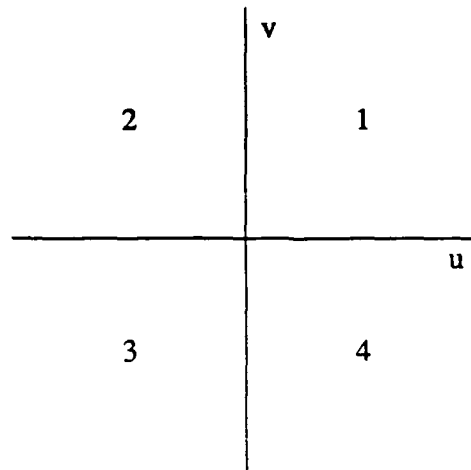


Figure 5.1 Quadrants of the uv plane.

specified. Selection of the threshold will be discussed later.

Because measuring simultaneously the u and v velocities is often difficult, Lu & Willmarth (1973) approximated the detection technique using only the streamwise velocity. The result of this simplification, the u -level technique, detects events in both the second and third quadrants. The classification of third quadrant events as ejections represent an error, but it is a necessary consequence of the simplification.

A major problem confronting the u -level detector is that the u signal does not remain consistently low during ejection. This problem occurs because a burst is a three dimensional structure. Therefore, a threshold which reliably detects the low level of u at the start of an ejection can indicate multiple detections in a single ejection. Therefore, the u -level technique was modified by Luchik & Tiederman (1987) in order

to avoid multiple detections of a single ejection while still accurately detecting ejections by modifying the start and end criteria so that they were different. The technique turns on at a higher threshold and avoids dropout in the middle of an ejection by turning off at a lower threshold. In equation form the modified u-level technique indicates the start of an injection when:

$$u(t) < -Lu' \quad (5.2a)$$

where L is a threshold which must be specified. The ejection continues until:

$$u(t) \geq -0.25Lu' \quad (5.2b)$$

Once detected, the ejections were grouped into bursts so that the burst period could be calculated. A method for grouping ejections into single- and multi-ejection bursts using a grouping time, τ_g , has been well established (Bogard and Tiederman, 1986; Luchik and Tiederman, 1987; Barlow & Johnston, 1988; Tiederman, 1990; White & Tiederman, 1990). The grouping of ejections was done by using a grouping time, τ_g , assuming all ejections separated by less than τ_g are from the same burst and those with larger temporal spacing are from different bursts. Ideally, a histogram of the time between ejections would have two separate distributions; one for ejections from the same burst and one for ejections from different bursts as represented in figure 5.2. In reality, the two distributions have some overlap which makes the choice of a grouping time more difficult. The assumption that a single grouping time is appropriate is incorrect. Nevertheless, a grouping time which reasonably separates these distributions can be determined by plotting the histogram of the time between ejections on a semi-log scale (Barlow & Johnston, 1985; Tiederman, 1990; White & Tiederman, 1990). It

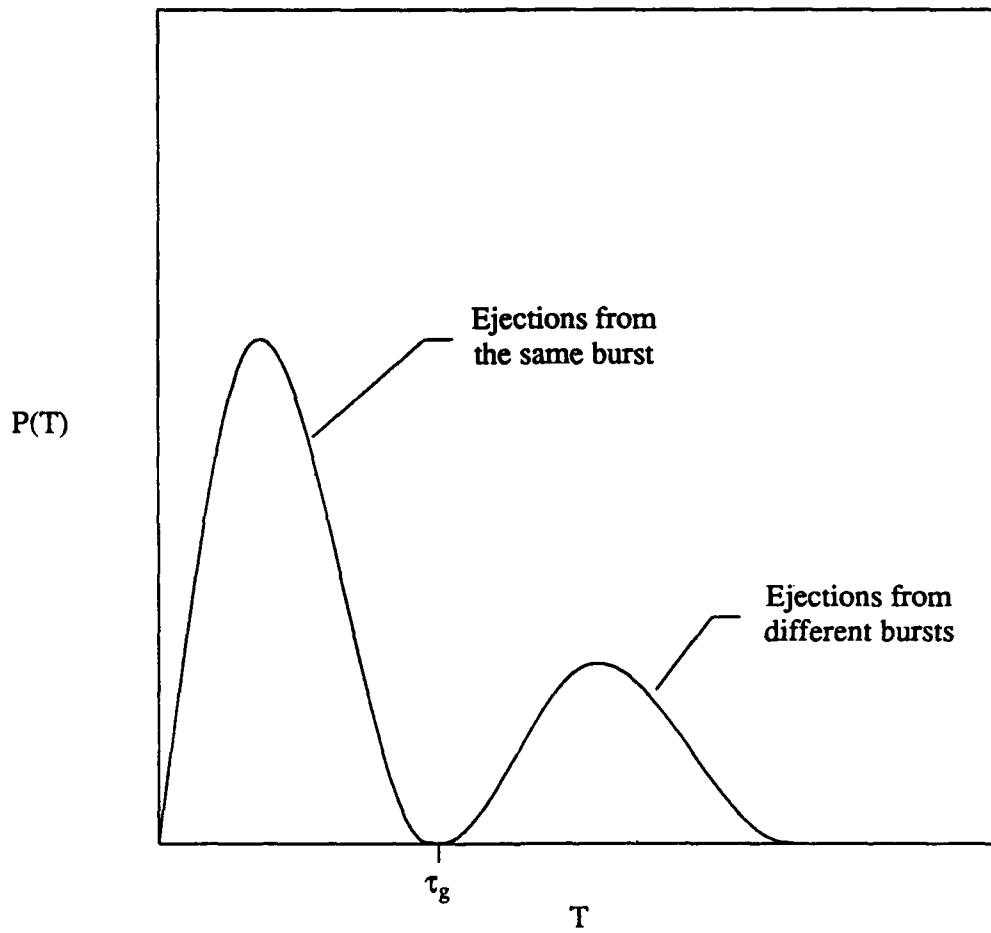


Figure 5.2 Schematic of idealized probability distribution of time between ejections. (after Luchik & Tiederman, 1987).

is assumed that the distribution of times between ejections within the same burst and the time between ejections in different bursts should both decrease exponentially. Therefore, this graph should yield two linear sections separated by a region where the distributions overlap. A typical application of this method is shown in figure 5.3 with the data at $y^+ = 20$ in the Newtonian zero pressure gradient boundary layer at $Re_\theta = 3527$. The detector was the second quadrant uv technique with a threshold of 0.4. A grouping time was chosen by looking at the breaks, τ_1 and τ_2 , in the curve. These breaks indicated the extent of the overlap region. Using the technique of White & Tiederman (1990), the grouping time was chosen as the average of the times indicated by τ_1 and τ_2 . The uncertainty in τ_g was half of the width between τ_1 to τ_2 . The propagation of this uncertainty is the major contributor to the uncertainty in the mean burst period \bar{T} .

Once this grouping technique has been combined with either detection technique, it is necessary to determine the appropriate value for the detector threshold, H or L. Fortunately, a range of thresholds exists over which the bursting period for grouped events is independent of threshold for the second quadrant uv technique (Bogard & Tiederman, 1986) and the modified u-level technique (Luchik & Tiederman, 1987). This independence from the choice of threshold is illustrated in figure 5.4 for the data used in figure 5.3.

5.1 Newtonian boundary layers

Burst records were acquired at two positions in the boundary layer, $y^+ = 15$ and $y^+ = 20$ based on u_τ and v in the Newtonian case at the chosen streamwise location.

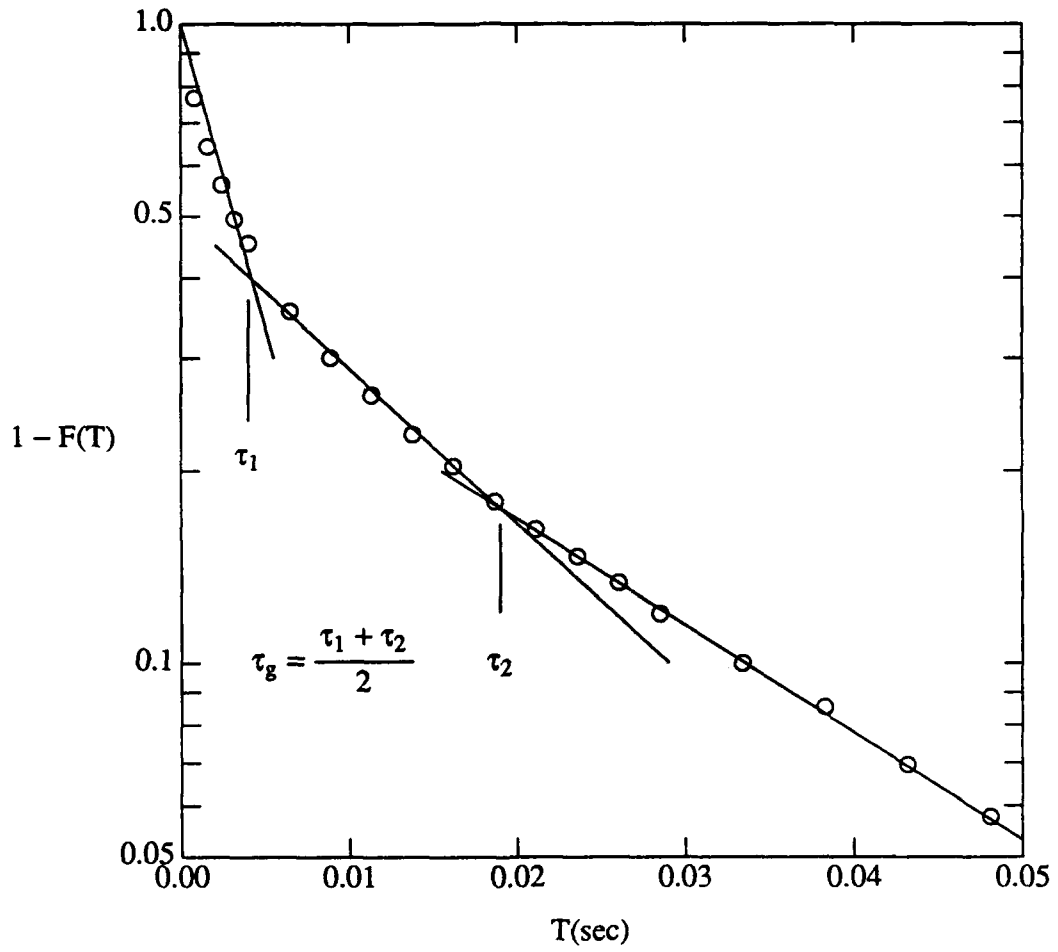


Figure 5.3 White & Tiederman method for determining grouping times.

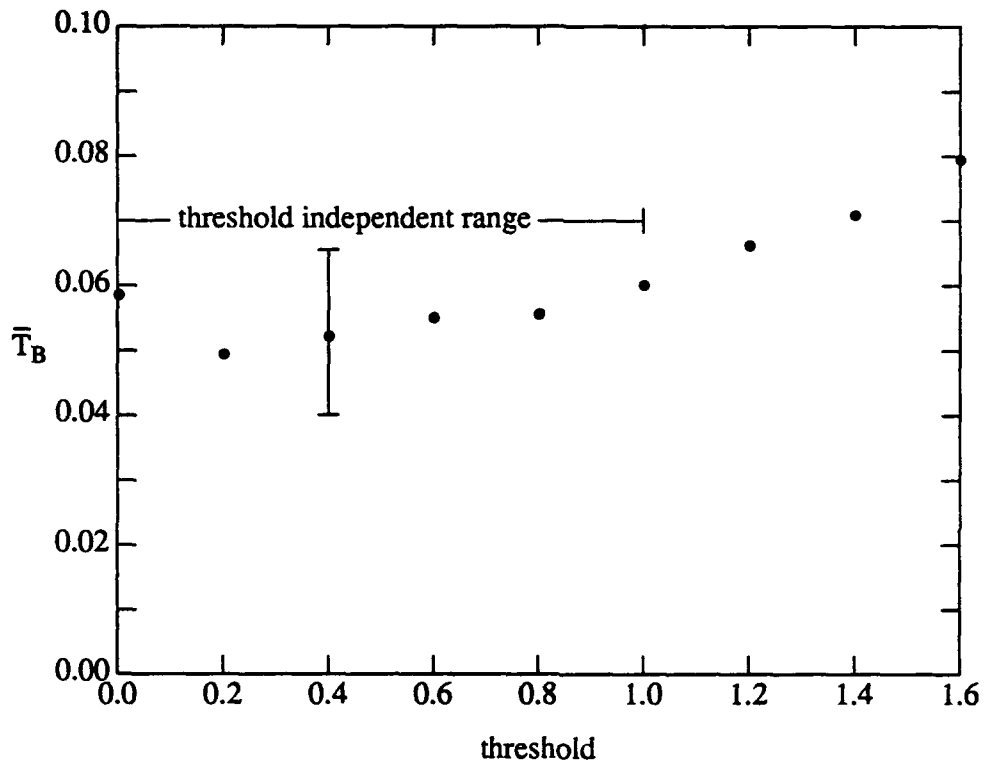


Figure 5.4 Computed average burst period as a function of threshold.

Data were acquired in the drag reduced boundary layers at the same physical locations. The present data are summarized in table 5.1 in inner normalized form. The drag reduced boundary layers will be discussed later. Bogard & Tiederman (1986) determined that the average burst period (not ejection period) remains relatively constant throughout the buffer region and well into the log region of a fully developed channel flow. Because the same trend is expected to occur in an equilibrium boundary layer the average burst periods determined for these two locations normal to the wall were compared as a consistency check of the data. As can be seen from the table, the value of $\bar{T}u_t^2/\nu$ determined by either method at $y^+ = 20$ is the same, within ten percent, as that determined by the same method at $y^+ = 15$. Furthermore, the differences between data sets is apparently random. It can also be seen that the results of the two measurement techniques are generally within 10 percent of each other for any given experiment. In the remainder of this chapter the results of the modified u-level technique applied at $y^+ = 20$ will be presented as representative.

Figure 5.5 compares the present zero pressure gradient boundary layer data with those of Shah & Antonia (1989), Antonia & Bisset (1990), Antonia, Bisset & Browne (1990), White & Tiederman (1990), and Barlow & Johnston (1988). The agreement between the present data, that of White & Tiederman and that of Barlow & Johnston is very good at any fixed Reynolds number. However, a strong Reynolds number dependence is apparent. All of the data of Antonia's group are higher than those of the other studies. At least some of Shah & Antonia's data, in particular the point at $Re_\theta = 2200$, are in error because they give significantly higher results than Antonia & Bisset for identical experiments. Antonia & Bisset attributed this error to problems in

Table 5.1 Summary of burst data.

$Re_{\theta} _N$	β	Q_i/Q_s	$y^+ = 15$		$y^+ = 20$	
			$\overline{Tu_t^2}/\nu$ uv ₂	$\overline{Tu_t^2}/\nu$ mulev	$\overline{Tu_t^2}/\nu$ uv ₂	$\overline{Tu_t^2}/\nu$ mulev
1358	0	0	65.6	71.4	66.4	72.5
3527	0	0	86.9	90.3	82.8	89.4
3527	0	2.6	120	117	117	124
3527	0	5.1	117	113	112	113
3566	1.8	0	75.3	69.7	70.6	63.9
3566	1.8	2.6	72.2	68.9	72.1	66.1
3566	1.8	5.1	79	70	79	68
4978	2.4	0	66.7	70.6	66.7	72.6
4978	2.4	2.6	-	70	-	75
4978	2.4	5.1	-	95	-	88

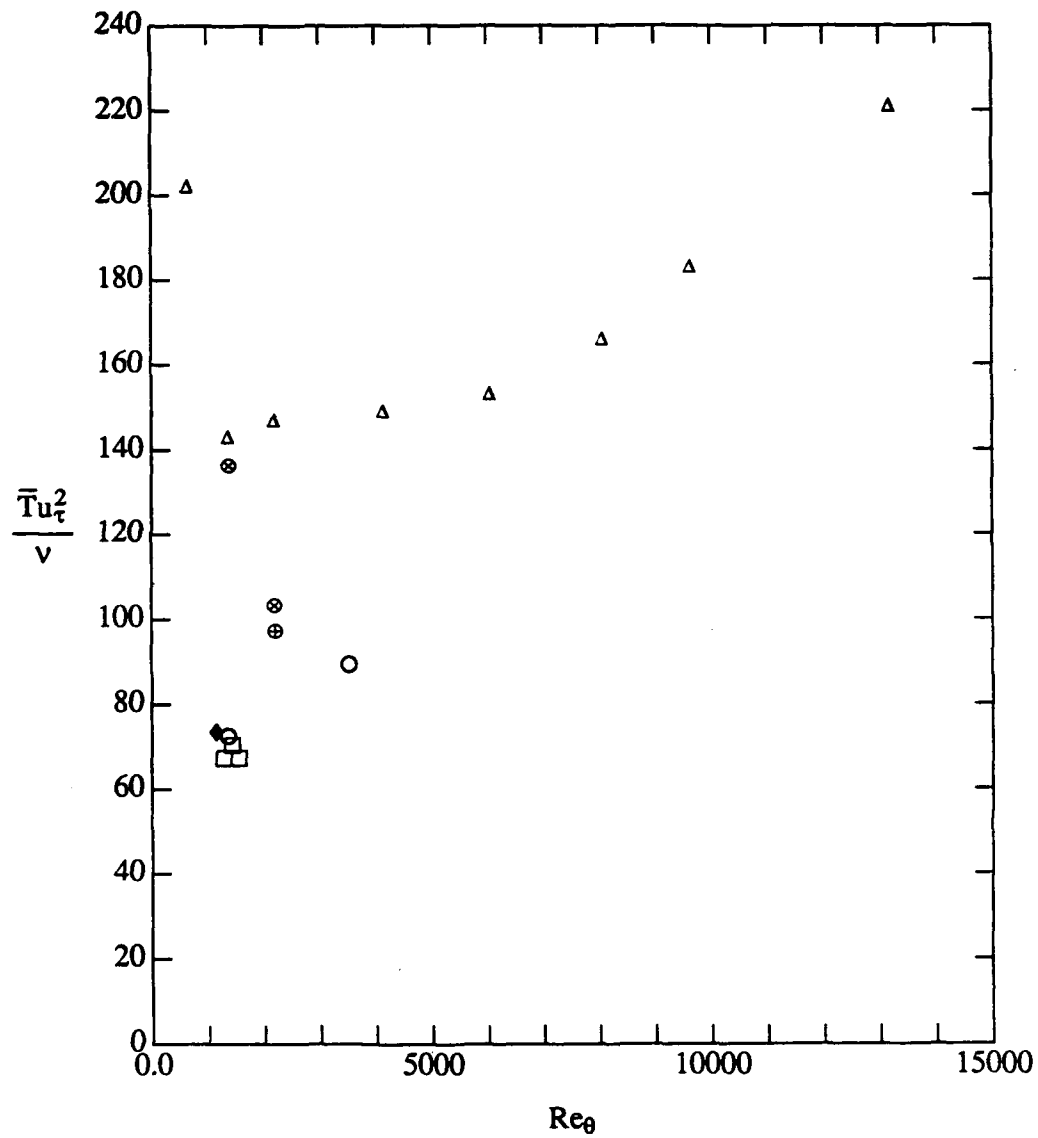


Figure 5.5 Inner normalized burst period for Newtonian zero pressure gradient boundary layers. ○ Koskie mulev; □ White & Tiederman mulev; △ Shah & Antonia mulev; ⊕ Antonia & Bisset mulev; ⊙ Antonia, Bisset & Browne mulev; ◆ Barlow & Johnston uv2.

determining the grouping time.

Figure 5.6 shows these zero pressure gradient data in inner, mixed and outer normalization. For simplicity, the results of Antonia & Bisset and Antonia, Bisset & Browne have been plotted with the same symbol because they represent the same boundary layer. Please note that Shah & Antonia's data have been omitted. Typical uncertainty bounds are shown on each plot. From these data alone, it is not clear which method of normalization is correct. However, when the adverse pressure gradient data from the present experiments and those of White & Tiederman are added in figure 5.7 some trends appear. Inner scaling appears unlikely, but should not be ruled out on this figure alone. Both mixed or outer scaling appear to collapse the present data and those of White & Tiederman to a single value for Reynolds numbers in excess of approximately 2000.

The three methods of normalizing the mean burst period were evaluated following Luchik and Tiederman's (1987) technique. This procedure begins by assuming values for each dimensionless bursting time. It was assumed that these values were constant for all Reynolds numbers and that deviations from this value are due to second order effects or are due to uncertainty. If all the data shown in figure 5.6 are considered, it is clear that this assumption cannot be valid for all the data. As will be discussed later, it was postulated that the actual differences between the constant value and the actual value were related to the method of tripping the boundary layer. Therefore, the present data and those of White & Tiederman were analyzed together because the two boundary layers were tripped using a tripping device with the same geometry in

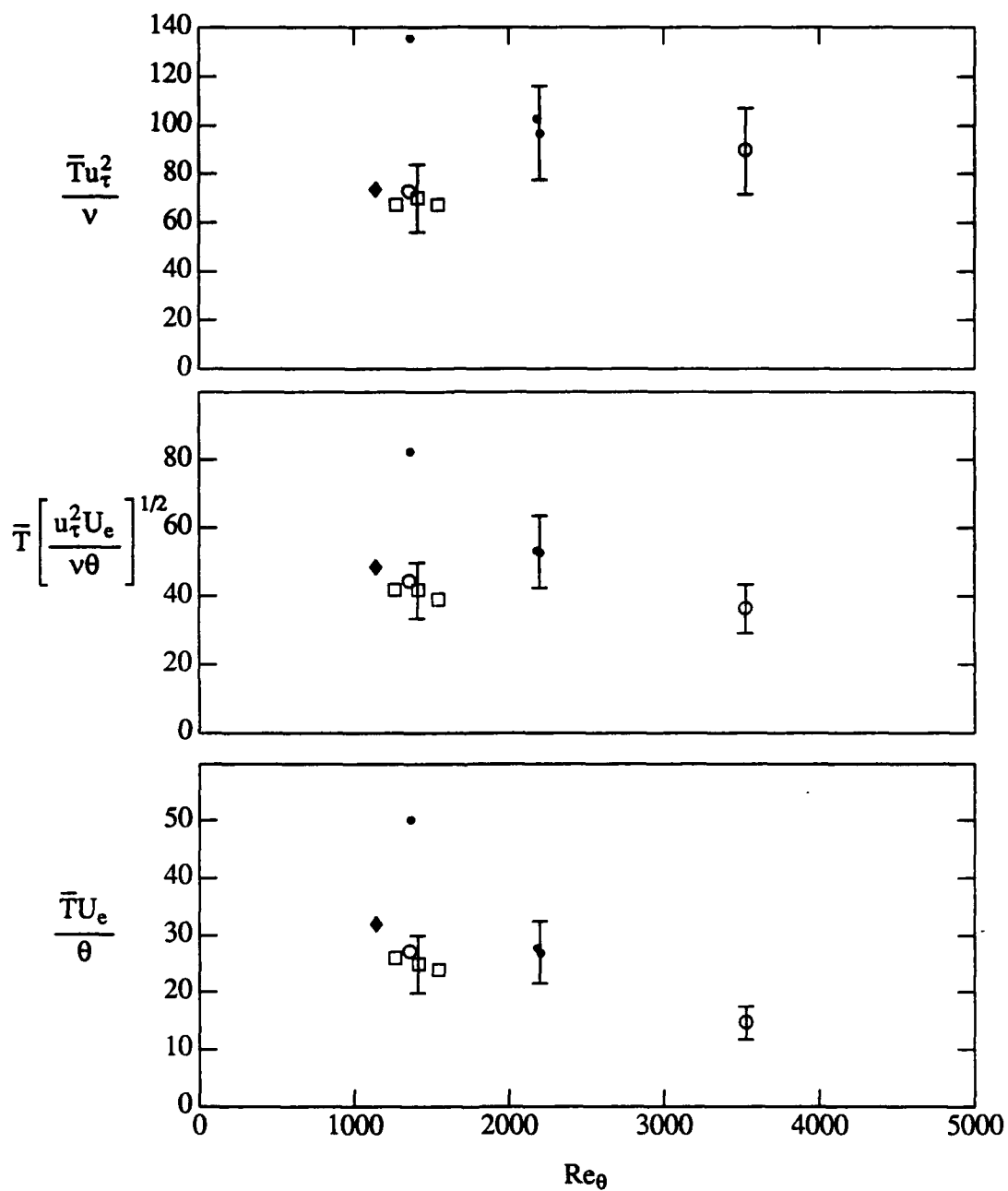


Figure 5.6 Burst period for Newtonian zero pressure gradient boundary layers normalized with inner, mixed and outer variables. \circ Koskie; \square White & Tiederman; \bullet Antonia & Bisset; \bullet Antonia, Bisset & Browne; \blacklozenge Barlow & Johnston.

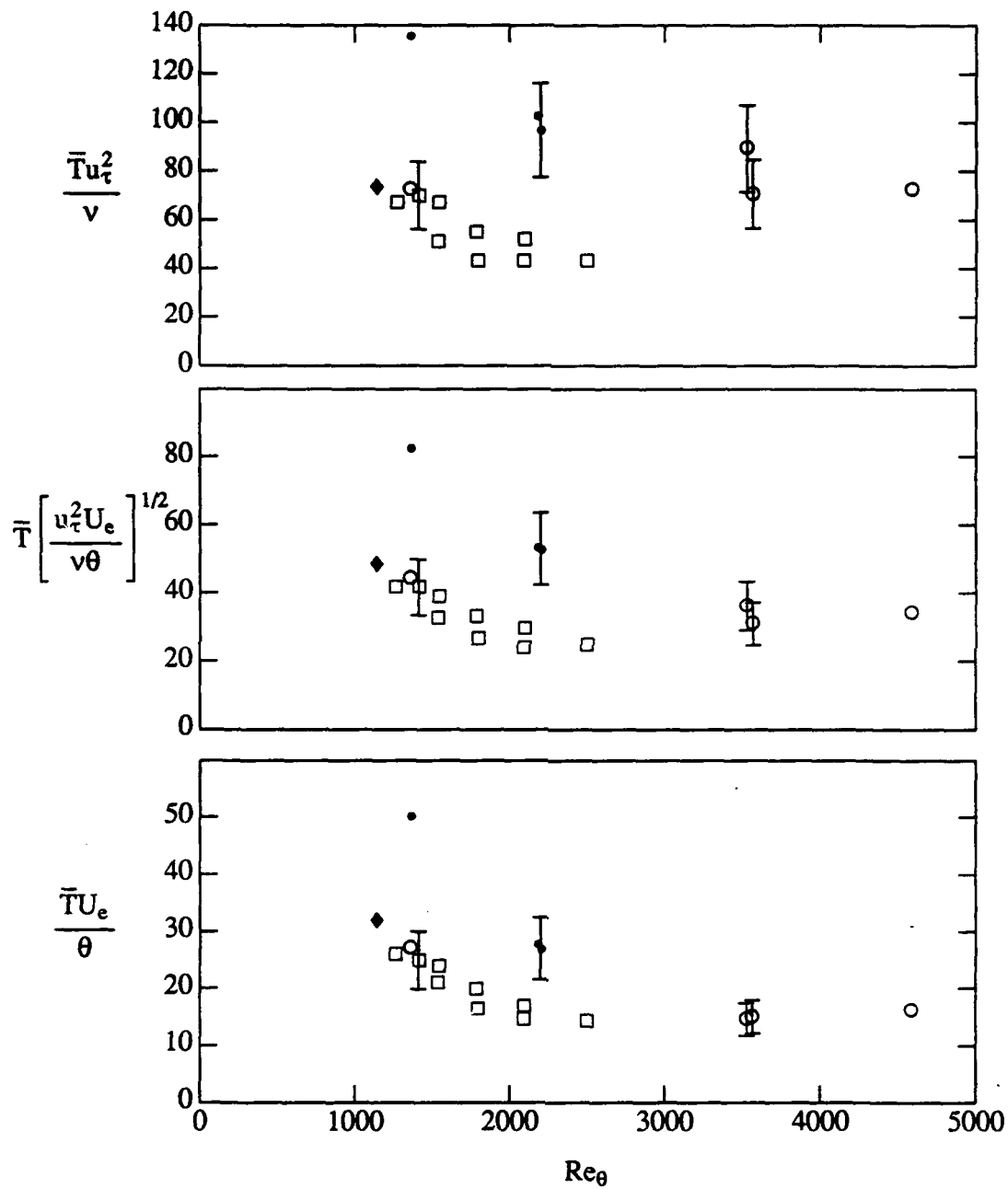


Figure 5.7 Burst period for Newtonian zero and adverse pressure gradient boundary layers normalized with inner, mixed and outer variables. \circ Koskie; \square White & Tiederman; \bullet Antonia & Bisset; \blacklozenge Antonia, Bisset & Browne.

dimensionless parameters. It was assumed that the influence of the trip was the same for these boundary layers and that it was a second order effect. The possible influence of the trip will be discussed later along with Antonia & Bisset and Antonia et al.'s data.

The assumed constant burst periods, only one of which can be valid, were:

$$\bar{T}u_{\tau}^2/\nu \cong 90 \quad (5.3)$$

$$\bar{T}(u_{\tau}^2 U_e/\nu\theta)^{1/2} \cong 35 \quad (5.4)$$

$$\bar{T}U_e/\theta \cong 15 \quad (5.5)$$

These were determined from the highest Reynolds number data in the zero pressure gradient boundary layer.

Given that one of these equations is valid, it is possible to derive relationships for the other dimensionless burst times as a function of Re_{θ} , u_{τ} and U_e . Luchik & Tiederman (1987) and Tiederman (1990) used an established correlation for the friction coefficient, c_f , in fully developed channel flows to write the burst time relationships as a function of Reynolds number alone. In boundary layers c_f becomes a function of not only Re_{θ} , but also of the shape factor, H . However in the special cases of zero pressure gradient and equilibrium boundary layers it is still possible to directly relate c_f to Re_{θ} . The shape factor is a unique function of Re_{θ} alone in zero pressure gradient boundary layers. Therefore, Coles (1962) was able to tabulate c_f as a function of Re_{θ} alone. The relationship between u_{τ} , U_e , and c_f becomes.

$$u_{\tau}^2 = 0.5U_e^2 c_f(Re_{\theta}) \quad (5.6)$$

Where $c_f(Re_{\theta})$ is Coles correlation.

It is first assumed that equation 5.3 (inner variables) is true. Equations 5.3 and 5.6 are substituted into the definitions for mixed and outer variables to obtain:

$$\bar{T}(u_{\tau}^2 U_e / \nu \theta)^{1/2} = 106 Re_{\theta}^{-1/2} [c_f(Re_{\theta})]^{-1/2} \quad (5.7)$$

$$\bar{T}U_e / \theta = 150 Re_{\theta}^{-1} [c_f(Re_{\theta})]^{-1} \quad (5.8)$$

The resulting curves are shown as solid lines in figure 5.8. The curves follow the trends of the data very well for both mixed and outer scaling, although they are outside the error bound of the lowest Reynolds number data. However, when the uncertainty in the constant value assumed in equation 5.3 is taken into account, these curves agree with the low Reynolds number data. Therefore, inner scaling appears possible in light of the present zero pressure gradient data.

Similarly, equation 5.4 (mixed scaling) is assumed to be valid and the following relationships are derived for inner and outer scaling:

$$\bar{T}u_{\tau}^2 / \nu = 24.7 Re_{\theta}^{1/2} [c_f(Re_{\theta})]^{1/2} \quad (5.9)$$

$$\bar{T}U_e / \theta = 49.5 Re_{\theta}^{-1/2} [c_f(Re_{\theta})]^{-1/2} \quad (5.10)$$

These curves are shown as dashed lines in figure 5.8. These curves also follow the trends of the data very reasonably. Therefore, mixed scaling appears possible in light of the present data.

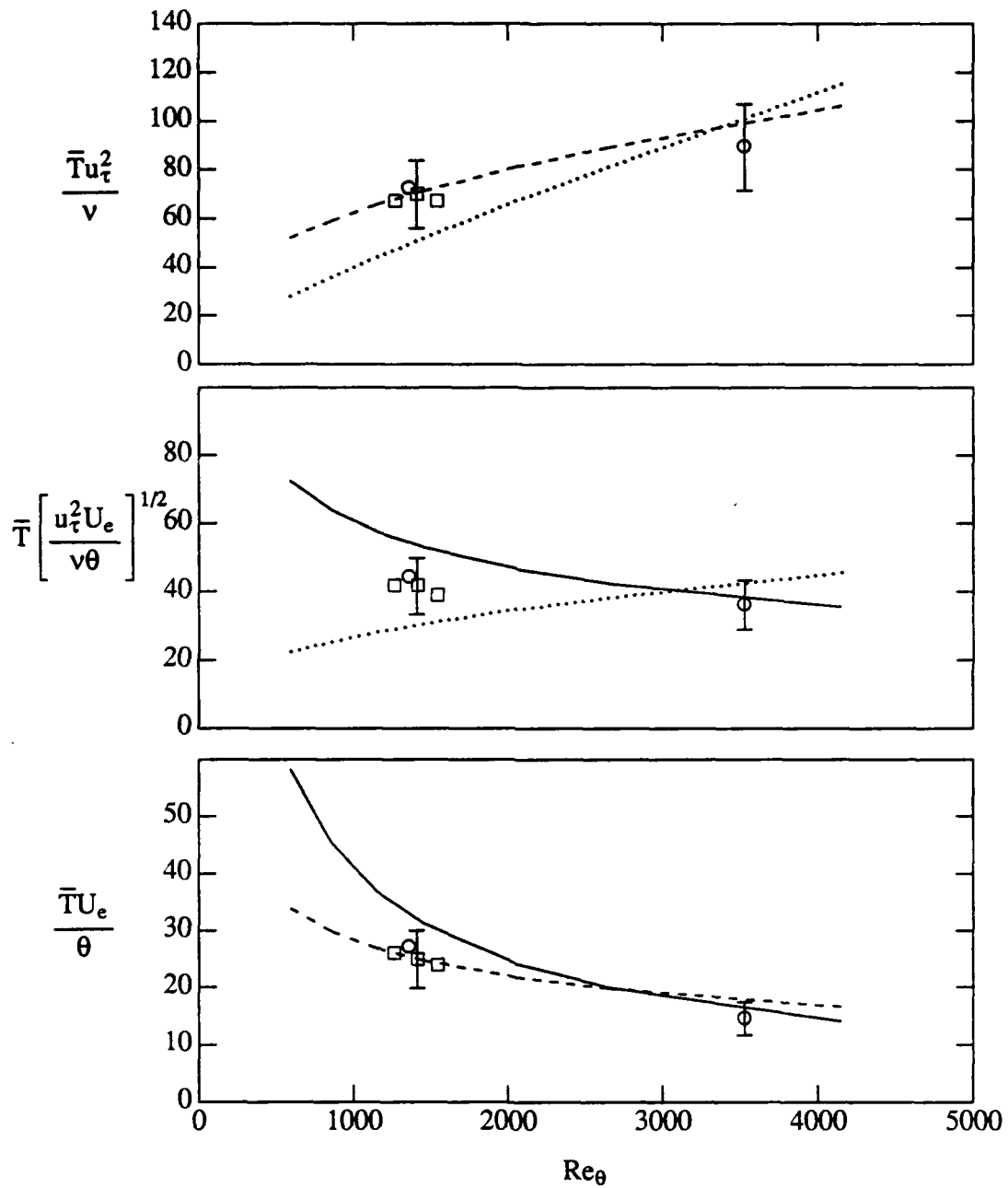


Figure 5.8 Burst period for Newtonian zero pressure gradient boundary layers normalized with inner, mixed and outer variables. \circ Koskie; \square White & Tiederman; — assumes inner scaling is valid; - - - assumes mixed scaling is valid; \cdots assumes outer scaling is valid.

Finally, equation 5.5 (outer scaling) is assumed to be valid with the result:

$$\bar{T}u_{\tau}^2/\nu = 7.5Re_{\theta}[c_f(Re_{\theta})] \quad (5.11)$$

$$\bar{T}(u_{\tau}^2 U_e/\nu\theta)^{1/2} = 10.6Re_{\theta}^{1/2}[c_f(Re_{\theta})]^{1/2} \quad (5.12)$$

These curves are shown as dotted lines in figure 5.8. The curve on the inner scaled section of the plot follows the data to some degree; however, the mixed scaling relationship incorrectly predicts an increasing trend in the data. Therefore outer scaling appears unlikely.

The same type of analysis was performed for the adverse pressure gradient data with $\beta = 1.8$. Equations 5.3 to 5.5 were again used except that the constant value assumed for inner scaling was changed from 90 to 75 so that $\bar{T}u_{\tau}^2/\nu \cong 75$. This new value was chosen because it appears to better fit the adverse pressure gradient data. The assumed values for mixed and outer scaling were not changed. It was also assumed that the pressure gradient has a second order effect on inner scaling. Therefore, no attempt was made to correlate the inner scaled burst period as a function of Reynolds number and pressure gradient. F. M. White's (1974) correlation (with Coles log-relationship coefficients) was used to relate c_f to H and Re_{θ} .

$$c_f = \frac{0.3e^{-1.33H}}{(\log_{10}Re_{\theta})^{1.74+0.31H}} \quad (5.13)$$

Because these boundary layers were in equilibrium, the shape factor can be related to c_f through the equation 5.14 (Clauser, 1954):

$$H = [1 - G(c_f/2)^{1/2}]^{-1} \quad (5.14)$$

Where G is the Clauser shape parameter which is a constant for equilibrium boundary layers. Equation 5.14 was substituted into equation 5.13 and the resulting implicit relationship for $c_f = f(Re_\theta)$ was solved numerically for several values of Re_θ . Equations 5.7 to 5.12 were then evaluated using this relationship for $c_f(Re_\theta)$. The results are shown in figure 5.9. Both mixed and outer scaling appear plausible on these plots; however, inner scaling predicts a trend which is not supported by the mixed scaled data. Therefore, either mixed or outer scaling is valid for these adverse pressure gradient data.

When these two results are combined, the only method of normalization which appears to be valid for both adverse and zero pressure gradient boundary layers is mixed scaling. This conclusion is consistent with Shah & Antonia's conclusion that mixed scaling is appropriate for zero pressure gradient boundary layers with Reynolds numbers in excess of 5000. However, their conclusion that inner scaling is valid for Reynolds numbers less than 5000 is limited to zero pressure gradient boundary layers. Because of the low Reynolds number range of the present study the conclusion that the mixed scaling normalized the average burst period may not apply to higher Reynolds numbers. Therefore, boundary layer experiments with Reynolds numbers well in excess of 5000 will be necessary to determine whether this conclusion is universal. During these experiments, the normalizing parameters for the average burst period (u_τ^2/ν and U_e/θ), should be varied significantly. Clearly, U_e/θ can be changed easily by simply increasing the Reynolds number or by changing the freestream velocity. However, because the variation of c_f with momentum thickness in a zero pressure gradient boundary layer becomes very small above $Re_\theta \cong 5000$, (see Coles, 1962) the

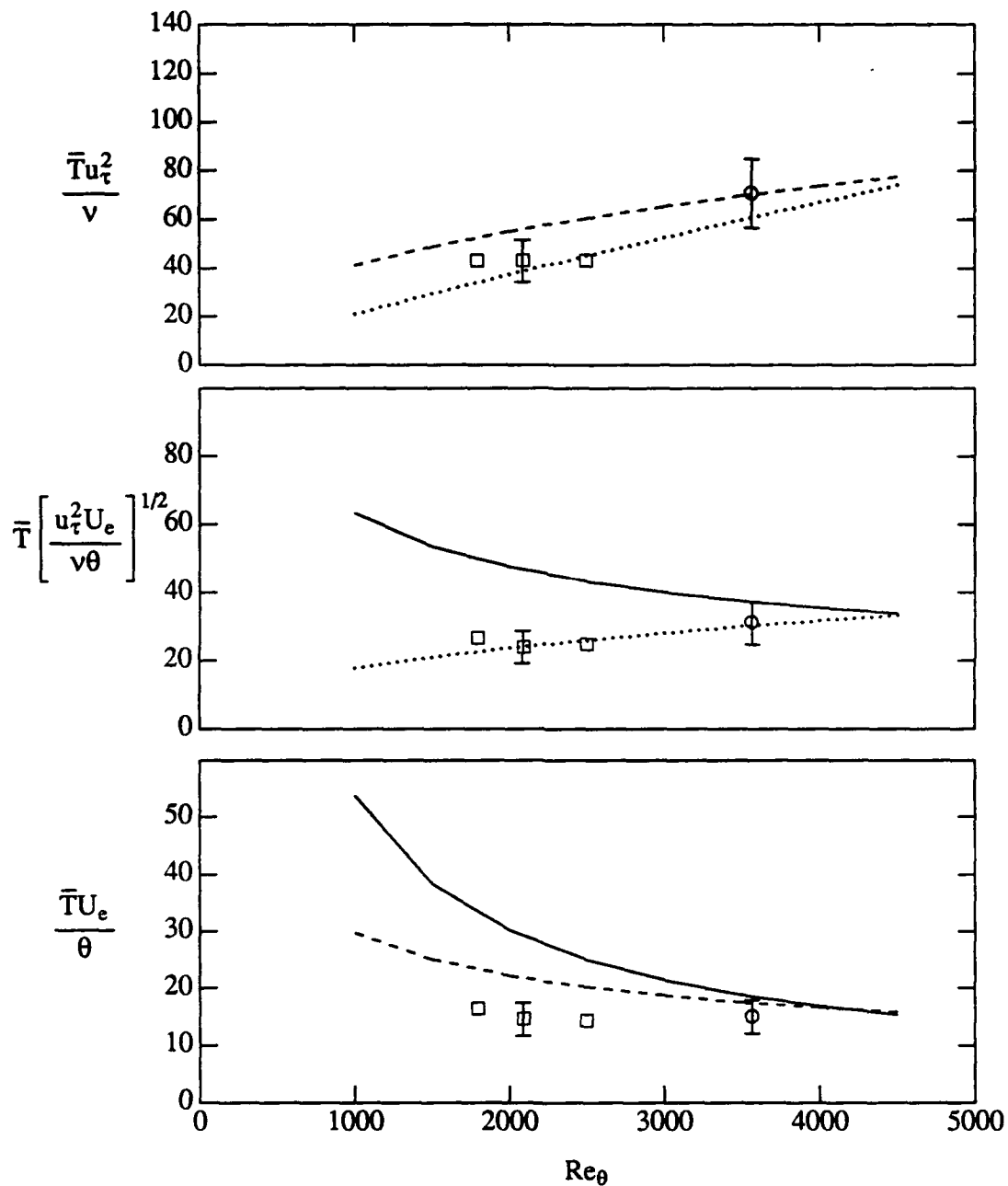


Figure 5.9 Burst period for Newtonian adverse pressure gradient boundary layers normalized with inner mixed and outer variables. \circ Koskie; \square White & Tiederman; — assumes inner scaling is valid; - - - assumes mixed scaling is valid; \cdots assumes outer scaling is valid.

value u_{τ}^2/ν will not change significantly at high Reynolds numbers unless U_e and/or ν are also varied. Therefore if future experiments are performed in a water tunnel, the freestream velocity should be increased significantly. Conducting these experiments in air rather than water may be easier because the change in viscosity alone would change u_{τ}^2/ν by an order of magnitude.

The present conclusion is different from Tiederman's (1990) conclusion that inner scaling is appropriate for fully developed channel flows. These conclusions are not necessarily contradictory. The entire velocity profile and velocity fluctuation statistics in a fully developed channel flow can be fully described by specifying one variable, the friction velocity or the Reynolds number. Therefore, specifying the friction velocity fixes all the mean velocity characteristics of the flow including the outer region. It is therefore reasonable that the friction velocity is sufficient to non-dimensionalize the burst period. However, in any boundary layer, specification of the friction velocity alone is not sufficient to fully characterize the flow. The boundary layer also responds to the freestream velocity conditions. Since the interaction of these two regions is fundamental to boundary layers it is logical to expect that events which produce the majority of Reynolds stress are influenced by the outer flow as well as the inner flow. Therefore, it is reasonable that mixed scaling is appropriate for boundary layers.

While the assumption of a constant value for the mixed scaled burst period provided a first approximation for the present data and that of White & Tiederman, the data of Antonia's group clearly points to other influences on the burst period. It was postulated that this other factor involved the method of tripping the boundary layer. The present

boundary layers and those of White & Tiederman used rods for trips which had the same dimensionless size according to Gibbing's (1959) criterion for all experiments. However, Antonia's group used a single physical trip for all their experiments which presumably changed in dimensionless form for different freestream velocities. Furthermore, their trip consisted of a rod followed by sandpaper, so it is unclear how to directly compare the trip to the present trip. Barlow & Johnston used a square rod as a trip.

It was shown by Coles (1962) that the wake parameter in a zero pressure gradient boundary layer is primarily a function of the boundary layer trip and the momentum thickness Reynolds number in a zero pressure gradient boundary layer. Therefore, the Coles wake parameter, Π , will be used to test the hypothesis that the trip influences the burst rate at low Reynolds numbers. Because the variation of the wake parameter as a function of pressure gradient would mask changes in Π which are related to the trip, the adverse pressure gradient data were not used in this analysis. Figure 5.10 shows the variation of the mixed normalized burst period as a function of the wake parameter for the zero pressure gradient data shown in figure 5.6. The values of Π for the Antonia group data comes from tabulated values. White & Tiederman's data was processed in the same manner as the present data to find Π (see chapter 3). A straight line fit to the data using mixed scaling and the high Reynolds number value of Π has the form:

$$\bar{T}(u_{\tau}^2 U_e / \nu \theta)^{1/2} = 35A(\Pi - 0.62) + 35 \quad (5.15)$$

Here A is the parameter determined by least squares fit. The value 0.62 is the constant value of Π determined by Coles (1967) for high Reynolds numbers. The final equation

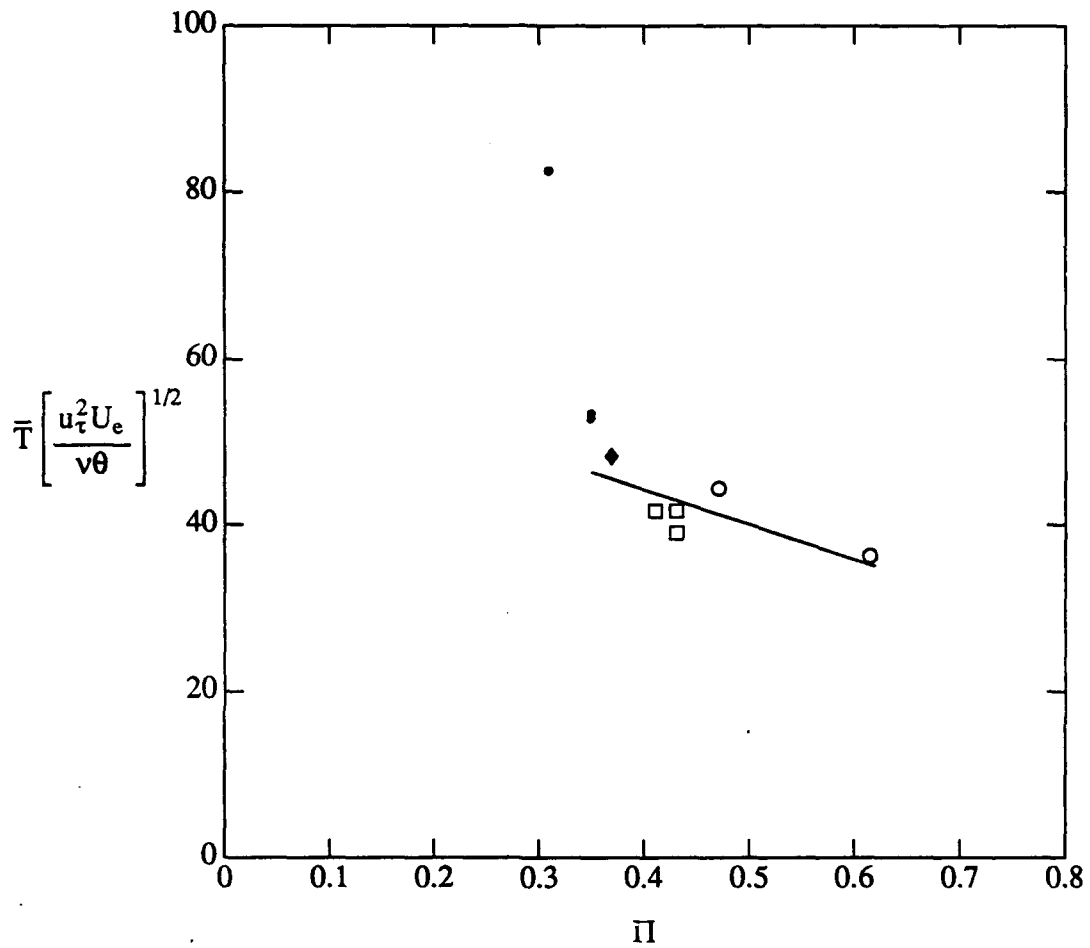


Figure 5.10 Normalized burst period for Newtonian zero pressure gradient boundary layers as a function of the Coles wake parameter, Π . ○ Koskie; □ White & Tiederman; ● Antonia & Bisset, Antonia, Bisset & Browne; ◆ Barlow & Johnston. — $\bar{T} \left(\frac{u_\tau^2 U_e}{\nu \theta} \right)^{1/2} = 42.4(\Pi - 0.62) + 35$.

with $A = 42.4$ is given on the plot. This line fit was then transformed into an equation for a new dimensionless burst period which compensated for the wake parameter:

$$\bar{T}_{\text{mod}} = \bar{T}(u_r^2 U_e / \nu \theta)^{1/2} + 42.4(\Pi - 0.62) \quad (5.16)$$

The resulting revised burst period is plotted in figure 5.11 as a function of Re_θ and shows that all the data except the lowest Reynolds number data of Antonia et al. are collapsed to a single value within the uncertainty bounds by this method. The remaining differences between the present data and those of Antonia's group are still consistent with the hypothesis. Antonia's data have wake parameter values which are slightly lower than Coles (1962) values indicating that their boundary layer was slightly understimulated. Shah & Antonia's data, which have similarly low wake parameters also have higher average burst periods. Whereas the present data and those of White & Tiederman which all have slightly high values of Π , suggesting slight overstimulation, have low turbulent burst periods.

5.2 Drag reduced boundary layers

The addition of drag reducing polymer to the boundary layer complicates the flow. None of the three methods of normalizing the data were able to collapse the drag reduced data to the water data. The burst period always increases. However, in fully developed channel flows of homogeneous low concentration (less than 2 wppm) polymer solutions the number of bursts simply decreases and the apparent relationship between streaks and grouped ejections remains the same. Therefore, the ratio of the average burst period in a polymer flow to that in a corresponding Newtonian flow is directly proportional to the dimensionless streak spacing. Oldaker & Tiederman

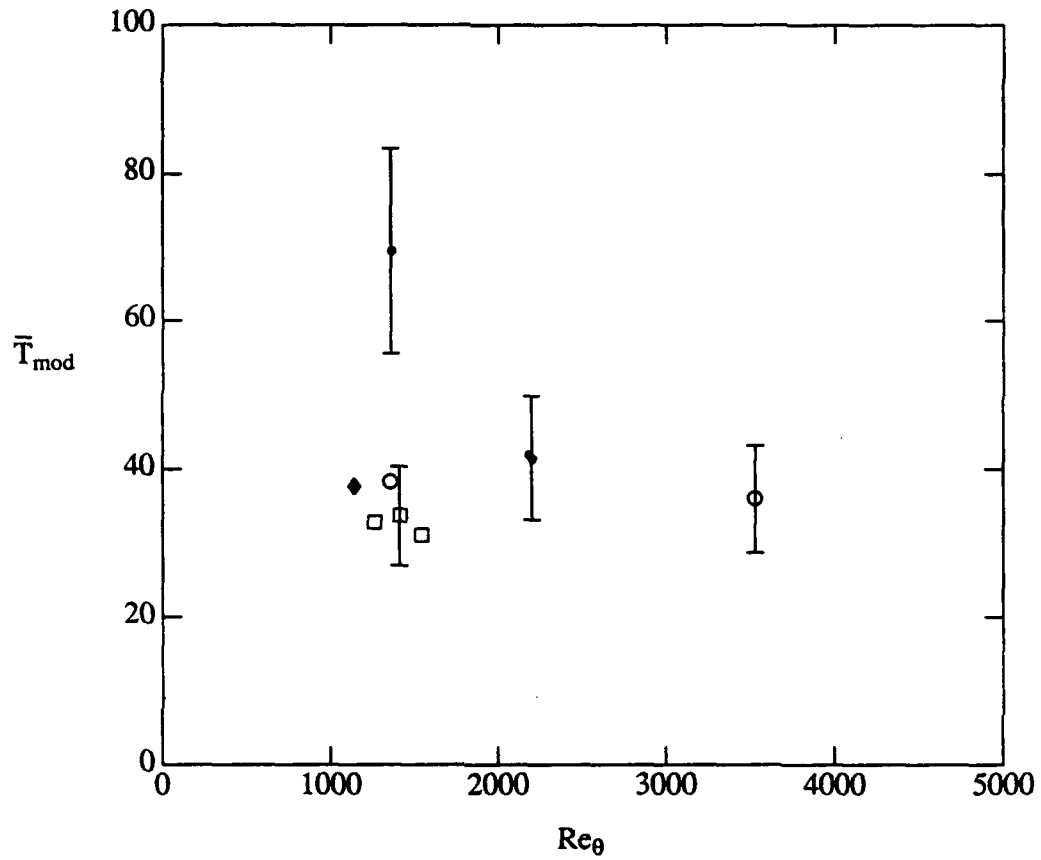


Figure 5.11 Burst period for Newtonian zero pressure gradient boundary layers using modified mixed normalization. \circ Koskie; \square White & Tiederman; \bullet Antonia & Bisset; \bullet Antonia, Bisset & Browne; \blacklozenge Barlow & Johnston.

showed that in fully developed channel flows of homogeneous polymer solutions this spacing varies linearly with drag reduction:

$$\lambda^+ = 99.7 + 1.9\%DR \quad (5.16)$$

Hence, the burst period can be related to drag reduction. However, Tiederman et al. (1985) and McComb & Rabie (1982) found that when significant polymer concentration gradients occurred normal to the wall the number of bursts per streak decreased during drag reduction.

It was hypothesized that the streak spacing in the present boundary layers varied with drag reduction according to Oldaker & Tiederman's relationship and that this relationship could predict the change in the turbulent burst period. The present data were examined to determine whether they support this hypothesis. The intercept (99.7) of equation 5.16 should be valid in boundary layers because the Newtonian value for the streak spacing is the same for channel flows and boundary layers and is independent of pressure gradient (Kline et al., 1967). Because the burst measurements were performed far from the injector slot, it was hoped that concentration gradients would be small enough that all of equation 5.16 would be valid. Figure 5.12 shows the variation of the burst period of the polymer flows normalized by the burst period in the Newtonian flow at the same location. The adverse pressure gradient data follow the same trend as the variation of streak spacing as determined by equation 5.16.

Although the uncertainty bound for the zero pressure gradient data crosses the line representing the hypothesized streak spacing, it is clear that this method of predicting the average burst period would yield poor results. However, this prediction does

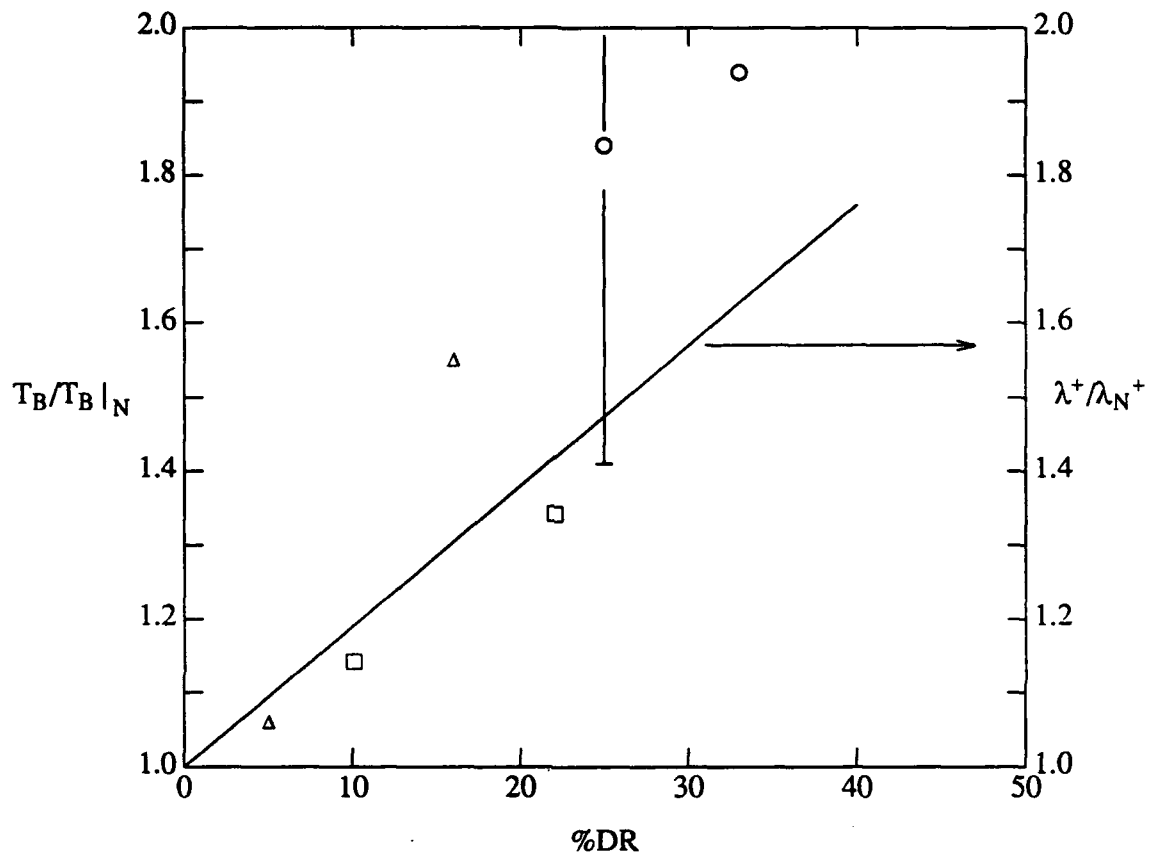


Figure 5.12 Ratio of the average burst period in a drag reduced boundary layer to that in the corresponding Newtonian boundary layer compared to the variation of inner normalized streak spacing in a fully developed channel flow of homogeneous polymer solutions. ○ $\beta = 0$; □ $\beta = 1.8$; Δ $\beta = 2.4$; — Oldaker & Tiederman $\lambda^+ = 99.7 + 1.9DR$.

provide a lower bound for the increase in the burst period. This problem for the zero pressure gradient case probably means that the polymer concentration gradient normal to the wall is too large for equation 5.16 to be valid. In conclusion, data from well mixed, fully developed channel flows provides a lower bound for the burst rate in boundary layers when drag reducing polymers are present.

CHAPTER 6: SUMMARY, CONCLUSIONS, AND RECOMMENDATIONS

This study examined one zero pressure gradient Newtonian boundary layer and two adverse pressure gradient equilibrium boundary layers. The momentum thickness Reynolds, Re_θ , numbers studied were in the range 1360 to 4980. The adverse pressure gradient boundary layers were characterized by equilibrium parameters, β , of 1.8 and 2.4. These boundary layers were modified by injecting a drag reducing polymer solution at 2.6 and 5.1 times the flow rate of the linear sublayer (assuming an extent of $y^+ = 5$). Profiles of the streamwise and normal velocity statistics with and without drag reduction were measured. In addition, the turbulent busting rate was measured in these boundary layers. The results of the Newtonian adverse pressure gradient boundary layers verified that there is no Reynolds number effect on the inner region velocity statistics in the range $3500 \leq Re_\theta \leq 25\ 000$.

At several locations in the drag reduced zero pressure gradient boundary layer, the sum of the viscous and Reynolds shear stresses was less than the total shear stress in the boundary layer, indicating the presence of a non-Newtonian shear stress. The mean streamwise velocity measurements in the zero pressure gradient, drag reduced boundary layers showed that both parameters, κ and B , of the logarithmic velocity profile changed during drag reduction. The slope parameter, κ , varied linearly with the percent drag reduction. Therefore, methods of determining wall shear stress which assume a constant slope of the logarithmic velocity profile cannot be used in polyacrylamide drag

reduced boundary layers. The measurements of the streamwise and normal velocity fluctuation statistics in the drag reduced boundary layers revealed that the magnitude of the peak in the root-mean-square streamwise velocity fluctuation remains essentially unchanged in the presence of polymer but its location moves away from the wall. The root-mean-square normal velocity fluctuations and the Reynolds shear stress were reduced in the inner region of the boundary layer during drag reduction. When non-Newtonian stresses were significant the Reynolds shear stress correlation coefficient was reduced and the production of Reynolds shear and normal stresses was virtually eliminated.

The adverse pressure gradient boundary layers did not separate during drag reduction even when large amounts of polymer were injected. The influence of the polymer on the turbulent boundary layer structure was greatly reduced, but the effects of polymer were consistent with those in the zero pressure gradient boundary layer. The logarithmic velocity profile parameters, κ and B , changed in a manner consistent with the change in drag reduced fully developed channel flows. The velocity fluctuation statistics also varied in essentially the same manner as the zero pressure gradient boundary layer, but the magnitude of these changes was greatly reduced as was the percent drag reduction.

The hypothesis that the extensional motions in the flow must be strong enough to stretch the polymer molecules so that stretched molecules will form an anisotropic viscosity that damps the small scales of the turbulence (Hinch, 1977) was supported by the present data. In the zero pressure gradient boundary layer the large extensional

motions in the flow persisted during drag reduction while the small scale motions were damped. This hypothesis also explains the behavior of the adverse pressure gradient boundary layers. It is postulated that the extensional motions in the adverse pressure gradient boundary layers were too small to significantly extend the polymer molecules. Therefore, the polymer molecules which were extended in the upstream section of the boundary layer relaxed and were unable to significantly modify these boundary layers. Comparison of the probability distribution functions of u and v in the moderate adverse pressure gradient boundary layer to those in the zero pressure gradient flow showed that the magnitude of the extensional motions in the adverse pressure gradient boundary layers were in fact smaller than those in the zero pressure gradient boundary layer. In addition, the drag reduction and velocity statistics indicated that the effectiveness of the polymer was greatly reduced in the adverse pressure gradient boundary layers. Both observations support the basic hypothesis.

Walker's (1985) modified mixing length model correctly predicted the wall shear stress coefficient, c_f , in all the drag reduced boundary layers as long as the measured polymer concentration in the linear sublayer was within the range of concentrations for which the model was derived and as long as non-Newtonian stresses were small. There are some combinations of non-Newtonian stresses and polymer concentration above which the model is no longer adequate. However, it is not clear how to quantify the maximum non-Newtonian stresses for which this model will work. This success demonstrates that turbulence models which are modified to account for polymer drag reduction using fully developed channel data can correctly predict wall shear stress in boundary layers within the above limitations.

Mixed scaling of the average time between bursts provides the best collapse for the present zero and adverse pressure gradient Newtonian boundary layer data. However, this scaling may not apply to higher Reynolds numbers than those investigated in the present study. Boundary layer experiments with Reynolds numbers in excess of 5000 will be necessary to determine whether this conclusion is universal. In order to change significantly the normalizing parameters for the average burst period (u_{τ}^2/ν and U_e/θ), it will be necessary to conduct these experiments at higher freestream velocities. It would be desirable to use another fluid, such as air, to change the viscosity in future experiments. At low Reynolds numbers below 2000, a second effect causes some variation in the data. The data were consistent with the hypothesis that this second effect is related to the boundary layer trip.

The increase in the average burst period in the drag reduced boundary layers could be predicted using data from fully developed channel flows of homogeneous polymer solutions only when the polymer concentration gradient normal to the wall was very small. In the present zero pressure gradient boundary layer in which the concentration gradients are significant this method only provides a lower bound for the average burst period.

REFERENCES

- ALFREDSSON, P.H. & JOHANSSON, A.V. 1984 Time scales for turbulent channel flows. *Phys. Fluids*, *27*, 1974-1981.
- ANTONIA, R.A. & BISSET, D.K. 1990 Spanwise structure in the near-wall region of a turbulent boundary layer. *J. Fluid Mech.*, *210*, 437-458.
- ANTONIA, R.A., BISSET, D.K. & BROWNE, L.W.B. 1990 Effect of Reynolds on the topology of the organized motion in a turbulent boundary layer. *J. Fluid Mech.*, *213*, 267-286.
- BALDWIN, B.S. & LOMAX, H. 1978 Thin layer approximation and algebraic model for separated turbulent flows. AIAA paper 78-257.
- BALINT, J.-L., WALLACE, J.M. & VUKOSLAVCEVIC, P. 1991 The velocity and vorticity vector fields of a turbulent boundary layer. part 2. Statistical properties. *J. Fluid Mech.*, *228*, 53-86.
- BARLOW, R.S. & JOHNSTON, J.P. 1985 Structure of turbulent boundary layers on a concave surface. Stanford University report MD-47.
- BARLOW, R.S. & JOHNSTON, J.P. 1988 Local effects of large-scale eddies on bursting in a concave boundary layer. *J. Fluid Mech.*, *191*, 177-195.
- BERMAN, N.S. 1978 Drag reduction by polymers. in: *Annual Review of Fluid Mechanics*, vol. 10, Van Dyke et al. eds., Annual Reviews Inc., Palo Alto, CA., 47-64.
- BEWERSDORFF, H.W. 1984 Heterogene widerstandsverminderung bei turbulenten rohrströmungen. *Rheologica Acta*, *23*, 522-543.
- BEWERSDORFF, H.W. & BERMAN, N.S. 1988 The influence of flow-induced non-Newtonian fluid properties on turbulent drag reduction. *Rheologica Acta*, *27*, 130-136.
- BOGARD, D.G. & TIEDERMAN, W.G. 1986 Burst detection with single-point velocity measurements. *J. Fluid Mech.*, *162*, 389-413.
- BRADSHAW, P. 1967 The turbulence structure of equilibrium boundary layers. *J. Fluid Mech.*, *29*, 625-645.
- BRADSHAW, P. 1969 The response of a constant-pressure turbulent boundary layer to the sudden application of an adverse pressure gradient. *Great Britain ARC*, RM-3575.
- CEBECI, T. & BRADSHAW, P. 1977 *Momentum Transfer in Boundary Layers*. Hemisphere, New York, NY., 245-271.

- CLAUSER, F.H. 1954 Turbulent boundary layers in adverse pressure gradients. *J. Aeronautical Sci.*, 21, 91-108.
- COLES, D.E. 1962 *The turbulent boundary layer in a compressible fluid*. Rand report R-403-PR.
- COLES, D.E. 1968 The Young Peoples Guide to the Data. In: *Proceedings Computation of Turbulent Boundary Layers, vol. II*, D.E. Coles and E.A. Hirst, eds., Stanford Univ., Stanford, CA., 1-19.
- CORINO, E.R. & BRODKEY, R.S. 1969 A visual investigation of the wall region in turbulent flow. *J. Fluid Mech.*, 37, 1-30.
- CRAWFORD, M.M. & KAYS, W.M. 1975 STAN5 - A program for numerical computational of two-dimensional internal/external boundary layer flows. Report HMT-23, Department of Mechanical Engineering, Stanford University, Stanford, CA.
- EAST, L.F. & SAWYER, W.G. 1979 An investigation of the structure of equilibrium turbulent boundary layers. *AGARD-CP-271*.
- EFRON, B. 1982 *The jackknife, the bootstrap and other resampling techniques*. Society for Industrial and Applied Mathematics, Philadelphia.
- EL REIDY, O.K. & LATTO, B. 1984 Energy spectra and turbulence intensity polymer injection flows. In: *Drag Reduction*, R.J.H Sellin and R.T.Moses, eds., Univ. of Bristol, Bristol, B.5.
- ERM, L.P.; SMITS, A.J. & JOUBERT, P.N. 1985 Low Reynolds number turbulent boundary layers on a smooth flat surface in a zero pressure gradient. *Proceedings 5th International Symposium Turbulent Shear Flows*, Cornell, Cornell NY.
- FONTAINE, A.A.; PETRIE, H.L. & BRUNGART, T.A. 1990 Turbulent boundary layer velocity profile statistics with slot injected drag reducing polymers. Pennsylvania State University. Report 90-279.
- FRUMAN, D.H. & TULIN, M.P. 1976 Diffusion of a tangential drag-reducing polymer injection on a flat plate at high Reynolds numbers. *J. Ship Research*, 20, 171-180.
- GIBBINGS, J.C. 1959 On boundary-layer transition wires. ARC technical report CP-462.
- GRANVILLE, P. S. 1977 in: *Drag Reduction, Papers presented at the Second International Conference on Drag Reduction* paper B1, BHRA, Cranfield. U.K..
- GRANVILLE, P. S. 1987 Baldwin-Lomax factors for turbulent boundary layers in pressure gradients. *AIAA J.*, 25, 1624-1627.
- GRANVILLE, P. S. 1989 A modified Van Driest formula for the mixing length of turbulent boundary layers in pressure gradients. *J. Fluids Eng.*, 111, 94-97.

- GYR, A. 1984 Direct evidence that drag reduction is an effect of the elongation of polymer molecules. *Drag reduction in fluid flows*, R.J.H. Sellin and R.T. Moses eds., Univ. Bristol, paper B10.
- HARDER, K. J. and TIEDERMAN, W. G. 1991 Drag reduction and turbulent structure in two-dimensional channel flows. *Phil. Trans. R. Soc. London. A*, 336 19-34.
- HINCH, E.J. 1977 Mechanical models of dilute polymer solutions in strong flows. *Phys. Fluids*, 20, S22-S30.
- HINZE, J.O. 1975 *Turbulence* second edition, McGraw Hill, New York, 223,327,399.
- HOYT, J.W. 1991 "Negative roughness" and polymer drag reduction. *Exp. Fluids*, 11, 142-146.
- JOHNSON P.L. & BARLOW, R.S. 1989 Effect of measuring volume length on two-component laser velocimeter measurements in a turbulent boundary layer. *Exp. Fluids*, 8, 137-144.
- KIM, H.T., KLINE, S.J.. & REYNOLDS, W.C. 1971 The production of turbulence near a smooth wall in a turbulent boundary layer. *J. Fluid Mech.*, 50, 133-160.
- KLEBANOFF, P.S. & DIEHL, Z.W. 1952 Some features of artificially thickened fully developed turbulent boundary layers with zero pressure gradient. NACA technical note TN 1110.
- KLEWICKI, J.C. & FALCO, R.E. 1990 On accurately measuring statistics associated with small-scale structure in turbulent boundary layers using hot-wire probes. *J. Fluid Mech.*, 219, 119-142.
- KLINE, S.J., REYNOLDS, S.J., SCHRAUB, F.A. & RUNSTADLER, P.W. 1967 The structure of turbulent boundary layers. *J. Fluid Mech.*, 30, 741-773.
- KOWALSKI, T. 1971 Effect of polymer additives on propeller performance. *J. Hydronautics*, 5, 11-14.
- KUMOR, S.M. & SYLVESTER N.D. 1973 Effects of a drag-reducing polymer on the turbulent boundary layer. *AIChE Symposium Series*, 130, vol. 69,1-13
- LATTO, B. & EL REIDY, O.K. 1984 Dispersion of polymer additives in a developing boundary layer. In: *Drag Reduction*, R.J.H Sellin and R.T.Moses, eds., Univ. of Bristol, B.6.
- LEAL, L.G. 1990 Dynamics of Dilute Polymer Solutions. In: *Structure of Turbulence and Drag Reduction*. A. Gyr., ed., Springer-Verlag, Berlin, 155-185.
- LU, S.S. & WILLMARTH, W.W. 1973 Measurements of the Reynolds stress in a turbulent boundary layer. *J. Fluid Mech.*, 60, 481-511.
- LUCHIK, T.S. & TIEDERMAN, W.G. 1987 Timescale and structure of ejections and bursts in turbulent channel flows. *J. Fluid Mech.*, 174, 529-552.

LUCHIK, T.S. & TIEDERMAN, W.G. 1988 Turbulent structure in low-concentration drag-reducing channel flows. *J. Fluid Mech.*, 190, 241-263.

MAKSIMOVIC, C. 1984 Turbulence structure of a developing duct flow with near-wall injection of drag reduction. In: *The Influence of Polymer Additives on Velocity and Temperature Fields*. B. Gampert ed., Springer-Verlag, Berlin, 359-368.

McCOMB, W.D. & RABIE, L.H. 1982 Local drag reduction due to injection of polymer solutions into turbulent flow in a pipe, part I: Dependence on local polymer concentration; part II: Laser-Doppler measurements of turbulent structure. *AIChE J.*, 28, 547-565.

MIZUSHINA, T. & USUI, H. 1977 Reduction of eddy diffusion for momentum and heat in viscoelastic fluid flow in a circular pipe. *Phys. Fluids*, 20, S100-S108.

MORKOVIN, M.V. 1965 On eddy diffusivity, quasi-similarity and diffusion experiments in turbulent boundary layers. *Int. J. Heat Mass Trans.*, 8, 129-145.

MURLIS, J.; TSAI, H.M., & BRADSHAW, P. 1982 The structure of turbulent boundary layers at low Reynolds numbers. *J. Fluid Mech.*, 122, 13-56.

OLDAKER, D.K. & TIEDERMAN, W.G. 1977 Spatial structure of the viscous sublayer in drag-reducing channel flows. *Phys. Fluids*, 20, S133-S144.

PANTON, R.L. 1990 Scaling turbulent wall flows. *J Fluids Engr.*, 112, 425-432.

PATANKAR, S.V. 1970 *Heat & mass transfer in boundary layers: a general calculation procedure*. Intertext, London.

POREH, M. & CERMAK, J.E. 1964 Study of diffusion from a line source in a turbulent boundary layer. *Int. J. Heat Mass Trans.*, 7, 1083-1095.

PURTELL, L.P., KLEBANOFF, P.S. & BUCKLEY, F.T. 1981 Turbulent boundary layer at low Reynolds number. *Phys. Fluids*, 24, 802-811.

REISCHMAN, M.M. & TIEDERMAN, W.G. 1975 Laser-Doppler anemometer measurements in drag-reducing channel flows. *J. Fluid Mech.*, 70, 369-392.

ROBINSON, S.K., KLINE, S.J. & SPALART, P.R. 1990 Quasi-coherent structures in the turbulent boundary layer: part II. Verification and new information from a numerically simulated flat-plate layer. *Near-Wall Turbulence*, S.J Kline & N.H. Afgan eds., Hemisphere, New York, NY., 218-247.

ROSHKO, A. 1955 On the development of turbulent wakes from vortex streets. NACA technical report TR 1191.

SANDBORN, V.A. 1958 Measurements of intermittency of turbulent motion in a boundary layer. *J. Fluid Mech.*, 6, 221-240.

SCHMID, A. 1984 Experimental investigation of drag reducing polymers on a turbulent channel flow. *Drag Reduction*, R.J.H Sellin and R.T.Moses, eds., Univ. of Bristol .Bristol, B.12.

- SHAH, D.A. & ANTONIA, R.A. 1989 Scaling of the "bursting" period in turbulent boundary layer and duct flows. *Phys. Fluids A*, 1, 318-325.
- SPALART, P.R. 1988 Direct simulation of a turbulent boundary layer up to $Re_{\theta} = 1410$. *J. Fluid Mech.*, 187, 61-98.
- SREENIVASAN, K. R. 1989, in *Frontiers in Experimental Fluid Mechanics* Gad-el-Hak ed. Springer-Verlag, Berlin, p. 159.
- TIEDERMAN, W.G.; LUCHIK, T.S. & BOGARD, D.G. 1985 Wall-layer structure and drag reduction. *J. Fluid Mech.*, 156, 419-437.
- TIEDERMAN, W.G. 1990 Eulerian detection of turbulent bursts, *Near-Wall Turbulence*, S.J Kline & N.H. Afgan eds., Hemisphere, New York, NY., 874-887.
- TOWNSEND A.A. 1961 Equilibrium layers and wall turbulence. *J. Fluid Mech.*, 11, 97-120.
- TUBERGEN, R.G. 1991 Evaluation of ejection detection schemes in turbulent flow. MS thesis, Purdue University, West Lafayette, IN.
- VAN DRIEST, E.R. 1956 On turbulent flow near a wall. *J. Aero. Sci.*, 23 1007-1011,1036.
- VDOVIN, A.V. & SMOL'YAKOV, A.V. 1978 Diffusion of polymer solutions in a turbulent boundary layer. *J. Appl. Mech. Tech. Phys.* 19, 66-73, Engl. trans. 196-201.
- VDOVIN, A.V. & SMOL'YAKOV, A.V. 1981 Turbulent diffusion of polymers in a boundary layer. *J. Appl. Mech. Tech. Phys.* 22, 98-104, Engl. trans. 526-531.
- VIRK, P.S. 1975 Drag reduction fundamentals. *AIChE J.*, 21, 625-656.
- WALKER, D.A. 1987 A fluorescence technique for measurement of concentration in mixing liquids. *J. Phys. E.*, 20, 217-223.
- WALKER, D.T. 1988 Turbulence structure and mass transport in a channel flow with polymer injection. Ph.D Thesis, Purdue University, West Lafayette, IN.
- WALKER, D.T. 1985 Injection of drag reducing additives into turbulent channel flows: optimization and modeling. MS thesis, Purdue University, West Lafayette, IN.
- WALKER, D.T.; TIEDERMAN, W.G. & LUCHIK, T.S. 1986 Optimization of the injection process for drag-reducing additives. *Exp. Fluids*, 4, 114-120.
- WALKER, D.T. & TIEDERMAN, W.G. 1989 The concentration field in a turbulent channel flow with polymer injection at the wall. *Exp. Fluids*, 8, 86-94.
- WALKER, D.T. & TIEDERMAN, W.G. 1990 Turbulent structure in a channel flow with polymer injection at the wall. *J. Fluid Mech.*, 218, 377-403.
- WHITE, F.M. 1974 *Viscous Fluid Flow* Mc Graw Hill, New York, NY., 518.

WHITE, J.B. 1989 The effect of adverse pressure gradient on the turbulent burst structure in low-Reynolds number equilibrium boundary layers. MS thesis, Purdue University, West Lafayette, IN.

WHITE, J.B. & TIEDERMAN, W.G. 1990 The effect of adverse pressure gradient on the turbulent burst structure in low-Reynolds number equilibrium boundary layers. in: Proceeding of the Twelfth Symposium on Turbulence, University of Missouri, Rolla, Rolla, MO.

WILLMARTH, W.W., & SHARMA, L.K. 1984 Study of turbulent structure with hot wires smaller than the viscous length. *J. Fluid Mech.*, 142, 121-149.

WILLMARTH, W.W., WEI, T. & LEE, C.O. 1987 Laser anemometer measurements of Reynolds stress in a turbulent channel flow with drag reducing polymer additives. *Phys. Fluids*, 30, 933-935.

WU, J. 1969 Lift reduction in additive solutions. *J. Hydronautics*, 3, 198-200.

YORK, B. & KNIGHT, D. 1985 Calculations of two-dimensional boundary layers using the Baldwin-Lomax model. *AIAA J.*, 23, 1849-1850.

Appendix A: Data Plots

This appendix presents plots of the data which were not included in the body of the text. They are arranged in the order in which they were referenced in the main text.

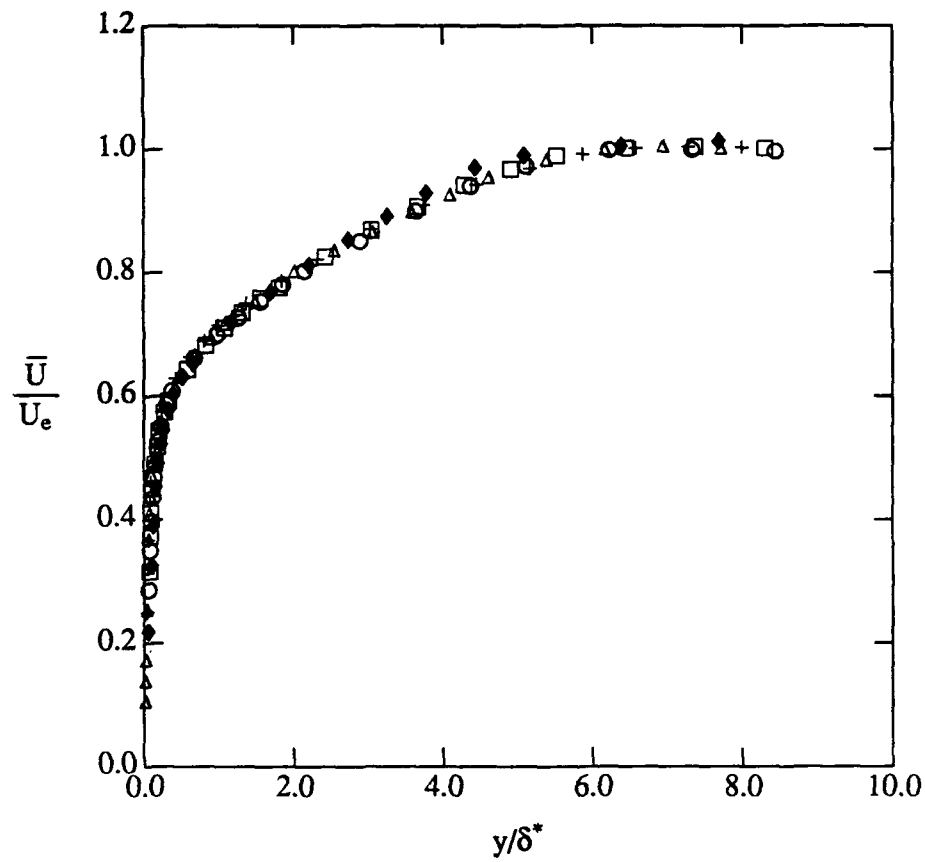


Figure A.1 Dimensionless velocity profiles for the zero pressure gradient boundary layer using outer normalization. \blacklozenge $Re_\theta = 1358$; \circ $Re_\theta = 2478$; \square $Re_\theta = 2978$; \triangle $Re_\theta = 3527$; $+$ $Re_\theta = 3935$.

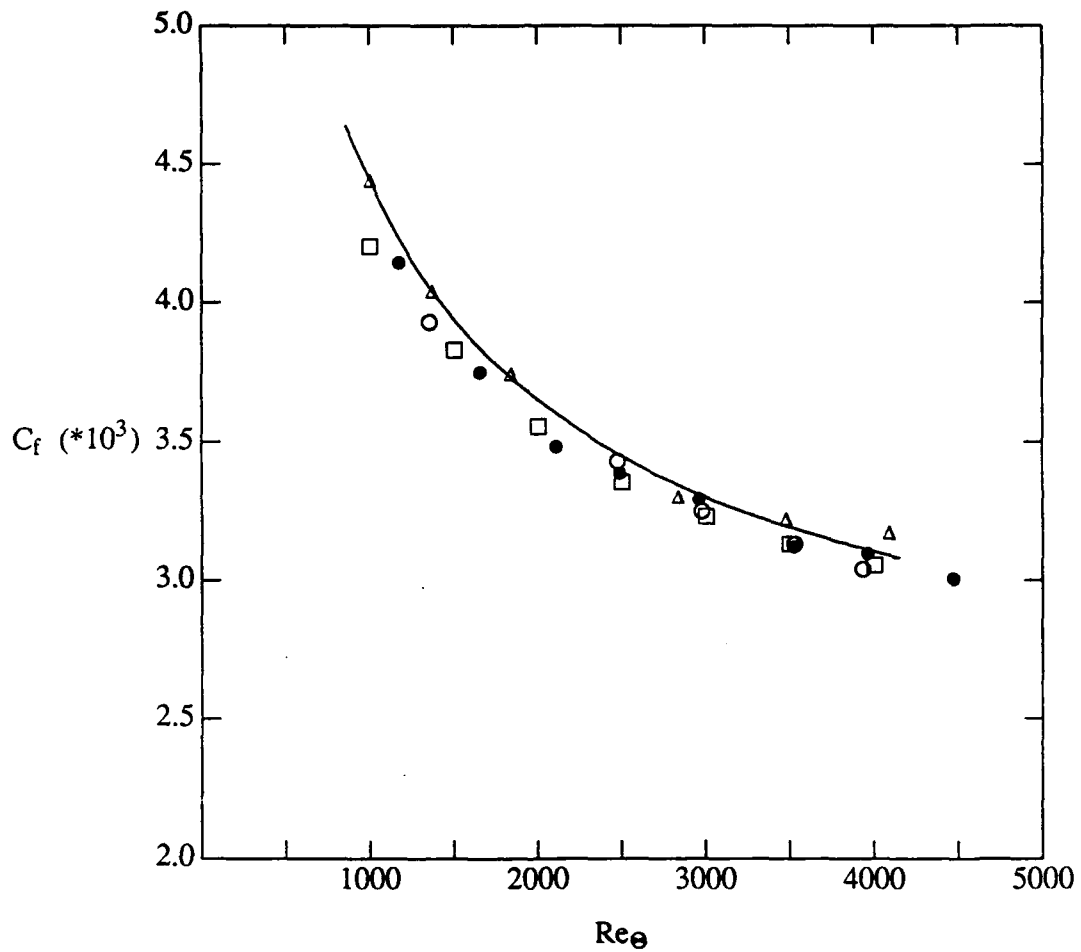


Figure A.2 Variation of skin friction coefficient, C_f , as a function of Re_θ for a Newtonian zero pressure gradient boundary layer: \circ present data; Δ Purtell et. al. (1981); \square Murliss et al. (1982); \bullet Wiegardt (Coles re-analysis, 1968); — Coles (1962).

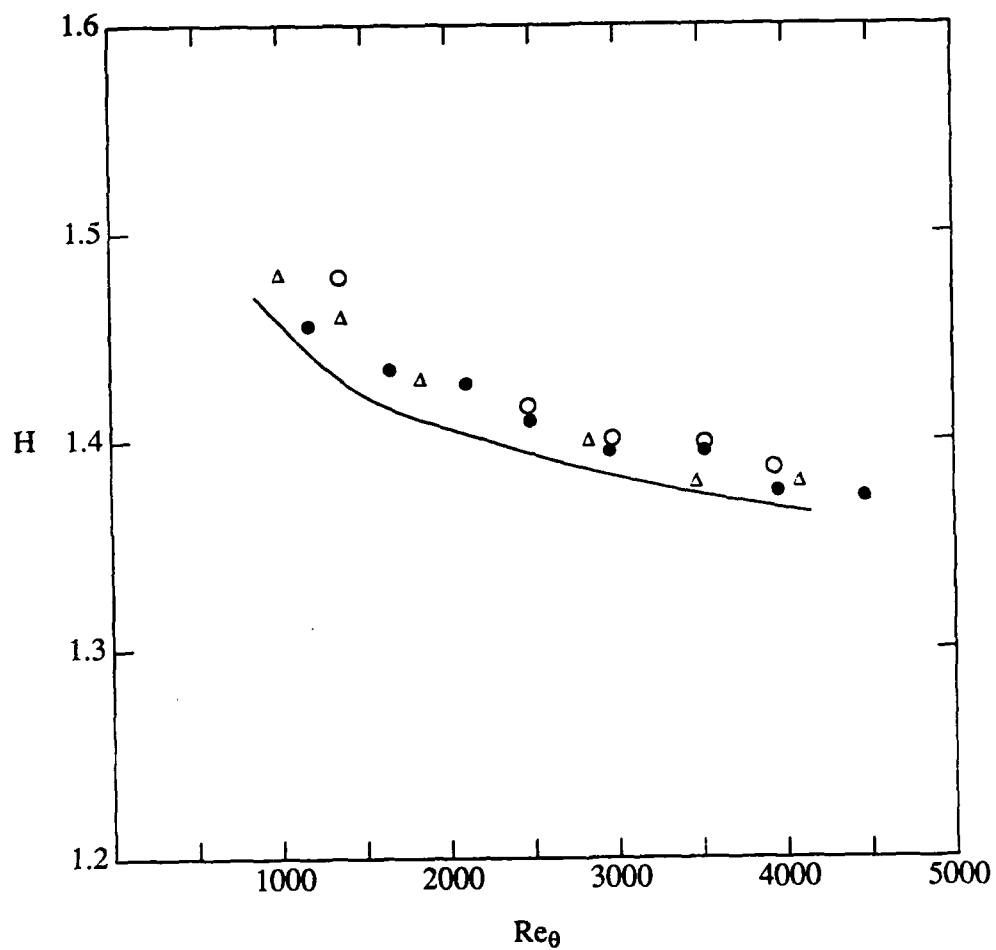


Figure A.3 Variation of shape factor, H , as a function of Re_θ for a zero pressure gradient Newtonian boundary layer: \circ present data; Δ Purtell et. al. (1981); \bullet Wieghardt (Coles re-analysis, 1968); — Coles (1962).

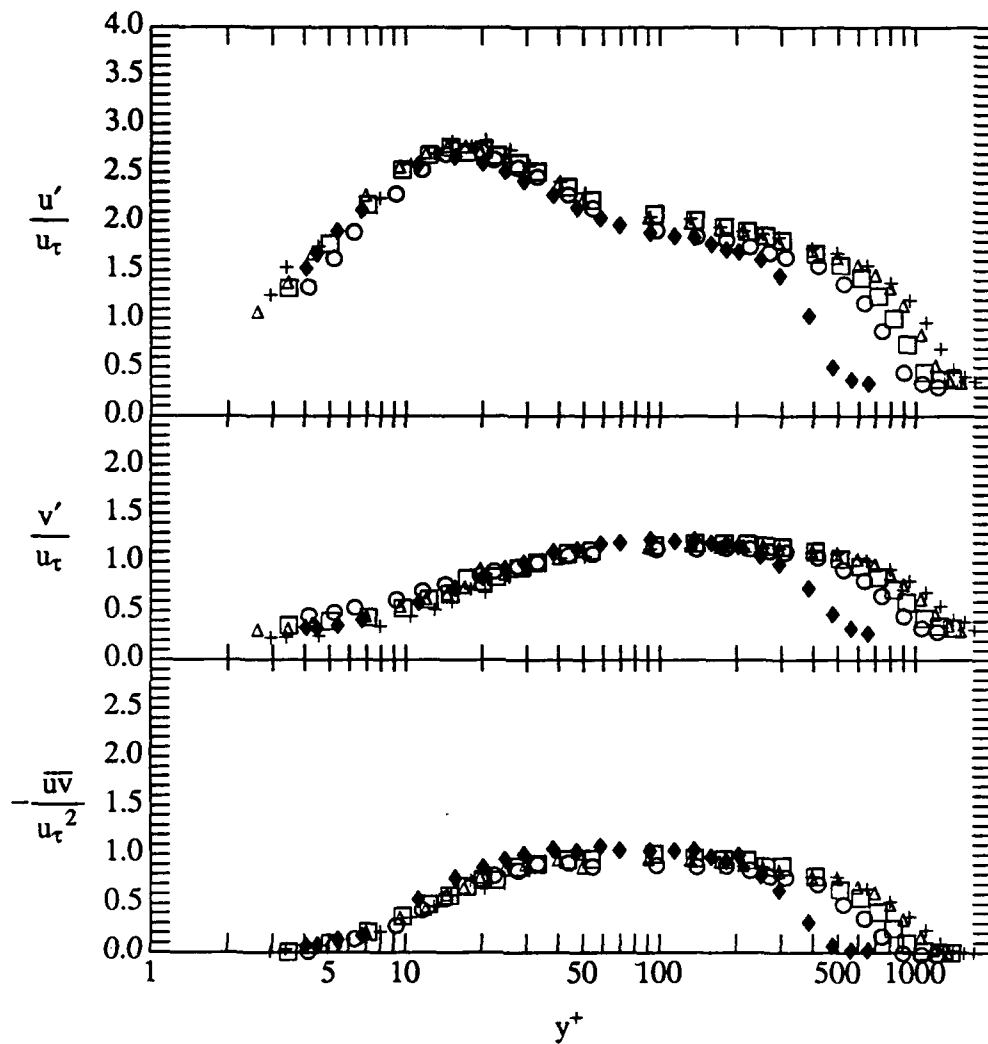


Figure A.4 Root-mean-square velocities and Reynolds shear stress in a Newtonian zero pressure gradient boundary layer without injection. \blacklozenge $Re_\theta = 1358$; \circ $Re_\theta = 2478$; \square $Re_\theta = 2978$; \triangle $Re_\theta = 3527$; $+$ $Re_\theta = 3935$.

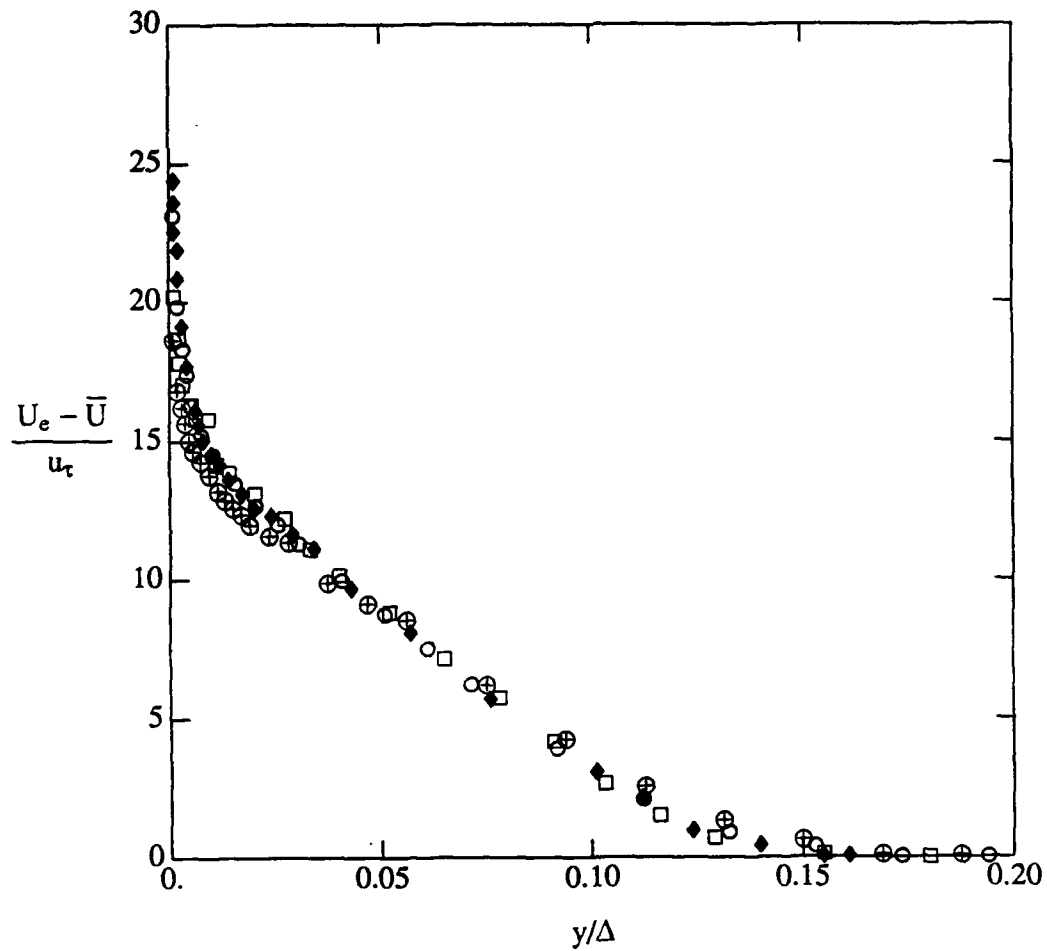


Figure A.5 Velocity defect profiles in an adverse pressure gradient boundary layer.
 ○ $Re_\theta = 3570, \beta = 1.8, G = 10.6$; ◆ J. B. White $Re_\theta = 2085, \beta = 1.9, G = 10.8$;
 □ East & Sawyer flow 5 $Re_\theta = 26800, \beta = 1.89, G = 10.60$; ⊕ Clauser flow 1 $Re_\theta = 14000, \beta = 1.89, G = 9.66$.

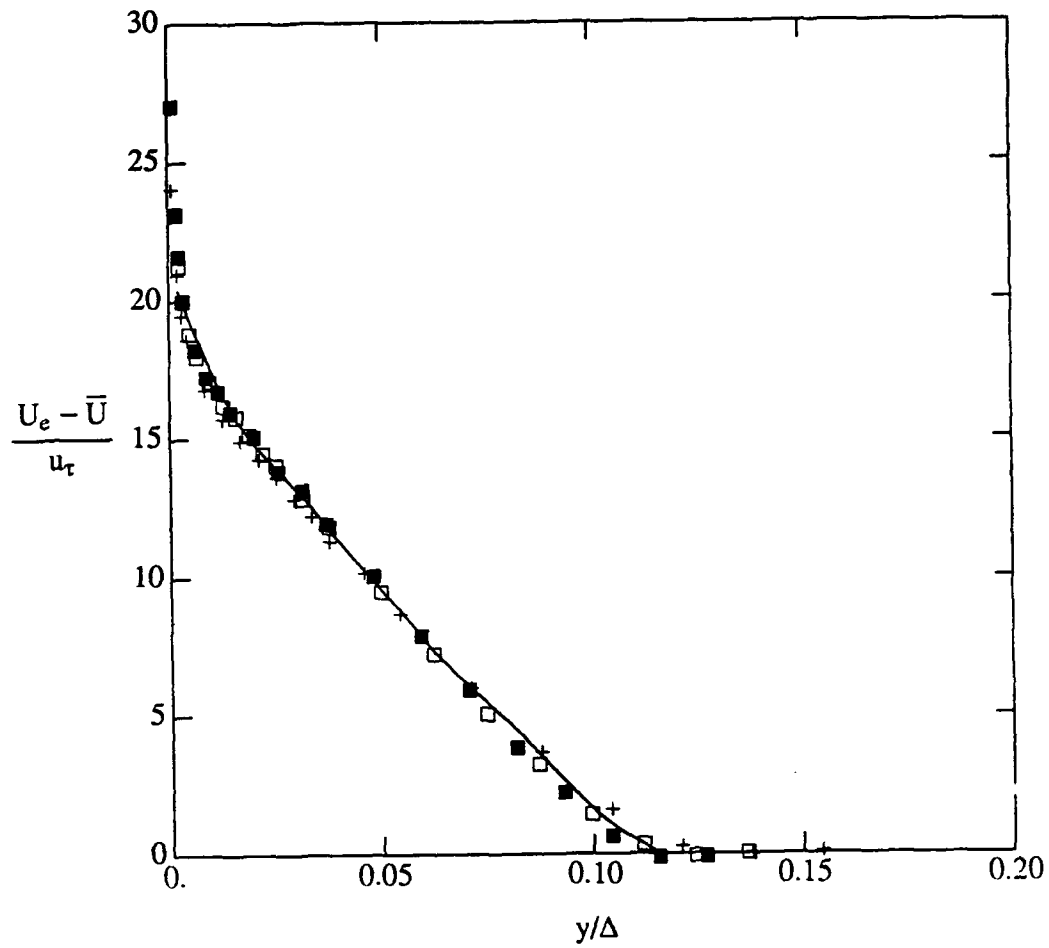


Figure A.6 Velocity defect profiles in an adverse pressure gradient boundary layer.
 + $Re_\theta = 3784$, $\beta = 2.4$, $G = 12.2$; \square $Re_\theta = 4588$, $\beta = 2.3$, $G = 13.0$; \blacksquare
 $Re_\theta = 4978$, $\beta = 2.7$, $G = 13.0$. — Bradshaw (1969)
 $Re_\theta = 22370$, $\beta = 2.9$, $G = 12.58$.

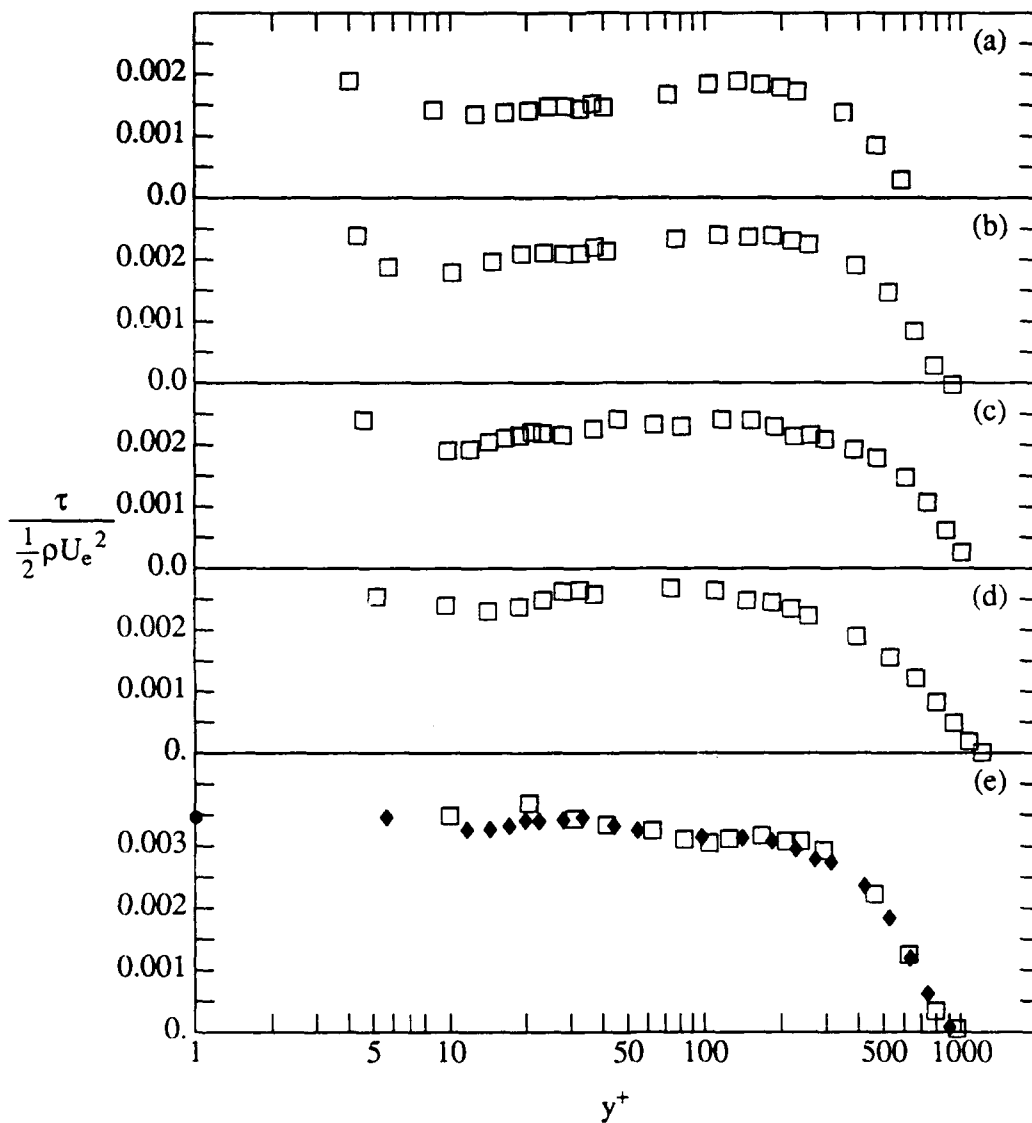


Figure A.7 Sum of viscous shear stress, $(\mu d\bar{U}/dy)$, and Reynolds shear stress, $(-\rho\bar{u}\bar{v})$, in a zero pressure gradient boundary layer with and without polymer injection at $Q_i/Q_s = 2.6$. (a) polymer injection $x^+ = 29000$; (b) polymer injection $x^+ = 43200$; (c) polymer injection $x^+ = 64400$; (d) polymer injection $x^+ = 81000$; (e) \square water injection, \blacklozenge no injection, $x^+ = 29000$. \bullet Wall shear stress determined from the log region.

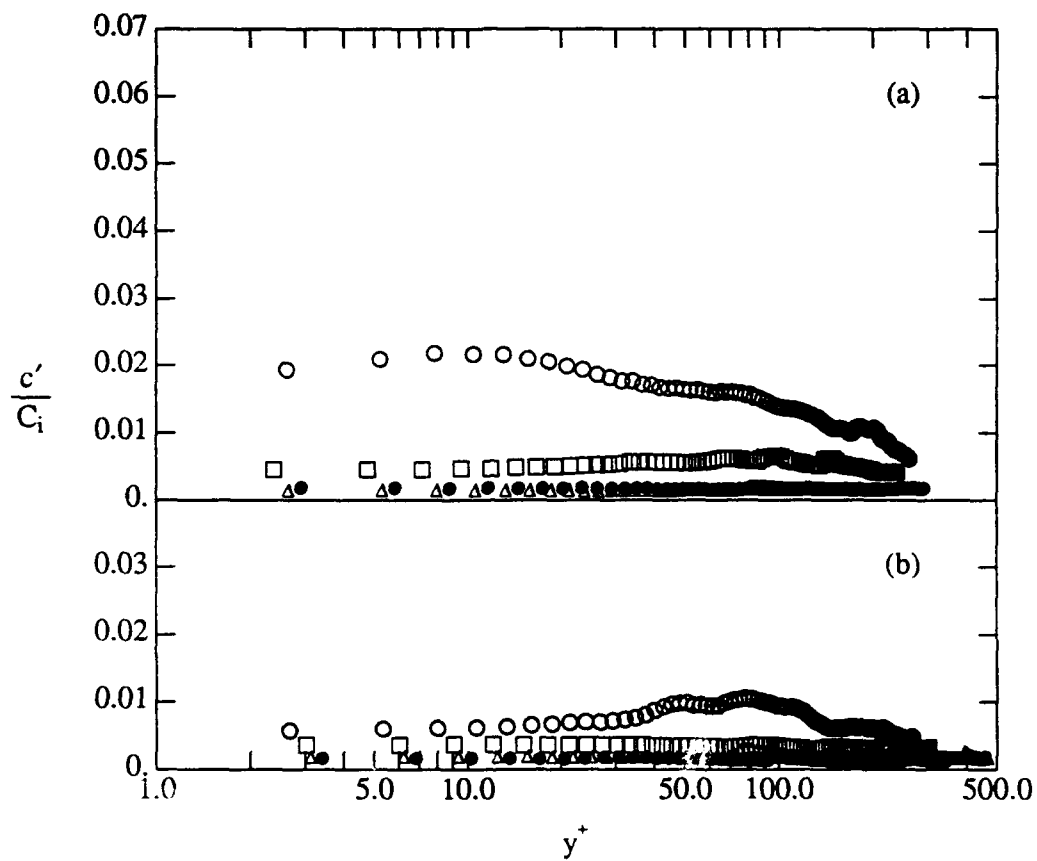


Figure A.8 Root-mean-square polymer concentration in the zero pressure gradient drag reduced boundary layers normalized by the injected concentration. (a): $Q_i/Q_s = 5.1$ (b): $Q_i/Q_s = 2.6$. \circ $x^+ = 29000$; \square $x^+ = 43200$; Δ $x^+ = 64400$; \bullet $x^+ = 81000$.

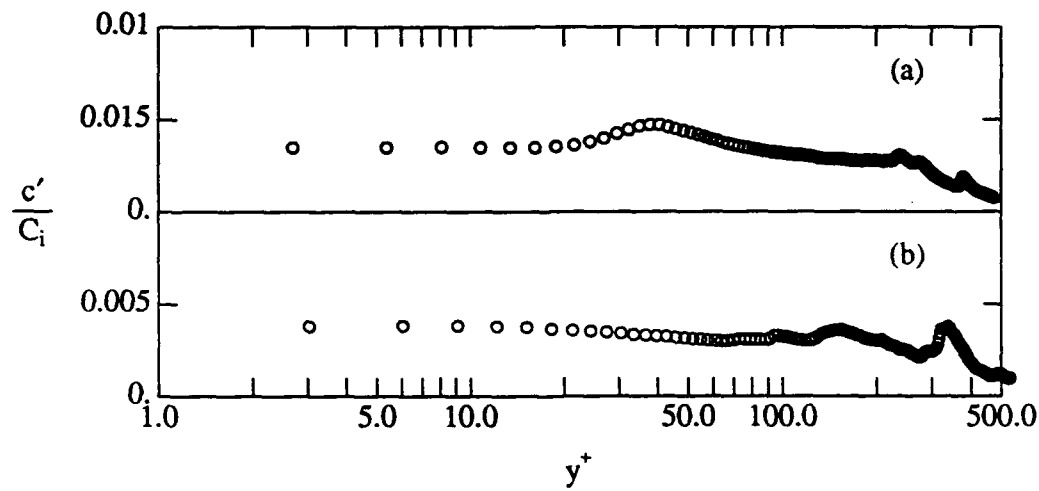


Figure A.9 Root-mean-square polymer concentration normalized by the injected concentration in the adverse pressure gradient boundary layer, $\beta = 1.8$, $x^+ = 33700$. Note larger scale. (a) $Q_i/Q_s = 5.1$ (b) $Q_i/Q_s = 2.6$.

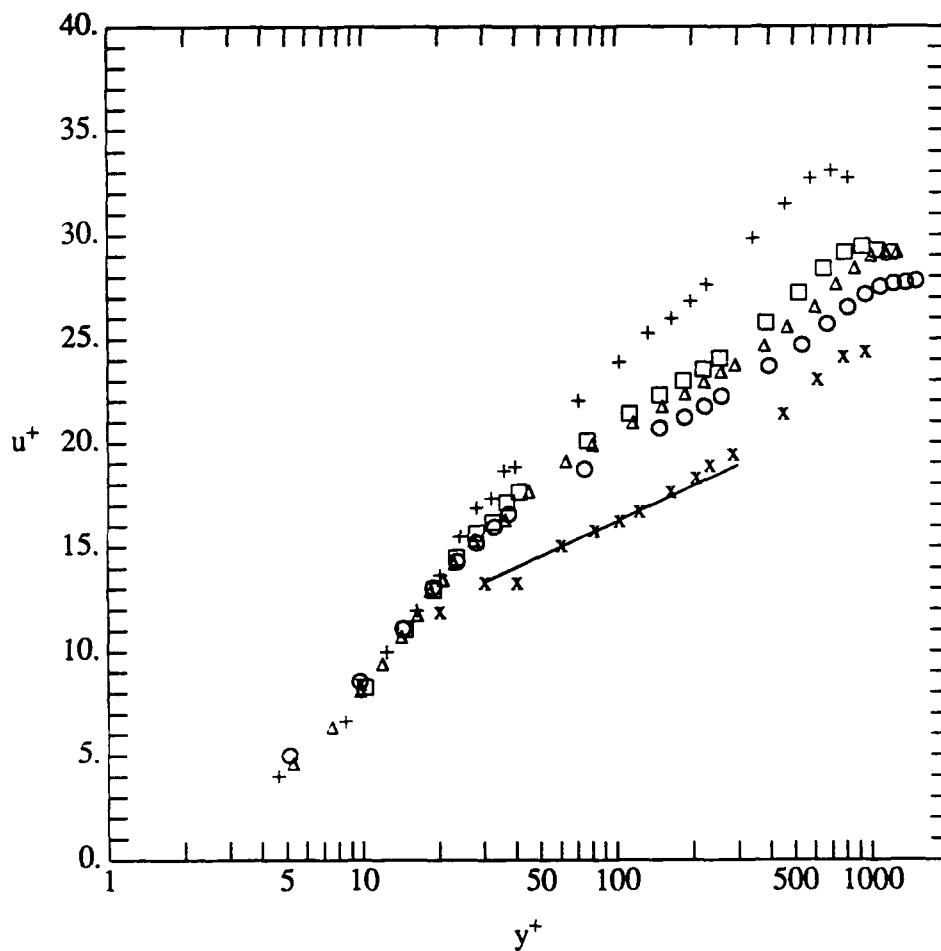


Figure A.10 Mean streamwise velocity for a zero pressure gradient boundary layer with and without drag reduction. Fluid injected at $Q_i/Q_s = 2.1$.
 + $(x - x_s)^+ = 29000$; □ $(x - x_s)^+ = 43200$; Δ $(x - x_s)^+ = 64400$;
 o $(x - x_s)^+ = 81000$; x $(x - x_s)^+ = 29000$, water injection.
 — $U^+ = (1/0.41) \ln y^+ + 5.0$.

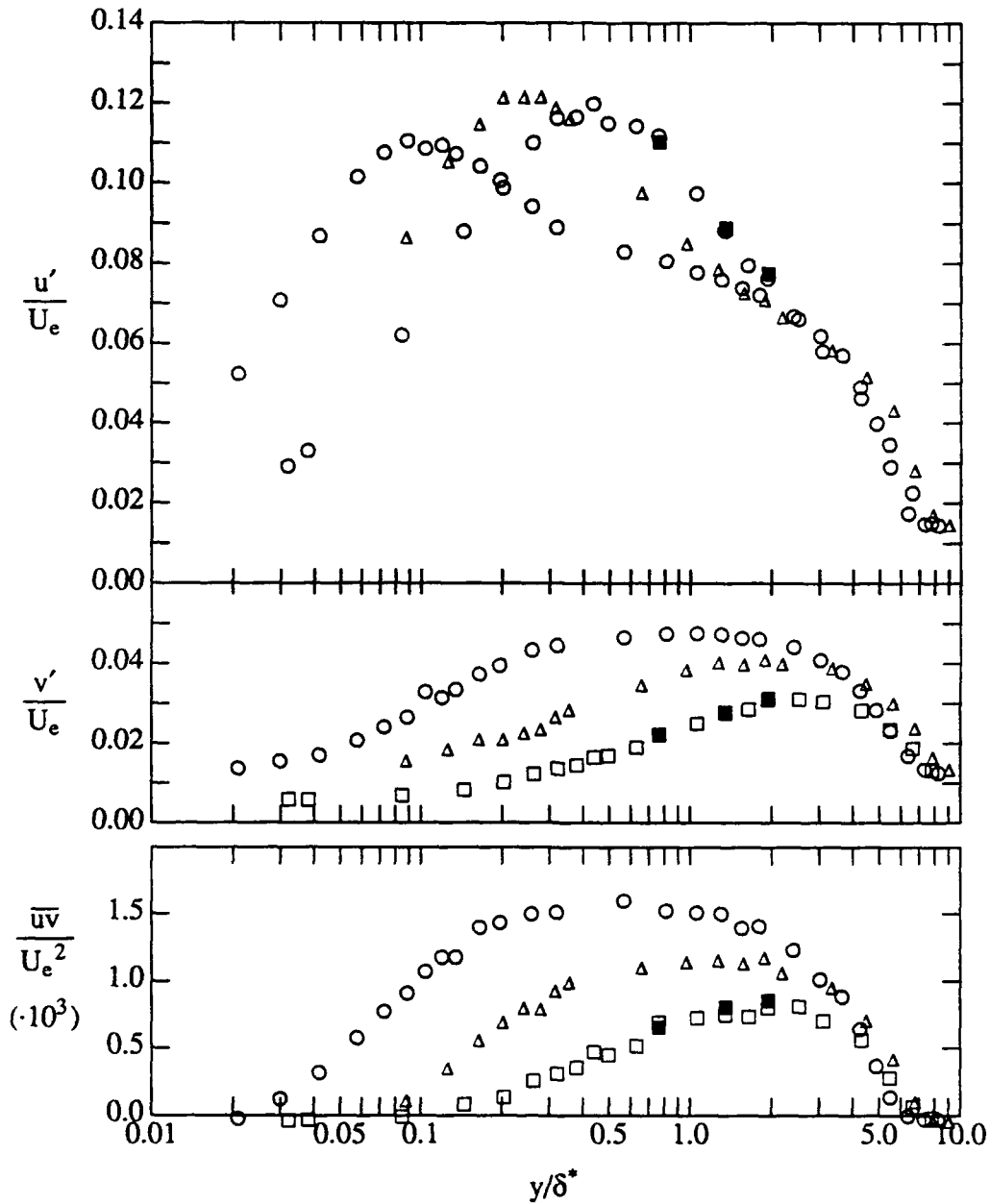


Figure A.11 Root-mean-square velocities and Reynolds shear stresses in a zero pressure gradient boundary layer with and without drag reduction. \circ $(x - x_s)^+ = 43200, Re_\theta = 2978$; \triangle polymer injection $Q_i/Q_s = 2.6$; \square polymer injection $Q_i/Q_s = 5.1$; \blacksquare $Q_i/Q_s = 5.1$, repeated points.

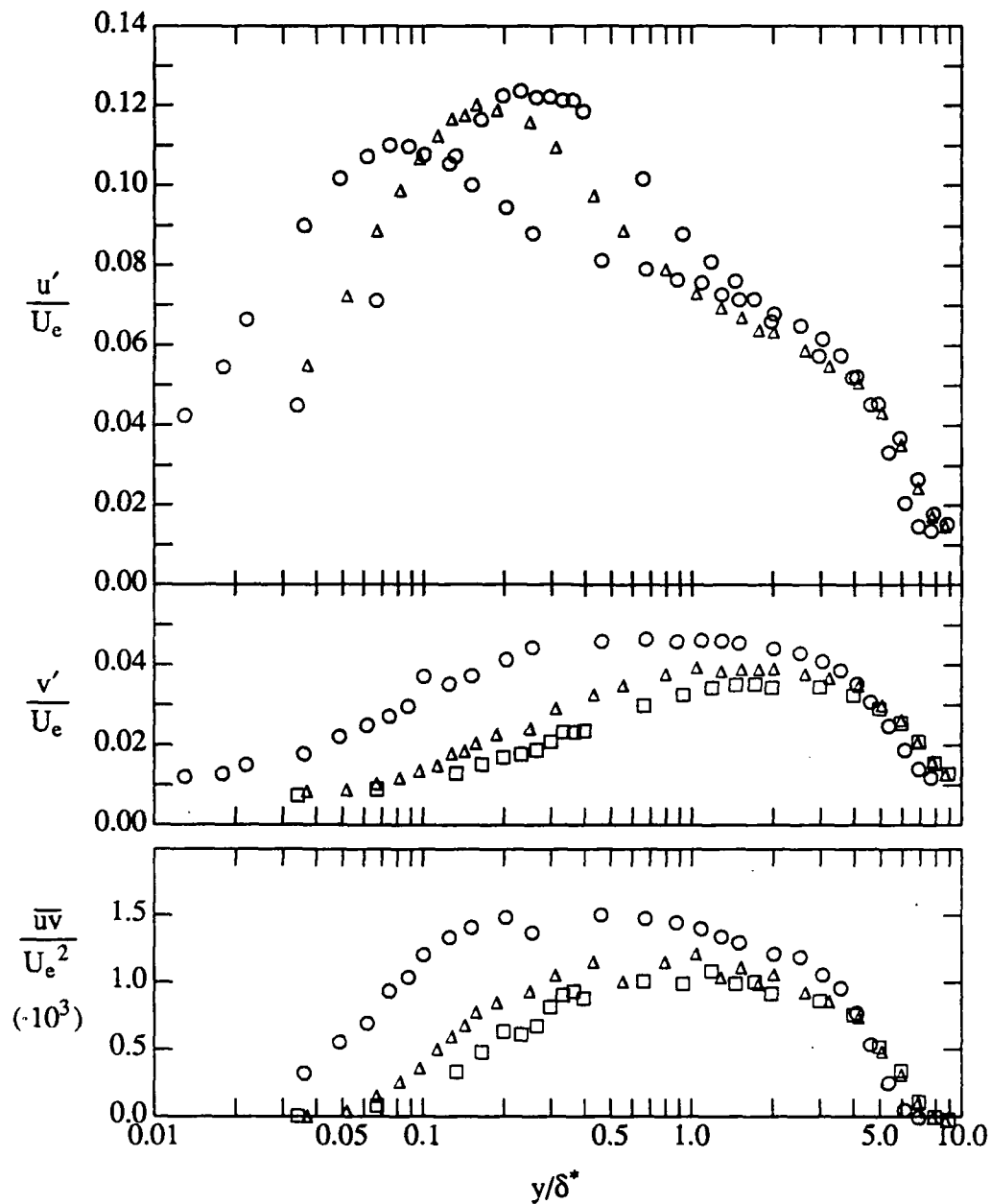


Figure A.12 Root-mean-square velocities and Reynolds shear stresses in a zero pressure gradient boundary layer with and without drag reduction.
 \circ $(x - x_s)^+ = 64400$, $Re_\theta = 3527$; \triangle polymer injection $Q_i/Q_s = 2.6$;
 \square polymer injection $Q_i/Q_s = 5.1$.

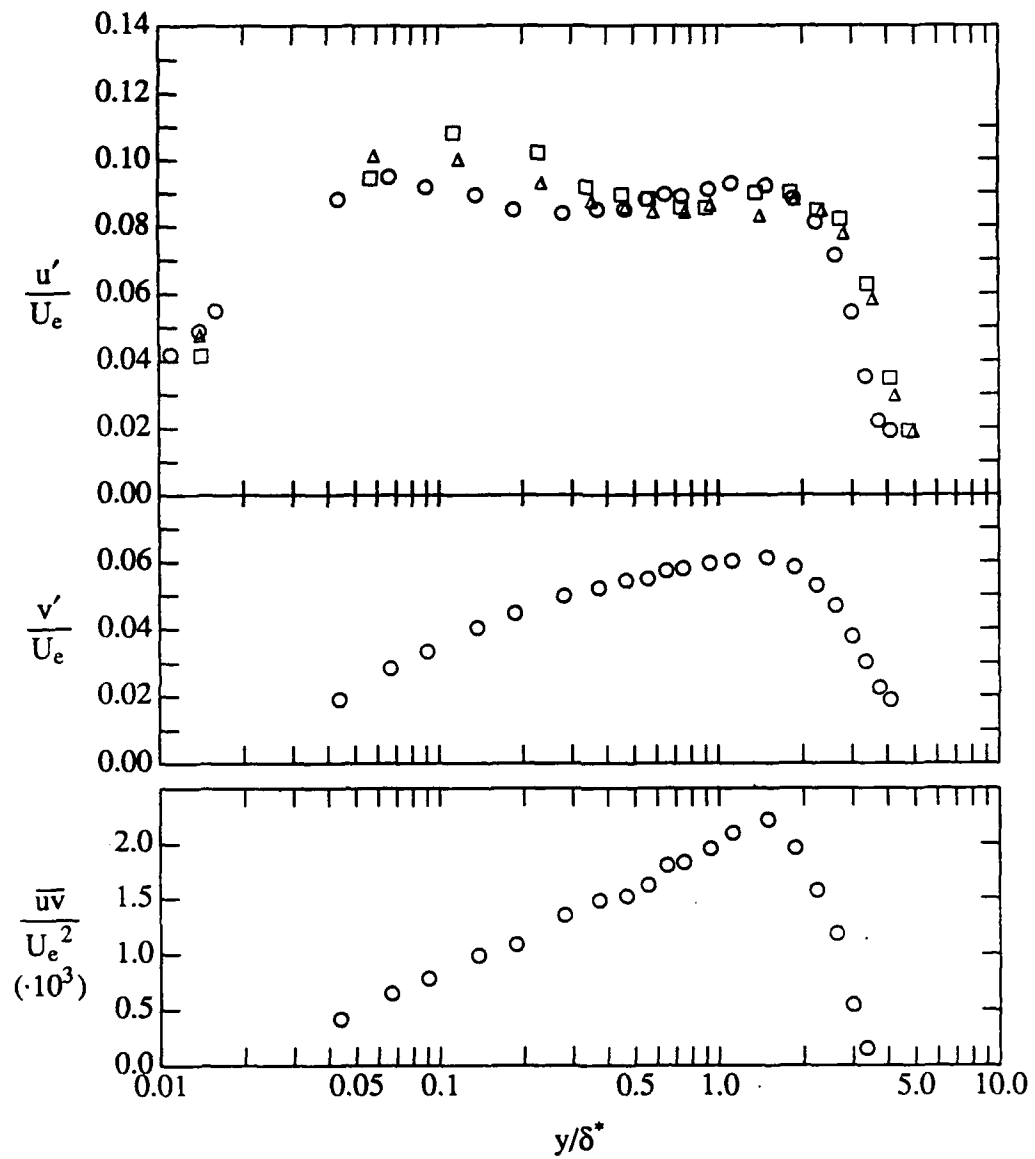


Figure A.13 Root-mean-square velocities and Reynolds shear stresses in the adverse pressure gradient boundary layer, $\beta = 2.4$ with and without drag reduction.
 \circ $(x - x_s)^+ = 40400$, $Re_\theta = 4588$;
 \triangle polymer injection $Q_i/Q_s = 2.6$; \square polymer injection $Q_i/Q_s = 5.1$.

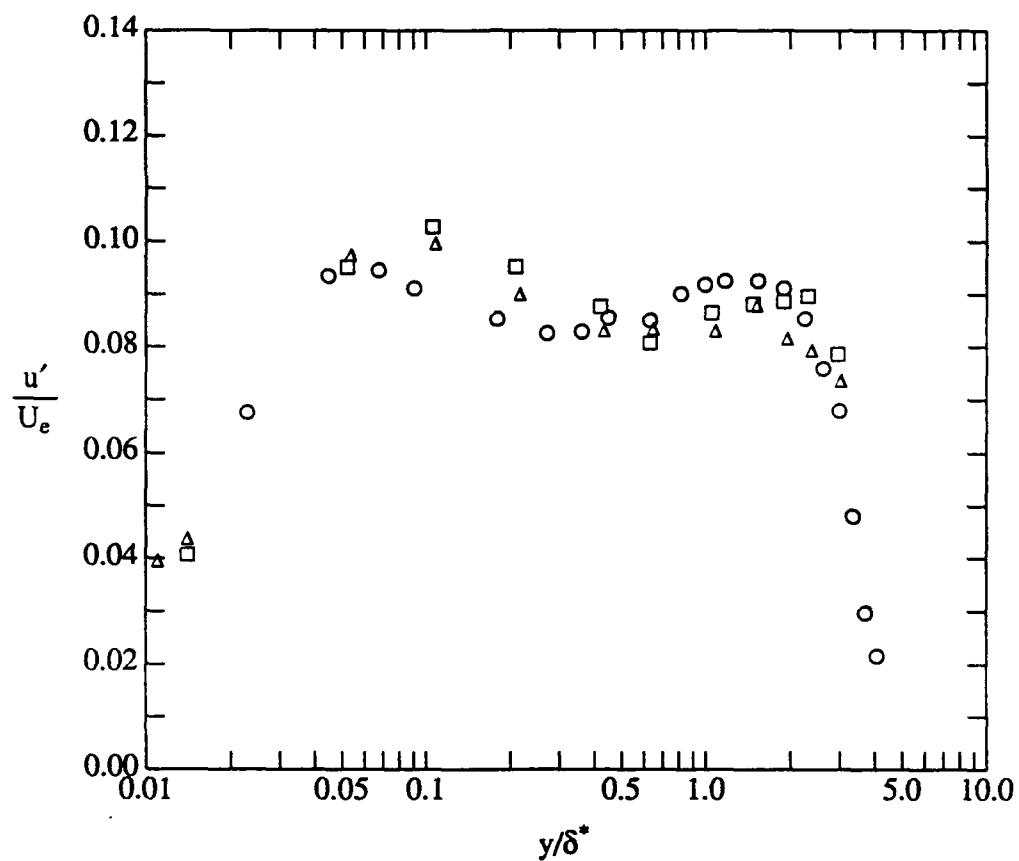


Figure A.14 Root-mean-square streamwise velocity in the adverse pressure gradient boundary layer, $\beta = 2.4$ with and without drag reduction.
 \circ $(x - x_s)^+ = 45200$, $Re_\theta = 4978$; \triangle polymer injection $Q_i/Q_s = 2.6$;
 \square polymer injection $Q_i/Q_s = 5.1$.

Appendix B: Experimental Data

This appendix summarized the types of data taken and locations in tables A.1 to A.4. The remainder of the appendix is a listing of the experimental velocity profiles. The listings are arranged according to their streamwise location in each boundary layer and each boundary layer is listed in the following order: Newtonian, zero pressure gradient, drag reduced, zero dp/dx , $Q_i/Q_s = 2.6$; drag reduced, zero dp/dx , $Q_i/Q_s = 5.1$; Newtonian, adverse dp/dx , $\beta = 1.8$; drag reduced, adverse dp/dx , $\beta = 1.8$, $Q_i/Q_s = 2.6$; drag reduced, adverse dp/dx , $\beta = 1.8$, $Q_i/Q_s = 5.1$; Newtonian, adverse dp/dx , $\beta = 2.4$; drag reduced, adverse dp/dx , $\beta = 2.4$, $Q_i/Q_s = 2.6$; drag reduced, adverse dp/dx , $\beta = 2.4$, $Q_i/Q_s = 5.1$. The integral parameters and other mean flow parameters are listed at the top of the listing. Please note the additional items listed for the drag reduced data. Velocity profiles are given in the lower part of the listing.

All linear dimensions are given in mm, all velocities in m/s, and viscosity in m^2/s .

Table A.1 Zero pressure gradient Newtonian data

$(x - x_t)$ (mm)	Re_θ	data measured		
		\bar{U}, u'	$\bar{u}v$	T_b
181	1358	X	X	X
754	2478	X	X	
1058	2978	X	X	
1513	3527	X	X	X
1867	3935	X	X	

Table A.2 Drag reduced zero pressure gradient data

$(x - x_t)$ (mm)	$Re_\theta _N$	Q_i/Q_s	DR	data measured			
				\bar{U}, u'	$\bar{u}v$	T_b	\bar{C}
754	2478	2.6	X	X	X		X
1058	2978	2.6	X	X	X		X
1513	3527	2.6	X	X	X	X	X
1867	3935	2.6	X	X	X		X
754	2478	5.1	X	X	X		X
1058	2978	5.1	X	X	X		X
1513	3527	5.1	X	X	X	X	X
1867	3935	5.1	X	X	X		X

Table A.3 Adverse pressure gradient Newtonian data

$(x - x_t)$ (mm)	Re_θ	G	β	data measured		
				\bar{U}, u'	\bar{uv}	T_b
747	3079	10.36	2.0	X		
854	3566	10.59	1.8	X	X	X
984	3868	11.04	1.7	X		
1104	4210	11.27	1.8	X	X	
840	3784	12.2	2.4	X		
1008	4588	13.0	2.3	X	X	X
1102	4978	13.0	2.7	X		

Table A.4 Adverse pressure gradient drag reduced data

$(x - x_t)$ (mm)	$Re_\theta _N$	β	Q_i/Q_s	DR	data measured			
					\bar{U}, u'	\bar{uv}	T_b	\bar{C}
488	-	1.8	2.6	X				
488	-	1.8	5.1	X				
854	3566	1.8	2.6	X	X	X	X	X
854	3566	1.8	5.1	X	X	X	X	X
490	-	2.4	2.6	X				
490	-	2.4	5.1	X				
840	3784	2.4	2.6	X				
840	3784	2.4	5.1	X				
1012	4588	2.3	2.6	X	X		X	
1012	4588	2.3	5.1	X	X		X	
1099	4978	2.7	2.6	X	X			
1099	4978	2.7	5.1	X	X			

Table A.5 Drag reduction and viscometry tests.

$(x - x_t)$ mm	Q_i/Q_s	β	date	5/8 in. tube test			viscosity (cps)		
				u_τ mm/s	%DR	u_τ mm/s	23.00 s^{-1}	11.50 s^{-1}	5.75 s^{-1}
1513	2.6	0	8/28/90	41.8	59.1	42.4	-	-	-
1867	2.6	0	9/1/90	44.3	69.5	42.4	27.5	37.0	53.8
1058	2.6	0	9/4/90	68.2	62.7	70.4	30.6	43.4	62.4
754	2.6	0	9/7/90	69.3	62.6	68.5	26.1	35.1	49.9
754	5.1	0	9/7/90	69.9	62.8	68.7	29.4	41.9	63.2
1513	5.1	0	9/9/90	70.0	64.4	68.5	31.0	42.9	59.9
1867	5.1	0	1/25/91	67.3	61.5	67.2	33.2	47.2	64.0
1058	5.1	0	1/28/91	65.8	67.6	66.1	33.9	48.0	66.3
1012	2.6,5.1	2.4	5/20/91	63.3	63.8	-	28.5	39.8	56.2
1099	2.6,5.1	2.4	5/25/91	64.1	67.5	63.1	24.6	33.5	46.8
1008	2.6,5.1	1.8	6/17/91	64.4	68.6	62.6	24.6	33.4	46.8

Flow zlna

Flow parameters								
Re_θ	$(x - x_i)$	$(x - x_s)$	U_∞	u_τ	θ	δ^*	β	G
1358	181	47	0.990	0.0439	1.32	1.95	0.	7.29
Π	$c_f (10^3)$	$\nu (10^6)$	δ					
0.48	3.93	.961	12.0					
Mean velocities and fluctuation statistics								
y^+	u^+	u'/u_τ	v'/u_τ	\overline{uv}/u_τ^2	$\overline{u^3}/(u^+)^3$	$\overline{v^3}/(u^+)^3$	$\overline{u^4}/(u^+)^4$	$\overline{v^4}/(u^+)^4$
2.95	2.98	1.284	0.339	-0.054	0.939	-2.720	3.96	14.70
3.53	3.62	1.457	0.389	-0.107	0.822	-2.780	3.75	14.80
4.07	3.99	1.575	0.381	-0.113	0.734	-2.320	3.41	12.40
5.25	4.84	1.815	0.380	-0.184	0.710	-1.850	3.26	12.20
8.18	7.25	2.423	0.494	-0.411	0.350	-0.634	2.52	8.82
11.05	8.74	2.576	0.588	-0.505	0.138	0.079	2.37	9.84
13.98	10.14	2.612	0.671	-0.650	0.002	-0.017	2.49	5.98
16.86	11.00	2.665	0.742	-0.758	-0.077	0.096	2.45	5.39
19.78	11.70	2.549	0.834	-0.845	-0.117	0.040	2.49	5.07
22.66	12.20	2.532	0.878	-0.836	-0.114	-0.052	2.58	4.39
28.46	12.96	2.414	0.999	-0.944	-0.164	0.058	2.67	3.75
34.26	13.52	2.306	1.055	-0.977	-0.203	0.021	2.77	3.56
45.91	14.16	2.134	1.144	-1.054	-0.153	0.146	2.74	3.40
57.10	14.65	2.047	1.189	-1.076	-0.133	0.047	2.90	3.38
103.70	16.15	1.831	1.192	-0.919	-0.110	0.121	2.80	3.08
150.29	17.25	1.764	1.206	-0.915	-0.143	0.165	2.70	3.03
196.89	18.23	1.700	1.179	-0.901	-0.189	0.191	2.82	3.18
243.03	19.16	1.620	1.110	-0.796	-0.347	0.258	2.92	3.08
289.62	20.02	1.515	1.033	-0.685	-0.426	0.414	2.82	3.33
336.22	20.88	1.349	0.930	-0.516				
394.23	21.81	1.078	0.772	-0.302				
452.25	22.27	0.724	0.592	-0.079				
568.28	22.60	0.431	0.374	0.017				
684.31	22.77	0.329	0.306	0.006				

Flow z3na

Flow parameters								
Re_δ	$(x - x_t)$	$(x - x_s)$	U_δ	u_τ	θ	δ^*	β	G
2478	754	620	0.982	0.0406	2.43	3.44	0.	7.09
Π	$c_f (10^3)$	$\nu (10^6)$	δ					
0.55	3.43	.961	24.0					
Mean velocities and fluctuation statistics								
y^+	u^+	u'/u_τ	v'/u_τ	\overline{uv}/u_τ^2	$\overline{u^3}/(u^+)^3$	$\overline{v^3}/(u^+)^3$	$\overline{u^4}/(u^+)^4$	$\overline{v^4}/(u^+)^4$
4.17	3.33	1.327	0.452	-0.009	0.848	-0.357	3.59	7.95
5.24	4.15	1.620	0.485	-0.072	0.823	-0.435	3.47	8.23
6.31	5.13	1.891	0.534	-0.139	0.679	-0.259	3.19	9.17
9.21	6.91	2.282	0.615	-0.272	0.454	0.189	2.82	8.32
11.68	8.44	2.533	0.703	-0.434	0.267	0.253	2.53	7.08
14.37	9.61	2.690	0.770	-0.548	0.157	0.336	2.36	6.35
19.74	11.34	2.729	0.865	-0.750	-0.032	0.311	2.42	5.52
22.41	11.82	2.638	0.908	-0.785	-0.084	0.196	2.48	4.96
27.78	12.75	2.555	0.958	-0.836	-0.148	0.145	2.57	4.42
33.15	13.31	2.463	0.998	-0.902	-0.201	0.184	2.64	4.21
43.89	14.21	2.275	1.067	-0.913	-0.191	0.202	2.83	3.91
54.62	14.73	2.137	1.086	-0.876	-0.131	0.181	2.65	3.75
97.57	16.01	1.912	1.136	-0.889	-0.039	0.110	2.59	3.35
140.51	16.93	1.848	1.141	-0.878	-0.008	0.145	2.69	3.07
183.46	17.60	1.809	1.143	-0.881	-0.018	0.139	2.81	3.24
226.41	18.23	1.742	1.141	-0.841	-0.066	0.111	2.86	3.25
269.35	18.90	1.678	1.114	-0.779	-0.108	0.139	2.81	3.27
312.30	19.43	1.635	1.104	-0.768				
419.66	20.59	1.543	1.049	-0.696				
527.02	21.77	1.361	0.925	-0.493				
634.38	22.75	1.165	0.813	-0.350				
741.74	23.55	0.879	0.656	-0.165				
902.79	24.17	0.446	0.448	0.008				
1063.83	24.19	0.338	0.329	0.021				
1224.87	24.13	0.299	0.288	0.022				

Flow z4nb

Flow parameters								
Re_θ	$(x - x_t)$	$(x - x_r)$	U_e	u_r	θ	δ^*	β	G
2978	1058	924	0.975	0.0393	2.94	4.11	0.	7.06
Π	$c_f (10^3)$	$v (10^6)$	δ					
0.59	3.25	.961	26.6					
Mean velocities and fluctuation statistics								
y^+	u^+	u'/u_r	v'/u_r	\overline{uv}/u_r^2	$\overline{u^3}/(u^+)^3$	$\overline{v^3}/(u^+)^3$	$\overline{u^4}/(u^+)^4$	$\overline{v^4}/(u^+)^4$
3.14	3.22	1.294	0.333	0.018	0.887	0.973	3.76	11.30
4.69	4.61	1.750	0.378	-0.071	0.715	0.220	3.26	15.50
6.75	5.95	2.151	0.415	-0.191	0.600	0.265	2.93	10.00
9.36	7.78	2.514	0.507	-0.350	0.372	0.674	2.66	11.50
11.98	9.16	2.667	0.592	-0.470	0.155	0.412	2.43	8.05
14.60	10.11	2.740	0.653	-0.557	0.068	0.085	2.43	6.64
17.18	11.10	2.690	0.812	-0.654	-0.026	0.310	2.49	5.67
19.75	11.53	2.712	0.774	-0.719	-0.047	0.070	2.52	5.45
22.37	12.11	2.658	0.827	-0.719	-0.083	0.087	2.57	5.04
27.56	12.77	2.583	0.920	-0.857	-0.108	0.072	2.63	4.34
32.76	13.43	2.495	0.979	-0.879	-0.152	0.079	2.72	4.34
43.14	14.16	2.336	1.074	-0.921	-0.094	0.066	2.63	3.72
53.53	14.62	2.202	1.097	-0.929	-0.079	0.176	2.73	3.40
95.41	15.91	2.054	1.151	-0.980	0.000	0.229	2.75	3.33
136.96	16.87	1.994	1.172	-0.935	-0.053	0.116	2.56	3.19
178.51	17.57	1.926	1.177	-0.925	-0.035	0.124	2.74	3.17
220.06	18.18	1.878	1.168	-0.918	-0.099	0.110	2.81	3.27
261.60	18.76	1.827	1.148	-0.854	-0.126	0.141	2.85	3.29
303.15	19.17	1.782	1.137	-0.862				
407.03	20.40	1.652	1.092	-0.753				
510.86	21.48	1.529	1.012	-0.619				
614.77	22.42	1.407	0.936	-0.539				
718.65	23.30	1.212	0.820	-0.392				
822.52	23.94	0.986	0.700	-0.220				
926.39	24.47	0.718	0.570	-0.078				
1082.20	24.77	0.426	0.410	0.008				
1238.01	24.83	0.360	0.326	0.024				
1393.82	24.78	0.351	0.305	0.025				

Flow z6nd

Flow parameters								
Re_0	$(x - x_1)$	$(x - x_2)$	U_0	u_τ	θ	δ^+	β	G
3527	1513	1379	0.969	0.0384	3.50	4.90	0.	7.22
Π	$c_f (10^3)$	$v (10^6)$	δ					
0.62	3.13	.961	33.5					
Mean velocities and fluctuation statistics								
y^+	u^+	u'/u_τ	v'/u_τ	\overline{uv}/u_τ^2	$\overline{u^3}/(u^+)^3$	$\overline{v^3}/(u^+)^3$	$\overline{u^4}/(u^+)^4$	$\overline{v^4}/(u^+)^4$
2.39	2.62	1.066	0.299	0.015	0.804	0.386	3.56	10.60
3.40	3.46	1.371	0.314	0.000	0.868	0.636	3.66	11.70
4.42	4.32	1.669	0.372	-0.039	0.779	1.330	3.38	14.30
5.48	6.39	2.266	0.442	-0.202	0.643	0.418	3.13	11.00
7.01	8.10	2.565	0.546	-0.347	0.302	0.465	2.57	8.41
9.55	9.26	2.702	0.619	-0.438	0.148	0.334	2.47	7.85
12.08	10.32	2.770	0.675	-0.590	0.126	0.461	2.50	7.82
14.61	11.03	2.766	0.739	-0.656	-0.010	0.148	2.43	6.46
17.15	11.88	2.714	0.929	-0.765	-0.080	0.319	2.51	5.21
19.68	12.49	2.658	0.880	-0.846	-0.120	0.275	2.53	5.06
24.75	13.05	2.525	0.934	-0.893	-0.122	0.099	2.59	4.24
29.81	14.03	2.382	1.040	-0.944	-0.164	0.158	2.74	4.34
39.95	14.71	2.215	1.117	-0.868	-0.125	0.282	2.80	3.87
50.08	15.93	2.042	1.152	-0.952	-0.031	0.194	2.65	3.54
90.63	16.78	1.986	1.169	-0.936	0.011	0.130	2.60	3.45
132.17	17.46	1.921	1.154	-0.916	-0.032	0.124	2.66	3.18
172.71	18.10	1.901	1.161	-0.887	-0.012	0.102	2.67	3.29
213.26	18.67	1.829	1.155	-0.848	-0.068	0.048	2.70	3.28
253.80	18.94	1.791	1.142	-0.819	-0.086	0.143	2.89	3.22
294.35	20.22	1.701	1.109	-0.767	-0.194	0.167	2.65	3.51
395.71	21.07	1.629	1.078	-0.753				
497.07	21.81	1.547	1.026	-0.667				
598.44	22.64	1.444	0.971	-0.605				
699.80	23.34	1.313	0.886	-0.487				
801.16	24.05	1.134	0.770	-0.337				
902.52	24.77	0.838	0.621	-0.155				
1054.57	25.22	0.517	0.465	-0.025				
1206.61	25.34	0.367	0.345	0.007				
1358.65	25.26	0.339	0.293	0.010				

Flow z7na

Flow parameters								
Re_0	$(x - x_t)$	$(x - x_e)$	U_0	u_t	θ	δ^*	β	G
3935	1867	1733	0.979	0.0385	3.86	5.36	0.	7.12
Π	$c_f (10^3)$	$v (10^6)$	δ					
0.59	3.09	.961	36.5					
Mean velocities and fluctuation statistics								
y^+	u^+	u'/u_t	v'/u_t	\overline{uv}/u_t^2	$\overline{u^3}/(u^+)^3$	$\overline{v^3}/(u^+)^3$	$\overline{u^4}/(u^+)^4$	$\overline{v^4}/(u^+)^4$
2.86	2.87	1.239	0.216	0.006	0.906	1.450	3.80	12.90
3.68	3.70	1.521	0.225	-0.025	0.797	1.770	3.43	20.00
4.57	4.58	1.735	0.239	-0.067	0.753	0.718	3.36	11.20
7.26	6.32	2.234	0.341	-0.200	0.518	0.751	2.86	12.90
9.81	8.11	2.585	0.435	-0.346	0.308	0.682	2.57	10.80
12.35	9.27	2.690	0.509	-0.462	0.202	0.201	2.49	7.26
14.57	10.10	2.811	0.590	-0.578	0.071	0.159	2.43	6.94
18.15	11.65	2.763	0.716	-0.729	-0.147	-0.107	2.45	5.22
19.97	10.86	2.830	0.684	-0.649	0.071	-0.116	2.39	6.31
25.06	12.42	2.734	0.850	-0.903	-0.162	-0.024	2.52	4.80
30.14	13.12	2.568	0.914	-0.838	-0.139	-0.025	2.60	4.06
41.03	14.02	2.403	1.038	-0.967	-0.175	0.100	2.68	3.77
51.20	14.56	2.288	1.055	-0.947	-0.146	0.158	2.87	3.45
91.87	15.94	2.043	1.132	-0.910	0.028	0.241	2.95	3.37
132.54	16.82	2.026	1.136	-0.891	-0.007	0.138	2.80	3.26
173.22	17.50	1.939	1.137	-0.864	-0.016	0.105	2.80	3.23
213.89	18.12	1.892	1.128	-0.875	-0.022	0.068	2.82	3.27
254.56	18.50	1.866	1.141	-0.871	-0.070	0.157	2.84	3.10
295.23	19.04	1.834	1.136	-0.829	-0.034	0.149	2.64	3.11
396.91	19.96	1.719	1.099	-0.763				
498.39	20.84	1.666	1.086	-0.767				
650.91	22.07	1.544	1.008	-0.649				
803.43	23.09	1.362	0.921	-0.512				
955.95	23.93	1.188	0.805	-0.362				
1108.46	24.60	0.959	0.684	-0.222				
1260.98	25.16	0.689	0.547	-0.083				
1413.50	25.43	0.470	0.410	-0.013				
1566.02	25.47	0.393	0.381	0.011				
1718.54	25.45	0.349	0.296	0.008				

Flow z3la

Flow parameters								
Re_θ	$(x - x_i)$	$(x - x_e)$	U_e	u_τ	θ	δ^*	β	G
2250	754	620	0.976	0.0297	2.20	3.25	0	10.6
Π	$c_f (10^3)$	$v (10^6)$	δ	Q_i/Q_e	$Re_\theta _N$	% DR	κ	B
0.14	1.85	.961	20.9	2.6	2478	46.1	0.21	1.9
Mean velocities and fluctuation statistics								
y^+	u^+	u'/u_τ	v'/u_τ	\overline{uv}/u_τ^2	$\overline{u^3}/(u^+)^3$	$\overline{v^3}/(u^+)^3$	$\overline{u^4}/(u^+)^4$	$\overline{v^4}/(u^+)^4$
4.67	4.00	1.660	0.236	0.015	1.330	0.024	5.22	8.56
8.59	6.62	1.945	0.241	-0.014	0.502	0.060	3.05	3.75
12.52	9.95	2.781	0.297	-0.104	0.344	0.030	2.77	1.07
16.44	11.93	3.214	0.344	-0.172	0.289	0.227	2.76	4.08
20.37	13.60	3.564	0.403	-0.287	0.165	0.367	2.51	3.64
24.29	15.50	3.836	0.466	-0.440	0.073	0.202	2.50	4.39
28.22	16.83	3.871	0.518	-0.488	0.011	0.072	2.48	4.05
32.14	17.31	3.749	0.539	-0.500	-0.059	0.086	2.53	4.89
36.07	18.61	3.852	0.657	-0.667	-0.131	0.148	2.46	4.49
39.99	18.79	3.779	0.628	-0.668	-0.157	0.059	2.47	4.15
71.39	22.00	3.369	0.882	-0.789	-0.357	-0.043	2.85	4.64
102.79	23.85	2.909	1.035	-0.916	-0.422	0.004	2.94	3.43
134.19	25.24	2.608	1.119	-0.980	-0.428	0.008	3.12	3.57
165.59	25.97	2.394	1.159	-0.933	-0.330	-0.016	2.53	3.67
196.99	26.78	2.249	1.165	-0.907	-0.375	-0.014	3.02	3.30
228.39	27.60	2.152	1.170	-0.903	-0.373	0.044	3.00	2.77
346.14	29.78	1.746	1.112	-0.700				
463.89	31.44	1.414	0.964	-0.455				
581.64	32.66	0.925	0.762	-0.107				
699.39	33.05	0.584	0.543	0.074				
817.14	32.70	0.530	0.439	0.092				

Flow z41a

Flow parameters								
Re_θ	$(x - x_t)$	$(x - x_s)$	U_θ	u_c	θ	δ^*	β	G
2412	1058	924	0.980	0.0336	2.36	3.32	0.	8.43
Π	$c_f (10^3)$	$\nu (10^6)$	δ	Q_i/Q_s	$Re_\theta _N$	% DR	κ	B
0.23	2.35	.961	23.2	2.6	2978	27.7	0.30	5.7
Mean velocities and fluctuation statistics								
y^+	u^+	u'/u_c	v'/u_c	\overline{uv}/u_c^2	$\overline{u^3}/(u^+)^3$	$\overline{v^3}/(u^+)^3$	$\overline{u^4}/(u^+)^4$	$\overline{v^4}/(u^+)^4$
5.73	4.90	1.531	0.387	0.048	0.525	0.482	3.23	6.12
10.17	8.21	2.517	0.448	-0.086	0.323	0.662	2.76	9.91
14.61	11.01	3.065	0.528	-0.291	0.164	0.367	2.50	10.30
19.06	12.88	3.339	0.604	-0.468	0.049	0.607	2.41	8.22
23.50	14.43	3.537	0.602	-0.581	-0.119	0.087	2.42	5.38
27.94	15.58	3.540	0.652	-0.673	-0.177	0.373	2.42	7.27
32.38	16.12	3.543	0.679	-0.664	-0.229	0.075	2.43	5.22
36.82	17.06	3.463	0.768	-0.781	-0.304	-0.004	2.56	3.92
41.26	17.59	3.377	0.824	-0.835	-0.353	-0.026	2.65	4.59
76.78	20.03	2.841	1.006	-0.931	-0.408	0.027	2.88	3.63
112.30	21.34	2.476	1.117	-0.964	-0.406	0.036	3.02	3.39
147.83	22.23	2.286	1.169	-0.976	-0.311	0.076	2.62	3.71
183.35	23.48	2.060	1.192	-0.994	-0.260	0.110	2.74	3.15
218.87	23.48	2.060	1.192	-0.994	-0.260	0.110	2.74	3.15
254.40	24.02	1.935	1.163	-0.893	-0.277	0.052	2.74	2.95
387.61	25.74	1.692	1.124	-0.799				
520.82	27.15	1.496	1.015	-0.593				
654.03	28.33	1.255	0.869	-0.350				
787.24	29.09	0.818	0.683	-0.078				
920.45	29.38	0.493	0.475	0.034				
1053.66	29.19	0.418	0.385	0.045				
1186.87	29.07	0.387	0.356	0.047				

Flow z61a

Flow parameters								
Re_θ	$(x - x_t)$	$(x - x_s)$	U_e	u_τ	θ	δ^*	β	G
3107	1513	1379	0.978	0.0336	3.05	4.17	0	7.82
Π	$c_f (10^3)$	$v (10^6)$	δ	Q_i/Q_s	$Re_\theta _N$	% DR	κ	B
0.29	2.36	.961	29.2	2.6	3527	24.6	0.33	6.7
Mean velocities and fluctuation statistics								
y^+	u^+	u'/u_τ	v'/u_τ	$\bar{u}v/u_\tau^2$	$\bar{u}^3/(u^+)^3$	$\bar{v}^3/(u^+)^3$	$\bar{u}^4/(u^+)^4$	$\bar{v}^4/(u^+)^4$
5.33	4.59	1.593	0.240	0.005	0.602	1.580	3.03	12.00
7.55	6.35	2.098	0.249	-0.028	0.389	0.785	2.73	7.51
9.77	8.06	2.579	0.295	-0.126	0.430	0.516	2.92	9.44
11.99	9.36	2.868	0.341	-0.216	0.320	0.564	2.60	9.91
14.21	10.67	3.105	0.390	-0.301	0.239	0.166	2.60	6.34
16.43	11.73	3.269	0.430	-0.420	0.142	-0.052	2.41	8.00
18.65	12.88	3.391	0.515	-0.501	0.007	0.264	2.35	6.43
20.87	13.40	3.416	0.534	-0.570	-0.002	0.352	2.34	6.27
23.09	14.21	3.498	0.589	-0.652	-0.086	0.151	2.32	6.52
27.53	15.30	3.457	0.655	-0.717	-0.222	-0.108	2.40	5.11
36.41	16.28	3.365	0.698	-0.789	-0.272	0.030	2.53	4.91
45.28	17.65	3.187	0.844	-0.885	-0.315	0.174	2.68	4.74
63.04	19.09	2.833	0.942	-0.973	-0.443	0.164	3.07	3.61
80.80	19.91	2.576	1.011	-0.845	-0.305	0.112	2.88	3.66
116.32	20.95	2.292	1.093	-0.973	-0.318	0.106	2.96	3.42
151.85	21.72	2.116	1.144	-1.026	-0.251	0.138	2.87	3.41
187.37	22.33	2.013	1.114	-0.875	-0.248	0.181	3.09	3.49
222.91	22.91	1.941	1.127	-0.935	-0.186	0.137	2.20	3.33
258.42	23.39	1.848	1.127	-0.833	-0.190	0.122	2.38	3.11
293.95	23.71	1.834	1.134	-0.891	-0.165	0.155	2.34	3.39
382.75	24.68	1.702	1.095	-0.781				
471.55	25.53	1.587	1.065	-0.721				
604.77	26.54	1.469	1.005	-0.621				
737.98	27.64	1.252	0.866	-0.408				
871.19	28.39	1.021	0.755	-0.258				
1004.40	28.99	0.706	0.594	-0.078				
1137.61	29.20	0.499	0.459	0.011				
1270.82	29.13	0.425	0.363	0.029				

Flow z71a

Flow parameters								
Re_0	$(x - x_c)$	$(x - x_s)$	U_c	u_c	θ	δ^+	β	G
3091	1867	1733	0.970	0.0350	3.06	4.11	0.	7.08
Π	$c_f (10^3)$	$v (10^6)$	δ	Q_i/Q_s	$Re_0 _{N}$	% DR	κ	B
0.27	2.60	.961	33.8	2.6	3935	15.9	0.36	6.8
Mean velocities and fluctuation statistics								
y^+	u^+	u'/u_c	v'/u_c	$\bar{u}v/u_c^2$	$\bar{u}^3/(u')^3$	$\bar{v}^3/(u')^3$	$\bar{u}^4/(u')^4$	$\bar{v}^4/(u')^4$
5.14	5.02	1.729	0.431	0.019	0.638	0.596	3.35	7.02
9.76	8.55	2.651	0.434	-0.168	0.380	0.626	2.72	12.40
14.39	11.09	3.090	0.552	-0.408	0.134	0.524	2.46	11.20
19.01	13.05	3.245	0.634	-0.546	-0.097	0.098	2.41	7.01
23.64	14.32	3.189	0.709	-0.653	-0.188	-0.137	2.46	7.92
28.26	15.19	3.177	0.800	-0.839	-0.250	0.051	2.48	6.38
32.89	15.97	3.051	0.866	-0.864	-0.300	0.166	2.66	4.43
37.51	16.58	2.909	0.884	-0.877	-0.372	0.035	2.79	4.12
74.52	16.58	2.909	0.884	-0.877	-0.372	0.035	2.79	4.12
111.52	18.73	2.395	1.080	-1.003	-0.351	0.157	3.05	3.52
148.52	20.70	2.011	1.136	-0.902	-0.175	0.067	2.92	3.47
185.53	21.21	1.936	1.143	-0.899	-0.148	0.107	3.01	3.58
222.53	21.73	1.896	1.139	-0.904	-0.140	0.169	2.04	3.18
259.53	22.23	1.809	1.120	-0.822	-0.083	0.137	2.31	3.42
398.29	23.68	1.626	1.055	-0.683				
537.06	24.70	1.482	1.005	-0.603				
675.82	25.73	1.321	0.906	-0.425				
814.58	26.51	1.129	0.801	-0.306				
953.34	27.14	0.937	0.712	-0.172				
1092.10	27.52	0.688	0.581	-0.047				
1230.86	27.66	0.525	0.489	0.012				
1369.63	27.71	0.451	0.412	0.035				
1508.39	27.80	0.415	0.363	0.030				

Flow z3ha

Flow parameters								
Re_θ	$(x - x_t)$	$(x - x_s)$	U_e	u_τ	θ	δ^*	β	G
2091	754	620	0.982	0.0284	2.43	3.44	0.	10.15
Π	$c_f (10^3)$	$v (10^6)$	δ	Q_i/Q_s	$Re_\theta _N$	% DR	κ	B
0.13	1.67	.961	18.8	5.1	2478	50.4	0.19	0.93
Mean velocities and fluctuation statistics								
y^+	u^+	u'/u_τ	v'/u_τ	\overline{uv}/u_τ^2	$\overline{u^3}/(u^+)^3$	$\overline{v^3}/(u^+)^3$	$\overline{u^4}/(u^+)^4$	$\overline{v^4}/(u^+)^4$
4.47	3.80	1.207	0.213	0.023	0.683	0.090	3.52	4.38
8.22	6.50	1.879	0.224	-0.002	0.614	0.018	3.16	0.77
11.97	9.16	2.556	0.267	-0.047	0.471	-0.040	3.10	1.93
15.72	11.05	2.917	0.305	-0.111	0.419	0.148	3.00	0.86
19.48	12.92	3.361	0.358	-0.214	0.381	0.206	2.80	3.82
23.23	14.22	3.519	0.394	-0.241	0.373	0.093	2.88	4.71
26.98	15.49	3.697	0.433	-0.310	0.248	0.149	2.71	5.46
30.73	16.65	3.732	0.467	-0.383	0.216	0.220	2.67	2.97
34.49	17.46	3.805	0.526	-0.364	0.136	0.179	2.55	4.02
38.24	18.05	3.802	0.552	-0.435	0.104	0.032	2.52	3.25
41.99	18.86	3.946	0.569	-0.519	0.051	0.042	2.49	6.01
45.75	19.50	3.837	0.607	-0.555	-0.017	0.041	2.52	4.03
53.25	20.51	3.829	0.659	-0.620	-0.093	0.175	2.49	2.85
60.76	21.67	3.764	0.708	-0.702	-0.120	-0.048	2.49	3.36
98.29	24.73	3.251	0.929	-0.965	-0.373	-0.104	2.77	4.28
135.82	26.29	2.840	1.069	-0.973	-0.374	-0.150	2.87	3.34
173.36	27.69	2.447	1.079	-0.934	-0.370	-0.159	2.79	4.02
210.89	29.13	2.155	1.122	-0.951	-0.445	-0.040	3.36	3.22
323.48	31.15	1.843	1.144	-0.870				
436.08	33.03	1.526	1.032	-0.562				
586.20	34.51	0.792	0.706	-0.006				
736.33	34.31	0.542	0.456	0.063				

Flow z4hb

Flow parameters								
Re_0	$(x - x_1)$	$(x - x_2)$	U_0	u_τ	θ	δ^*	β	G
2320	1058	924	0.961	0.0265	2.31	3.41	0.	10.32
Π	$c_f (10^3)$	$v (10^6)$	δ	Q_1/Q_2	$Re_0 _N$	% DR	κ	B
0.14	1.52	.961	21.8	5.1	2978	55.7	0.19	3.3
Mean velocities and fluctuation statistics								
y^+	u^+	u'/u_τ	v'/u_τ	\overline{uv}/u_τ^2	$\overline{u^3}/(u^+)^3$	$\overline{v^3}/(u^+)^3$	$\overline{u^4}/(u^+)^4$	$\overline{v^4}/(u^+)^4$
3.03	3.04	1.053	0.233	0.031	0.705	0.553	3.58	5.79
3.58	3.47	1.193	0.229	0.024	0.701	0.481	3.59	5.60
8.00	7.89	2.239	0.269	-0.007	0.478	0.449	3.03	4.95
13.51	11.61	3.182	0.322	-0.122	0.340	-0.052	2.93	4.87
19.03	14.13	3.574	0.386	-0.195	0.220	-0.044	2.72	8.13
24.54	16.29	3.981	0.463	-0.359	0.123	0.206	2.62	5.92
30.06	18.14	4.202	0.511	-0.429	0.056	0.117	2.48	6.51
35.57	18.80	4.216	0.543	-0.486	0.023	0.170	2.53	8.23
41.09	20.24	4.341	0.610	-0.642	-0.091	0.099	2.49	3.67
46.60	20.94	4.161	0.628	-0.611	-0.124	0.163	2.49	6.99
59.01	22.91	4.133	0.704	-0.698	-0.238	-0.030	2.54	3.05
71.42	23.63	4.050	0.825	-0.929	-0.299	-0.030	2.63	4.57
99.00	26.22	3.525	0.925	-0.969	-0.446	0.032	2.87	4.93
126.57	27.67	3.191	1.016	-0.999	-0.485	-0.013	2.99	4.28
154.15	28.82	2.877	1.056	-0.983	-0.539	0.056	3.41	4.38
181.72	29.37	2.754	1.141	-1.073	-0.479	0.044	3.00	4.06
236.87	30.89	2.382	1.145	-1.087	-0.467	-0.064	2.74	3.56
292.02	32.04	2.093	1.125	-0.947	-0.465	0.133	2.03	3.18
402.33	34.05	1.668	1.043	-0.756				
512.63	35.56	1.249	0.874	-0.389				
622.93	36.16	0.813	0.693	-0.104				
733.23	36.26	0.537	0.495	0.006				
71.42	23.24	4.018	0.815	-0.881	-0.240	0.118	2.58	6.00
126.57	27.26	3.242	1.026	-1.077	-0.468	0.017	3.09	3.80
181.72	29.01	2.826	1.158	-1.146	-0.442	-0.024	2.91	3.81

Flow z6hb

Flow parameters								
Re_θ	$(x - x_t)$	$(x - x_s)$	U_∞	u_τ	θ	δ^*	β	G
2830	1513	1379	0.992	0.0321	2.74	3.86	0.	8.97
Π	$c_f (10^3)$	$\nu (10^6)$	δ	Q_i/Q_s	$Re_\theta _N$	% DR	κ	B
0.19	2.09	.961	26.5	5.1	3527	32.9	0.27	4.6
Mean velocities and fluctuation statistics								
y^+	u^+	u'/u_τ	v'/u_τ	\overline{uv}/u_τ^2	$\overline{u^3}/(u^+)^3$	$\overline{v^3}/(u^+)^3$	$\overline{u^4}/(u^+)^4$	$\overline{v^4}/(u^+)^4$
4.33	4.03	1.382	0.224	0.003	0.641	-0.255	3.43	6.88
8.58	7.12	2.191	0.270	-0.072	0.480	-0.070	2.99	9.54
17.07	11.87	3.312	0.395	-0.311	0.179	0.040	2.51	7.75
21.31	13.52	3.593	0.464	-0.453	0.095	0.197	2.45	7.96
25.55	15.04	3.780	0.521	-0.600	-0.082	0.268	2.38	5.63
29.80	15.71	3.818	0.545	-0.581	-0.103	0.213	2.42	6.63
34.04	16.52	3.765	0.575	-0.641	-0.143	0.065	2.48	4.10
38.28	17.31	3.772	0.641	-0.773	-0.215	0.149	2.43	5.49
42.52	18.14	3.744	0.713	-0.857	-0.259	0.162	2.44	4.79
46.76	18.28	3.742	0.715	-0.886	-0.277	-0.012	2.53	4.46
51.01	18.71	3.659	0.721	-0.836	-0.301	0.075	2.59	4.78
84.94	21.17	3.135	0.918	-0.957	-0.408	0.125	2.86	3.98
118.88	22.67	2.708	1.001	-0.940	-0.362	0.040	2.87	3.64
152.82	23.47	2.491	1.057	-1.033	-0.375	0.049	2.87	3.31
186.75	24.21	2.344	1.077	-0.942	-0.365	0.087	3.05	2.91
220.69	24.84	2.201	1.085	-0.955	-0.315	0.135	2.86	3.01
254.63	25.34	2.026	1.056	-0.867	-0.303	0.109	2.77	3.70
381.89	27.01	1.766	1.063	-0.817				
509.16	28.18	1.602	0.998	-0.720				
636.42	29.21	1.393	0.891	-0.492				
763.69	30.13	1.136	0.782	-0.323				
890.95	30.80	0.814	0.637	-0.102				
1018.21	31.01	0.547	0.477	0.006				
1145.48	30.87	0.466	0.393	0.026				

Flow z7hb

Flow parameters								
Re_θ	$(x - x_t)$	$(x - x_s)$	U_θ	u_τ	θ	δ^*	β	G
3620	1867	1733	0.979	0.0294	2.94	4.03	0.	9.01
Π	$c_f (10^3)$	$v (10^6)$	δ	Q_i/Q_s	$Re_\theta _N$	% DR	κ	B
0.13	1.80	.961	31.6	5.1	3935	37.7	0.28	7.3
Mean velocities and fluctuation statistics								
y^+	u^+	u'/u_τ	v'/u_τ	\overline{uv}/u_τ^2	$\overline{u^3}/(u^+)^3$	$\overline{v^3}/(u^+)^3$	$\overline{u^4}/(u^+)^4$	$\overline{v^4}/(u^+)^4$
0.18	2.79	1.042	0.169	0.003	0.698	0.719	3.50	11.10
4.59	5.16	1.668	0.197	-0.032	0.578	0.487	3.33	12.60
9.18	8.99	2.578	0.266	-0.156	0.424	0.130	3.08	16.20
13.77	11.74	3.292	0.351	-0.365	0.192	0.358	2.64	3.94
18.36	13.96	3.571	0.404	-0.481	0.036	0.281	2.56	5.30
27.53	16.79	3.840	0.531	-0.756	-0.165	0.300	2.51	5.31
36.71	18.58	3.772	0.639	-0.840	-0.251	0.119	2.60	7.03
52.01	20.38	3.708	0.752	-0.979	-0.341	0.082	2.61	4.48
67.30	21.75	3.424	0.833	-1.033	-0.429	0.079	2.87	4.51
97.90	23.34	2.987	0.971	-1.075	-0.501	0.004	3.08	3.45
128.49	24.35	2.730	1.061	-1.096	-0.437	0.090	3.09	3.88
159.08	25.24	2.477	1.084	-1.004	-0.436	0.101	3.22	3.26
189.68	25.99	2.305	1.076	-0.961	-0.397	0.122	3.23	3.90
250.86	26.93	2.100	1.128	-1.049	-0.411	0.117	3.17	4.20
312.05	27.54	1.858	1.071	-0.874				
434.42	28.74	1.684	1.026	-0.791				
556.80	29.80	1.496	0.956	-0.636				
709.76	31.02	1.211	0.806	-0.381				
862.73	31.78	0.870	0.671	-0.198				
1015.69	32.12	0.539	0.476	-0.029				
1168.66	32.19	0.437	0.369	-0.006				
128.49	24.32	2.626	1.035	-1.025	-0.477	0.130	3.09	3.67
159.08	25.18	2.367	1.052	-1.008	-0.463	0.106	3.18	3.93
250.86	26.57	2.062	1.102	-0.960	-0.379	0.062	2.51	3.86

Flow m3na

Flow parameters								
Re_θ	$(x - x_t)$	$(x - x_s)$	U_e	u_τ	θ	δ^*	β	G
3566	854	720	0.798	0.0276	4.29	6.78	1.8	10.6
Π	$c_f (10^3)$	$\nu (10^6)$	δ					
1.58	2.39	.961	32.2					
Mean velocities and fluctuation statistics								
y^+	u^+	u'/u_τ	v'/u_τ	\overline{uv}/u_τ^2	$\overline{u^3}/(u^+)^3$	$\overline{v^3}/(u^+)^3$	$\overline{u^4}/(u^+)^4$	$\overline{v^4}/(u^+)^4$
2.01	2.02	0.938	0.253	0.032	0.842	0.419	3.71	6.47
2.87	2.93	1.303	0.248	0.021	0.807	0.387	3.67	6.68
3.73	3.77	1.619	0.261	-0.003	0.824	0.386	3.50	5.07
5.75	5.81	2.291	0.369	-0.124	0.623	0.334	3.05	10.60
11.49	9.10	2.798	0.613	-0.423	0.207	-0.059	2.61	6.61
17.24	10.63	2.839	0.797	-0.623	0.101	-0.024	2.63	5.01
22.98	11.54	2.761	0.980	-0.863	0.029	0.003	2.66	4.71
28.73	12.64	2.719	1.146	-0.884	-0.023	-0.057	2.79	4.44
43.09	13.73	2.577	1.323	-0.990	0.027	0.059	2.80	3.82
57.45	14.43	2.526	1.421	-1.117	0.072	0.032	2.81	3.64
86.18	15.44	2.479	1.501	-1.216	0.150	-0.060	2.83	3.28
114.91	16.27	2.502	1.555	-1.343	0.114	-0.032	2.73	3.17
143.63	16.95	2.526	1.589	-1.430	0.097	0.004	2.69	3.18
172.36	17.64	2.547	1.631	-1.491	0.073	-0.010	2.67	3.14
229.81	18.98	2.540	1.639	-1.564	0.006	0.019	2.69	2.97
287.26	20.18	2.527	1.639	-1.601	-0.066	0.104	2.73	2.97
344.72	21.41	2.458	1.582	-1.429				
402.17	22.71	2.362	1.547	-1.265				
517.07	25.03	2.088	1.336	-0.952				
631.98	26.84	1.644	1.116	-0.537				
746.88	28.04	1.077	0.820	-0.130				
861.79	28.56	0.648	0.586	0.047				
976.70	28.91	0.505	0.441	0.068				
1091.60	28.95	0.482	0.407	0.084				

Flow m4na

Flow parameters								
Re_0	$(x - x_t)$	$(x - x_s)$	U_e	u_t	θ	δ^*	β	G
4210	1101	967	0.744	0.0245	5.44	8.61	1.8	11.17
Π	$c_f (10^3)$	$v (10^6)$	δ					
1.80	2.00	.961	41.2					
Mean velocities and fluctuation statistics								
y^+	u^+	u'/u_t	v'/u_t	\overline{uv}/u_t^2	$\overline{u^3}/(u^+)^3$	$\overline{v^3}/(u^+)^3$	$\overline{u^4}/(u^+)^4$	$\overline{v^4}/(u^+)^4$
1.53	1.52	0.776	0.435	0.142	0.461	0.560	3.48	5.81
2.30	2.31	1.056	0.370	0.119	0.764	0.344	3.68	4.94
3.06	3.05	1.338	0.388	0.123	0.791	0.486	3.56	5.06
5.11	5.12	2.066	0.446	0.098	0.723	0.530	3.33	6.10
10.21	8.81	2.929	0.639	-0.207	0.299	0.117	2.64	6.27
15.32	11.08	3.023	0.812	-0.402	0.015	0.091	2.60	5.53
20.42	12.15	3.005	0.951	-0.562	0.008	-0.090	2.70	4.91
25.53	12.95	2.934	1.080	-0.678	-0.006	-0.010	2.82	4.83
38.29	14.17	2.712	1.243	-0.867	0.020	0.032	2.90	3.95
51.05	14.92	2.618	1.339	-0.908	0.068	0.043	2.85	3.68
76.58	15.87	2.582	1.470	-1.090	0.095	-0.028	2.82	3.46
102.10	16.57	2.604	1.526	-1.227	0.108	-0.054	2.81	3.44
127.63	17.15	2.608	1.593	-1.313	0.099	-0.039	2.66	3.49
153.15	17.63	2.585	1.614	-1.345	0.087	-0.096	2.72	3.18
204.20	18.69	2.647	1.679	-1.504	0.047	-0.010	2.66	3.23
255.25	19.71	2.653	1.685	-1.532	0.003	0.017	2.69	3.12
306.31	20.61	2.649	1.721	-1.558				
357.36	21.55	2.644	1.714	-1.562				
459.46	23.60	2.524	1.645	-1.416				
561.56	25.21	2.365	1.534	-1.210				
663.66	26.81	2.091	1.362	-0.874				
765.76	28.42	1.730	1.158	-0.556				
867.87	29.67	1.218	0.917	-0.167				
969.97	30.27	0.753	0.692	-0.014				

Flow m3la

Flow parameters								
Re_θ	$(x - x_t)$	$(x - x_s)$	U_e	u_τ	θ	δ^*	β	G
3523	854	720	0.802	0.0263	4.22	6.60	1.8	10.99
Π	$c_f (10^3)$	$v (10^6)$	δ	Q_i/Q_e	$Re_\theta _N$	% DR	κ	B
1.2	2.15	.961	37.5	2.6	3570	10.	0.35	4.3
Mean velocities and fluctuation statistics								
y^+	u^+	u'/u_τ	v'/u_τ	\overline{uv}/u_τ^2	$\overline{u^3}/(u^+)^3$	$\overline{v^3}/(u^+)^3$	$\overline{u^4}/(u^+)^4$	$\overline{v^4}/(u^+)^4$
1.64	2.23	1.050	0.280	0.054	0.845	0.148	3.77	4.94
2.46	3.06	1.313	0.289	0.070	0.839	0.483	3.68	6.22
3.28	3.75	1.557	0.331	0.057	0.767	0.496	3.50	6.34
6.84	7.01	2.669	0.479	-0.134	0.451	0.461	2.75	8.25
13.68	11.07	3.228	0.741	-0.511	0.049	0.182	2.50	5.61
20.53	12.96	3.230	0.876	-0.653	-0.081	0.251	2.60	5.07
27.37	14.03	3.039	0.972	-0.718	-0.128	0.031	2.79	4.74
41.05	14.95	2.855	1.191	-0.944	-0.126	0.076	2.87	3.90
54.73	15.86	2.741	1.331	-1.118	-0.024	0.096	2.83	3.89
82.10	16.93	2.625	1.447	-1.272	0.014	-0.010	2.85	3.45
109.47	17.69	2.596	1.546	-1.510	0.100	-0.026	2.90	3.24
164.20	19.20	2.597	1.625	-1.656	0.012	-0.053	2.76	3.21
218.94	20.24	2.645	1.646	-1.724	-0.030	-0.018	2.75	2.96
328.41	22.61	2.545	1.662	-1.669				
437.88	24.81	2.358	1.550	-1.410				
547.35	26.97	2.109	1.405	-1.110				
656.82	28.80	1.700	1.134	-0.656				
766.29	30.07	1.183	0.861	-0.238				
875.75	30.70	0.664	0.627	-0.006				
985.22	30.35	0.522	0.452	0.035				

Flow m3ha

Flow parameters								
Re_0	$(x - x_t)$	$(x - x_t)$	U_0	u_t	θ	δ^*	β	G
3567	854	720	0.804	0.0246	4.26	6.75	1.8	12.04
Π	$c_f (10^3)$	$v (10^6)$	δ	Q_i/Q_0	$Re_0 _N$	% DR	κ	B
0.66	1.87	.961	37.5	5.1	3570	22.	0.29	3.2
Mean velocities and fluctuation statistics								
y^+	u^+	u'/u_t	v'/u_t	\overline{uv}/u_t^2	$\overline{u^3}/(u^+)^3$	$\overline{v^3}/(u^+)^3$	$\overline{u^4}/(u^+)^4$	$\overline{v^4}/(u^+)^4$
1.54	1.99	0.885	0.283	0.061	0.622	0.320	3.29	4.57
2.30	2.88	1.223	0.298	0.073	0.717	0.412	3.49	5.43
3.07	3.63	1.474	0.323	0.049	0.647	0.331	3.27	5.16
6.40	7.49	2.854	0.512	-0.153	0.451	0.461	2.75	8.25
12.80	10.78	3.414	0.619	-0.369	0.174	0.190	2.57	5.76
19.20	13.08	3.570	0.793	-0.593	-0.044	0.184	2.55	6.43
25.60	14.16	3.518	0.865	-0.705	-0.059	-0.001	2.72	5.18
38.40	15.92	3.286	1.104	-0.970	-0.142	-0.115	2.82	4.36
51.20	16.71	3.190	1.258	-1.107	-0.114	-0.097	2.85	4.00
76.80	17.93	2.977	1.486	-1.415	-0.089	-0.029	2.99	3.40
102.39	18.87	2.930	1.619	-1.693	-0.003	-0.037	2.88	3.36
153.59	20.32	2.884	1.724	-1.909	-0.035	-0.035	2.86	3.20
204.79	21.62	2.936	1.774	-2.068	-0.068	0.034	2.84	3.13
307.18	24.00	2.863	1.777	-2.089				
409.57	26.36	2.701	1.703	-1.857				
511.97	28.79	2.326	1.497	-1.350				
614.36	30.76	1.852	1.240	-0.777				
716.75	32.20	1.270	0.952	-0.288				
819.15	32.88	0.734	0.687	-0.022				
921.54	32.53	0.566	0.489	0.036				

Flow s3nc

Flow parameters								
Re_θ	$(x - x_t)$	$(x - x_s)$	U_∞	u_τ	θ	δ^*	β	G
3784	840	706	0.780	0.0249	4.66	7.626	2.44	12.2
Π	$c_f (10^3)$	$\nu (10^6)$	δ					
2.10	2.05	.961	32.7					
Mean velocities and fluctuation statistics								
y^+	u^+	u'/u_τ	v'/u_τ	\overline{uv}/u_τ^2	$\overline{u^3}/(u')^3$	$\overline{v^3}/(u')^3$	$\overline{u^4}/(u')^4$	$\overline{v^4}/(u')^4$
3.12	3.28	1.475			0.936		3.91	
4.15	4.08	1.801			0.870		3.71	
4.93	4.84	2.112			0.772		3.45	
8.05	7.26	2.696			0.430		2.82	
14.54	10.35	3.100			0.148		2.62	
21.03	11.83	3.001			0.032		2.69	
27.52	12.70	2.878			-0.002		2.68	
53.48	14.52	2.712			0.122		2.86	
79.45	15.56	2.659			0.124		2.77	
105.41	16.37	2.630			0.199		2.86	
131.37	17.04	2.719			0.176		2.77	
157.33	17.67	2.714			0.085		2.69	
183.30	18.45	2.810			0.116		2.73	
209.26	19.09	2.860			0.069		2.65	
235.22	19.98	2.885			0.016		2.61	
285.59	21.13	2.875			-0.043		2.63	
337.51	22.63	2.803						
441.36	25.30	2.563						
545.21	27.64	2.173						
649.06	29.70	1.685						
752.91	31.03	1.036						
856.76	31.27	0.587						
960.61	31.21	0.482						

Flow s4nc

Flow parameters								
Re_0	$(x - x_1)$	$(x - x_2)$	U_e	u_c	θ	δ^*	β	G
4588	1008	874	0.733	0.0229	6.015	10.07	2.33	13.0
Π	$c_f (10^3)$	$v (10^6)$	δ					
2.20	1.96	.961	43.0					
Mean velocities and fluctuation statistics								
y^+	u^+	u'/u_c	v'/u_c	\overline{uv}/u_c^2	$\overline{u^3}/(u^+)^3$	$\overline{v^3}/(u^+)^3$	$\overline{u^4}/(u^+)^4$	$\overline{v^4}/(u^+)^4$
2.86	2.91	1.335	0.280	0.032	0.776	0.144	3.55	4.06
3.57	3.54	1.556	0.308	0.020	0.821	-0.285	3.58	6.63
4.05	4.11	1.752	0.316	0.019	0.773	0.053	3.49	4.74
11.20	8.76	2.813	0.603	-0.418	0.190	-0.084	2.55	5.97
17.16	10.60	3.029	0.900	-0.660	0.179	-0.072	2.65	5.63
23.11	11.89	2.930	1.064	-0.796	0.065	0.022	2.75	4.55
35.03	13.14	2.853	1.286	-1.006	0.085	-0.054	2.83	3.70
47.66	13.94	2.712	1.422	-1.110	0.070	-0.125	2.91	3.51
71.49	14.83	2.680	1.584	-1.378	0.107	-0.028	2.73	3.37
95.32	15.62	2.713	1.665	-1.512	0.134	-0.083	2.93	3.34
119.15	16.09	2.710	1.731	-1.553	0.192	-0.106	2.90	3.44
142.98	16.73	2.813	1.754	-1.655	0.173	-0.096	2.84	3.33
166.81	17.35	2.860	1.829	-1.838	0.146	-0.046	2.85	3.22
190.63	17.88	2.838	1.851	-1.866	0.080	-0.108	2.78	3.20
238.29	19.10	2.908	1.900	-1.992	0.078	-0.065	2.78	3.10
285.95	20.05	2.963	1.921	-2.138	0.069	-0.013	2.76	3.08
381.27	22.45	2.941	1.952	-2.262				
476.59	24.79	2.819	1.863	-1.995				
571.90	26.86	2.590	1.688	-1.607				
667.22	28.68	2.274	1.494	-1.206				
762.54	30.48	1.734	1.203	-0.552				
857.86	31.60	1.126	0.958	-0.147				
953.17	32.00	0.701	0.712	0.061				
1048.49	31.90	0.608	0.598	0.114				

Flow s4na

Flow parameters								
Re_θ	$(x - x_c)$	$(x - x_c)$	U_c	u_c	θ	δ^*	β	G
4978	1102	968	0.728	0.0226	6.57	11.0	2.73	13.0
Π	$c_f (10^3)$	$v (10^6)$	δ					
2.20	1.93	.961	47.0					
Mean velocities and fluctuation statistics								
y^+	u^+	u'/u_c	v'/u_c	\overline{uv}/u_c^2	$\overline{u^3}/(u^+)^3$	$\overline{v^3}/(u^+)^3$	$\overline{u^4}/(u^+)^4$	$\overline{v^4}/(u^+)^4$
1.41	1.32	0.796			1.030		4.39	
1.88	1.78	0.975			1.030		4.28	
2.59	2.50	1.245			0.966		3.98	
5.88	5.10	2.174			0.788		3.45	
11.76	9.00	3.003			0.236		2.68	
17.64	10.52	3.037			0.199		2.58	
23.52	10.52	3.037			0.199		2.58	
47.03	13.90	2.744			0.153		2.87	
70.55	14.90	2.658			0.182		2.89	
94.07	15.42	2.665			0.197		2.91	
117.59	16.17	2.752			0.140		2.87	
164.62	17.06	2.737			0.102		2.79	
211.65	18.29	2.895			0.107		2.77	
258.69	19.00	2.952			0.095		2.81	
305.72	20.19	2.975						
399.79	22.08	2.975						
493.86	24.26	2.930						
587.93	26.22	2.745						
682.00	28.29	2.439						
776.07	29.92	2.185						
870.14	31.50	1.541						
964.20	32.25	0.955						
1058.27	32.23	0.690						

Flow s4la

Flow parameters								
Re_θ	$(x - x_t)$	$(x - x_s)$	U_e	u_τ	θ	δ^*	β	G
Π	$c_f (10^3)$	$v (10^6)$	δ	Q_i/Q_e	$Re_\theta _N$	% DR	κ	B
4114	1012	876	0.726	0.0233	5.44	8.46	2.33	11.12
1.58	2.06	.961	38.0	2.6	4588	5.	0.35	5.8
Mean velocities and fluctuation statistics								
y^+	u^+	u'/u_τ	v'/u_τ	\overline{uv}/u_τ^2	$\overline{u^3}/(u^+)^3$	$\overline{v^3}/(u^+)^3$	$\overline{u^4}/(u^+)^4$	$\overline{v^4}/(u^+)^4$
1.70	2.18	1.057			0.972		3.99	
2.91	3.40	1.482			0.849		3.76	
12.12	9.43	3.148			0.302		2.60	
24.25	13.15	3.115			-0.163		2.60	
48.49	15.91	2.896			-0.231		2.83	
72.74	16.70	2.720			-0.026		2.84	
96.98	17.55	2.662			-0.011		2.90	
121.23	18.20	2.622			0.101		2.80	
157.60	18.93	2.624			0.102		2.70	
193.96	19.60	2.690			0.102		2.90	
290.95	21.72	2.585			-0.001		2.77	
387.93	23.43	2.737						
484.91	25.14	2.632						
581.89	27.13	2.415						
727.37	29.53	1.815						
872.84	30.89	0.920						
1018.31	31.18	0.592						

Flow s41b

Flow parameters								
Re_θ	$(x - x_i)$	$(x - x_s)$	U_c	u_τ	θ	δ^*	β	G
4380	1099	966	0.716	0.0223	5.88	9.22	2.73	11.63
Π	$c_f (10^3)$	$\nu (10^6)$	δ	Q_i/Q_s	$Re_\theta _N$	% DR	κ	B
1.60	1.94	.961	33.4	2.6	4978	0.	0.38	6.8
Mean velocities and fluctuation statistics								
y^+	u^+	u'/u_τ	v'/u_τ	\overline{uv}/u_τ^2	$\overline{u^3}/(u^+)^3$	$\overline{v^3}/(u^+)^3$	$\overline{u^4}/(u^+)^4$	$\overline{v^4}/(u^+)^4$
1.62	1.98	1.004			0.970		3.88	
2.32	2.80	1.270			0.868		3.55	
3.02	3.37	1.403			0.736		3.48	
11.60	9.72	3.124			0.321		2.66	
23.20	13.80	3.197			-0.045		2.68	
46.41	15.72	2.885			0.015		2.79	
92.82	17.85	2.667			0.015		2.88	
139.23	18.87	2.679			0.112		2.80	
232.05	20.80	2.666			0.097		2.96	
324.87	22.25	2.820						
417.69	24.32	2.615						
510.51	26.01	2.547						
649.74	28.54	2.363						

Flow s4ha

Flow parameters								
Re_θ	$(x - x_1)$	$(x - x_2)$	U_e	u_τ	θ	δ^+	β	G
4238	1012	876	0.727	0.0212	5.60	8.82	2.33	12.5
Π	$c_f (10^3)$	$\nu (10^6)$	δ	Q_i/Q_s	$Re_\theta _N$	% DR	κ	B
1.50	1.70	.961	41.9	5.1	4588	16.	0.32	5.7
Mean velocities and fluctuation statistics								
y^+	u^+	u'/u_τ	v'/u_τ	\overline{uv}/u_τ^2	$\overline{u^3}/(u^+)^3$	$\overline{v^3}/(u^+)^3$	$\overline{u^4}/(u^+)^4$	$\overline{v^4}/(u^+)^4$
1.54	2.16	1.060			0.837		3.76	
2.65	3.28	1.450			0.815		3.67	
11.03	9.52	3.266			0.385		2.81	
22.06	13.89	3.733			0.040		2.78	
44.12	16.95	3.526			-0.116		2.69	
66.18	18.32	3.169			0.029		2.92	
88.24	19.10	3.092			-0.017		2.98	
110.30	19.66	3.049			0.089		2.75	
143.39	20.43	2.958			-0.004		2.68	
176.48	21.33	2.953			0.134		2.69	
264.72	23.21	3.114			-0.046		2.60	
352.97	25.27	3.117						
441.21	27.52	2.926						
529.45	29.66	2.841						
661.81	32.28	2.176						
794.17	33.87	1.222						
926.53	34.31	0.676						

Flow s4hb

Flow parameters								
Re_θ	$(x - x_i)$	$(x - x_s)$	U_c	u_c	θ	δ^*	β	G
4528	1099	966	0.717	0.0200	6.07	9.56	2.73	13.1
Π	$c_f (10^3)$	$v (10^6)$	δ	Q_i/Q_s	$Re_\theta _N$	% DR	κ	B
1.70	1.56	.961	34.7	5.1	4980	5.	0.36	7.40
Mean velocities and fluctuation statistics								
y^+	u^+	u'/u_c	v'/u_c	\overline{uv}/u_c^2	$\overline{u^3}/(u^+)^3$	$\overline{v^3}/(u^+)^3$	$\overline{u^4}/(u^+)^4$	$\overline{v^4}/(u^+)^4$
1.46	2.12	1.082			0.987		4.11	
2.08	2.73	1.242			0.863		3.70	
2.71	3.46	1.477			0.752		3.49	
10.41	10.15	3.428			0.367		2.80	
20.81	15.03	3.703			-0.070		2.67	
41.62	17.90	3.429			-0.055		2.85	
83.25	19.86	3.158			0.029		2.86	
124.87	21.00	2.913			0.091		2.89	
208.12	22.94	3.115			0.103		2.88	
291.36	24.61	3.175			0.033		2.81	
374.61	26.60	3.193						
457.86	28.50	3.231						
582.73	31.32	2.837						

DISTRIBUTION LIST

Scientific Officer Code: 1132F
Lawrence P. Purtell
Office of Naval Research
800 North Quincy Street
Arlington, VA 22217-5000
(3 copies)

Administrative Grants Officer
Office of Naval Research
Resident Representative N62880
Administrative Contracting Officer
536 South Clark Street
Chicago, IL 60605-1588

Director, Naval Research Laboratory
Attn: Code 2627
Washington, DC 20375

Defense Technical Information Center
Building 5, Cameron Station
Alexandria, VA 22304-6145
(2 copies)

Mechanical Engineering Business Office
Purdue University
West Lafayette, IN 47907

Professor R.F. Blackwelder
University of Southern California
Dept. of Aerospace Engr.
University Park
Los Angeles, CA 90089-1191

Prof. D.G. Bogard
Dept. of Mechanical Engr.
The University of Texas
Austin, TX 78712

Dr. R.J. Hansen
Code 1215
Office of Naval Research
800 North Quincy Street
Arlington, VA 22217

Eric W. Hendricks
Code 634
Naval Ocean System Center
San Diego, CA 92152

Mr. G.W. Jones
DARPA/NTO
1515 Wilson Blvd.
Arlington, VA 22209

Dr. O. Kim
Code 6124
Naval Research Laboratory
Washington, DC 20375

Prof. S.J. Kline
Thermosciences Division
Dept. of Mechanical Engineering
Stanford University
Stanford, CA 94305

G. Leal
Dept. of Chemical & Nuclear Engr.
University of California
Santa Barbara, CA 93106

Justin H. McCarthy
Code 1540
David Taylor Research Center
Bethesda, MD 20084

Richard H. Nadolink
Code 821
Naval Underwater Systems Center
Bldg. 679/1
Newport, RI 02841-5047

W.G. Souders
Code 1543
David Taylor Research Center
Bethesda, MD 20084

Dr. M.M. Reishman
College of Engineering
101 Hammond Building
Pennsylvania State University
University Park, PA 16802

J.D. Swearingen
Code 4420
Naval Research Laboratory
Washington, DC 20375

Steve Robinson
M.S. 163
NASA-Langley Research Center
Hampton, VA 23665

Prof. David. T. Walker
Dept. of Naval Architecture & Marine Engr.
North Campus
Ann Arbor, MI 48109-2145